Shipman, Michael A. (2020) *Electrochemical and catalytic routes to small-molecule activation.* PhD thesis.

https://theses.gla.ac.uk/79018/

Electrochemical and Catalytic routes to Small-molecule activation

Michael A. Shipman MSci

Submitted in fulfilment of the requirements for the
Degree of Doctor of Philosophy

School of Chemistry
College of Science and Engineering
University of Glasgow

February 2020

Abstract

The work in this thesis is organised into five chapters:

In chapter 1 we discuss the importance of Ammonia and the various methods of synthesising it, with an emphasis on electrochemistry. During this introduction we will discuss the current and historical advances being made in the field, and comparing the various methods being employed to synthesise ammonia.

Chapter 2 is information about the various techniques and equipment used throughout the thesis. This should contextualise the methods used, so that the reader can understand why they have been employed.

Chapter 3 is the first research chapter, investigating the previously reported ability of Sn (II) Phthalocyanine complexes to reduce dinitrogen to ammonia. It was determined that there is no evidence for any catalysis in cyclic voltammetry or bulk electrolysis, and that any observed ammonia generation is either from contaminated Sn (II) Phthalocyanine, or due to electro-decomposition of these complexes under cathodic bias

In chapter 4, we investigate if stereoselective electrosynthesis is possible, in the context of the molecule 2,5-diacetoxy-2,5-dihydrofuran. We determined that in comparison to chemical methods prefer the *cis* isomer (2:1 *cis:trans*) as the major product, whereas the electrochemical synthesis prefers the trans product (7:5 *cis:trans*). In the course of this investigation, we solve the 3D crystal structure for 2,5-diacetoxy-2,5-dihydrofuran for the first time, as well as determined that it is possible to electrochemically synthesise 2,5-dibutoxy-2,5-dihydrofuran.

The 6th and final chapter is concerned with supramolecular coordination complexes (cages) and their ability to conduct host-guest reactions. We focused on small aromatic aldehydes and the Fe_4L_6 Nitschke cage. During our investigations we have shown that the cage molecule does indeed activate the carbonyl carbon for reaction with a weak hydride source. While the yields varied quite drastically, we have determined that smaller aldehydes (i.e. ones with less steric bulk) and ones with electronegative groups convert to the highest extent.

Table of contents

List of illustrations

Chapter 1

Chapter 2

Chapter 3

Chapter 4

Chapter 5

List of tables

Chapter 1

Chapter 3

Chapter 4

Chapter 5

List of abbreviations

AAS	Atomic Absorption Spectroscopy
AC	Alternating Current
ADP	Adenosine diphosphate
AES	Atomic Emission Spectroscopy
ATP	Adenosine triphosphate
b.p.	boiling point
BE	Bulk Electrolysis
CC	Carbon Cloth
CE	Counter Electrode
CEM	Cation Exchange Membrane
COSY	Correlation Spectroscopy
CV	Cyclic Voltammetry
DC	Direct Current
ECEC	Electrochemical-Chemical-Electrochemical-Chemical
EM	Electromagnetic
Et	Ethyl
EtOH	Ethanol
Fc	Ferrocene
FeMo	Iron-Molybdenum
FID	Free Induction Decay
GC	Glassy Carbon
HER	Hydrogen Evolution Reaction
HMQC	Heteronuclear Multiple Quantum Coherence
ICP	Inductively-Coupled Plasma
IR	Infrared
iR	Internal Resistance
ITO	Indium Tin Oxide
Me	Methyl
MOF	Metal-Organic Framework
Mr	Molecular Mass
MS	Mass Spectroscopy
NEMCA	Non-Faradaic Electrochemical Modification of Catalytic Activity
NHE	Normal Hydrogen Electrode
NMR	Nuclear Magnetic Resonance
NOE	Nuclear Overhauser effect
NOESY	Nuclear Overhauser Effect Spectroscopy
NRR	Nitrogen Reduction Reaction
PFPE	Perfluoropolyether
RE	Reference Electrode
RHE	Regular Hydrogen Electrode
SCE	Standard Calomel Electrode
SCY	Strontia-ceria-ytterbia
SHE	Standard Hydrogen Electrode
THF	Tetrahydrofuran
TMS	Trimethylsilyl
UK	United Kingdom

UV	Ultraviolet
WE	Working Electrode
XRD	X-Ray Diffraction

Acknowledgements

First and foremost I would like to thank my parents, for without their love, understanding (and money) my academic career would not have been possible. I would also like to thank Dr Symes for his unyielding patience and guidance on the journey of my PhD, and uncle Harry for the initial motivation to become a doctor in the first place.

Tom, Hallam, Jake, Alex, James & Aisling, and Kirsty: thank you for your help in keeping me sane throughout the last 4 years. Equal praise for this also goes to Phil, who was always there for me when I needed her.

The members of the Symes group: Paddy, Callum, Thanasis and Beth are also deserving of thanks for their reintroduction of banter to the group dynamic and just generally being cool people to work with. I would also like to acknowledge Avi for all of the help he has given in the lab, and for sharing in the endless columns.

To the many friends I have made in my time at Glasgow (in no particular order): 'Tiny' Sam, Lisa, Emily, Becky, Annmarie, Dan, Kate, Bart, Micky, Jakki, Sarah, 'mini' Ross, Isa, Penny, Sofia, Francois, Catherine, Siobhan, Simon, Davide, Nic, Alex, Carolina, Liam, Alan, Alisha, Annelouise, Mairi, Alin, Pannenkoek, Alex, Susan, Valery, David, Michaele, Stefan, John, Liam, Stefanie, Lorna, Guillame, Lewis, Edu, Eddie, Andrius, Marcus, James, Niall, Jim, Jess, Albane, Laura, Dan, Gregor, Glen, Stuart, Matt, Finley, Kopano, Laura, Tim, Selma, Wendy, Roberta, Jess, Moya, Alexandra, Angelos, Nicola, Justin, Smita. It's been real.

Big thanks to Drs Sproules and Wilson for the sharing of their expertise with my research, without which at least 2 chapters of this thesis would be not real. I would also like to thank Dr Draper and Prof. Adams for their academic support and life guidance.

The staff of the chemistry department are also worthy mentions: Karen, Lucy, Jess, Debbie, Frank, Stewart, Findlay and C.J. Without you, the department would be chaos.

Finally I would like to thank Dr. Harry Miras and Dr. Paul Lusby for taking the time to examine both me and my thesis.

Author's Declaration

I declare that, except where explicit reference is made to the contribution of others, this thesis is the result of my own work and has not been submitted for any other degree at the University of Glasgow or any other institution

I declare that this thesis has been produced in accordance with the University of Glasgow's Code of Good Practice in Research.

I acknowledge that if any issues are raised regarding good research practice based on review of the thesis, the examination may be postponed pending the outcome of any investigation of the issues.

Michael A. Shipman

Chapter 1

Recent Progress towards the Electrosynthesis of Ammonia from Sustainable Resources

Acknowledgements and declaration

This chapter includes extended and updated sections from the following paper:

“Recent Progress towards the Electrosynthesis of Ammonia from Sustainable Resources” **Shipman. M. A**; Symes. M. D, Catalysis today, **2017**, 286, 57-58

Paper was written through the contribution of all cited authors

Synopsis

Ammonia (NH_3) is a key commodity chemical of vital importance for fertilizers. It is made on an industrial scale *via* the Haber Bosch process, which requires significant infrastructure to be in place such that ammonia is generally made in large, centralized facilities. If ammonia could be produced under less demanding conditions, then there would be the potential for smaller devices to be used to generate ammonia in a decentralized manner for local consumption. Electrochemistry has been proposed as an enabling technology for this purpose as it is relatively simple to scale electrolytic devices to meet almost any level of demand. Moreover, it is possible to envisage electrosynthetic cells where water could be oxidized to produce protons and electrons at the anode which could then be used to reduce and protonate nitrogen to give ammonia at the cathode. If this nitrogen were sourced from the air, then the only required infrastructure for this process would be supplies of water, air and electricity, the latter of which could be provided by renewables. Hence an electrosynthetic cell for ammonia production could allow NH_3 to be generated sustainably in small, low-cost devices requiring only minimal facilities. In this Chapter, we describe recent progress towards such electrosynthetic ammonia production devices, summarizing also some of the seminal literature in the field. Comparison is made between the various different approaches that have been taken, and the key remaining challenges in the electrosynthesis of ammonia are highlighted.

1.1- Introduction

Ammonia is essential for fertilisers in order to feed the World's growing population. Indeed, it is estimated that between a third and half of us would starve to death if ammonia-based fertilisers were not available, and ammonia's industrial-scale synthesis from its elements is arguably the single biggest scientific discovery of the 20th century.[1] In 2018, total worldwide NH_3 production exceeded 140 million tons, and demand for ammonia continues to grow.[2]

Industrially, ammonia is produced almost exclusively *via* the Haber Bosch process. This process reacts high purity streams of N_2 and H_2 together at high temperatures and pressures (300 – 500 °C and 200 – 300 atm.) over iron or ruthenium-based catalysts, as in Equation 1:

$$\mathbf{3H_2 + N_2 \rightarrow 2NH_3} \qquad \text{(Equation 1)}$$

High temperatures are needed in order to off-set the sluggish kinetics of this reaction, however, the thermodynamics of this process favour ammonia decomposition to nitrogen and hydrogen at elevated temperatures and hence the need for high pressure. Including the energy required to obtain the pure feed gases, pressurization and so forth, ammonia synthesis by the Haber Bosch process typically requires an energy input of around 485 kJ mol^{-1}.[3] Whilst this is indeed a large amount of energy (especially in comparison to the Natural systems, see below), and therefore methods that reduce this requirement would be welcome, we shall see that this is in fact a very challenging target. Much is made of the inefficiencies of the Haber Bosch process and its requirement for pure H_2 (often obtained from fossil fuels), but currently there is no scalable ammonia synthesis technology that comes close to matching its performance.

Nitrogen reduction to ammonia on a heterogeneous surface can proceed by two broad classes of mechanism: *Associative* and *Dissociative* (see Figure 1.1). In an associative mechanism, the two nitrogen centres in N_2 remain bound to each other as the molecule is hydrogenated, with NH_3 being released only once the final N-N bond is broken. Hydrogenation in an associative mechanism can then itself be envisaged to occur through two possible pathways. Hydrogenation might occur preferentially on the nitrogen furthest away from the surface (assuming an end-on coordination mode for the N_2 molecule), leading to the release of one equivalent of NH_3 and leaving behind a metal nitrido ($M{\equiv}N$) unit which will itself be hydrogenated to give a second equivalent of ammonia. This is known as a *distal* associative pathway. The second type of associative mechanism (the *alternating* pathway) calls for each of the two nitrogen centres to undergo single hydrogenation events in turn, until such time as one of the nitrogens is converted into NH_3 and the N-N bond is broken. In a *dissociative* mechanism on the other hand, the N≡N bond is broken before any hydrogenation takes place, leaving individual N-adatoms on the surface which are converted into NH_3 independently. Current evidence suggests that the Haber Bosch process operates through a dissociative mechanism.

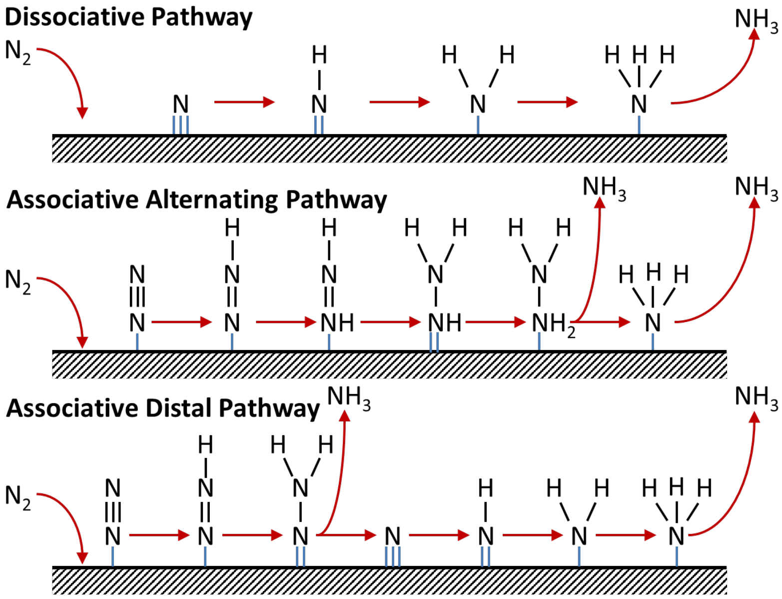

Figure 1.1. Generic mechanisms for nitrogen reduction to ammonia on heterogeneous catalysts.

In Nature, nitrogen reduction to ammonia is achieved by a class of enzymes called the nitrogenases and presents a very different picture to the Haber Bosch process. The most effective nitrogenases are the FeMo nitrogenases, which consist of two fused iron-sulfur clusters with a carbon atom at their junction and a molybdenum atom in one of the apical positions.[4, 5] It appears that a minimum of 16 equivalents of ATP (adenosine triphosphate) are required in order to reduce one N_2 molecule (Equation 2), meaning that 244 kJ are required per mole of NH_3 produced: [6]

$$\mathbf{N_2 + 8H^+ + 8e^- + 16ATP \rightarrow 2NH_3 + H_2 + 16ADP + 16P_i} \qquad \text{(Equation 2)}$$

Where ADP is adenosine diphosphate and P_i denotes “inorganic phosphate” (a mixture of HPO_4^{2-} and $H_2PO_4^-$ ions). The formation of H_2 as a side-product may well be obligatory, and indeed more H_2 than suggested by Equation 2 may be formed, rendering the energetic requirements for ammonia synthesis somewhat greater (depending on how much H_2 is actually produced). In contrast to the Haber Bosch process, the mechanism of formation is believed to be associative (with the N_2 molecule coordinating to a metal centre in the FeMo nitrogenase end-on), although whether hydrogenation proceeds by a distal or an associative pathway is still open to debate.[7] Regardless of the details of the mechanism operating, however, it is clear that nitrogenase enzymes are able to catalyse the production of ammonia from air and water under very mild conditions (room temperature and pressure, aqueous media) with impressive energy efficiency. Reproducing similar chemistry in a format applicable to industrial-scale production is in many respects the ultimate goal of all nitrogen reduction studies.

Against this backdrop, electrochemistry has emerged as an alternative technology by which to reduce nitrogen to ammonia.[8] In particular, an electrochemical system that oxidises water in order to obtain protons and electrons for the reduction of nitrogen would be very attractive, as the only inputs required would be N_2 (which could conceivably come from the air), water and electricity (which could conceivably come from renewable sources). The basic equations for such a process can be expressed as:

Anode (acidic conditions): $$\mathbf{3H_2O \rightarrow 3/2O_2 + 6H^+ + 6e^-} \qquad \text{(Equation 3a)}$$

Anode (basic conditions): $$\mathbf{6OH^- \rightarrow 3H_2O + 3/2O_2 + 6e^-} \qquad \text{(Equation 3b)}$$

Cathode (acidic conditions): $$\mathbf{N_2 + 6H^+ + 6e^- \rightarrow 2NH_3} \qquad \text{(Equation 4a)}$$

Cathode (basic conditions): $$\mathbf{N_2 + 6H_2O + 6e^- \rightarrow 2NH_3 + 6OH^-} \qquad \text{(Equation 4b)}$$

Overall: $$\mathbf{N_2 + 3H_2O \rightarrow 3/2O_2 + 2NH_3} \qquad \text{(Equation 5)}$$

Hence no fossil fuels would need to be consumed to generate ammonia. Furthermore, by exploiting the inherent flexibility of electrochemical systems, NH_3 production could be carried out at either a small or a large scale as required. It has been estimated that such a system could be up to 20% more energy-efficient than a Haber Bosch process using coal as the hydrogen source, although with today's technology it would remain 30% less efficient than a Haber Bosch process using natural gas as its hydrogen source.[9]

In this chapter, we shall examine recent progress towards electrochemical systems that produce ammonia by the reduction of nitrogen. We shall look in turn at systems where H_2, sacrificial reagents and water are used as the proton sources, and we shall also explore systems where air can be used directly as the source of nitrogen. It must be stated at the outset that all the electrochemical systems described herein produce ammonia at much slower rates and much less efficiently than does the Haber Bosch process. However, we hope that by highlighting some of the key advances and remaining challenges in this area that we will inspire the next generation of electrochemists to investigate this fascinating field, which may well have important implications for our food supply and for mitigating climate change in the near future.

1.2- Electrochemical ammonia production from N_2 and H_2

We shall begin our review by considering the electrosynthesis of ammonia from its elements, which is in some ways the exact electrochemical analogue of the Haber Bosch process. An important milestone in this field was set by Furuya and Yoshiba in 1990,[10] who demonstrated the production of ammonia from nitrogen and hydrogen in aqueous solution (1 M KOH) at room temperature using a back-to-back cell configuration. The authors screened 26 different cathode materials. ZnSe was found to be the most efficacious catalyst for N_2 reduction at an applied potential of –1 V *vs.* RHE, achieving a Faradaic yield for ammonia production of 1.3% whilst producing ammonia at an electrode area-normalized rate of 0.23 mol h^{-1} m^{-2} (see Table 1). Whilst this rate of ammonia formation is impressive in comparison to other electrochemical systems, the Faradaic yield is much less so. This is presumably because at these very negative cell potentials, water reduction to produce hydrogen becomes the dominant cathode reaction (especially given the high relative concentration of H_2O in the aqueous electrolyte employed). As we shall see throughout this chapter, suppressing the hydrogen evolution side-reaction is possibly the single biggest challenge facing N_2 reduction in the presence of water.

Subsequently, Marnellos and Stoukides managed to reduce the effects of competitive hydrogen evolution by employing a solid-state proton-conducting electrolyte in a cell reactor such as that shown in Figure 1.2.[11] In this design, both the cathode and anode were palladium, in-between which the ceramic H^+-conductor $SrCe_{0.95}Yb_{0.05}O_3$ was sandwiched as the electrolyte. Under atmospheric pressure at 570 °C, hydrogen supplied to the anode chamber was dissociated into electrons and protons when modest current densities (around 2 mA cm^{-2}) were applied to the cell.

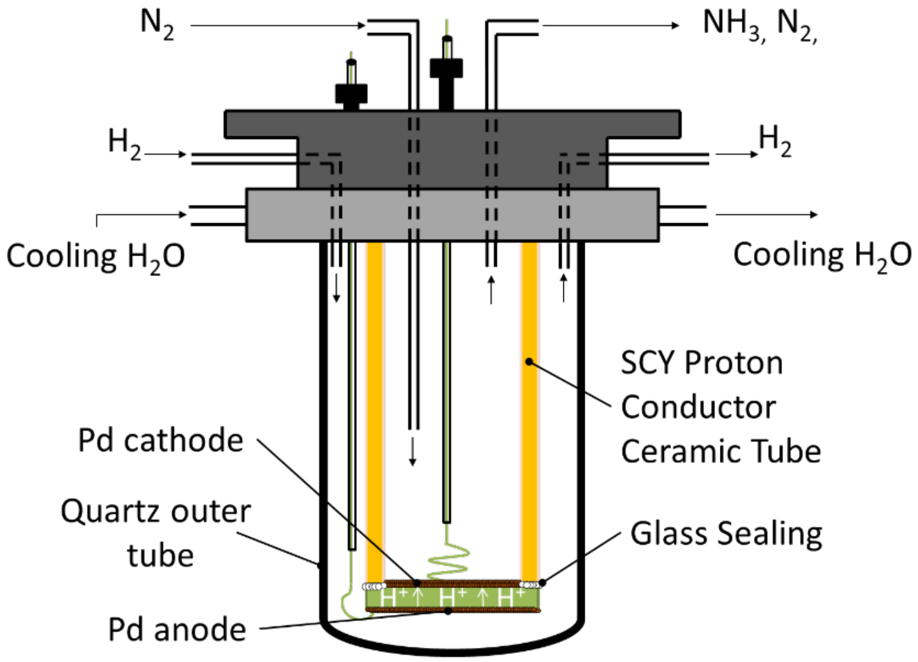

Figure 1.2: Marnellos and Stoukides' solid-electrolyte ammonia synthesis reactor.[11] SCY = Strontia-ceria-ytterbia.

When N_2 was present at the cathode, ammonia was produced according to Equation 4a. In contrast, no ammonia was observed in the absence of an applied bias. At 570 °C, a linear relationship was observed between the rate of ammonia production and the rate of electrochemical hydrogen supply (the latter calculated by dividing the current flowing by 2 × Faraday's constant for the two-electron oxidation of H_2 to protons), whilst the rate of ammonia formation was essentially independent of the partial pressure of N_2 over the range 0.3 to 1.8 kPa. This is in agreement with Equation 1: three times the number of moles of H_2 are required relative to moles of N_2, and so the rate of supply of H_2 (and hence protons and electrons) is likely to be limiting. Under the conditions probed, at least 78% of the electrochemically-dissociated hydrogen was converted into ammonia detectable in the product stream (*i.e.* the apparent Faradaic yield was at least 78%). The difference from ideal behaviour may be at least partially explained by product ammonia decomposition back to N_2 and H_2 within this high-temperature cell: the authors estimated in a separate experiment that up to 20% of a stream of NH_3 sent through the cell at 570 °C decomposed in this way. A maximum rate of ammonia production of 0.18 mol h^{-1} m^{-2} was obtained, although the authors noted that this rate was limited in large part by the high ohmic resistance of the proton conductor, which prevented current densities in excess of 2 mA cm^{-2} from being applied.

An interesting extension to this work was described independently by the Stoukides group[12] and by Vayenas and co-workers.[13] In the system described by the latter authors, a proton-conducting ceramic disc of $CaIn_{0.1}Zr_{0.9}O_{3-\alpha}$ was covered on one side with a layer of silver (to act as a hydrogen oxidation catalyst) and on the other side with a commercial iron-based Haber Bosch catalyst. An external electrical connection was established to allow bias potentials to be supplied and hence facilitate the movement of protons through the ceramic electrolyte (Figure 1.3). However, unlike the original Stoukides report, [11] a mixed N_2/H_2 stream was allowed to access both electrodes. At the anode under an applied bias, this resulted in oxidation of H_2 to protons and electrons at a rate that was measurable by examining the current flowing in the external circuit. However, the rate of ammonia production under these conditions was found to exceed that which could be expected on the basis of the rate of proton delivery to the cathode as given by Equation 4a. Indeed, it was found that for every proton arriving at the cathode, *two* molecules of NH_3 were formed. Clearly then, NH_3 production was not simply occurring in a Faradaic fashion as per Equation **4a**, but also catalytically as per Equation 1.

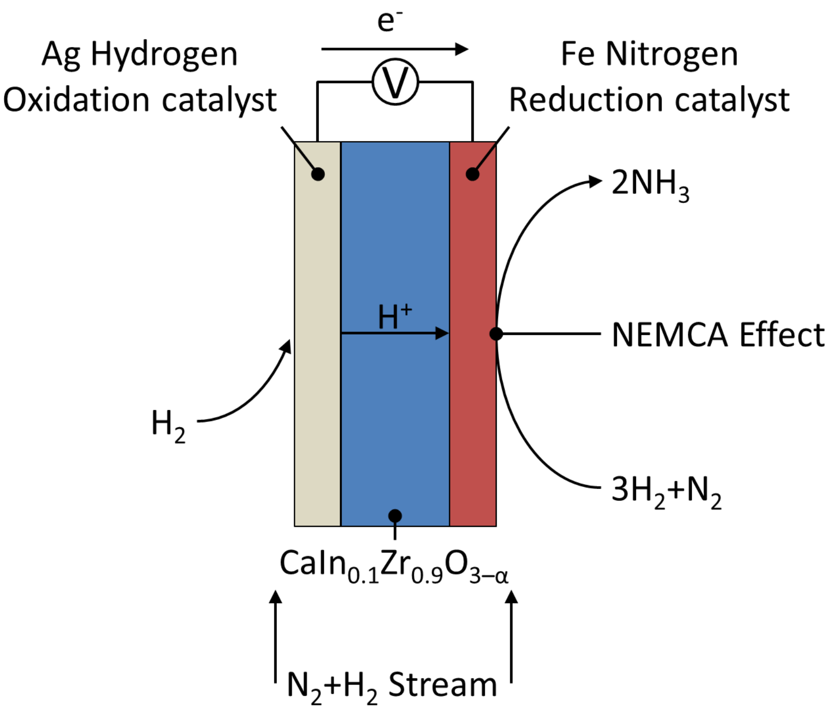

Figure 1.3. Vayenas' reactor for the electrochemical promotion of the catalytic synthesis of ammonia from its elements.[13]

Importantly, when no bias was applied to the cell (and hence no protons were supplied to the cathode, such that Equation 1 alone was operating in a manner similar to that in the conventional Haber Bosch reactor), the rate of ammonia production decreased by a factor of up to 1300%, depending on the ratio of N_2 to H_2 in the feed gas. The underlying cause of this behaviour is the phenomenon known as *Non-Faradaic Electrochemical Modification of Catalytic Activity* (NEMCA)[14-16] whereby an applied potential can be used to pump ions to or from a catalyst, thus improving its (non-Faradaic) catalytic activity. These results were subsequently re-visited by Stoukides *et al.*, who suggested that the cause of the NEMCA effect in this instance was a lowering of the Fe catalyst work function by the electrochemically-driven influx of protons from the anode, with this lowering of the work function facilitating N_2 chemisorption (generally held to be the rate-determining step) on the Fe catalyst.[17]

Molten salt electrolytes have also been explored for the electrosynthesis of NH_3 from its elements. For example, Ito and co-workers reported the electrosynthesis of ammonia in a molten salt eutectic mixture of LiCl-KCl-CsCl at 723 K.[18] A schematic of their experimental set-up is given in Figure 1.4. Hence nitrogen gas was introduced into the cell through the porous nickel gas diffusion cathode, where it was reduced to nitride according to the equation:

$$\mathbf{N_2 + 6e^- \rightarrow 2N^{3-}} \qquad \text{(Equation 6)}$$

The same group had already established that the electrochemical reduction of nitrogen gas at a nickel cathode in a molten LiCl-KCl system produced nitride ions almost quantitatively according to Equation 6.[19] Meanwhile, the anode reaction during Ito's electrochemical reduction of nitrogen to ammonia as shown in Figure 1.4 can be described by the equation:

$$\mathbf{2N^{3-} + 3H_2 \rightarrow 2NH_3 + 6e^-} \qquad \text{(Equation 7)}$$

This reaction is also performed over porous nickel. Under continuous operation for 1 h, a Faradaic efficiency for ammonia production of 72% was obtained, with ammonia being synthesised at an electrode area-normalised rate of 0.12 mol h^{-1} m^{-2}. The remaining 28% of the charge passed was speculated to be consumed in the non-productive re-oxidation of nitride to nitrogen (Equation 8), which is a possible competing anode reaction.

$$\mathbf{2N^{3-} \rightarrow N_2 + 6e^-} \qquad \text{(Equation 8)}$$

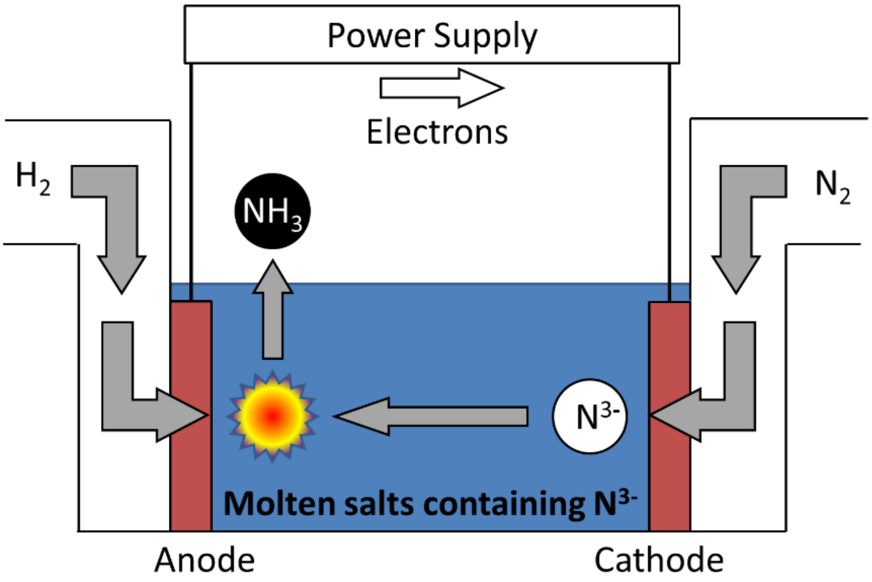

Figure 1.**4.** Ito's reactor for the electrosynthesis of ammonia in molten salt eutectics.[18]

Recently, the groups of both Ma and Tao have demonstrated increased rates of ammonia formation from nitrogen and hydrogen using more sophisticated ceramic electrode/electrolyte combinations. Ma's cell consisted of a $Ba_{0.5}Sr_{0.5}Co_{0.8}Fe_{0.2}O_{3-\alpha}$ cathode, a porous nickel-based anode and an interstitial membrane of $BaCe_{0.85}Y_{0.15}O_{3-\alpha}$ as the solid-state electrolyte.[20] Under an applied current of 2 mA cm^{-2} at 530 °C, a maximum rate of ammonia production of 0.15 mol h^{-1} m^{-2} was obtained with a Faradaic efficiency of H_2 conversion to NH_3 of 60%. This was further researched by the Otomo group, who were varying the exsolved size and mass of the Ru-nanoparticles.[21] However they only managed to achieve a maximum rate of ammonia production of 0.00396 mol h^{-1} m^{-2} using their Ni-doped $BaCe_{0.9}Y_{0.1}O_3$ electrolyte and an applied bias of -0.3 V. While they were only able to get a faradaic yield of ~0.2%, they were able to conclude that while the amount of Ru did have a large effect on ammonia formation, it appears to be a fine balance of efficiency and electrical conductivity introduced by the Ni-doping. Meanwhile, Tao and co-workers assembled a cell that used a composite samarium-doped cerium / ternary carbonate (Li_2CO_3- Na_2CO_3- K_2CO_3) electrolyte with a $La_{0.6}Sr_{0.4}Fe_{0.8}Cu_{0.2}O_{3-\delta}$ -$Ce_{0.8}Sm_{0.2}O_{2-\delta}$ composite cathode and a nickel oxide / samarium-doped cerium anode.[22] The optimum rate of ammonia production of 0.19 mol h^{-1} m^{-2} was achieved at a cell bias of 0.8 V and a temperature of 450 °C. An overall electrical energy efficiency of 7700 kJ mol^{-1} of NH_3 produced has been estimated for this system by Hetterscheid and co-workers,[6] which is an energy requirement around 15 times greater than that required by a Haber Bosch-type system even before the costs of obtaining H_2 for this electrosynthesis are considered. This in many ways indicates the scale of the challenge facing electrocatalytic methods of nitrogen reduction if they are ever to approach the efficiency of existing routes to NH_3 production.

As noted above, lower temperature devices reduce the extent of ammonia decomposition back to N_2 and H_2. With this in mind, Liu and co-workers investigated the electrosynthesis of ammonia from nitrogen and hydrogen at atmospheric pressure and relatively low temperatures (up to 100 °C) in a cell containing a $SmBaCuNiO_x$ nitrogen reduction cathode, a $Ni\text{-}Ce_{0.8}Sm_{0.2}O_{2-\delta}$ ceramic pellet anode and using Nafion as the electrolyte.[23] Nafion is used widely in numerous electrochemical devices such as hydrogen-oxygen fuel cells and proton-exchange membrane electrolyzers,[24] is physically very flexible, is produced on a large scale, and has excellent chemical and mechanical stability. An optimal rate of ammonia production of 0.31 mol h^{-1} m^{-2} was obtained from this cell at a temperature of 80 °C and a bias across the cell of 2.5 V. On account of the known practicality of Nafion in commercial electrochemical devices, cells such as this have great potential as the basis of low-temperature ammonia electrosynthesis platforms, provided the rate and efficiency of ammonia production can be kept acceptably high.

Finally in this section, Wessling and co-workers have recently used Rh and Ru catalysts on Ti felt supports as catalysts for the production of ammonia from N_2 and H_2 in aqueous acidic electrolyte. Ru was found to be the more desirable catalyst of the two, on account of its superior catalysis of ammonia production (a rate for NH_3 generation of 0.0043 mol h^{-1} m^{-2} was measured), its lower cost, and because it is easier to plate onto the robust Ti support than Rh.[25] However, no Faradaic yields for ammonia production were quoted and we may speculate that significant H_2 evolution may have occurred, on account of precious metals such as Ru and Rh being good proton reduction catalysts. These results, and others from Section 2, are summarized in Table 1.

Table 1.1: Examples of systems that generate ammonia electrochemically from its elements with selected metrics and conditions. A "-" indicates that this data is not given in the source reference.

Entry	Electrolyte	Optimal Temperature (°C)	Optimal rate of NH_3 production (mol h^{-1} m^{-2})	Faradaic yield for NH_3	Reference
1	1 M KOH	25	0.23	1.3%	10
2	$SrCe_{0.95}Yb_{0.05}O_3$	570	0.18	>78%	11
3	LiCl-KCl-CsCl	450	0.12	72%	18
4	$BaCe_{0.85}Y_{0.15}O_{3-\alpha}$	530	0.15	60%	20
5	Ni-doped $BaCe_{0.9}Y_{0.1}O_3$	500	0.00396	>0.2%	21
6	Sm-doped Ce / (Li_2CO_3-Na_2CO_3- K_2CO_3)	450	0.19	-	22
7	Nafion	80	0.31	-	23
8	0.5 M H_2SO_4	30	0.0043	-	25

1.3- Electrochemical ammonia production using sacrificial proton donors

An alternative to the use of H_2 as a source of protons and electrons for N_2 hydrogenation is to use sacrificial reactants that are destroyed as they are oxidised. Whilst this is probably even less sustainable than a fossil fuel-fed Haber Bosch reactor, the use of sacrificial reagents that can be easily handled and added to the reduction reaction in specific amounts has historically allowed useful insights into the mechanism of NH_3 electrosynthesis to be gained. We shall briefly survey a few of the more seminal works in this area in this Section, before moving on to discuss the electrosynthesis of ammonia using water as the proton source in Section 4.

Perhaps the most important work in which sacrificial reagents were used in the electroreduction of N_2 to ammonia was performed in the mid-1980s by Pickett and Talarmin.[26] Building on Chatt's discovery that *cis*-$[W(N_2)_2(PMe_2Ph)_4]$ reacts with protons to produce two equivalents of ammonia,[27] the authors reasoned that electroreduction of analogous tungsten complexes in the presence of nitrogen and a suitable proton source would lead to ammonia formation. Accordingly the authors reacted *trans*-$[W(N_2)_2(Ph_2PCH_2CH_2PPh_2)_2]$ with *p*-toluenesulfonic acid, and then performed controlled potential electrolysis on the resulting adduct in a THF-based electrolyte at a mercury electrode. As mercury is a very poor hydrogen evolution electrocatalyst, competing hydrogen evolution was thus kept to a minimum, allowing both NH_3 and hydrazine to be detected after electrolysis. Although a catalytic cycle was not possible with this system, it proved to be the first example of the electroreduction of nitrogen to ammonia at a well-defined, molecular and mononuclear complex by successive electron and proton transfers, with important implications for the study of both natural and artificial nitrogen reduction platforms. This approach was subsequently extended by Becker and Avraham to a range of other W and Mo complexes.[28]

At around the same time as Pickett's study, Shilov, Strelets and co-workers reported a series of molybdenum complexes that mediated the electroreduction of nitrogen to ammonia at a mercury cathode.[29, 30] The reactions were conducted in basic methanolic solutions, suggesting that methanol was a sacrificial reagent providing the necessary protons. However, due to the amorphous nature of the catalytic species and a lack of certainty over the optimal composition, firm conclusions on the nature of the most active catalyst from this system could not be obtained. Indeed, subsequent work by some of the same authors identified two possible catalysts: one containing Mo alone and one containing both Mo and Mg salts.[31]

An alternative approach was taken by Sakata and co-workers, who hypothesized that the spontaneous reaction of lithium metal with nitrogen could be exploited to generate lithium nitrides, which could in turn be reacted with proton donors to give ammonia at room temperature (see Figure 1.5).[32] Hence the authors reduced lithium salts in a mixed THF/ethanol solvent medium at very cathodic potentials (–4 V *vs.* Ag/AgCl), in the hope that lithium metal species would deposit on the cathode.

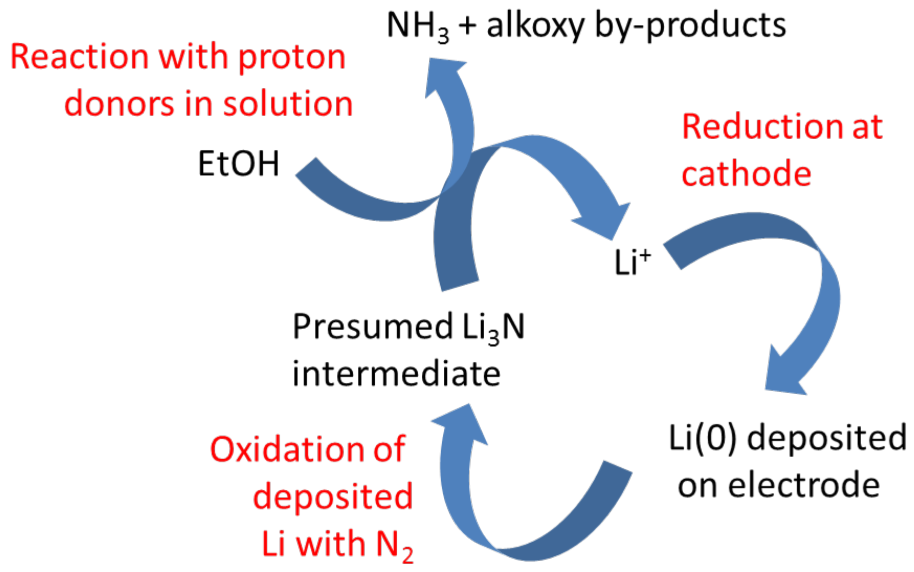

Figure 1.5: The putative cycle for Li-mediated electrosynthesis of ammonia as proposed by Sakata.[31]

Sakata's team explored numerous cathode materials for this reaction, and found that silver and titanium gave the best Faradaic yields for ammonia production under 1 atm. of N_2 (8.4 and 8.2% respectively). Electrodes such as copper displayed poorer efficiencies for NH_3 production due to their higher efficacy for hydrogen evolution under these conditions.[33] Moreover, metals that readily form alloys with lithium (such as tin, lead and aluminium) were also found to give poor conversion efficiencies to ammonia, which lends credence to the proposed cycle in Figure 1.5: the lithium metal must be deposited on the electrode surface (and not alloyed with it) in order to form the nitride intermediate. This intermediate then reacts with the ethanol in solution to produce ammonia. When ethanol was omitted, only traces of ammonia were produced, supporting the conclusion that ethanol is the source of protons for this reaction. The authors did not detect any hydrazine production with this system, which they suggested was evidence that the mechanism was *via* Li_3N species (*i.e.* implying a dissociative mechanism in which the N≡N bond was broken before the formation of any N-H bonds). Intriguingly, the team were even able to use air as the nitrogen source, reporting a Faradaic yield of 3.7% for NH_3 production from air (1 atm.) and ethanol on a silver cathode. The reduced Faradaic efficiency in air compared to pure N_2 is presumably due to reaction of oxygen with the Li(0) deposits to give lithium oxides in a wasteful side-reaction.

More recently than the examples given above, Köleli and Röpke reported the electroreduction of nitrogen to ammonia at polyaniline-decorated electrodes.[34] Hence polyaniline films were first deposited onto platinum supports from solutions of aniline in 0.5 M H_2SO_4. These films were then transferred to a cell suitable for electrolyses at elevated pressures. In an electrolyte of methanol/$LiClO_4$ containing 0.03 M H_2SO_4 as a proton source, reduction at –0.12 V *vs.* NHE under 50 atm. of nitrogen gave an optimum Faradaic yield for ammonia production of 16%. The efficiency for conversion to ammonia under 1 atm. of nitrogen was only 1.3%, which the authors attributed to the lower concentration of N_2 in solution at lower pressures. If the acid was omitted from the electrolyte, no ammonia was produced. However, if concentrations greater than 0.03 M were used, competitive hydrogen evolution prevented any ammonia from being generated. A subsequent study of the same materials as cathodes for the electrochemical reduction of N_2 in an all-aqueous system (0.1 M Li_2SO_4 / 0.03 M H_2SO_4) also produced ammonia, although no Faradaic yield or rate were quoted.[35] These results were intriguing in suggesting that metals catalysts are not essential for N_2 electroreduction to ammonia, of which we shall see another example in Section 4.2.

1.4 - Electrochemical ammonia production using water as the proton source

As mentioned in the Introduction, water is a ubiquitous and sustainable source of protons and electrons for nitrogen hydrogenation to ammonia. Electrochemical systems employing water in this fashion have (in theory at least) the advantage of being able to oxidise water to O_2, protons and electrons at the anode and then feed these protons and electrons to N_2 at the cathode, co-generating O_2 and NH_3 in the same device (see Equations 3-5). In practice, reducing N_2 at the cathode in preference to forming H_2 from these protons and electrons is extremely challenging. However, some progress has been made in this regard in recent years, and we shall examine a cross-section of the key literature in this field in Section 4. This Section is further sub-divided into those cells that operate above 100 °C (and hence employ water vapour as the proton source, Section 4.1) and those operating at temperatures below 100 °C (and therefore using liquid water, Section 4.2). The key data from Sections 4.1 and 4.2 are summarised in Table 2.

1.4.1 - Ammonia electrosynthesis using water as the proton source at temperatures above 100 °C

Based on their results showing nitride formation by reduction of N_2 in molten salt eutectics,[19] the Ito group have also demonstrated the electrosynthesis of ammonia from water vapour and nitrogen at 300 °C.[36] The system was operated on a batch-type basis. Initially, Li_3N was added to the LiCl-KCl-CsCl eutectic as a nitride source, without the application of any bias. Water vapour was supplied to the melt in the form of a stream of wet argon, with the conversion of this water to ammonia being essentially quantitative. This was hypothesised to leave behind O^{2-} ions in the eutectic according to the equation:

$$\mathbf{3H_2O + 2N^{3-} \rightarrow 2NH_3 + 3O^{2-}} \qquad \text{(Equation 9)}$$

The cell was then placed under a nitrogen atmosphere and a bias of 2.9 V (*vs.*Li^+/Li) applied to the glassy carbon anode. This led to the removal of the O^{2-} ions from the melt as both O_2 and CO_2 (the latter by reaction with the electrode under anodic bias), whilst N_2 was reduced to N^{3-} at the counter electrode. Once all the O^{2-} ions had been removed from the melt in this way (and the electrolyte replenished with nitride ions), water vapour was again passed through the eutectic to generate NH_3 and the cycle was repeated. An overall Faradaic yield for ammonia production of 23% was reported, with the remaining charge suggested to be consumed in the non-productive re-oxidation of nitride to N_2 (as in Equation 8), or in the reduction of any unreacted water to hydrogen. The rate of ammonia production was dominated by the time required for electrolysis (around 1 hour, compared to the H_2O/Ar bubbling step which took only 30 seconds) and was found to be 0.72 mol h^{-1} m^{-2}. Some of the same authors later showed that substitution of the glassy carbon anode for boron doped diamond allowed the O^{2-} ions to be removed from solution exclusively as O_2 (which would therefore be more environmentally sustainable in any large scale process), with initial Faradaic yields for this process as high as 80%.[37] However, these yields again fell off on account of nitride re-oxidation to nitrogen. The electrical energy consumption for this process has been calculated as 3100 kJ mol^{-1} of ammonia produced,[6] making this system around six times less efficient overall than the Haber Bosch process. In terms of efficiency and overall rate of NH_3 production, this represents a high-water mark for NH_3 electrosynthesis from N_2 and H_2O. The Ito group have also demonstrated that ammonia can be produced by an analogous process, but using HCl as the proton donor.[38] In this case, the nitride reacts with bubbled HCl gas to produce ammonia and chloride ions. These chloride ions can then be removed from the melt electrolytically as Cl_2.

Stoukides has also extended his solid-state reactor approach (see Figure 2) to the electrosynthesis of ammonia from nitrogen and steam using cells containing both proton-conducting and O^{2-}-conducting electrolytes.[39] In the proton-conducting device, a $SrCe_{0.95}Yb_{0.05}O_{3-\alpha}$ membrane was employed as the electrolyte, onto which a Pd anode and a commercial Ru/MgO ammonia synthesis catalyst cathode were deposited. As the electrical conductivity of the Ru/MgO catalyst was low, a thin layer of Ag was deposited on the electrolyte in-between the ceramic and the Ru/MgO. At 650 °C, a stream of wet helium gas was fed to the anode side of the cell. The H_2O in this feed was oxidised at cell voltages of 2 V to give oxygen, protons and electrons. These protons travelled through the membrane to the cathode compartment, where reduction of N_2 occurred to give NH_3. An optimum rate of NH_3 production of around 1.4×10^{-5} mol h^{-1} m^{-2} was reported. A very similar rate was obtained in an analogous cell based on the O^{2-}-conductor yttria-stabilized-zirconia. In this cell, the anode was Ag and the cathode was again Ru/MgO. Both nitrogen and steam were supplied to the cathode chamber where the following reduction occurred:

$$\mathbf{3H_2O + N_2 + 6e^{-} \rightarrow 2NH_3 + 3O^{2-}} \qquad \text{(Equation 10)}$$

The O^{2-} ions then migrated through the membrane to the anode where they were oxidised to O_2. Optimal performance was again reached at 650 ^{0}C with a 2 V bias across the cell. The poor rates of ammonia production in both configurations were attributed to the low electrical conductivity of the Ru/MgO catalyst, and the tendency for parasitic hydrogen evolution to occur on the Ag film that was deposited on the electrolyte membrane to mitigate this lack of conductivity. Nevertheless, this work gave the first examples of ammonia synthesis from N_2 and H_2O (as opposed to N_2 and H_2) in cells using solid-state electrolytes. For a short review focusing specifically on solid state ammonia production methods, the reader is directed to Reference [40].

In a similar vein, Amar *et al.* reported the electrosynthesis of ammonia from wet nitrogen in a mixed metal oxide / carbonate salt electrolyte cell where O^{2-} ions were again the charge carriers.[41] A calcium-gadolinium-doped-ceria ($Ce_{0.8}Gd_{0.18}Ca_{0.02}O_{2-\delta}$) perovskite-based oxide was used throughout the device as a support for the anode, cathode and electrolyte. The nitrogen reduction cathode consisted of $La_{0.75}Sr_{0.25}Cr_{0.5}Fe_{0.5}O_{3-\delta}$ and the anode was $Sm_{0.5}Sr_{0.5}CoO_{3-\delta}$. In-between these catalysts, the separating membrane was impregnated with a ternary carbonate (Li_2CO_3- Na_2CO_3- K_2CO_3) electrolyte as a conductor for O^{2-} ions. At 375 ^{0}C and an applied bias of 1.4 V across the cell, ammonia was formed at a rate of 0.014 mol h^{-1} m^{-2} with a Faradaic efficiency of 3.9%. The same group have also reported the direct synthesis of ammonia from wet air (as opposed to wet N_2) in a single chamber reactor that generates NH_3 at a rate of 0.004 mol h^{-1} m^{-2} and with a peak Faradaic yield for ammonia of over 5%.[42] The cell employed a tri-layer design, where both the anode and cathode catalysts were $Pr_{0.6}Ba_{0.4}Fe_{0.8}Cu_{0.2}O_{3-\delta}$ supported on a composite $Ce_{0.8}Gd_{0.2}O_{2-\delta}$ matrix. In-between these catalyst layers, the supporting matrix was again impregnated with a ternary carbonate (Li_2CO_3- Na_2CO_3- K_2CO_3) electrolyte as a conductor for O^{2-} ions. The optimal yields of ammonia stated above were achieved at 400 °C and 1.4 V bias across the cell.

Yoo and co-workers compared the rates of ammonia formation from steam and nitrogen in all-solid state cells that used $BaZr_{0.8}Y_{0.2}O_{3-\delta}$ as the proton-conducting electrolyte (selected due to its high chemical stability) and three different catalysts: Ag, Pt and the mixed oxide $La_{0.6}Sr_{0.4}Co_{0.2}Fe_{0.8}O_{3-\delta}$.[43] Three different cells were thus constructed, where the anode and cathode catalysts were both the same in the respective cells. The cell using Pt anode and cathode catalysts displayed negligible NH_3 production, possibly on account of Pt being an excellent hydrogen evolution electrocatalyst and therefore performing this reaction in preference to nitrogen reduction. $La_{0.6}Sr_{0.4}Co_{0.2}Fe_{0.8}O_{3-\delta}$ was found to be the most effective catalyst over short timespans (the rate of NH_3 production at 550 °C was 0.0031 mol h^{-1} m^{-2} with a Faradaic yield of 0.33%), but this performance could not be sustained due to delamination of the electrocatalyst from the solid electrolyte. Silver was therefore the preferred catalyst as it exhibited greater stability under operation (see Table 2).

Exciting recent work in this area has been performed by Licht *et al.*, who have examined the electrosynthesis of ammonia from air and steam in a molten salt electrolyte at modest temperatures (200 – 250 °C).[44] These comparatively low temperatures were made possible by using a 1:1 NaOH-KOH eutectic. A schematic of the cell set-up is given in Figure 1.6.

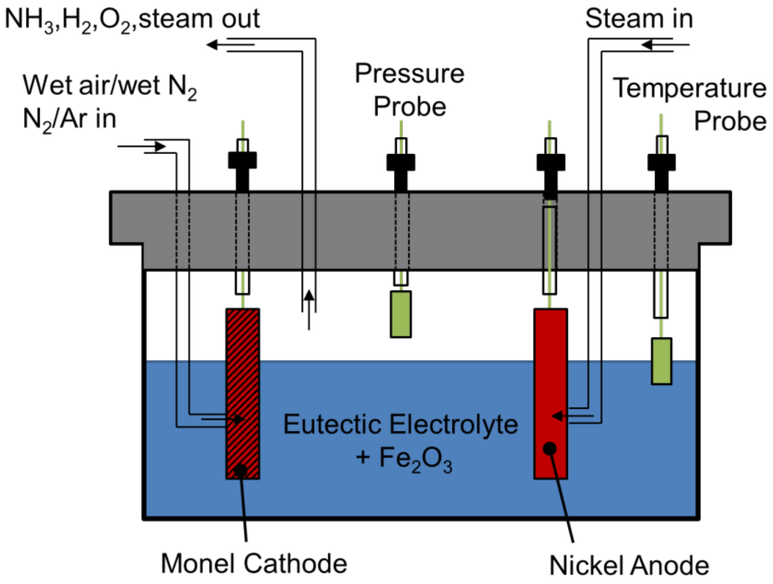

Figure 1.6. Licht's reactor for the electrosynthesis of ammonia from air and water in a low-temperature eutectic.[44]

Under a cell bias of 1.2 V at 200 °C (giving a total current density of 2 mA cm^{-2}), nitrogen was introduced into the electrolyte through a porous Monel (Ni-Cu alloy) cathode, whilst water vapour was supplied to the nickel anode. When finely divided Fe_2O_3 (of diameter 20 – 40 nm) was added to the electrolyte under these conditions, ammonia was produced at a rate of 0.086 mol h^{-1} m^{-2} and a maximal Faradaic efficiency of 35%. This is the highest Faradaic yield for electrolytic ammonia production using water as the proton source yet reported (see Table 2) and crucially this yield was not significantly affected by replacing the N_2 feed with air. However, using the methods of Hetterscheid and co-workers,[6] the overall efficiency of this system is still sub-optimal, requiring around 1000 kJ per mole of NH_3 that is produced (at a current density of 2 mA cm^{-2}). The remaining electrons not used in ammonia production were consumed in hydrogen production. The rate of ammonia production was found to increase with increasing cell potential (and hence increasing current density), being 0.24 mol h^{-1} m^{-2} at 25 mA cm^{-2} and 0.36 mol h^{-1} m^{-2} at 200 mA cm^{-2}. However, the Faradaic yield for ammonia decreased with increasing cell potential as competitive hydrogen evolution became more and more dominant. The energy efficiency for ammonia production also decreased for the same reason. Subsequently, Li and Licht were able to prevent any hydrogen formation and increase the Faradaic yield of NH_3 to 71% by operating at even lower current densities (0.7 mA cm^{-2}, produced at cell voltages ~1 V), although the overall rate of production of ammonia was naturally much slower at these low biases.[45]

The Licht group have also gone some way towards establishing the mechanism of this N_2 reduction reaction. For example, in the absence of Fe_2O_3 nanoparticles, no ammonia is formed regardless of cell potential or the nature of the feed gases, implying a strict requirement for the iron catalyst. Moreover, in a reaction medium containing Fe_2O_3 nanoparticles but with no applied bias, no ammonia is formed whether N_2 and water vapour or N_2 and H_2 are supplied to the cell. This implies that the iron oxide is not simply functioning as a catalyst for the thermodynamically-downhill formation of NH_3 from N_2 and H_2 (whether the H_2 is fed to the cell directly, or produced electrolytically by the reduction of water vapour).43 Instead, it seems that electron transfer from the cathode to the Fe_2O_3 nanoparticles is a necessary step in the mechanism, in support of which the authors found that Fe metal powder reacts with nitrogen and water to produce ammonia at a rate which increases with decreasing particle size. Hence the authors suggested the following key steps in the nitrogen reduction mechanism:[45]

$$\mathbf{Fe_2O_3 + 3H_2O + 6e^- \rightarrow 2Fe + 6OH^-}$$

(Reduction of iron oxide nanoparticles at the cathode)

$$\mathbf{2Fe + 3H_2O + N_2 \rightarrow Fe_2O_3 + 2NH_3}$$

(Chemical reduction of N_2 to ammonia at Fe particles in the electrolyte)

A computational modelling study on this system has been described recently, in which density functional theory was used to evaluate the various pathways for NH_3 formation on hematite.[46] It was found that an associative mechanism is more energetically favourable, proceeding first by adsorption of N_2 to the surface (indicated as $*N_2$), and then proceeding through sequential coupled electron and proton transfers from the electrode and electrolyte respectively (a Heyrovsky mechanism) according to the scheme:

$*N_2 \rightarrow *NNH \rightarrow *NHNH \rightarrow *NHNH_2 \rightarrow *NH + NH_3 \rightarrow *NH_2 + NH_3 \rightarrow *NH_3 + NH_3 \rightarrow * + 2NH_3$

(Where * indicates a surface binding site.)

Of these steps, the initial formation of *NNH (*i.e.* the first proton-coupled-electron transfer to adsorbed nitrogen) was found to be the most difficult, requiring around 1.14 eV in order for the proton transfer to be spontaneous. This agrees well with the cell biases (~1.2 V) that were found to be required experimentally by Licht *et al.* [44] The authors of this computational study went on to suggest that hematite itself could be used as a cathode material in such cells in future, in place of the nickel-based materials used in Licht's original reports.

1.4.2 - Ammonia electrosynthesis using water as the proton source at temperatures below 100 °C

The use of temperatures below 100 °C, in conjunction with using water and air as the reactants for ammonia synthesis has long been seen as something of a Holy Grail in the field, as these conditions approach those under which the nitrogenases operate. In this subsection, we will briefly review some of the classical electrochemical literature in this area, before moving on to some current examples of devices that produce NH_3 under these very mild conditions.

In the late 1960s, van Tamelen and Seeley reported that the reduction of titanium isopropoxide species under an N_2 atmosphere at an aluminium cathode gave rise to ammonia upon subsequent hydrolysis of the electrolyte solution with aqueous sodium hydroxide.[47] Yields of ammonia of up to 600% (based on the amount of titanium complex present) were reported. This quite possibly constitutes the earliest claim of electrocatalytic ammonia production from N_2 using water as the ultimate proton source. However as the aluminium cathode is consumed during this process (by conversion first to aluminium nitride and then likely becoming Al_2O_3 upon hydrolysis, according to the authors), the overall process does not lend itself to large-scale production.

Subsequently, a mixed $Ti(OH)_3$-Mo(III) system produced by the electroreduction of $MoCl_5$ and $TiCl_4$ in sodium methylate at a mercury pool electrode was reported by Gorodyskii *et al.* to mediate the reduction of nitrogen to ammonia when poised at –1.9 V *vs.* SCE (the standard calomel electrode).[48] The authors noted that addition of up to 3% water into the electrolyte was necessary in order to obtain any NH_3, which suggested that water was the ultimate source of protons in this synthesis.

In 1983, Sclafani and co-workers moved into purely aqueous electrolytes and reported the electroreduction of nitrogen to ammonia in 6 M KOH solution at an iron cathode.[49] At 45 °C, a peak rate of ammonia electrosynthesis of 0.5 μmol per hour was obtained at a potential of –1.07 V *vs.* SCE, with a Faradaic yield of around 1%. Lowering the temperature to 25 °C was found to lower the rate of NH_3 formation, but had little effect on the Faradaic yield. In contrast, applying reduction potentials more cathodic than –1.07 V *vs.* SCE led to a significant reduction in the overall Faradaic yield for ammonia production, which was attributed to increased competitive absorption of hydrogen rather than nitrogen on the electrode, and hence an increased level of undesired H_2 evolution.

At the turn of the century, Kordali *et al.* employed a solid polymer electrolyte cell containing both a Nafion membrane and a liquid electrolyte (2 M KOH) in order to produce ammonia from nitrogen and water at temperatures in the range 20 – 100 °C (see Figure 1.7).[50] The cathode was formed from Ru electrodeposited on carbon felt and the anode was Pt. Optimal performance was obtained at 90 °C, at which the rate of ammonia production was 7.2×10^{-4} mol h^{-1} m^{-2} and the Faradaic yield for ammonia approached 1%. As in previous attempts to produce ammonia in aqueous solution, the efficiency of the process was severely hampered by hydrogen evolution at the cathode occurring in preference to nitrogen reduction. This prevented efforts to improve the rate of production by using more cathodic reduction potentials: the rate of ammonia production was actually found to decrease with more cathodic potentials (much as in the study by Sclafani[48]) as hydrogen production became more and more dominant.

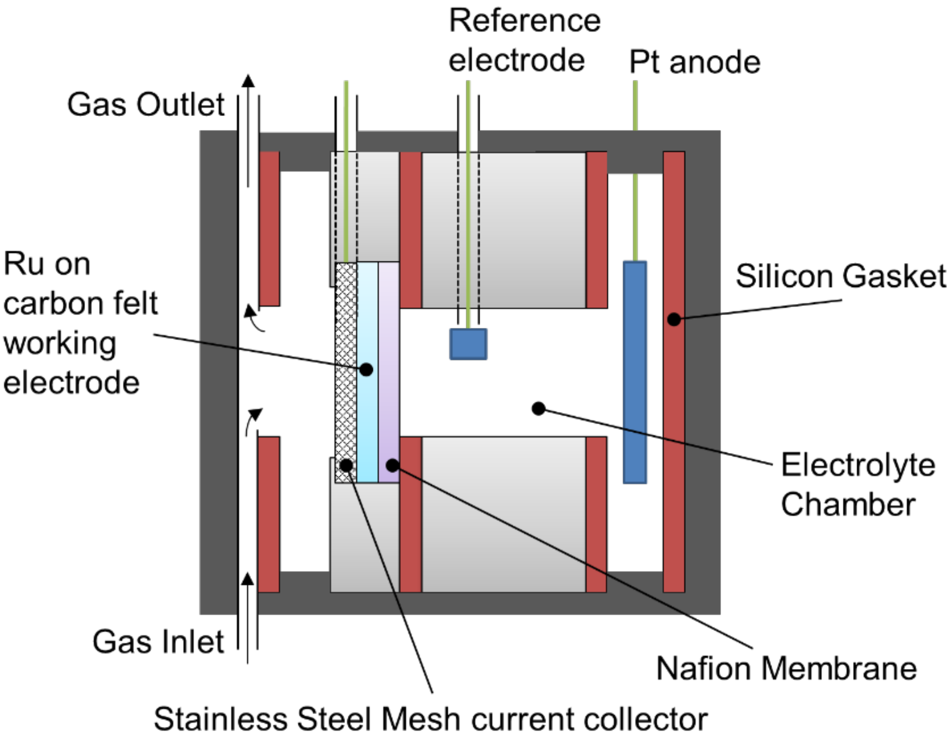

Figure 1.7. The Nafion/liquid electrolyte ammonia synthesis cell reported by Kordali et al.[50]

Non-metal catalysts have also been reported to be capable of N_2 reduction to ammonia using water as the ultimate proton and electron source. To this end, Pospíšil and co-workers used C_{60} encapsulated in γ-cyclodextrin as an electron relay for ammonia electrosynthesis in 0.1 M KCl at 60 °C,[51] building on earlier work showing that C_{60} was able to mediate the photochemical reduction of N_2 to NH_3 in the presence of chemical reductants.[52] In Pospíšil's electrochemical system, potentials of –1.2 V *vs.* Ag/AgCl were applied using a mercury pool cathode, which reduced the C_{60}-γ-cyclodextrin complexes by two electrons in two successive one-electron steps. This reduced relay species was then postulated to react with N_2 to produce N_2H_2, which was then reduced to ammonia either by direct electron transfers from the electrode or by electron transfers from other reduced relay complexes.[53] The use of the cyclodextrin was critical in ensuring that the C_{60} species were sufficiently water-soluble for this chemistry to occur. Moreover, as mercury has a very large overpotential requirement for the hydrogen evolution reaction, competitive formation of H_2 during reduction was minimised.

The viability of metal-free systems for ammonia synthesis has been further investigated by the Wu group, who successfully managed to use a Metal-Organic Framework-derived nanoporous framework for ammonia synthesis.[54] By taking the MOF (in this case ZIF-8) and subjecting it to high temperatures of 700-1200°C to graphitize it, a nitrogen-doped and highly disordered nanoporous carbon structure was left behind. This structure was decorated onto glassy-carbon rotating-disc electrode and placed in a sealed three-electrode cell filled with 0.1 M KOH solution. It was found that at room temperature and a bias of -0.3 V *vs.* RHE, an ammonia synthesis rate of 0.036 mol h^{-1} m^{-2} at 10.2% faradaic efficiency could be achieved. By increasing the temperature to 60 °C, this rate could be increased to 0.073 mol h^{-1} m^{-2}. The same authors also sought to probe the effects of Fe-doping on this same system, but it was found that transition metal doping had only a negative effect on the yield of the reaction, leading only to an increased propensity for the HER to occur.

Lan *et al*. have reported the direct synthesis of ammonia from air and water in a back-to-back membrane electrode assembly-type cell using a Nafion electrolyte and Pt/C as both the anode and cathode (see Figure 1.8).[55] At 25 °C and a cell bias of 1.8 V, the maximal rate of ammonia production using air as the nitrogen source was measured as being 0.04 mol h^{-1} m^{-2} (up to 0.126 mol h^{-1} m^{-2} was possible when pure N_2 was used in place of air). The Faradaic yield for ammonia production from air was around 0.5%, largely on account of competing hydrogen evolution from the aqueous reaction medium (Pt/C is an excellent hydrogen evolution electrocatalyst). The same authors subsequently improved the Faradaic efficiency of this system to 0.8% by moving to an operating temperature of 80 °C and a cell bias of 1.2 V.[56]

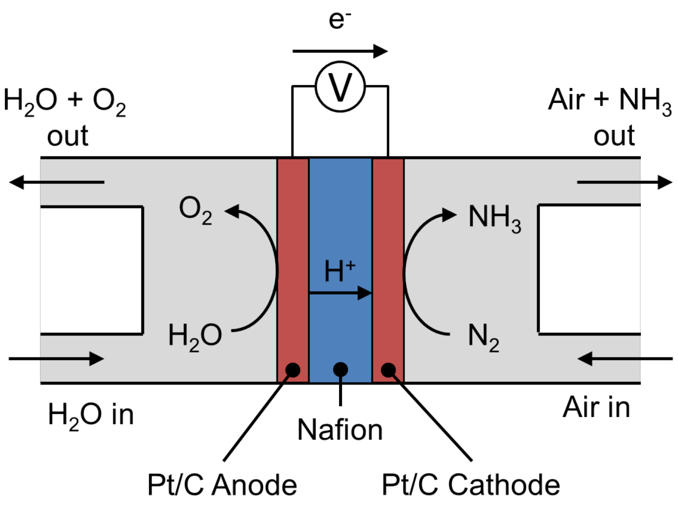

Figure 1.8. The back-to-back membrane-electrolyte-assembly cell for ammonia synthesis reported by Lan et al. [55]

Au has also been used as nitrogen reduction electrocatalyst. The Sayed group sought to determine the effect of the morphology of gold nanoparticles on their subsequent ammonia synthesis rates.[57] To create a working electrode, gold nanoparticles were drop-cast in Nafion solution onto the surface of an Indium Tin Oxide (ITO) slide, which along with a Pt gauze anode and 3 M Ag/AgCl reference electrode were placed into a cation exchange membrane (CEM)-separated two-compartment cell filled with 0.5 M $LiClO_4$.

In this system the cage morphology of the Au nanoparticles perform significantly better than the other morphologies investigated; a synthesis rate of 0.039 mol h^{-1} m^{-2} and a faradaic efficiency of 15% was determined at potential of -0.5 V vs. RHE. By decreasing the potential slightly to -0.4 V vs. RHE they achieved a Faradic yield of 30%. This could be further increased to 40.5 % if the reaction temperature was increased from 20 °C to 50 °C. As has been seen with previous literature however, although the efficiency at this potential increased, it occurred at a cost of synthesis rate.

The last few years has seen an increase in the amount of research undertaken on non-noble metal systems. To this end, the Sun group have investigated the efficacy of electrochemical systems using molybdenum disulfide (MoS_2) to try and mimic the FeMo cofactor used by biological nitrogen fixation in nature.[58] Testing was performed in a two-compartment cell containing 0.1 M Na_2SO_4 and separated by a Nafion membrane. A graphite rod functioned as the anode, and the potential was referenced to a saturated Ag/AgCl electrode. MoS_2 nanosheets were hydrothermally grown on carbon cloth (CC) to be used as a cathode. At 25 °C and a bias of -0.5 V vs. RHE an ammonia production rate of 0.0029 mol h^{-1} m^{-2} was achieved, corresponding to a faradaic yield of 1.17%. It was also discovered that there was nitrogen reduction occurring even when HCl was used as the electrolyte – despite the strong increase in the amount of competing hydrogen evolution that the acidic conditions promote.

In a similar vein, Qu *et al.* developed an array of vanadium nitride (VN) nanowires grown on carbon cloth.[59] This system has excellent specificity for the NRR at the same time as suppressing hydrogen evolution, despite using 1 M HCl as the electrolyte. This is largely due to the Mars-Van Krevelen mechanism in place, where the nitrogen for ammonia synthesis originates from the surface of the catalyst. The catalyst is subsequently regenerated with nitrogen gas. When a potential of -0.3 V vs. RHE was applied to the nanowire array under ambient conditions they reached a peak synthesis rate of 0.00892 mol h^{-1} m^{-2}, and a faradaic yield of 3.58% were achieved with little to no catalyst poisoning. Below this potential, they determined that efficiency and rate of ammonia production decreases significantly due to increased competitive adsorption of H species. Interestingly they also report that the catalyst functions competitively even at higher temperatures and pressures, albeit not to the same efficiency.

Finally in this section, the Feng and coworkers sought a more Haber-Bosch inspired route utilising Fe/Fe oxide nanoparticles.[60] Their system used 0.1 M phosphate buffer electrolyte in a standard gastight two-compartment cell, with the compartments separated by a Nafion 115 membrane. The cathode material used was carbon paper decorated with Fe/Fe_3O_4 nanoparticles, along with a Pt gauze anode and a saturated Ag/AgCl reference. At a temperature of 20 °C and a bias of -0.3 V vs. RHE, the authors achieved a faradaic efficiency of 8.29%. In addition, they found the Fe/Fe_3O_4 to be relatively selective for the NRR, with an affinity to suppress hydrogen evolution. In this way, they found the composite electrode to outperform the equivalent decorated with just Fe, Fe_3O_4, or Fe_2O_3 nanoparticles.

Table 1.2: Examples of systems that generate ammonia electrochemically using water as the proton source, together with selected metrics and conditions. A “-“ indicates that this data is not given in the source reference. Cell biases are given as absolute voltages applied across the cell (two-electrode configuration) unless noted otherwise. ^{a} Reference *vs.* Li^+/Li. ^{b} With Ag as the electrode material. ^{c} At a current density of 2 mA cm^{-2}. ^{d} Reference *vs.* Ag/AgCl.

No.	Electrolyte	Cell Bias (V)	Optimal Temperature (°C)	Nitrogen source	Optimal rate of NH_3 production (mol h^{-1} m^{-2})	Faradaic yield for NH_3 (%)	Ref.
1	LiCl-KCl-CsCl	2.9	300	N_2	0.72	23	35
2	$SrCe_{0.95}Yb_{0.05}O_{3-\alpha}$	2	650	N_2	1.4×10^{-5}	-	38
3	$Ce_{0.8}Gd_{0.18}Ca_{0.02}O_{2-\delta}$ / Li_2CO_3- Na_2CO_3- K_2CO_3	1.4	375	N_2	0.014	3.9	40
4	$Ce_{0.8}Gd_{0.2}O_{2-\delta}$ / Li_2CO_3- Na_2CO_3- K_2CO_3	1.4	400	Air	0.004	5.3	41
5	$BaZr_{0.8}Y_{0.2}O_{3-\delta}$	0.8	550	N_2	0.0018	0.46^{b}	43
6	NaOH / KOH	1.2	200	Air	0.0864	35^{c}	44
7	2 M KOH	1^{d}	90	N_2	7.2×10^{-4}	0.9	50
8	0.1 M KOH	-0.3	25	N_2	0.036	10.2	54
9	0.1 M KOH	-0.3	60	N_2	0.073	-	54
10	Nafion	1.8	25	N_2	0.126	0.7	55
11	Nafion	1.8	25	Air	0.040	0.5	55
13	Nafion	1.2	80	Air	0.034	0.83	56
14	0.5 M LiClO4	-0.4	50	N_2	0.022	40.5	57
15	0.1 M Na2SO4	-0.5	25	N_2	0.0029	1.17	58
16	1 M HCl	-0.3	25	N_2	0.00892	3.58	59
17	0.1 M PBS	-0.3	20	N_2	-	8.29	60

1.5 - Recent Theoretical Insights into Electrocatalytic Nitrogen Reduction

The foregoing discussion describes approaches towards the electrosynthesis of NH_3 driven largely by experiment and chemical intuition. Within the last four or five years however, there has been increased interest in electrocatalytic N_2 reduction from a theoretical standpoint. These studies are often interested in suggesting materials on which the reduction of water or protons might be suppressed, in favour of the reduction of N_2 to ammonia in aqueous media. As this is perhaps the biggest single challenge within the whole subject area of "The Electrosynthesis of Ammonia from Sustainable Resources" it is pertinent here to review some of the key findings of these modelling studies and how they might influence future approaches to electrochemical ammonia production.

In a landmark paper in 2012, Skúlason *et al.* undertook a theoretical analysis of the electrochemical formation of ammonia on pure transition metal electrodes and calculated trends in the expected catalytic activity at various applied bias potentials.[61] Volcano diagrams were created showing the most active surfaces, with Mo, Fe, Rh, and Ru predicted to be the most active for NH_3 generation. However, these same surfaces were also predicted to be more effective at promoting hydrogen formation than N_2 reduction. In order to circumvent excessive competing hydrogen evolution, the authors suggested that the surfaces of the early transition metals (*e.g.* Sc, Y, Ti, and Zr) should be examined as nitrogen reduction electrocatalysts. These early transition metals bind N-adatoms more strongly than they bind H-adatoms. Hence in a dissociative mechanism (where nitrogen and hydrogen atoms do not react until the N≡N and H-H bonds have been broken) these surfaces should be covered to a significant degree in N-adatoms. Protons from the electrolyte would then add directly to these adsorbed nitrogen centres in a Heyrovsky-type reaction, forming ammonia (rather than H_2, which by contrast would occur by a combination of electrolyte protons with adsorbed hydrogen). Potentials of between –1 and –1.5 V (*vs.* NHE) were suggested for this ammonia-producing process on the early transition metals. These findings were also held to account for the generally poor rates of ammonia production compared to hydrogen production in much of the existing literature: according to this analysis, the commonly used Ru and Pt electrodes would be covered with adsorbed hydrogen at negative bias, preventing nitrogen from accessing the surface in order to bind and become reduced. Hence it was suggested to use metals such as Sc, Y, Ti, and Zr such that N-adatoms would bind more strongly than H-adatoms, and thus favour NH_3 formation over H_2 formation. To our knowledge, however, no experimental verification (or refutation) of these predictions has yet been reported.

An alternative strategy to disfavour competitive hydrogen evolution would be to consider using cathodes other than the pure metals. In this regard, recent modelling of metal nitrides as cathodes for nitrogen reduction suggests that ZrN and VN would form ammonia at potentials of –0.76 V and –0.51 V (*vs.* NHE) respectively: potentials at which these nitrides would not be covered in adsorbed H-atoms.[62] NbN and CrN may also act in a similar fashion.[63] As yet, it would again seem that no such nitride materials have been tested experimentally as cathodes for nitrogen electroreduction, and so it would be very interesting to see if they performed as anticipated in real-world situations. It would also be very useful if the same kind of theoretical investigations that have been performed on these simple nitrides could be extended to binary nitrides. Species such as Co_3Mo_3N are amongst the most active catalysts for ammonia synthesis,[64] and their catalytic properties under conventional Haber Bosch conditions have recently been modelled.[65] A thorough investigation of their electrocatalytic properties, both from a theoretical and an experimental viewpoint, seems warranted.

1.6 - Conclusions

In this chapter, we have examined some of the seminal literature describing the electrosynthesis of ammonia from commonly available feedstocks. Systems that use purified H_2 and N_2 tend to display the highest Faradaic yields and conversion rates, but by using the same starting materials as the Haber Bosch process they surrender a key potential advantage of an electrochemical approach: the ability to generate protons *in situ* from sources other than fossil fuels. Water is an obvious candidate for this latter purpose, and it is encouraging that systems where water and nitrogen are used as the starting materials for generating ammonia have been reported. Even more encouragingly, there are now examples of systems where air and water can be used as the feedstocks. This opens up the possibility that ammonia synthesis devices could be scaled down to sizes suitable for decentralized production, where the only requirements would be supplies of water, air and electricity. Fertiliser production could therefore become a more democratic process, and ammonia might even find utility as a carbon-neutral fuel produced at a local scale using renewable power.[66]

The challenges facing this vision are still enormous, however. In any system where water is present, suppression of competing hydrogen evolution will be crucial. This is the single biggest reason behind the low Faradaic yields reported for ammonia synthesis from water-fed devices. Heterogeneous catalysts that bind nitrogen atoms to their surfaces more strongly than they bind hydrogen atoms may reduce hydrogen evolution, but this seems likely to require employing catalysts that are not optimal for the nitrogen reduction reaction itself, such as the early transition metals.[61] Then again, given the thermodynamics of the nitrogen hydrogenation reaction, low temperature devices are to be favoured in order to prevent the wasteful decomposition of NH_3 into H_2 and N_2. The precise balance in temperature necessary in order to minimise the required cell potentials and maintain suitable rates for N_2 reduction on the one hand and to reduce NH_3 decomposition on the other will vary depending on the design of system in question and the materials from which the cell is constructed. Systems operating using water vapour inputs at temperatures between 100 and 300 ^{0}C may well prove to be the most effective in this regard.

Assuming that hydrogen production can be completely suppressed by selective catalysts and optimal operating conditions, what are the prospects for electrochemical ammonia-producing cells displacing the Haber Bosch process as the chief means of generating NH_3 in the near future? According to the calculations of Skúlason *et al.*, [61] no catalytic activity is expected above –0.5 V *vs.* NHE for NH_3 production on pure transition metal surfaces, equivalent to an energy input of 288 kJ mol^{-1}. [6] It is possible that more efficient catalysis could be achieved with composite or molecular catalysts, and in this regard we note that Schrock,[67] Peters,[68] Nishibayashi[69] and others[70] have all reported molecular systems which yield ammonia upon reduction in the presence of a proton source (we also note that although these systems have yet to be driven electrochemically, there remains the prospect that they could be). In terms of pure transition metal surfaces, the value of 288 kJ mol^{-1} of ammonia produced quoted above is already greater than the minimum required by the nitrogenase enzymes and leaves little scope for significantly improving on the efficiency of Haber Bosch process. Thus is seems that although there are several reasons as to why we might wish to investigate electrochemical alternatives to the Haber Bosch process (*e.g.* the ability to work at both large and small scales, with minimal infrastructure and using only sustainable, widely available resources), increased overall efficiency is unlikely to be a driver of innovation in this area. One thing, however, is almost certainly true. As a prominent electrochemist in his day,[71] Haber would have approved of the ongoing search to find an efficient route to the electrosynthesis of ammonia.

1.7 – Thesis aims

As it has been shown in this chapter, there are numerous ways to conduct experiments that bypass the need for ‘traditional’ chemical methods (traditional chemical methods in this regard being those reactions using charged or radical species to promote product formation). In the example of ammonia synthesis, there are two main ways described to overcome the large energy and pressure requirements of the haber-bosch methodology: Use of electrons directly to break the nitrogen triple-bond and generate ammonia, and using a sacrificial proton donor as a mediator to change the nature of the reaction as a whole (in terms of not simply trying to associate hydrogen atoms to a nitrogen). In addition all of the methods outlined so far can be distilled down to a question of how well can one control the reduction and oxidation properties of molecules within a given system. As such there are three main investigatory aims for this thesis: to assess the direct control one can gain over redox activity, to compare the efficiency of reactions conducted electrochemically and chemically, and to probe the effects of adding a non-sacrificial mediator to push the reaction in favour of product formation.

Thus, the three experimental chapters (3, 4 and 5) will address these aims. Chapter three will be about assessing the efficacy of direct reduction of nitrogen to ammonia, where strict control over redox activity is essential to maintain as high a yield as possible. The main aim for Chapter four is to compare a chemical and an electrochemical synthesis of a small chiral molecule. In this way we will be able to assess the ease at which the reaction takes place, as well as establishing secondary features such as stereoselectivity due to the chiral nature of the product species. Finally, the main aim for chapter five is to assess the effect that changing the environment a reactant is in has on product yield, with a view to determine the extent that host-guest systems affect redox behaviour of a given chemical conversion.

1.8 – References

1. Smil, V., *Detonator of the population explosion.* Nature, 1999. 400(6743): p. 415.
2. U.S. Geological Survey, 2019, Mineral commodity summaries 2019: U.S.G.S, p 117, https://doi.org/10.3133/70202434
3. Ehrfeld, W., V. Hessel, and V. Haverkamp, Ullmann's Encyclopedia of Industrial Chemistry, 1999.
4. Spatzal, T., et al., *Evidence for interstitial carbon in nitrogenase FeMo cofactor.* Science, 2011. 334(6058): p. 940.
5. Lancaster, K.M., et al., *X-ray emission spectroscopy evidences a central carbon in the nitrogenase iron-molybdenum cofactor.* Science, 2011. 334(6058): p. 974-977.
6. van der Ham, C.J., M.T. Koper, and D.G. Hetterscheid, *Challenges in reduction of dinitrogen by proton and electron transfer.* Chem Soc Rev, 2014. 43(15): p. 5183-91.
7. Seefeldt, L.C., B.M. Hoffman, and D.R. Dean, *Mechanism of mo-dependent nitrogenase*, in *Annual Review of Biochemistry*. 2009. p. 701-722.
8. Giddey, S., S.P.S. Badwal, and A. Kulkarni, *Review of electrochemical ammonia production technologies and materials.* International Journal of Hydrogen Energy, 2013. 38(34): p. 14576-14594.
9. Kugler, K., et al., *Towards a carbon independent and CO2-free electrochemical membrane process for NH3 synthesis.* Physical Chemistry Chemical Physics, 2014. 16(13): p. 6129-6138.
10. Furuya, N. and H. Yoshiba, *Electroreduction of nitrogen to ammonia on gas-diffusion electrodes loaded with inorganic catalyst.* Journal of Electroanalytical Chemistry, 1990. 291(1-2): p. 269-272.
11. Marnellos, G. and M. Stoukides, *Ammonia synthesis at atmospheric pressure.* Science, 1998. 282(5386): p. 98-100.
12. Marnellos, G., S. Zisekas, and M. Stoukides, *Synthesis of ammonia at atmospheric pressure with the use of solid state proton conductors.* Journal of Catalysis, 2000. 193(1): p. 80-87.
13. Yiokari, C.G., et al., *High-pressure electrochemical promotion of ammonia synthesis over an industrial iron catalyst.* Journal of Physical Chemistry A, 2000. 104(46): p. 10600-10602.
14. Stoukides, M. and C.G. Vayenas, *The effect of electrochemical oxygen pumping on the rate and selectivity of ethylene oxidation on polycrystalline silver.* Journal of Catalysis, 1981. 70(1): p. 137-146.
15. Vayenas, C.G., S. Bebelis, and S. Neophytides, *Non-faradaic electrochemical modification of catalytic activity.* Journal of Physical Chemistry, 1988. 92(18): p. 5083-5085.
16. Metcalfe, I.S., *Electrochemical Promotion of Catalysis: II: The Role of a Stable Spillover Species and Prediction of Reaction Rate Modification.* Journal of Catalysis, 2001. 199(2): p. 259-272.
17. Ouzounidou, M., et al., *Catalytic and electrocatalytic synthesis of NH3 in a H+ conducting cell by using an industrial Fe catalyst.* Solid State Ionics, 2007. 178(1-2): p. 153-159.
18. Murakami, T., et al., *Electrolytic synthesis of ammonia in molten salts under atmospheric pressure.* Journal of the American Chemical Society, 2003. 125(2): p. 334-335.
19. Goto, T. and Y. Ito, *Electrochemical reduction of nitrogen gas in a molten chloride system.* Electrochimica Acta, 1998. 43(21-22): p. 3379-3384.

20. Wang, W.B., et al., *Ammonia synthesis at atmospheric pressure using a reactor with thin solid electrolyte BaCe 0.85 Y 0.15 O 3-α membrane.* Journal of Membrane Science, 2010. 360(1-2): p. 397-403.
21. Kosaka, F.N., T; Otomo, J, *Mixed Protonic-Electronic Conducting Cathodes with Exsolved Ru-Nanoparticles in Proton Conducting Electrolysis Cells.* Journal of the Electrochemical Society, 2017. 164(13): p. 1323-1330.
22. Amar, I.A., et al., *Electrochemical synthesis of ammonia based on doped-ceria-carbonate composite electrolyte and perovskite cathode.* Solid State Ionics, 2011. 201(1): p. 94-100.
23. Zhang, Z., Z. Zhong, and R. Liu, *Cathode catalysis performance of SmBaCuMO5+δ (M=Fe, Co, Ni) in ammonia synthesis.* Journal of Rare Earths, 2010. 28(4): p. 556-559.
24. Carmo, M., et al., *A comprehensive review on PEM water electrolysis.* International Journal of Hydrogen Energy, 2013. 38(12): p. 4901-4934.
25. Kugler, K., et al., *Galvanic deposition of Rh and Ru on randomly structured Ti felts for the electrochemical NH3 synthesis.* Phys Chem Chem Phys, 2015. 17(5): p. 3768-82.
26. Pickett, C.J. and J. Talarmin, *Electrosynthesis of ammonia.* Nature, 1985. 317(6038): p. 652-653.
27. Chatt, J., A.J. Pearman, and R.L. Richards, *The reduction of mono-coordinated molecular nitrogen to ammonia in a protic environment.* Nature, 1975. 253(5486): p. 39-40.
28. Becker, J.Y. and S. Avraham, *Nitrogen fixation. Part III. Electrochemical reduction of hydrazido (-NNH2) Mo and W complexes. Selective formation of NH3 under mild conditions.* Journal of Electroanalytical Chemistry, 1990. 280(1): p. 119-127.
29. Didenko, L., et al., Nouv. J. Chim., 1986. 10.
30. Pospíšil, L., L.P. Didenko, and A.E. Shilov, *The electrochemical properties of nitrogen-fixating Mo(III) and the reduction of Mo(V) in alkaline methanolic media influenced by Mg 2+ ions.* Journal of Electroanalytical Chemistry, 1986. 197(1-2): p. 305-316.
31. Strelets, V.V., A.B. Gavrilov, and L. Pospíšil, *The role of ligands in the electrochemical behaviour and catalytic activity of molybdenum-containing catalyst for dinitrogen fixation under mild conditions.* Journal of Electroanalytical Chemistry, 1987. 217(2): p. 425-433.
32. Tsuneto, A., A. Kudo, and T. Sakata, *Efficient electrochemical reduction of N2 to NH3 catalyzed by lithium.* Chem. Lett., 1993. 22: p. 851-854.
33. Tsuneto, A., A. Kudo, and T. Sakata, *Lithium-mediated electrochemical reduction of high pressure N2 to NH3.* Journal of Electroanalytical Chemistry, 1994. 367(1-2): p. 183-188.
34. Köleli, F. and T. Röpke, *Electrochemical hydrogenation of dinitrogen to ammonia on a polyaniline electrode.* Applied Catalysis B: Environmental, 2006. 62(3-4): p. 306-310.
35. Köleli, F. and D.B. Kayan, *Low overpotential reduction of dinitrogen to ammonia in aqueous media.* Journal of Electroanalytical Chemistry, 2010. 638(1): p. 119-122.
36. Murakami, T., et al., *Electrolytic ammonia synthesis from water and nitrogen gas in molten salt under atmospheric pressure.* Electrochimica Acta, 2005. 50(27): p. 5423-5426.
37. Murakami, T., et al., *Electrolytic synthesis of ammonia from water and nitrogen under atmospheric pressure using a boron-doped diamond electrode as a*

nonconsumable anode. Electrochemical and Solid-State Letters, 2007. 10(4): p. E4-E6.

38. Murakami, T., et al., *Electrolytic ammonia synthesis from hydrogen chloride and nitrogen gases with simultaneous recovery of chlorine under atmospheric pressure.* Electrochemical and Solid-State Letters, 2005. 8(8): p. D19-D21.
39. Skodra, A. and M. Stoukides, *Electrocatalytic synthesis of ammonia from steam and nitrogen at atmospheric pressure.* Solid State Ionics, 2009. 180(23-25): p. 1332-1336.
40. Amar, I.A., et al., *Solid-state electrochemical synthesis of ammonia: A review.* Journal of Solid State Electrochemistry, 2011. 15(9): p. 1845-1860.
41. Amar, I.A., R. Lan, and S. Tao, *Synthesis of ammonia directly from wet nitrogen using a redox stable La0.75Sr0.25Cr0.5Fe0.5O3-δ-Ce0.8Gd0.18Ca0.02O2-δ composite cathode.* RSC Advances, 2015. 5(49): p. 38977-38983.
42. Lan, R., et al., *Synthesis of ammonia directly from wet air at intermediate temperature.* Applied Catalysis B: Environmental, 2014. 152-153(1): p. 212-217.
43. Yun, D.S., et al., *Electrochemical ammonia synthesis from steam and nitrogen using proton conducting yttrium doped barium zirconate electrolyte with silver, platinum, and lanthanum strontium cobalt ferrite electrocatalyst.* Journal of Power Sources, 2015. 284: p. 245-251.
44. Licht, S., et al., *Ammonia synthesis by N2and steam electrolysis in molten hydroxide suspensions of nanoscale Fe2O3.* Science, 2014. 345(6197): p. 637-640.
45. Li, F.F. and S. Licht, *Advances in understanding the mechanism and improved stability of the synthesis of ammonia from air and water in hydroxide suspensions of nanoscale Fe2O3.* Inorganic Chemistry, 2014. 53(19): p. 10042-10044.
46. Nguyen, M.T., N. Seriani, and R. Gebauer, *Nitrogen electrochemically reduced to ammonia with hematite: Density-functional insights.* Physical Chemistry Chemical Physics, 2015. 17(22): p. 14317-14322.
47. van Tamelen, E.E. and D.A. Seeley, *The Catalytic Fixation of Molecular Nitrogen by Electrolytic and Chemical Reduction.* Journal of the American Chemical Society, 1969. 91(18): p. 5194.
48. Gorodyskii, A.V., et al., *Electrocatalytic properties of the Ti(OH)3-Mo(III) system in the reduction of molecular nitrogen.* Reaction Kinetics and Catalysis Letters, 1979. 11(4): p. 337-342.
49. Sclafani, A., V. Augugliaro, and M. Schiavello, *Dinitrogen Electrochemical Reduction to Ammonia over Iron Cathode in Aqueous Medium.* Journal of the Electrochemical Society, 1983. 130(3): p. 734-735.
50. Kordali, V., G. Kyriacou, and C. Lambrou, *Electrochemical synthesis of ammonia at atmospheric pressure and low temperature in a solid polymer electrolyte cell.* Chemical Communications, 2000(17): p. 1673-1674.
51. Pospíšil, L., et al., *Electrochemical conversion of dinitrogen to ammonia mediated by a complex of fullerene C60 and γ-cyclodextrin.* Chemical Communications, 2007(22): p. 2270-2272.
52. Nishibayashi, Y., et al., *A non-metal system for nitrogen fixation.* Nature, 2004. 428(6980): p. 279-280.
53. Pospíšil, L., et al., *Electrochemical impedance of nitrogen fixation mediated by fullerene-cyclodextrin complex.* Electrochimica Acta, 2008. 53(25): p. 7445-7450.
54. Mukherjee, S., et al., *Metal-organic framework-derived nitrogen-doped highly disordered carbon for electrochemical ammonia synthesis using N2 and H2O in alkaline electrolytes.* Nano Energy, 2018. 48: p. 217-226.
55. Lan, R., J.T.S. Irvine, and S. Tao, *Synthesis of ammonia directly from air and water at ambient temperature and pressure.* Scientific Reports, 2013. 3.

56. Lan, R. and S. Tao, *Electrochemical synthesis of ammonia directly from air and water using a Li+/H+/NH4+ mixed conducting electrolyte.* RSC Advances, 2013. 3(39): p. 18016-18021.
57. Nazemi, M., S.R. Panikkanvalappil, and M.A. El-Sayed, *Enhancing the rate of electrochemical nitrogen reduction reaction for ammonia synthesis under ambient conditions using hollow gold nanocages.* Nano Energy, 2018. 49: p. 316-323.
58. Zhang, L., et al., *Electrochemical Ammonia Synthesis via Nitrogen Reduction Reaction on a MoS2 Catalyst: Theoretical and Experimental Studies.* Adv Mater, 2018. 30(28): p. e1800191.
59. Zhang, X., et al., *Highly efficient electrochemical ammonia synthesis via nitrogen reduction reactions on a VN nanowire array under ambient conditions.* Chem Commun (Camb), 2018. 54(42): p. 5323-5325.
60. Hu, L., et al., *Ambient Electrochemical Ammonia Synthesis with High Selectivity on Fe/Fe Oxide Catalyst.* ACS Catalysis, 2018. 8(10): p. 9312-9319.
61. Skúlason, E., et al., *A theoretical evaluation of possible transition metal electro-catalysts for N2 reduction.* Physical Chemistry Chemical Physics, 2012. 14(3): p. 1235-1245.
62. Abghoui, Y., et al., *Enabling electrochemical reduction of nitrogen to ammonia at ambient conditions through rational catalyst design.* Phys. Chem. Chem. Phys., 2015. 17(7): p. 4909-4918.
63. Abghoui, Y., et al., *Electroreduction of N2 to Ammonia at Ambient Conditions on Mononitrides of Zr, Nb, Cr, and V: A DFT Guide for Experiments.* ACS Catalysis, 2016. 6(2): p. 635-646.
64. Jacobsen, C.J.H., *Novel class of ammonia synthesis catalysts.* Chemical Communications, 2000(12): p. 1057-1058.
65. Zeinalipour-Yazdi, C.D., J.S.J. Hargreaves, and C.R.A. Catlow, *Nitrogen Activation in a Mars-van Krevelen Mechanism for Ammonia Synthesis on Co3Mo3N.* Journal of Physical Chemistry C, 2015. 119(51): p. 28368-28376.
66. Schüth, F., et al., *Ammonia as a possible element in an energy infrastructure: Catalysts for ammonia decomposition.* Energy and Environmental Science, 2012. 5(4): p. 6278-6289.
67. Yandulov, D.V. and R.R. Schrock, *Catalytic reduction of dinitrogen to ammonia at a single molybdenum center.* Science, 2003. 301(5629): p. 76-78.
68. Anderson, J.S., J. Rittle, and J.C. Peters, *Catalytic conversion of nitrogen to ammonia by an iron model complex.* Nature, 2013. 501(7465): p. 84-87.
69. Arashiba, K., Y. Miyake, and Y. Nishibayashi, *A molybdenum complex bearing PNP-type pincer ligands leads to the catalytic reduction of dinitrogen into ammonia.* Nature Chemistry, 2011. 3(2): p. 120-125.
70. Sivasankar, C., et al., *Lessons learned and lessons to be learned for developing homogeneous transition metal complexes catalyzed reduction of N2 to ammonia.* Journal of Organometallic Chemistry, 2014. 752: p. 44-58.
71. Stock, J.T., *Fritz Haber (1868-1934) and the electroreduction of nitrobenzene.* Journal of Chemical Education, 1988. 65(4): p. 337-338.

Chapter 2

Overview of Experimental Techniques

Synopsis

In this chapter we will briefly explain the main experimental techniques used in chapters 3 – 5 to allow a theoretical background prior to encountering them in the text. Thus, it will be clear to the reader as to why a particular technique has been chosen, and how the combinations of techniques complement each other for different applications.

2.1 - Electrochemical techniques

Broadly speaking, it is possible to delineate electrochemical techniques into four main categories, depending on the variable being changed:

a) Controlled potential, with varying currents
b) Controlled current, but with varying potential
c) Total charge passed
d) Whether the impedance is being measured (this is based on an alternating current rather than direct, and so does not fit into either of the previous categories)

The following section gives a brief explanation of the electrochemical techniques used in this thesis, as well as a breakdown of the experimental method, and reasons why a particular technique might be preferred. We will also give an overview of different electrodes used, as well as a small comparison of differing set ups that may be used.

2.1.1 - Linear sweep and Cyclic Voltammetry

In the majority of cases when a species in solution is to be examined electrochemically, it may be prudent to first examine the redox activity of the material. By varying the potential (measured in volts) applied to the working electrode and recording the resulting current in amps as a function of said potential, it is possible to obtain a profile of how the species in question reacts to different biases applied.

Both Linear Sweep and Cyclic Voltammetry are very similar experiments, but carry one crucial difference. In Linear-sweep voltammetry, the applied bias is swept across a potential gradient in a linear line. This is performed at a constant rate from a starting potential E_1 to a final potential E_2. In cyclic voltammetry once the final potential E_2 has been reached, the sweep direction is reversed. This is to bring the applied voltage back to starting potential E_1, thus turning the single gradient into a cycle. (see figure 2.1).

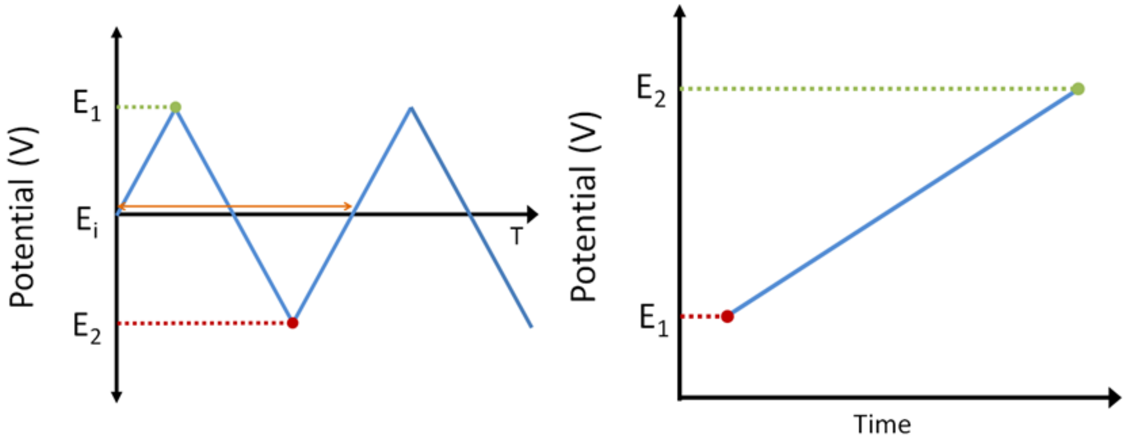

Figure 2.1a (left): Representative waveforms of a cyclic voltammogram. **2.1b (right)** Linear sweep voltammogram.

It is this ‘send and return’ cycle that makes cyclic voltammetry such an attractive technique in electrochemical studies. With the introduction of a return scan in the same experiment comes the possibility of analysing the reversibility of the electrochemical reaction (for more information, see subsection 2.1.2). This is not to say that Linear Sweep does not have its own merits; at slow scan speeds (~2 mV/s) it is possible to generate a Tafel slope (a measure of the rate of an electrochemical reaction compared to the applied potential). But with modern equipment this may be obtained more reliably using bulk electrolysis.

One important point of note with both linear and cyclic voltammetry is that the electrolyte / sample solution must be kept as still as possible. This is so any changes in peak intensity are attributed purely to electrochemical / chemical processes, and the effects of mass transport within the solution are limited as much as possible. For similar reasons, it is often prudent to perform voltammograms in an inert atmosphere to limit the effects of atmospheric gasses such as oxygen on the redox species in question.

2.1.2 - Reversibility of redox processes

In electrochemical studies the term ‘reversibility’ is used ubiquitously. In context, this is usually relating to the electrochemical reversibility of a particular species, as opposed to the chemical reversibility of a reaction. To ascertain a difference between these two terms, consider the half-equation:

$$\mathrm{Ox} + n\mathrm{e}^- = \mathrm{Red} \qquad \text{Equation 1}$$

In a chemically reversible reaction, the species **Ox** accepts $\boldsymbol{n}$ electrons to be reduced to species **Red** and **Red** can form the oxidised species **Ox** if it loses $\boldsymbol{n}$ electrons. If either of these processes is interrupted (such as the decomposition of the reduced species upon transfer of electrons) then the process is deemed chemically irreversible. Electrochemical systems function in much the same way, but one has to take into account both the charge transfer and mass transport (from the electrode to the active species in bulk solution, and vice versa). Given these caveats, it is more appropriate to break the equation down into two concerted processes:

$$\mathrm{Ox}_{bulk} \rightarrow \mathrm{Ox}_{surface} \qquad \text{Equation 2}$$

$$\mathrm{Ox}_{surface} + n\mathrm{e}^- \underset{\mathrm{k_{red}}}{\overset{\mathrm{k_{ox}}}{\leftrightarrow}} \mathrm{Red}_{surface} \qquad \text{Equation 3}$$

If the rates of reduction and oxidation at the electrode surface are both large (and larger than the rate of mass transport in equation 2, the reaction pertaining to equation 3 remains at equilibrium. Under this condition, the process is defined as electrochemically reversible. If the rates of reduction and oxidation are small, then equilibrium cannot be sustained. At this point, depending on which has the highest rate constant, one of the processes takes over and the reaction is deemed to be electrochemically irreversible.

There exists a third type of electrochemically reversible reaction, in which the rate of mass transport is in balance with the rates of reduction and oxidation. As this is somewhere between the two previously stated electrochemical reactions it is not truly reversible, as such it is known as a quasi-reversible.

The net result of a cyclic voltammetry experiment can be seen in figure 2.2 (below), which shows an example cyclic voltammogram of the ferrocene/ferrocenium couple. It also shows the most important pieces of information about a voltammogram: the cathodic peak potential (**E_{pc}**), anodic peak potential (**E_{pa}**), cathodic and anodic currents (**i_{pc}** and **i_{pa}** respectively). The reduction/oxidation peak spacing and integrated ratio are an important factor of the CV; if the ratio of the reduction and oxidation peaks is close to 1:1 the process can be considered reversible. Conversely, if the ratio is far from this it can indicate that the species does not undergo one of the redox processes (either reduction or oxidation, depending on the peak). In addition, the currents being passed give a measure of the rate of reaction, with larger currents denoting increased redox activity

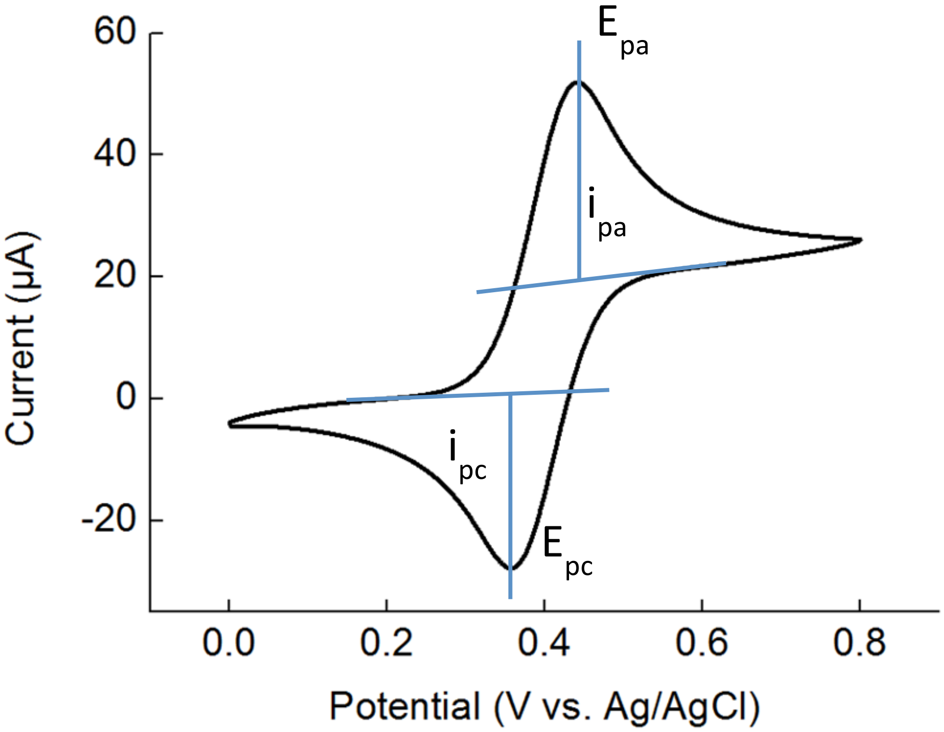

Figure 2.2: A typical cyclic voltammogram, showing both reduction and oxidation peaks for a reversible ferrocene / ferrocenium couple

2.1.3 - Bulk Electrolysis

Traditionally, bulk electrolyses were performed using a power supply set to a particular current, and the potential of the reaction was monitored as a function of time. This is known as chronopotentiometry (or galvanostatic) electrolysis. With the advent of more sophisticated equipment however, it is easier to hold the experiment at a fixed potential. This invariably gives more control over the experiment as a whole, as instead of the potentiostat increasing the potential to compensate for a low current being passed (which can alter the redox processes happening), a fixed potential ensures that a specific redox species can be studied. This is known as chronoampetometry.

The monitoring of current not only gives a measure of the activity of a certain process; integrating current and time gives a measure of the overall charge passed through the course of the reaction. As charge is measured in coulombs (C), this process is known as chronocoulometry. It is based on Faraday's law:

$$\mathbf{Q = nFM} \qquad \text{Equation 4}$$

Where **Q** = Total charge passed (in coulombs), **n** = number of electrons passed in the process, **F** = Faradays constant (96485 coulombs mol^{-1}), and **M** = number of moles of the active species.

As chronoampetometry / coulometry is concerned with current, by looking at a typical bulk electrolysis trace (see figure 2.3) it is possible to monitor the state of a reaction as it happens. Current decreases asymptotically, so by holding the potential at a point between 0.1 – 0.2 V above the point at which a redox process happens and monitoring the current drop off, it is possible to see when a reaction has run to completion. This is generally considered to be a drop to 1/ 100th of the initial current, with the current remaining stable.

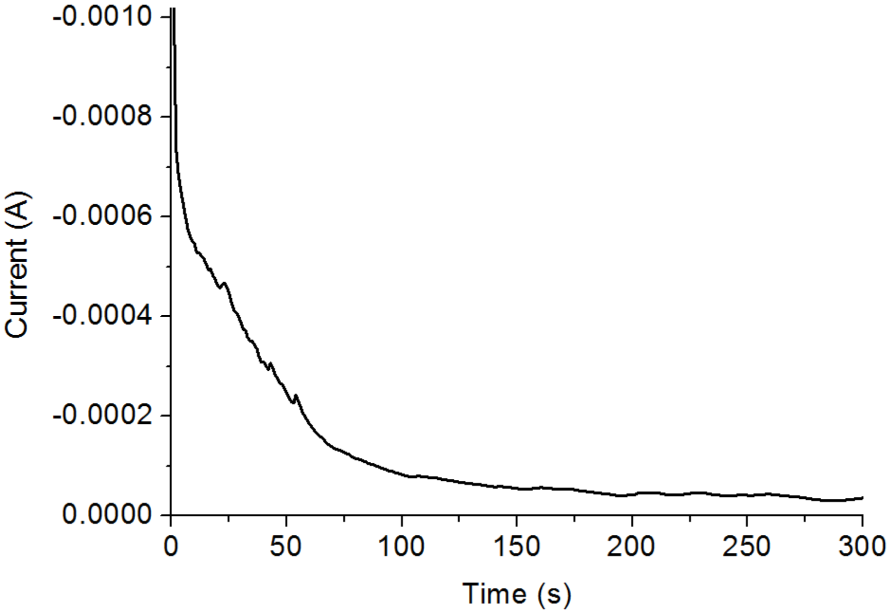

Figure 2.3: A typical bulk electrolysis trace, showing current drop-off until around 200 s, when the reaction can be said to have run to completion.

In contrast to linear / cyclic voltammetry;, as bulk electrolysis relies on being able to measure current arising from redox processes as they happen, it is often very important to have as high mass-transport within the cell as possible. This is to ensure that cell does not have to rely on electrostatic forces or diffusion, and that enough material to be electrolysed comes into contact with the electrodes.

2.1.4 – Two-electrode vs. three-electrode set up

A conventional liquid-state electrochemical setup usually consists of three electrodes: a working electrode, a counter electrode, and a reference electrode. This terminology is used instead of the standard 'cathode or anode' as the positive / negative electrodes can change depending on the potential applied.

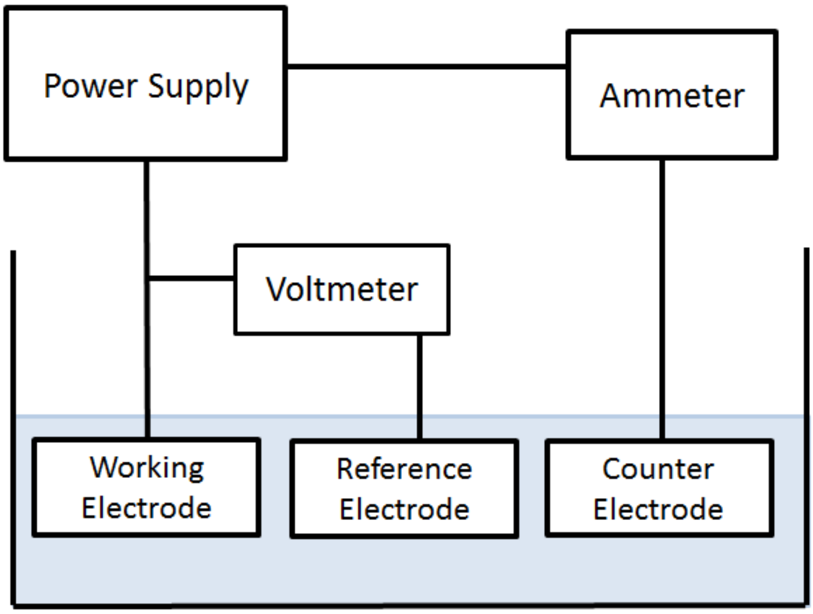

Figure 2.4: A schematic representation of a standard three-electrode configuration

The Working Electrode (W.E.) is the main electrode used for testing; it may be made of any material appropriate for the experiment. The counter electrode (C.E.) is where the opposite reaction (be it oxidation or reduction) takes place, and simply serves to close the circuit so that the cell may conduct. Counter electrodes are made of an inert material such as platinum in order to stop the electrode taking part in the electrochemical reaction being studied. A reference electrode is used to gain a measure of the potential that is applied to the working electrode (this is explained in more detail in section 2.1.5). Strictly speaking it is possible to work without a reference electrode, and instead attach the reference to the counter electrode. The problem with this is that it measures the difference in potential across the entire cell, rather than measuring the current applied for one half-reaction in a cell.

2.1.5 - Reference Electrodes

In order to compare potentials from different electrochemical species, a reference point is needed. This is where the reference electrode is used. The conventional reference point is defined by the half-reaction of the reduction of protons to hydrogen:

$$\mathbf{2H^+ + 2e^- \rightarrow H_2} \qquad \text{Equation 5}$$

This half-reaction is assigned the standard reduction potential (E^o) of 0.00 V, and serves as the baseline for all other electrochemical processes. A Normal Hydrogen Electrode (NHE, figure 2.5b right) is based on this principle, but unfortunately is generally too cumbersome to fit in a large number of electrochemical cells. A way round this is to use a different electrochemical system of a known potential, and reference this back to the NHE standard. An example of this is the Ag/AgCl reference electrode, which has a standard potential of 0.209 V *vs.* NHE and consists of a silver wire situated in a solution of AgCl, and separated from the bulk solution in the cell by a porous tip (see figure 2.5a, left). There are many types of references available for use in aqueous media, depending on the pH of the solution.

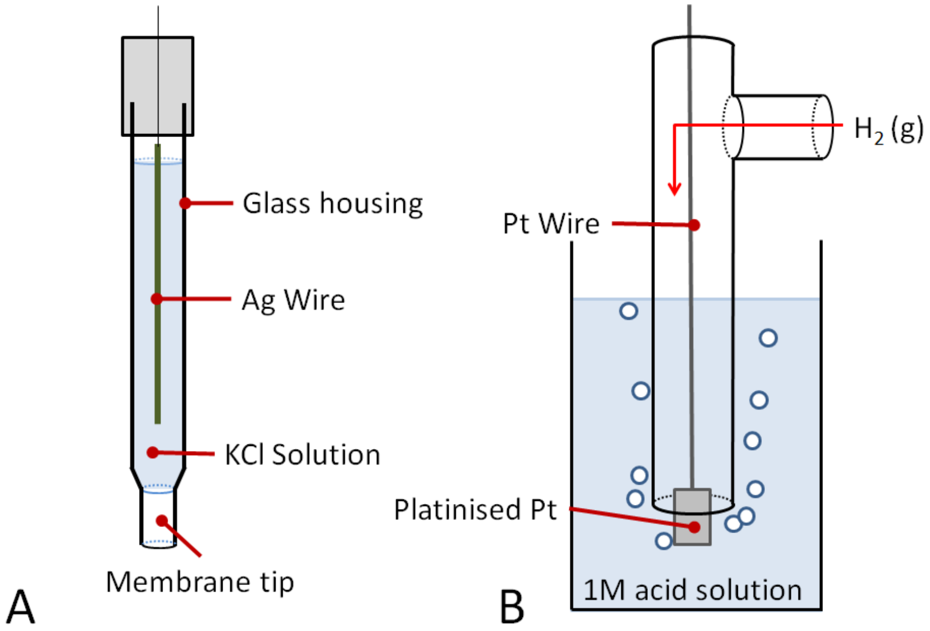

Figure 2.5a (left): Cross-section view of an Ag/AgCl reference electrode . **2.5b (right)** Cross section of a Standard Hydrogen Electrode

An issue with a reference electrode arises if one wishes to perform experiments in organic solvents, which render aqueous references useless. Unfortunately there are no organic references with consistent standard potentials available. In this case, a pseudo-reference is used, and the potential related to the ferrocene / ferrocenium couple (+0.750 V vs SHE). An example pseudo-reference electrode would be a silver wire immersed in a solution of 0.1 M $AgNO_3$ in MeCN (if this is inappropriate, an Ag or Pt wire may be used).

2.2 – Nuclear Magnetic Resonance (NMR) spectroscopy

2.2.1- The Fundamentals of NMR

Nuclear Magnetic Resonance spectroscopy is a technique that studies the effects of magnetic fields on magnetically active nuclei within a molecule. As such, it may afford a detailed analysis of the structure of a molecule depending on the experiment to be run. NMR is only possible in atoms that possess what is known as a magnetic moment. The magnetic moment (**μ**) is given by the formula:

$$\boldsymbol{\mu = I\gamma \frac{h}{2\pi}} \qquad \text{Equation 6}$$

Where $\boldsymbol{I}$ = the quantum number for the nuclear spin (determined by the number of protons and neutrons in the nucleus), $\boldsymbol{\gamma}$ = the gyromagnetic ratio (the ratio of its magnetic moment to its angular momentum), and $\boldsymbol{h}$ = Planck's constant.

In atoms such as ^{1}H and ^{13}C, protons and neutrons are present in odd numbers. This gives quantum numbers such as 1/2 (in the case of hydrogen; others include: 3/2, 5/2, etc.). With quantum numbers such as these NMR is a relatively straightforward process. In atoms such as ^{13}C however, protons and neutrons are present in an even number. The effect of this is that the spins couple, leading to $\boldsymbol{I}$ = 0. The result is that there is no interaction between the atom and the spectrometer / applied magnetic field.

There are also situations where the number of protons and neutrons in an atom are both odd numbers, leading to an even integer for a quantum number. In this instance studying the nuclei *via* NMR is still technically possible, but in practice quite difficult.

Magnetic moments within atoms can be thought of as analogous to the needle of a compass (they are usually aligned along specific directions, but may be re-orientated with an external magnetic field). When an NMR-active nucleus is subjected to a magnetic field, the nuclear spin of the atom is re-orientated to align to the external field $\mathbf{B_0}$, with the possible orientations dictated by the quantum number **m**. This magnetic moment does not remain in one place, but precesses (a spinning motion similar to a gyroscope) around the direction of $\mathbf{B_0}$. For a ^{1}H spectra there are only two possible orientations: **m** = ½, which is the state aligned with the external field and has lower energy than **m= -**½, which is aligned against the external field.

If all of the magnetic moments are combined, the resultant vector is known as the magnetization vector $\mathbf{M_0}$. The magnetic moments do not completely cancel each other out; a small population will remain with spin aligned to B_0. If this is assigned to a z-axis, a radio pulse can be introduced along the x axis, with the absorption of energy causing the magnetization vector to reorient from along the z-axis to closer to the xy-plane. Due to the angular momentum of the magnetic moment, the magnetization vector is now precessing around the z-axis; by aligning a detector with the y-axis, as the magnetization vector precesses the signals can be visualised as an oscillating wave (see figure x, below).

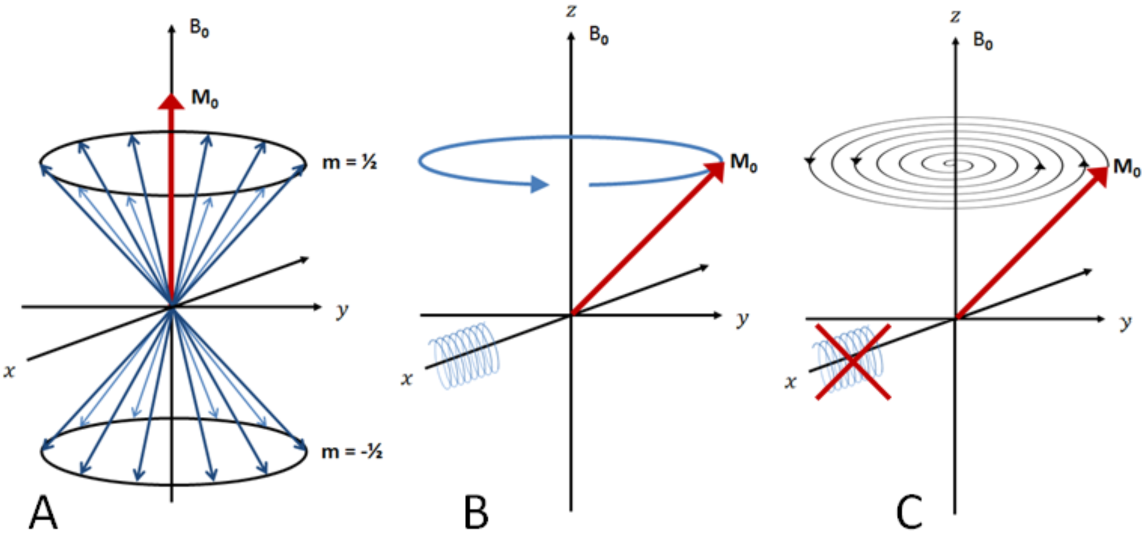

Figure 2.6a: The net result of the sum of magnetic moments causes the magnetization vector ($\mathbf{M_0}$) to be aligned with the applied magnetic field $\mathbf{B_0}$ along the z-axis **2.6b**: The magnetisation vector shifts towards the xy-plane and begins precessing around the z-axis under radiofrequency irradiation. **2.6c**: Halting radiofrequency irradiation causes the vector to slowly relax towards $B_{0,}$ spiralling inwards as it does so.

When the frequency generator is switched off, the nuclei are still resonating from the absorbed energy, and emit a signal in the radiofrequency range. This signal decays over time as the absorbed energy is slowly released, leading to the M-vector spiralling inwards from its $\mathbf{M_y}$ position back to $\mathbf{M_0}$ (and therefore relaxing to the ground state). There are two ways this energy can be released: spin-spin relaxation, which considers the interaction of spin with surrounding protons, and spin-lattice relaxation which is where the spin interacts with surrounding molecules. This relaxation and oscillation can be visualised as a Free Induction decay (FID) diagram:

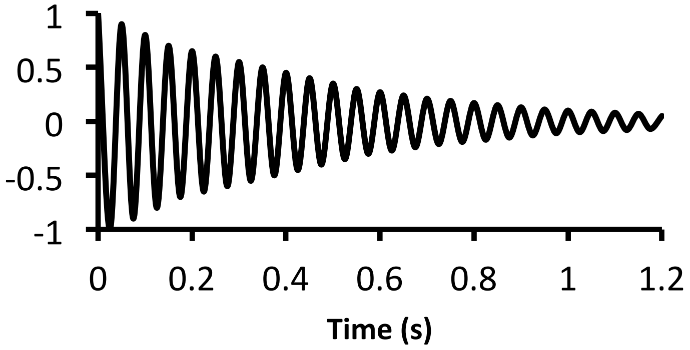

Figure 2.7: An example of a free induction decay (FID) signal

In early NMR machines, the irradiation was performed successively and with increasing frequencies to account for all possible excitation frequencies of the nuclei. This has several disadvantages, chief of which is that this method takes a long time to complete. Modern NMR machines use a multiple frequency radiowave pulse, which excites all the nuclei simultaneously. By applying a Fourier Transform to the resulting data, it is possible to distinguish the different environments the atoms are in.

The chemical environment that atoms are in can affect the frequency of the resonating nuclei. In general, a proton experiences more or less effective electron density depending on the electron density of its neighbouring atom. When protons are subjected to an external magnetic field, a small internal magnetic field $\mathbf{B_i}$ is induced that is opposite to the external field $\mathbf{B_0}$, albeit much smaller. If the proton is bound to an atom with high electronegativity such as oxygen or nitrogen, it experiences a decrease in electron density itself resulting in a less intense induced magnetic field, and an increase in resonance frequency. Conversely, if the atom to which it is bound has a low electron density (such as carbon) the opposite is true; there is an increase in electron density, more intense induced field, and therefore a decrease in resonance frequency. This phenomenon is known as the shielding effect, and change in resonance frequency due to different chemical environments is commonly referred to as chemical shift.

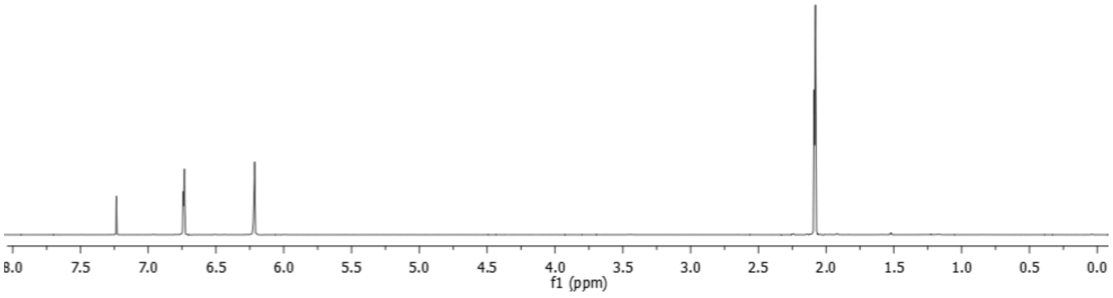

Figure 2.8: An example ^{1}H NMR, showing both high frequency deshielded (7.25-6.25 ppm), and low frequency shielded (2.1 ppm) proton signals.

The chemical shift of atoms are measured in parts per million (ppm), usually between 0-14 ppm for a ^{1}H spectra and 0-240 ppm for a ^{13}C spectra. To quantify where a chemical environment sits in relation to this scale, a standard is needed. General convention dictates that the hydrogen signals of $Si(CH_3)_4$ (tetramethyl silane, or TMS) are set to 0. The reason for this being that the protons in TMS are highly shielded (resonating at low frequency) and have a high-intensity singular peak due to the fact that the protons are all in the same chemical environment. Unfortunately NMR machines are not all run at a uniform power, but can be found to have higher or lower operating frequencies. As the chemical shift is proportional to the external applied magnetic field, spectrometers using different applied fields will induce a different response per chemical environment. To counteract this, instead of absolute chemical shift, relative chemical shift (**δ**) can be used:

$$\boldsymbol{\delta} = \frac{\boldsymbol{v}_{\boldsymbol{H}} - \boldsymbol{v}_{\boldsymbol{reference}}}{\boldsymbol{Spectrometer\ frequency}} \qquad \text{Equation 7}$$

By utilising this relative shift rather than absolute shift, it allows for any chemical environment to be studied or analysed on any power of spectrometer, regardless of the applied magnetic field. In addition to this, with modern techniques one does no longer need to add TMS as an internal standard to every sample, and can use the residual protic signals in the deuterated solvent as a reference for the rest of the spectrum.

2.2.2 – Two-dimensional NMR spectroscopy (2D NMR)

As it has been shown in section 2.2.1 it is possible to determine the chemical environments that protons and carbons are found in. ^{1}H and ^{13}C NMR spectroscopies are acceptable if one is to only try and analyse small molecules (or molecules that only contain few chemical environments to delineate), but are insufficient if one were to be interested in larger molecules. This is due to the fact that many of the same groups of NMR active atoms will be in similar chemical environments, thus increasing the propensity of the signals to overlap. The overall effect of this is generally to generate a very difficult spectrum to analyse. To combat this two-dimensional NMR may used to great effect.

2D NMR can be broadly defined in terms of two types of experiment:

1) Homonuclear - Signals are derived from the same isotope, which is usually ^{1}H
2) Heteronuclear – signals are derived from different magnetically-active nuclei (such as correlating protons to ^{13}C or ^{15}N

Homonuclear

There are two main homonuclear experiments that we will concern ourselves with for the scope of this thesis: COSY (Correlation Spectroscopy) and NOESY (Nuclear Overhauser Effect Spectroscopy). In a COSY experiment, proton signals are correlated according to their proximity (in terms of number of bonds apart). This type of experiment can only correlate protons that are two or three bonds apart, as the coupling constants for any further than this approach zero. To this end, it is a very valuable experiment to probe structural properties within molecules. In a NOESY experiment, the nuclear overhauser effect (N.O.E) is used to spacially correlate any proton that is within 5 Å of another. With this type of experiment even if the two protons would be far apart molecularly (such as two protons from opposing ends of an amino acid sequence), if they are spatially within the observation distance due to tertiary structure conformations, the N.O. effect applies. A NOESY spectrum is therefore invaluable in delineating large structures such as proteins, or host-guest experiments, where protons from the incorporated species may interact with their host.

Heteronuclear

For large structures such as proteins and inorganic clusters that have many magnetically active nuclei in them, correlating protons to each other based on distance may not be practical. For this application, it is more appropriate to run a Heteronuclear correlation. There are two main types available: Heteronuclear Multiple Quantum Correlation (HMQC) and Heteronuclear Multiple Bond Correlation (HMBC). With an HMQC, the chemical shift of a particular proton environment is correlated to the directly bonded magnetic nuclei (such as ^{13}C or ^{15}N). By cross-referencing the proton peaks to the carbon or nitrogen peaks, one can directly ascertain the one-bond coupling shift. HMBC is a similar experiment, but utilises multiple-bond couplings over two to four bonds in distance. The directly bonded species peaks are supressed so as not to make the resulting spectra too confusing.

2.3 –X-ray diffraction

As subsequently seen with other spectroscopic techniques such as UV-vis spectroscopy, the interaction of electromagnetic radiation with molecules can be a useful tool in probing characteristics.

X-ray diffraction is a technique that relies on the scattering of X-rays from different planes within a crystalline structure. Crystals are highly ordered structures in a lattice formation; as such they scatter electromagnetic radiation in regular ways. X-rays are particularly suited to this task, as the wavelengths of X-rays are on the same order of magnitude (1-100 Å) as the plane spacing in the crystal.

Although the majority of the scattered radiation is cancelled out by destructive interference, a portion of this radiation adds together via constructive interference. The relationship between these is denoted by Bragg's Law:

$$\boldsymbol{2d\sin\theta = n\lambda} \qquad \text{Equation 8}$$

Where $\boldsymbol{d}$ is the spacing between the crystal planes, $\boldsymbol{\theta}$ is the incident angle (or angle of the X-ray source), n is any integer, and $\boldsymbol{\lambda}$ is the wavelength of the scattered beam. A graphical representation of this may be found in figure 2.9:

The spots generated with the constructive interference are known as reflections, and each reflection arises from a set of crystal planes. As such it is necessary that the crystal sample lacks defects in its structure such as cracks or inclusions which might scatter electrons unexpectedly. The pattern of reflection spots is collectively known as a diffraction pattern, and they are collected at regular spacings throughout the total angle change about the sample. The equipment used to obtain a diffraction pattern is known as a diffractometer.

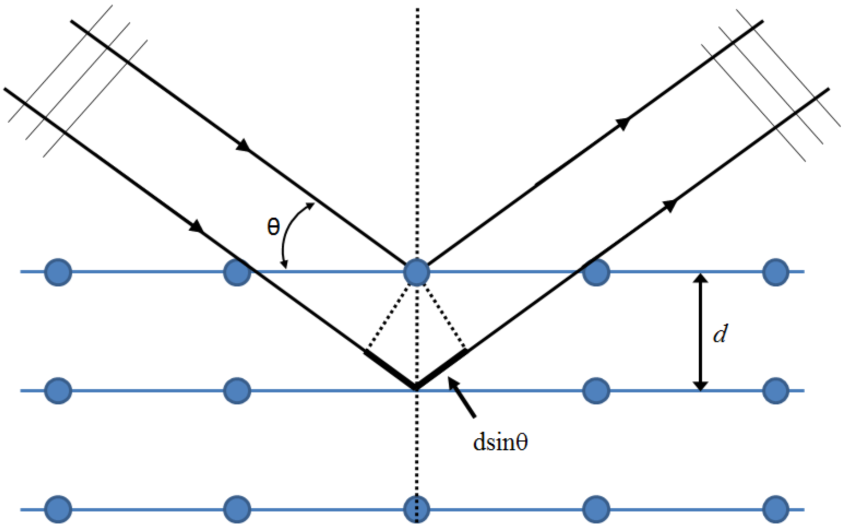

Figure 2.9: Graphical representation of Braggs law - two X-ray beams diffracting from the first and second layer of a crystal lattice

During diffractometer operation, a crystal sample of sufficient size and purity (<0.1 mm sized crystals are required) is mounted in a sample holder capable of being rotated about two axes. The two axes of movement allow the sample and detector to be gradually rotated throughout the experiment, ensuring the diffraction patterns from each crystal plane are properly detected. In addition, it is very important that the sample mount itself be transparent to X-rays so that the diffraction pattern obtained is solely from the crystal sample itself. Typical examples of this are to coat a crystal sample in an oil such as perfluropolyether (PFPE) and freeze the sample *in situ* on a polymer-tipped mounting pin using a stream of cooled nitrogen. Once the sample is mounted, a metal anode (typically Cu, but Fe, Mo and Co may be used depending on the sample) in the X-ray chamber is exposed to a high-energy electron beam. Due to the photoelectric effect this causes X-rays of wavelengths characteristic to the metal to be emitted. The X-rays travel through a monochromator and mirrors focus the monochromatic bream onto the sample, where it is diffracted. The different diffraction patterns are collected with a detector. Once the reflections from every orientation of the crystal are recorded, they are combined computationally to produce/ refine a model of the atomic arrangement of the crystal sample. The refinement is generally then stored in a public database.

2.4 – Optical Spectroscopy techniques

Optical spectroscopic techniques are based on the principle of observing the changes in molecules following excitation by photons of light. There are two techniques used in this thesis that are classed as optical spectroscopies; Infra-red (IR) spectroscopy and UV-vis spectroscopy. The differences between UV-vis (see section 2.4.1) and IR (section 2.4.2) spectroscopies are discussed more in-depth in their respective sections.

2.4.1 – Ultraviolet-Visible light (UV-Vis) Spectroscopy

UV-visible spectroscopy is a technique that correlates the relationship between the light absorbance in the wavelength range of 190-750 nm (with a crossover from ultraviolet into visible light range at *circa.* 380 nm) of a sample and the concentration of any absorbing species. This correlation is outlined in the beer-lambert law:

$$\boldsymbol{A = \varepsilon_\lambda l C} \qquad \text{Equation 9}$$

Where **A** = the absorbance of a sample, **ε** = the molar extinction coefficient (specific to the species under observation), $\boldsymbol{l}$ = the path length of the sample (usually standardised to 1 cm), and **C** = the concentration of the species absorbing the specified wavelength of light. Once a series of samples of known concentration have been analysed (and a calibration curve generated) by using the Beer-Lambert law, it is possible to determine the extinction coefficient of the species under observation. Once this is determined, one can simply extrapolate the concentration of the unknown. This is achieved using a UV-vis spectrometer.

As seen in figure 2.10 (overleaf) a UV-vis spectrometer consists of two sources of light, a mirror and monochromator array to direct the produced light into the sample chamber, two sample holders (one for a blank sample and one for the sample to be analysed), a detector and an amplifier.

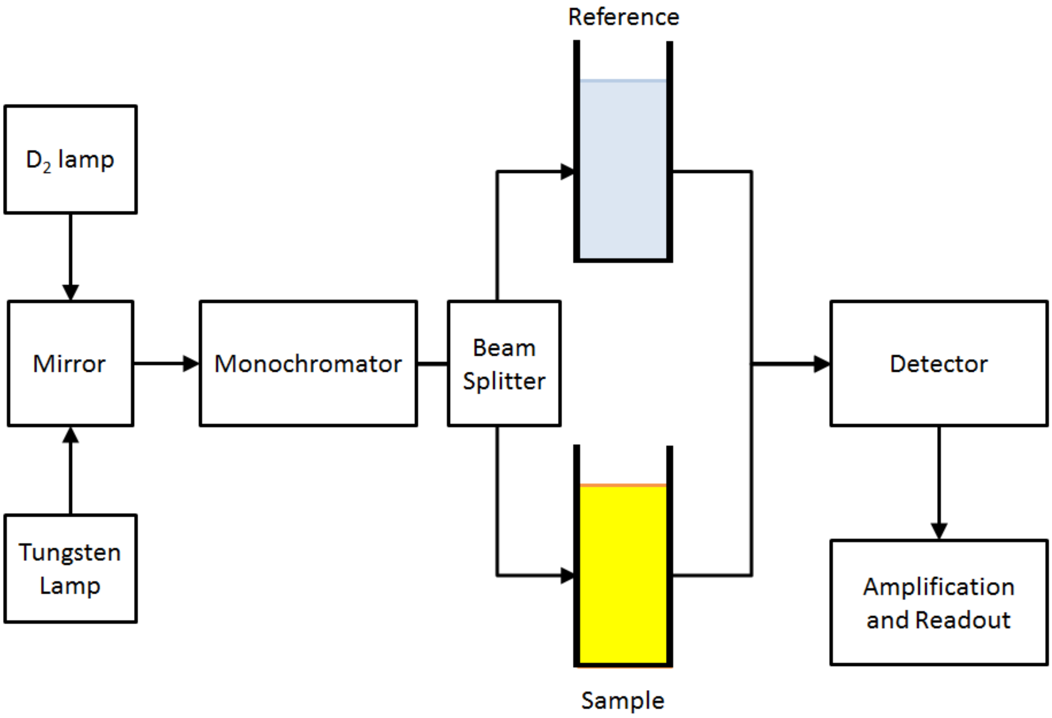

Figure 2.10: A schematic diagram of the workings of a UV-Vis spectrometer

Two example sources of light used in a UV-vis spectrometer are deuterium and tungsten; tungsten emits white light which is easily monochromated to specific wavelengths across the entire visible spectrum, and deuterium provides an easily generated source of UV light. The use of two lamps concurrently allows for a facile and seamless crossover between ultraviolet and visible light, and therefore an uninterrupted spectrum. The choice of sample holder (known as a cuvette) is quite important in this type of spectroscopy. The two choices of cuvette are either plastic or quartz. Quartz is generally perceived as superior, as it is optically transparent in the full region of wavelengths down to circa 200 nm. Plastic cuvettes on are less expensive, but begin to absorb light at <350 nm, making them almost useless if one was inclined to run experiments in the ultraviolet region.

The use of a split-beam path through two samples is an important part of the spectrometer. The first sample is the sample to be analysed, and the second is a reference sample. The reference affords a measure of the background characteristics of the solution (such as the solvent and any dissolved species) and is deducted from the sample signal. This ensures that the output response from the detector is solely from the species being analysed.

2.4.2 – Infrared (IR) spectroscopy

In contrast to utilising light in the ultraviolet or visible region, Infrared (IR) spectroscopy is a technique utilising the interaction of molecules with photons in the infrared region. Starting at the opposite end of the visible light region to ultraviolet (>700 n[i]m), infrared light can be subdivided into three regions depending on their proximity to the visible light areas of the EM spectrum: near-IR, mid-IR, and far-IR. Near-IR is the region nearest the visible light portion of the EM spectrum (~14000-4000 cm^{-1}), and has the highest energy of the three. As such, it may be used to incite overtone or harmonic vibrations within a molecule. Mid-IR is slightly further away (~4000-400 cm^{-1}) with lower energy appropriate for use in probing fundamental vibrations within molecules, and their associated rotational or vibrational structure. Far-IR, lying next to the microwave region (~400-10 cm^{-1}) has the lowest energy, and as such can only determine rotational relationships within molecules. An important note that should be made of IR region “classifications” is that these are only loosely based on molecular or electromagnetic properties.

2.5 – Inductively-coupled plasma Mass spectrometry (ICP-MS)

ICP-MS is the combination of a plasma-based atomiser with a mass spectrometer for analysis. It is a highly accurate technique for analysing elemental composition in a given sample, with the emphasis in the context of this thesis on metal content. It has several advantages over optical techniques such as Atomic Absorption/Emission spectroscopy (AAS / AES), in that it has superior detection limits, as well as being able to analyse more than one element at a time. The resulting mass spectra are also generally easier to interpret than one generated by optical techniques, especially so in the case of lanthanides, actinides, and some transition metals.

In the procedure of an experiment using ICP-MS, a sample solution is fed into a nebuliser (where it is converted into a uniform fine mist) with an inert carrier gas such as argon. This mist is then fed into a plasma stream, which serves to atomise and ionise the sample. The ionised sample is then fed through a differential vacuum (where it expands, cooling the sample) into a separation chamber which removes the carrier gas, electrons, and molecular species, leaving the cations. The cations are then electrostatically accelerated and fed through a mass analyser, which separates and quantifies the cations according to their mass-charge (m/z) ratio. In most cases the mass analyser used is a quadrupole mass analyser, which uses two sets of parallel metal rods charged with a radio frequency voltage to select only specific m/z ratio ions. By varying the applied voltage a range of different m/z ratio ions can be detected, with the net result being a spectrum comprising isotopic peaks of all the analytes in the sample. The detected range of m/z ratios are then compared to a calibration curve to determine the total concentration of the species of interest. This process is shown schematically in figure 2.11, below.

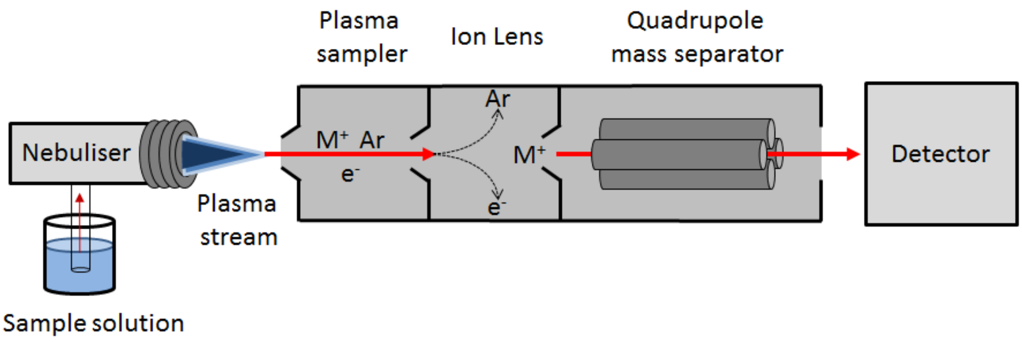

Figure 2.11: Schematic diagram of an ICP-Mass spectrometer

2.6 - References

1. D. Pletcher, *A First Course in Electrode Processes*, 2nd edition, RSC Publishing, 2009
2. A. J. Bard; L.R.Faulkner, *Electrochemical Methods – fundamentals and applications*, 2nd edition, Wiley, 2001
3. J. Keller, *Understanding NMR spectroscopy*, 2nd edition, Wiley, 2010
4. C.Giacovazzo, *Fundamentals of Crystallography*, 2nd edition Oxford University Press, 2002
5. J.M. Hollas, *Modern Spectroscopy*, 4th edition, Wiley, 2004
6. W. Clegg, *Crystal Structure Determination*, Oxford University Press, 2004

Chapter 3

A re-evaluation of Sn(II) phthalocyanine as a catalyst for the electrosynthesis of ammonia

Acknowledgements and declaration

This chapter includes extended and updated sections from the following paper:

M. A. Shipman; M. D. Symes, *A re-evaluation of Sn(II) phthalocyanine as a catalyst for the electrosynthesis of ammonia*, 2017, Electrochimica Acta, 258, 618-622

Unless otherwise stated all other experimental work was performed by M. A. Shipman and the paper was co-authored by M. A. Shipman, and M. D. Symes.

Synopsis

The electrosynthesis of ammonia from nitrogen and water is a topic of considerable interest in the quest for sustainable and decentralized NH_3 production. Tin(II) phthalocyanine complexes have been proposed as electrocatalysts for nitrogen reduction to ammonia in aqueous solution, with Faradaic yields approaching 2% having been reported. Herein, however, we show that such complexes are not electrocatalysts for this transformation, with the amount of ammonia detected being essentially the same under N_2 and under Ar. Instead, we suggest that apparent ammonia generation could arise either through contaminants in the as-prepared tin(II) phthalocyanine complexes, or by the electro-decomposition of these complexes under cathodic bias.

3.1 - Introduction

Ammonia is a key commodity chemical, essential for fertilisers, detergents, plastics and explosives. In 2016, total worldwide NH_3 production exceeded 140 million tons, and demand for ammonia continues to grow [1]. The industrial production of ammonia is currently achieved almost exclusively *via* the Haber Bosch process. This process reacts gaseous N_2 and H_2 together at high temperatures and pressures and has revolutionised the chemical industry[2]. However, because the hydrogen used in the Haber Bosch process is normally obtained from fossil fuels, there have been increasing efforts in recent years to develop more sustainable procedures for the synthesis of ammonia. One of the most attractive of these alternative methodologies is electrochemistry, and the state-of-the-art regarding the electrosynthesis of ammonia has been reviewed recently by ourselves [3] and others [4-6].

Of the various electrochemical approaches that can be envisioned, the one that most appealed to us from a sustainability point of view was the direct electroreduction of nitrogen to ammonia at room temperature, using water as the source of the required protons and electrons. Such systems have been reported previously with various cathodes, including studies by Sclafani and co-workers (Fe) [7], Kordali *et al.* (Ru/C)[8], Wessling and co-workers (Ru and Rh) [9], Lan *et al.* (Pt/C) [10, 11], Kim *et al.* (Ni) [12] Yan and co-workers (Au) [13], Wang and co-workers (polymer cathodes) [14] and Chen *et al.* (Fe-carbon nanotubes) [15]. Generation of ammonia by nitridation of lithium (at elevated temperature) followed by hydrolysis (at room temperature) has also been reported recently [16].

However, the approach that most intrigued us was the use of metal-phthalocyanine complexes (especially those based on Sn) as nitrogen reduction electrocatalysts, as reported by Furuya and Yoshiba in two communications some years ago [17, 18].

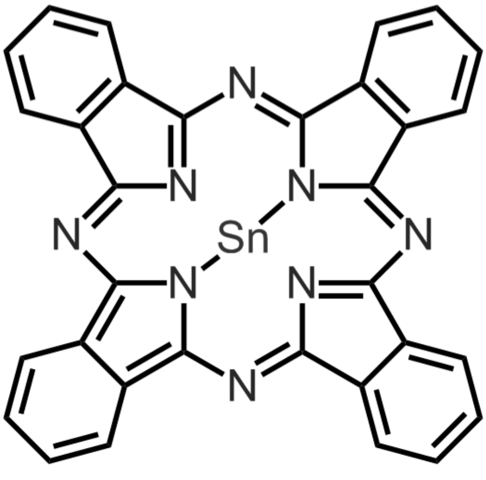

Figure 3.1: The Sn (II) Phthalocyanine molecule

Their results suggested that Sn(II) phthalocyanine complexes were capable of the direct electroreduction of nitrogen to ammonia in 1 M KOH at modest potentials, with a Faradaic efficiency of nearly 2%. However, the only electrochemical technique used in these papers to establish catalytic activity was bulk electrolysis. This, coupled to the lack of reports reproducing this data, suggested to us that a more thorough investigation of this system was required.

The initial aims were to verify and corroborate the findings of the Furuya-Yoshiba system, hopefully yielding insights into the mechanism of catalytic activity. This would then allow improvements to be obtained in both the rate and yield of ammonia production. We show however that more in-depth study of the Furuya-Yoshiba system fails to support the claims that these complexes are acting as nitrogen reduction electrocatalysts. We find no evidence for electrocatalysis by cyclic voltammetry, nor do bulk electrolysis experiments under a nitrogen atmosphere produce more ammonia than manifests under an argon atmosphere. Instead, we show that not only is the as-purchased Sn(II) phthalocyanine contaminated with ammonium salts (or other species that decompose to release ammonia), but also that the Sn(II) phthalocyanine itself seems to decompose under cathodic bias. It is thus to these non-electrocatalytic sources of NH_3 that we attribute the presence of the small amounts of ammonia that we do detect.

3.1.2 - Ammonia Detection

Given that excess fixed nitrogen can be a major environmental pollutant, there is already a well-established field for facile and accurate determination of ammonia. There are currently three main methods commonly in use for ammonia detection: Ion Chromatography, Nessler’s reagent and the Indophenol test (based on the Berthelot reaction). All three methodologies are valid techniques for ammonia determination, however there are some caveats that shape which method is more suitable given the sample. Ion Chromatography is a sensitive and highly reproducible technique, but can be quite costly to run (especially in the case of a large sample size), as well as requiring comparatively complex equipment to perform. More importantly within the context of this research, Ion chromatography is not as appropriate in basic media.[19] An alternative to ion chromatography is to use a colourometric method, such as Nessler’s reagent or the indophenol method. While both of these methods have drawbacks, Nessler’s reagent tests contain mercury salts that must be treated with caution. The resulting product solution also has the propensity to generate colloidal suspensions which may interfere with spectrometry readings, as well as the reagents having a comparably short shelf-life.

The indophenol test remains one of the most accurate methods of ammonia detection to date, and sees use worldwide in research as well as governmental bodies. Moreover, the test may be conducted without requiring potentially environmentally devastating toxic metal salts or complex instrumentation. It relies on the formation of the indophenol molecule, a deep-blue azine dye used industrially: [20]

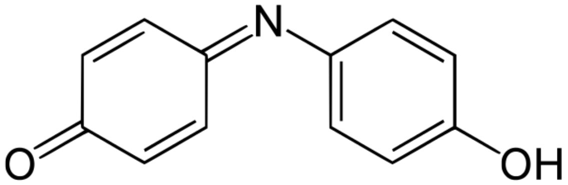

Figure 3.2: The indophenol molecule

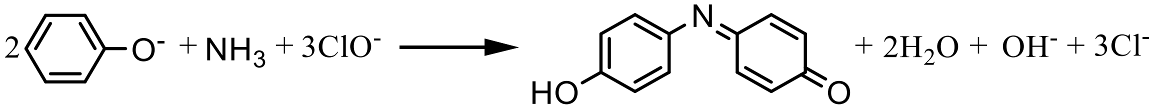

Scheme 1: reaction of phenol with hypochlorite and ammonia, resulting in the indophenol blue molecule.

The indophenol molecule is formed when ammonia reacts with phenol in an alkaline environment (see scheme 1). As it relies on ammonia being present, the resulting intensity of blue colour is directly proportional to the concentration of ammonia solution. The methodology has not changed much since the discovery of the reaction, with the exception of the addition of sodium nitroprusside as a catalyst to facilitate colour change, chelating molecules to limit interference from metal ions and buffers to stabilise the pH.

Despite these improvements, there are still issues relating to this method of detection: the methodology only works on high pH samples, at high concentrations of ammonia the calibration curve can be inaccurate, and if there are any species other than indophenol that absorb at ~640 nm, false positives can arise. Despite these issues, given that the expected experimental ammonia concentration is low, the low solubility of Sn (II) phthalocyanine in aqueous solution, and the electrolyte of choice being 1 M KOH solution (pH ~13) the indophenol method is undoubtedly the most appropriate to use.

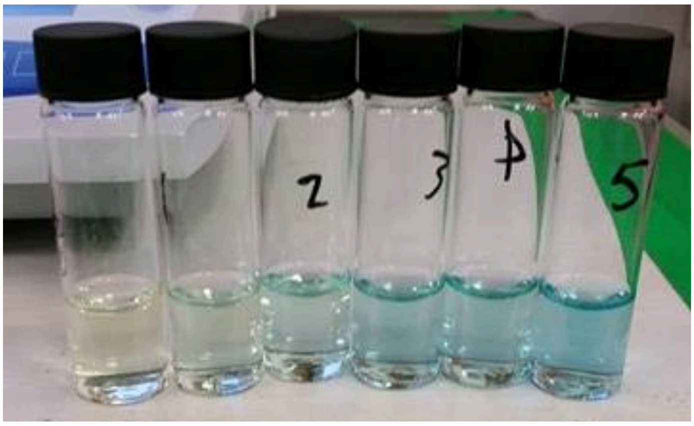

Figure 3.3: Samples used in the indophenol calibration curve (see section 3.4.2), showing increasing amounts of ammonia concentration, and the resulting increase in colour intensity

3.2 - Results and Discussion

We began our investigation of tin phthalocyanines as nitrogen reduction electrocatalysts by conducting cyclic voltammetry as shown in Figures 3.4A and 3.4B. Comparison of a glassy carbon foil electrode (area = 2 cm^2) functionalised with Sn(II) phthalocyanine by drop-casting from suspension in ethanol (loading = 1 mg cm^{-2}, see Materials and Methods section) with an unmodified (bare) glassy carbon electrode is shown in Figure 3.4A. Hence the modified electrode showed a number of reductive waves under a nitrogen atmosphere, the biggest of which occurred at around −0.2 V (*vs.* RHE). Meanwhile, the bare electrode showed no such waves over this potential range under both nitrogen and argon atmospheres.

We were initially encouraged by this result, but considerable confusion subsequently arose when we conducted control reactions with the modified electrode under argon (Figure 3.4B). These studies suggested that all the waves present for the Sn(II) phthalocyanine complex under nitrogen were also present under argon with at least an equivalent intensity. We repeated this control experiment multiple times, and in no cases were we ever able to identify processes occurring under nitrogen that did not occur to a similar extent under argon. Hence (by cyclic voltammetry at least), our data provide no evidence for any electrocatalytic processes connected explicitly with nitrogen reduction by Sn(II) phthalocyanine under these conditions. Instead, by analogy to previous literature on the reduction of main group phthalocyanine complexes, we tentatively assign the cathodic processes evident in Figure 3.4 to reduction of the phthalocyanine ring.[21, 22] It is noteworthy that the original communications do not report any controls under argon, and only show data collected under a nitrogen atmosphere. [17, 18]

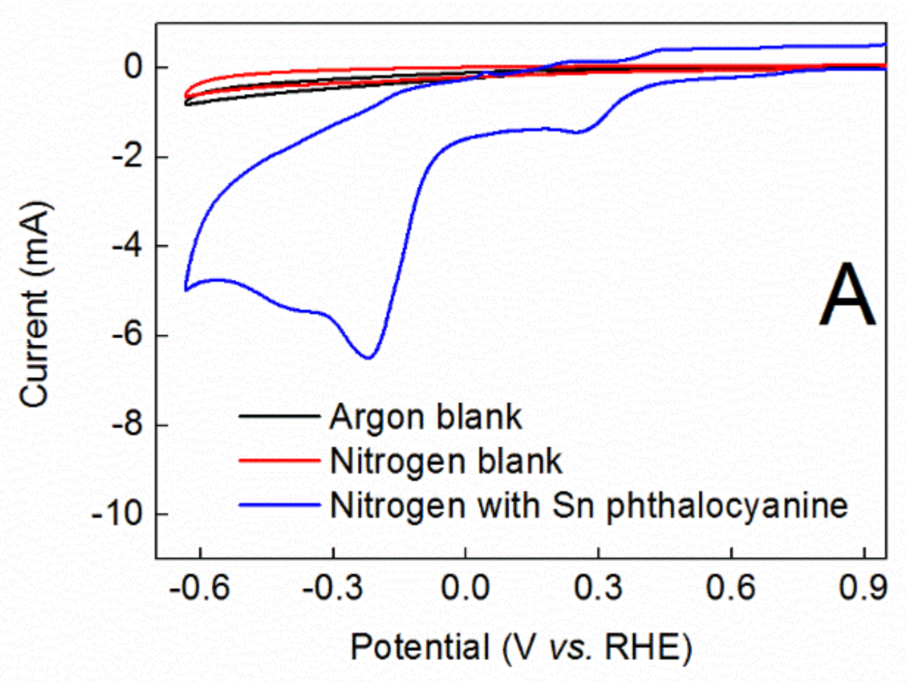

Figure 3.4A: Cyclic voltammograms of a bare 2 cm^2 carbon foil electrode under argon (black line) and nitrogen (red line), and the same electrode after decoration with Sn(II) phthalocyanine (blue line; loading = 1 mg cm^{-2}).

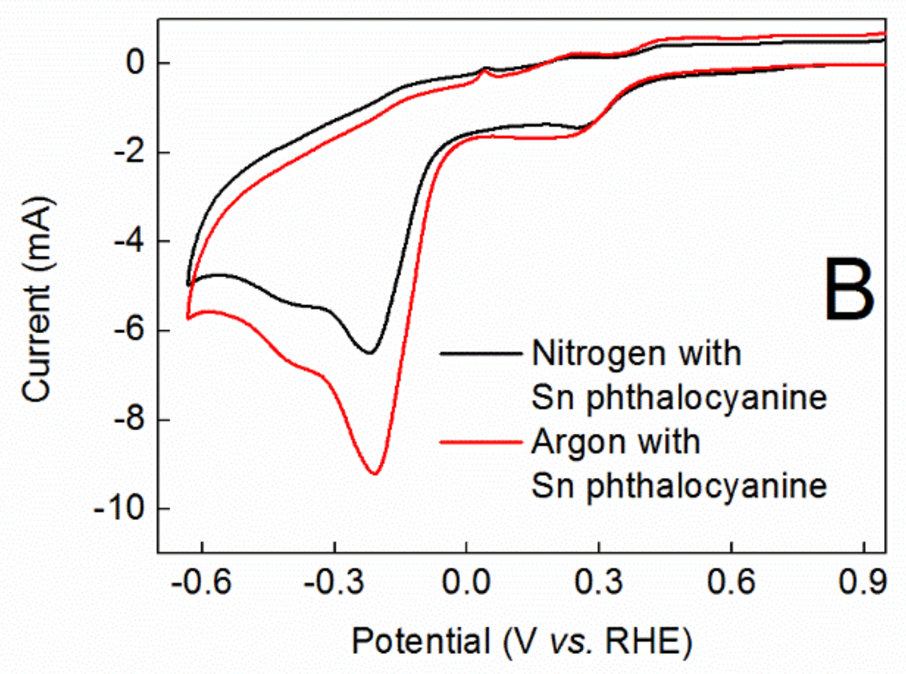

Figure 3.4B: Cyclic voltammograms of a 2 cm^2 carbon foil electrode decorated with Sn(II) phthalocyanine (loading = 1 mg cm^{-2}) under nitrogen (black line) and argon (red line). In all the spectra, a Pt counter electrode and Hg/HgO reference electrode were used in 1 M KOH at a scan rate of 100 mV/s.

The original reports of activity with this material do not report any cyclic voltammetry data, and instead rely on the use of a colorimetric ammonia detection protocol in conjunction with bulk electrolysis. In order to determine if ammonia was produced by this system under bulk electrolysis conditions, we therefore conducted bulk electrolysis with our modified electrodes in 1 M KOH at an applied bias of −0.4 V (*vs.* RHE), as in the original reports. We note at this juncture that all our electrolyses were conducted over a period of 45 minutes compared to around 22 minutes in the original work. Our loading of Sn(II) phthalocyanine complex was also around five times higher than that previously investigated, in order to provide the best chance of observing catalytic activity if any were present.

The first problem we encountered with this method was that simply immersing modified electrodes in the electrolyte was observed to lead to a significant rise in the ammonia concentration in solution. We attribute this to the possible presence of urea in the as-purchased Sn(II) phthalocyanine (heating a mixture of urea and phthalanhydride in the presence of the relevant metal salt is a common route to the generation of metal phthalocyanine complexes [23]), with this urea then undergoing hydrolysis to yield ammonia[24]. Accordingly, we washed our Sn(II) phthalocyanine complex with water multiple times, in order to remove any extraneous urea and/or ammonium salts that were present (see Materials and Methods section). Analysis of the aqueous washing solutions indicated that at least two such washes were required in order to bring the level of ammonia in solution down to a steady baseline value. In this regard, it is important to note that the original communications do not report any washing procedures for the complex, our assumption therefore being that these were used as supplied.

Electrodes modified with Sn(II) phthalocyanine that had been washed in this manner were then subjected to bulk electrolysis at −0.4 V (*vs.* RHE) under various conditions as summarised in Figure 3.5. In all cases, experiments were conducted for 45 minutes, after which time the electrolyte was tested for ammonia using the indophenol method. The level of ammonia in solution was then compared to the level found in the electrolyte prior to immersion of the electrode. Figure 3.5A shows yields of ammonia obtained in this manner under various conditions; each set of conditions was probed multiple times, and the data reported are averages. Hence it is apparent that when no Sn(II) phthalocyanine is present on the electrode surface, then the yield of ammonia under both argon and nitrogen is very low. Similarly, when Sn(II) phthalocyanine is dropcast onto the electrode surface and then that electrode is merely immersed in the electrolyte, then the amount of ammonia detected is also low. This demonstrates that our washing procedure is effective in removing any ammonia (or ammonia-producing species) that are present in the as-purchased materials. In contrast, if electrodes decorated with Sn(II) phthalocyanine are subjected to potentials of −0.4 V (*vs.* RHE), then there is appreciable ammonia formation. However, this activity manifests under *both* nitrogen and argon (and if anything, more ammonia is detected when argon is used than when nitrogen is used), which calls into question whether the supplied nitrogen is the feedstock for generation of this ammonia.

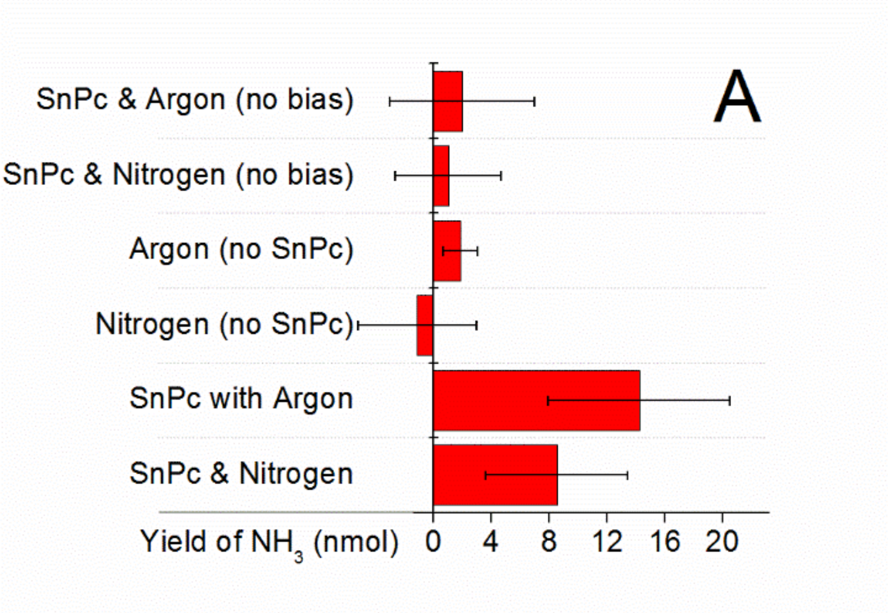

Figure 3.5A: Histograms showing the net yield (in nmol) of ammonia produced under various conditions (per 7.5 mL of electrolyte).

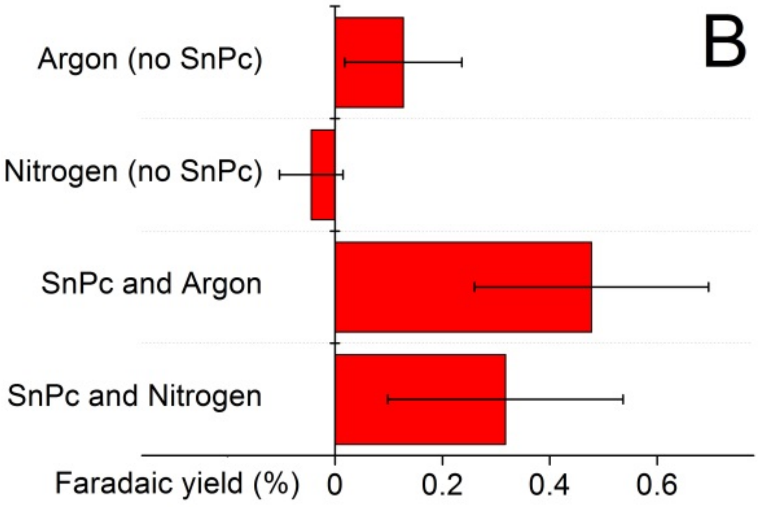

Figure 3.5B: Histograms showing Faradaic yields for ammonia production for those systems where electrical currents were flowing. In both panels, the data shown by the bars are averages of multiple runs (normally five, but four for Ar (no SnPc), six for SnPc with

Nitrogen and seven in the case of Nitrogen (no SnPc)), and the error bars correspond to the standard deviation of these runs. The labels used are as follows: SnPc & Argon (no bias) = decorated electrode immersed in 1 M KOH under an argon atmosphere without any current flowing; SnPc & Nitrogen (no bias) = decorated electrode immersed in 1 M KOH under a nitrogen atmosphere without any current flowing; Ar (no SnPc) = bare carbon electrode held at −0.4 V for 45 minutes under argon; Nitrogen (no SnPc) = bare carbon electrode held at −0.4 V for 45 minutes under nitrogen; SnPc with Argon = decorated electrode immersed in 1 M KOH and held at −0.4 V for 45 minutes under argon; SnPc with Nitrogen = decorated electrode immersed in 1 M KOH and held at −0.4 V for 45 minutes under nitrogen.

Figure 3.5B then shows the production of ammonia from the four systems which were probed by electrochemistry in terms of their Faradaic yields for NH_3 generation. In the two cases where no Sn(II) phthalocyanine was employed, both of these yields are very low (−0.04 ± 0.06% under N_2 and 0.13 ± 0.11% under Ar), suggesting that what little charge is passed during these electrolyses is overwhelmingly not directed towards NH_3 generation. The apparent Faradaic yields when Sn(II) phthalocyanine is present on the electrode are much higher; however, this behaviour is again observed under both nitrogen and argon. Moreover, in both these latter cases, the Faradaic yield is much lower than that quoted by Furuya and Yoshiba (who quoted values of 1.85% at the start of electrolysis, falling to 1.2% after 20 minutes at −0.4 V). Clearly then, the ammonia that is detected in our studies is not emanating from the reduction of the supplied nitrogen stream, as better apparent metrics (both in terms of Faradaic efficiency for NH_3 generation and overall production of NH_3) are evident under argon.

Given that essentially no ammonia is detected when there is no phthalocyanine complex present, our suspicions for the source of the ammonia we detected in these experiments thus fell on the Sn(II) phthalocyanine itself. Any ammonium salts (or species decomposing to such salts) that were present in the as-purchased materials had been removed by washing prior to electrolysis (see above). However, it was possible that the Sn(II) phthalocyanine itself might decompose under an applied bias to liberate ammonia, as is the case with thermal and photochemical degradation of metal-phthalocyanine complexes [25, 26] In support of this, Inductively Coupled Plasma Mass Spectrometry (ICP-MS) performed on our electrolytes showed considerably higher levels of tin to be in solution after a bias potential of −0.4 V had been applied for 45 minutes than when no potential had been applied (see Table 1).

Table 3.1: The levels of tin detected by ICP-MS in various electrolytes (the labels correspond to those given in Figure 3.5).

Sample	**[Sn] in electrolyte (μg L^{-1})**
SnPc & Argon (no bias)	115 (±5.4)
SnPc & Nitrogen (no bias)	146 (±6.2)
Argon with no SnPc	155 (±8.0)
Nitrogen with no SnPc	175 (±10.9)
SnPc with Argon	321 (±7.1)
SnPc with Nitrogen	426 (±1.3)

As the Sn(II) phthalocyanine complex is essentially insoluble in 1 M KOH, it thus seems likely that the elevated levels of tin detected in our electrolytes after electrolysis have their origins in the decomposition of the Sn(II) phthalocyanine under an applied cathodic bias. Cyclic voltammetry seems to confirm that the complex decomposes when reduced; Figure 3.6 (below) shows how the current observed at a given potential decreases markedly over three reduction cycles similar to those shown in Figure 3.4B.

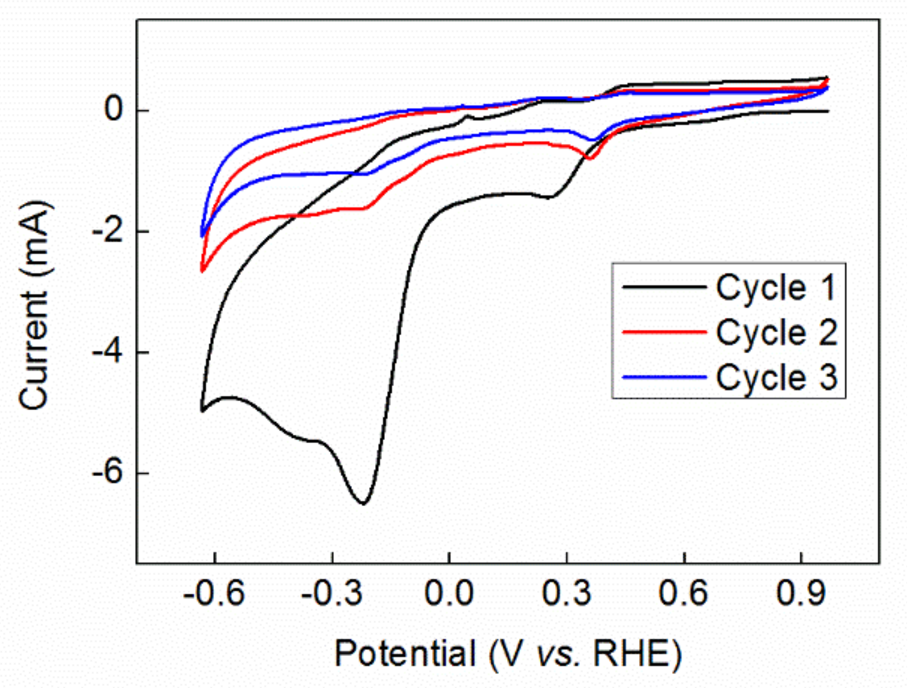

Figure 3.6: Cyclic voltammograms of 2 cm^2 carbon foil electrode decorated with Sn(II) phthalocyanine (loading = 1 mg cm^{-2}) under nitrogen over successive cycles as indicated.

A Pt counter electrode and Hg/HgO reference electrode were used in 1 M KOH at a scan rate of 100 mV/s.

3.3 - Conclusions

In summary, we have shown that Sn(II) phthalocyanine complexes are not electrocatalysts for the reduction of nitrogen to ammonia in 1 M KOH. When a cathodic bias is applied to such complexes, the concentration of ammonia in the electrolyte does increase, but this increase is of the same magnitude under both N_2 and Ar. Moreover, there is no evidence for electrocatalysis by cyclic voltammetry. Ammonia (or species producing ammonia) are present in as-supplied Sn(II) phthalocyanine, and this complex also seems to decompose under cathodic bias (as indicated by cyclic voltammetry and ICP-MS). On the basis of these results, we suggest that any apparent ammonia formation is due to the decomposition of (or possible impurities in) the Sn(II) phthalocyanine, and not electro-reduction of N_2 as previously claimed.

3.4 – Experimental methods and materials

3.4.1 - Materials

Sulfuric acid (95%) was purchased from Fisher. Potassium hydroxide (90%), sodium hydroxide (98-100.5%), phenol (99%), ammonium chloride (99.5%+) and sodium phosphate dibasic (98.5%) were purchased from Sigma Aldrich. Sodium citrate tribasic (99%), tin(II) phthalocyanine, and sodium pentacyanonitrosylferrate(II) (98%) were purchased from Alfa Aesar. Ethanol (100%) and acetone (99%) were purchased from VWR. Propan-2-ol was purchased from Honeywell. All chemical reagents were used as purchased, except for Sn(II) phthalocyanine (see washing procedure below). All aqueous solutions were prepared with ultrapure grade water (18.2 MΩ cm^{-1} resistivity), obtained from a Sartorius Arium Comfort combined water system. pH determinations were made with a Hanna HI 9124 waterproof pH meter. Glassy carbon foil substrates (Carbon-Vitreous 3000C (C) foil, 1.0 mm thickness) were obtained from GoodFellow. All other materials were obtained as stated in the text.

3.4.2 - Ammonia determination

Ammonia was determined colorimetrically using Scheiner's indophenol protocol [27]. Briefly, a 2.5 mL sample of electrolyte was placed in a clean glass sample vial. 1 mL of phenol-nitroprusside buffer and 1.5 mL of alkaline hypochlorite solution were promptly added, the mixture shaken and left in a dark place to develop. After 45 minutes, a UV-vis spectrum was taken, with the value of the absorbance at 635 nm noted (see figure 3.7).

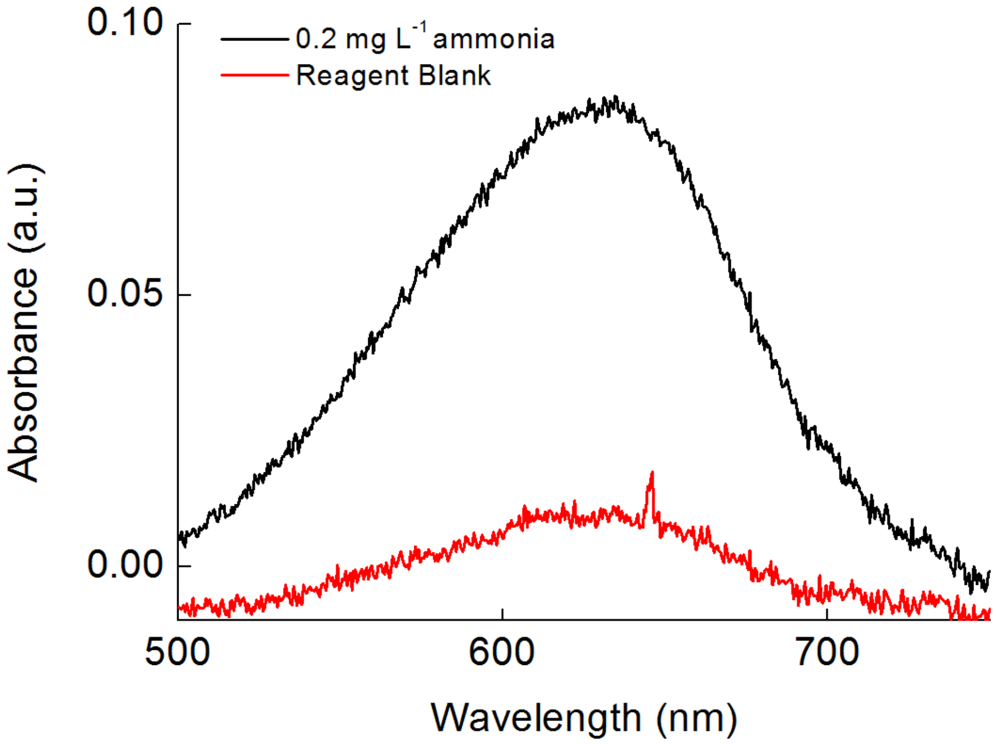

Figure 3.7: UV-vis spectra of indophenol reagents, both with and without ammonia present. Important to note is that due to environmental contamination, there is always a positive result for ammonia.

A calibration curve was also established by this procedure, using ammonium chloride diluted to various concentrations over the range 0.04 - 0.20 mg L^{-1} in 1 M KOH (giving a range of 0.02 – 0.10 mg L^{-1} after being further diluted by the indophenol test reagents: see Figure 3.8). UV-Vis spectra were collected in solution using quartz cuvettes on a JASCO V-670 spectrophotometer, unless otherwise noted. The cuvettes were washed successively with acetone and deionized water prior to use. The Sn(II) phthalocyanine complex is essentially insoluble in 1 M KOH, and suspensions of Sn(II) phthalocyanine in 1 M KOH at the loadings we report here do not produce significant absorption at 635 nm.

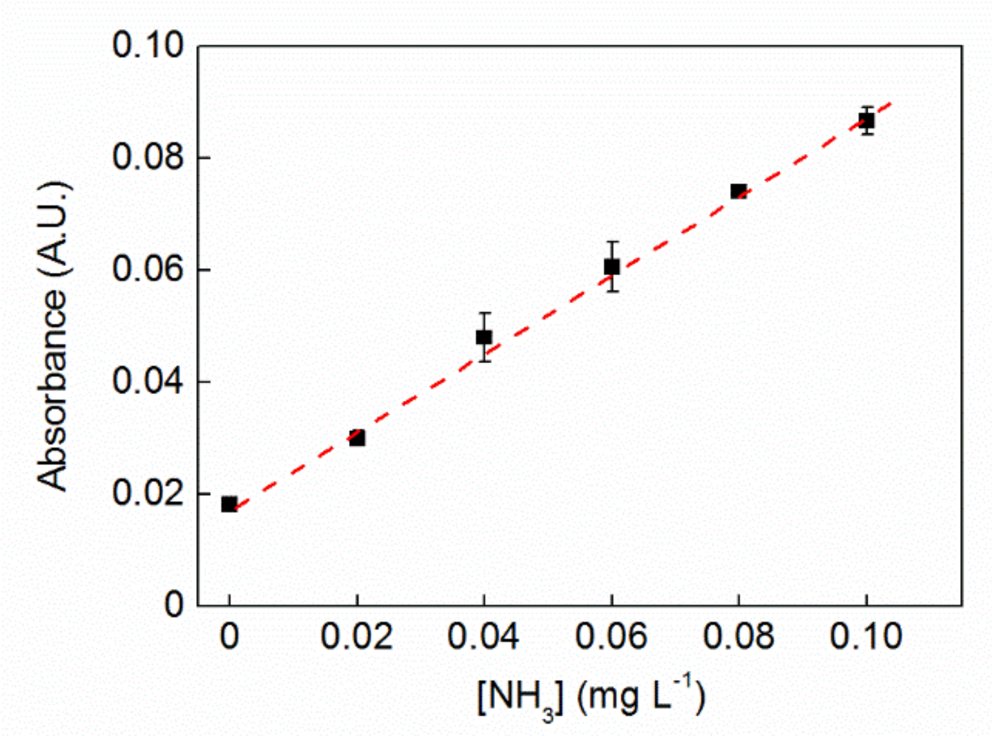

Figure 3.8: Calibration curve used to determine ammonia concentrations in solution. Values for the number of moles of ammonia produced in a given experiment were taken from the amount measured in the electrolyte post electrolysis minus that determined to be in solution prior to electrolysis. Pre-electrolysis values were typically around 0.015 mg L^{-1} in indophenol test samples (and therefore around 0.03 mg L^{-1} in the electrolyte). Each point in the calibration curve is the average of three separate determinations and the error bars are standard deviations.

3.4.3 - Electrochemical methods

Electrochemical studies were performed in a three-electrode configuration as shown in figure 3.9, using a CH Instruments CHI760D potentiostat. Platinum wire was used as the counter electrode and was washed with acetone and deionized water and then sonicated in ultrapure water before each experiment. An Hg/HgO reference electrode (1 M NaOH, CH Instruments) was used. A glassy carbon foil electrode (2 × 1 cm) was used as the working electrode. The working electrode was polished with 0.5 μm diamond polishing solution and washed with ultrapure water and propan-2-ol prior to use. Three-electrode potentials were converted to the RHE reference scale using $E(\mathrm{RHE}) = E(\mathrm{Hg/HgO}) + 0.140\ \mathrm{V} + (0.059 \times \mathrm{pH})$ [28].

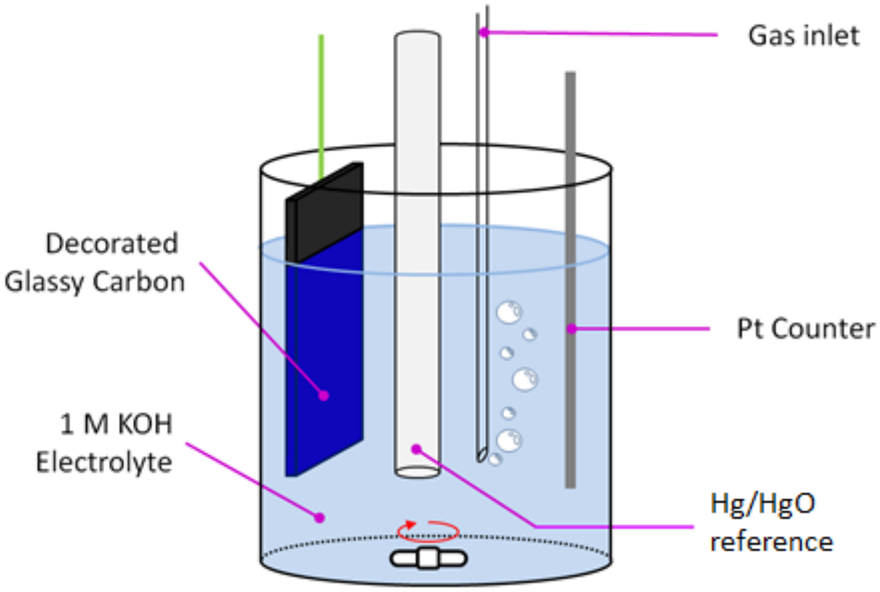

Figure 3.9: A typical electrochemical cell set-up for both the cyclic voltammetry and bulk electrolysis reported in this paper

3.4.3a - Cyclic voltammetry

Cyclic voltammograms were collected in a single chamber cell at room temperature (20 °C) using a scan rate of 100 mV/s in 1 M KOH. Measurements were compensated for the *i*R drop and conducted without stirring. The *i*R test function available on the CH potentiostats uses the general method developed by He and Faulkner [29].

3.4.3b - Bulk electrolysis

Bulk electrolyses were performed in a three-electrode configuration in single compartment electrochemical cells. Solutions were agitated by gas bubbling (either with nitrogen or argon), at equivalent rates of bubbling through the solutions. Bulk electrolyses were conducted without considering any resistive losses; solution resistances were measured using the *i*R test function (as for cyclic voltammetry) and were found to be on average 3.7 Ω for a bare 2 × 1 cm carbon foil electrode, and 5.0 Ω for a 2 × 1 cm carbon foil electrode with Sn(II) phthalocyanine deposited on it (see procedure below). At the currents typically passing in these experiments, voltage drops caused by this uncompensated resistance were thus on the order of 1 - 5 mV, and could be neglected.

3.4.4 Washing procedure for the Sn(II) phthalocyanine

50 mg of Sn(II) phthalocyanine was suspended in 10 mL ultrapure-grade water, and the Sn(II) phthalocyanine then pelleted from this suspension by centrifugation. The supernatant was then decanted and the pellet re-suspended in 10 mL fresh ultrapure-grade water. This process was repeated five times with each 50 mg batch of Sn(II) phthalocyanine (figure 3.10, below) The supernatant solution after each centrifugation was subjected to the indophenol test, giving approximate ammonia concentrations of 0.08 mg L^{-1} in the first wash supernatant and an average of 0.006 mg L^{-1} in the supernatant after 3-5 washes. After the fifth wash, the pelleted material was suspended in acetone and re-pelleted by centrifugation (to help remove water) before isolation and drying at elevated temperature to give dry powder. A comparison of the UV-vis spectra of Sn(II) phthalocyanine before and after washing is made in Figure 3.11A (below). Due to the poor solubility of Sn(II) phthalocyanine in conventional solvents, these spectra are reported in concentrated sulfuric acid, in which Sn(II) phthalocyanine is both reasonably soluble and stable for at least 24 h [30]. The spectra are in good agreement with those reported for Sn(II) phthalocyanine in the literature [24, 31]. Meanwhile, the infrared spectrum of the washed Sn(II) phthalocyanine (collected in the solid state on a Shimadzu IRAffinity-1S Fourier Transform Infrared Spectrophotometer) is shown in Figure 3.11B. The spectrum displays key bands as indicated, which Kroenke and Kenney have shown to be characteristic of Sn(II) phthalocyanine [32].

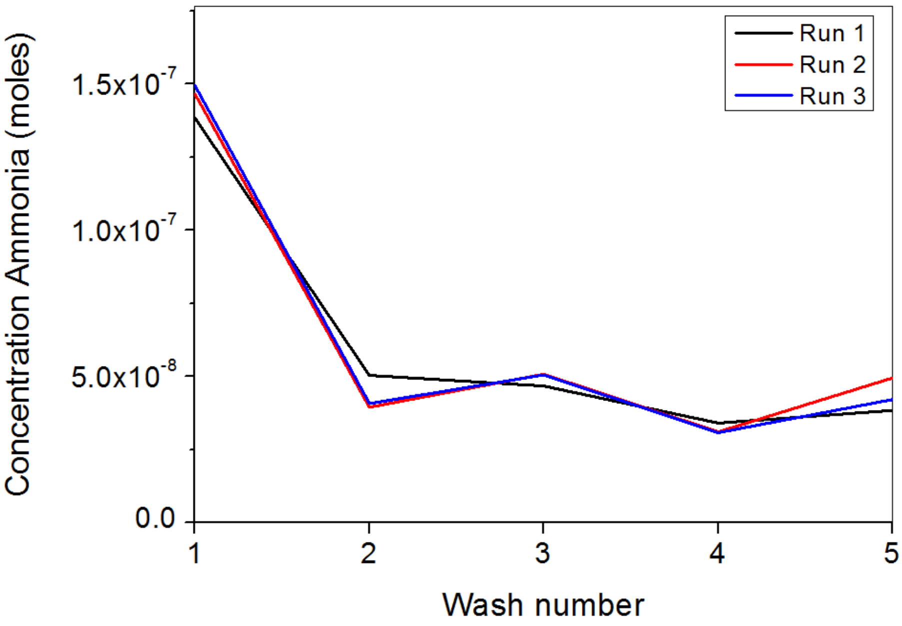

Figure 3.10: Comparison of ammonia concentration in the aqueous washings of Sn (II) phthalocyanine (as supplied)

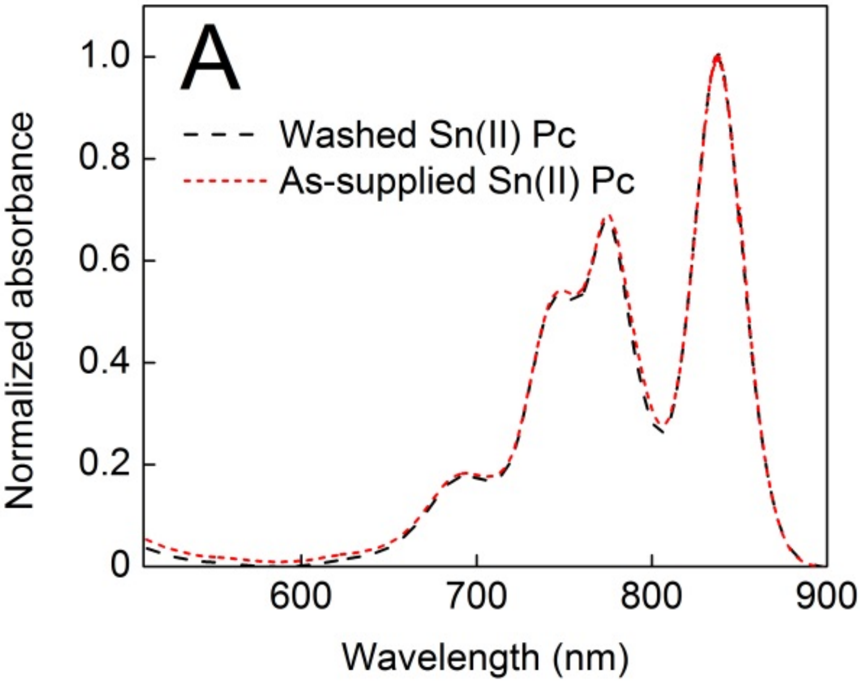

Figure 3.11A: Normalized UV-vis spectra of Sn(II) phthalocyanine in concentrated sulfuric acid before and after the washing procedure described above. The concentration of Sn(II) phthalocyanine was 35 µM in each case and plastic cuvettes were used.

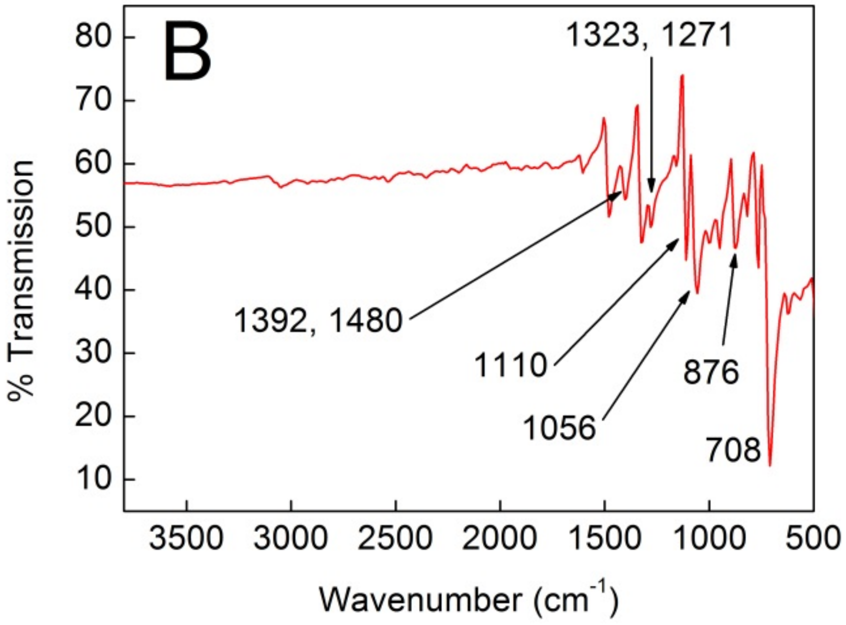

Figure 3.11B: Infrared spectrum of Sn(II) phthalocyanine in the solid state after the washing procedure described above.

3.4.5 - Working Electrode preparation

After washing, 50 mg Sn(II) phthalocyanine was placed into 10 mL of ethanol and sonicated to make a suspension. A 25 µL aliquot of this suspension was then placed on the 2 × 1 cm carbon foil electrode surface and allowed to dry. Successive 25 µL aliquots of the suspension were then placed on the electrode in the same way (with some perturbation of the previously-deposited layer(s) so as to make as even a layer as possible) until a loading of 1 mg cm^{-2} (total loading of 2 mg) of Sn(II) phthalocyanine was achieved (as gauged by measuring the mass difference of a dry electrode after each drop-casting cycle).

3.4.6 - Inductively Coupled Plasma Mass Spectrometry

Samples of various electrolytes were analysed by Inductively Coupled Plasma Mass Spectrometry on an Agilent 7700 ICP-MS instrument at the Department of Pure and Applied Chemistry at the University of Strathclyde (UK). All samples were treated with concentrated nitric acid to aid analysis (final pH of samples was pH 1 – 1.3).

3.5 – References

1. Government, U.S., *U.S. Geological Survey: Mineral Commodity Summaries 2019*, U.S.D.o.t. Interior, Editor. 2019. p. 200.
2. Smil, V., *Detonator of the population explosion.* Nature, 1999. **400**(6743): p. 415-415.
3. Shipman, M.A. and M.D. Symes, *Recent progress towards the electrosynthesis of ammonia from sustainable resources.* Catalysis Today, 2017. **286**: p. 57-68.
4. Giddey, S., S.P.S. Badwal, and A. Kulkarni, *Review of electrochemical ammonia production technologies and materials.* International Journal of Hydrogen Energy, 2013. **38**(34): p. 14576-14594.
5. van der Ham, C.J., M.T. Koper; D.G. Hetterscheid, *Challenges in reduction of dinitrogen by proton and electron transfer.* Chem Soc Rev, 2014. **43**(15): p. 5183-91.
6. Kyriakou, V., et al., *Progress in the Electrochemical Synthesis of Ammonia.* Catalysis Today, 2017. **286**: p. 2-13.
7. Sclafani, A., V. Augugliaro, and M. Schiavello, *Dinitrogen Electrochemical Reduction to Ammonia over Iron Cathode in Aqueous Medium.* Journal of the Electrochemical Society, 1983. **130**(3): p. 734-735.
8. Kordali, V., G. Kyriacou, and C. Lambrou, *Electrochemical synthesis of ammonia at atmospheric pressure and low temperature in a solid polymer electrolyte cell.* Chemical Communications, 2000(17): p. 1673-1674.
9. Kugler, K., et al., *Galvanic deposition of Rh and Ru on randomly structured Ti felts for the electrochemical NH 3 synthesis.* Physical Chemistry Chemical Physics, 2015. **17**(5): p. 3768-3782.
10. Lan, R., J.T.S. Irvine, and S. Tao, *Synthesis of ammonia directly from air and water at ambient temperature and pressure.* Scientific Reports, 2013. **3**.
11. Lan, R. and S. Tao, *Electrochemical synthesis of ammonia directly from air and water using a Li+/H+/NH4+ mixed conducting electrolyte.* RSC Advances, 2013. **3**(39): p. 18016.
12. Kwiyong Kim, N.L., Chung-Yul Yoo, Jong-Nam Kim, Hyung Chul Yoon, and a.J.-I. Han, *Electrochemical Reduction of Nitrogen to Ammonia in 2-Propanol under Ambient Temperature and Pressure.* J. of the Electrochem. Soc. , 2016. **163**(7): p. 610-612.

13. Bao, D., et al., *Electrochemical Reduction of N2 under Ambient Conditions for Artificial N2 Fixation and Renewable Energy Storage Using N2 /NH3 Cycle.* Adv Mater, 2017. **29**(3).

14. Chen, G.F., et al., *Ammonia Electrosynthesis with High Selectivity under Ambient Conditions via a Li(+) Incorporation Strategy.* J Am Chem Soc, 2017. **139**(29): p. 9771-9774.

15. Chen, S., et al., *Electrocatalytic Synthesis of Ammonia at Room Temperature and Atmospheric Pressure from Water and Nitrogen on a Carbon-Nanotube-Based Electrocatalyst.* Angew Chem Int Ed Engl, 2017. **56**(10): p. 2699-2703.

16. McEnaney, J.M., et al., *Ammonia synthesis from N2 and H2O using a lithium cycling electrification strategy at atmospheric pressure.* Energy & Environmental Science, 2017. **10**(7): p. 1621-1630.

17. N. Furuya; H. Yoshiba, *Electroreduction of nitrogen to ammonia on gas-diffusion electrodes modified by Fe-Phthalocyanine.* J. Electroanal. Chem. , 1989. **263**: p. 171-174.

18. N. Furuya; H. Yoshiba, *Electroreduction of nitrogen to ammonia on gas-diffusion electrodes modified by metal pthalocyanines.* J. Electroanal. Chem. , 1989. **272**: p. 263-266.

19. Zhao, Y., et al., *Ammonia Detection Methods in Photocatalytic and Electrocatalytic Experiments: How to Improve the Reliability of NH3 Production Rates?* Adv Sci (Weinh), 2019. **6**(8): p. 1802109.

20. Ullmann, F., et al., *Ullmann's encyclopedia of industrial chemistry*. 1985: VCH publishers.

21. P.C.Minor, A.B.P.L., *Electrochemistry of Main-Group Phthalocyanines.* Inorg. Chem, 1981. **20**: p. 4015-4017.

22. J. Silver; C.S. Frampton, G.R.Fern; D.A. Davies; .J.R.Miller; J.L.Soza-Sanchez., *Novel Seven Coordination Geometry of Sn(IV) Crystal Structures of Phthalocyaninato Bis(undecylcarboxylato)Sn(IV), Its Si(IV) Analogue, and Phthalocyaninato Bis (chloro)silicon(IV). The electrochemistry of the Si (IV) analogue and related compounds.* Inorg. Chem, 2001. **40**: p. 5434-5439.

23. BekaroĞlu, Ö., *Synthesis of phthalocyanines and related compounds.* Journal of Porphyrins and Phthalocyanines, 2000. **4**(5): p. 465-473.

24. Lynn, K., *Kinetics of base-catalyzed hydrolysis of urea.* The Journal of Physical Chemistry, 1965. **69**(2): p. 687-689.

25. Lawton, E.A., *The thermal stability of copper phthalocyanine.* The Journal of Physical Chemistry, 1958. **62**(3): p. 384-384.
26. Schreiver, I., et al., *Formation of highly toxic hydrogen cyanide upon ruby laser irradiation of the tattoo pigment phthalocyanine blue.* Sci Rep, 2015. **5**: p. 12915.
27. Scheiner, D., *Determination of ammonia and Kjeldahl nitrogen by indophenol method.* Water research, 1976. **10**(1): p. 31-36.
28. Meites, L., *Handbook of analytical chemistry.* Soil Science, 1963. **96**(5): p. 358.
29. He, P. and L.R. Faulkner, *Intelligent, automatic compensation of solution resistance.* Analytical Chemistry, 1986. **58**(3): p. 517-523.
30. Ghani, F., J. Kristen, and H. Riegler, *Solubility Properties of Unsubstituted Metal Phthalocyanines in Different Types of Solvents.* Journal of Chemical & Engineering Data, 2012. **57**(2): p. 439-449.
31. Kubiak, R., G. Dyrda, and K. Ejsmont, *Examples of UV–Vis profiles use as tool for evidence of the metallophthalocyanines transformation.* Journal of Molecular Structure, 2017. **1130**: p. 559-564.
32. Kroenke, W.J. and M.E. Kenney, *The infrared spectra of some tin and lead phthalocyanines.* Inorganic Chemistry, 1964. **3**(5): p. 696-698.

Chapter 4

Towards a Better Understanding of the Electrosynthesis of 2,5-dicarboxy-2,5-dihydrofurans: Structure, Mechanism and Influence over Stereochemistry

Acknowledgements and declaration

This chapter includes extended and updated sections from the following paper:

"Towards a Better Understanding of the Electrosynthesis of 2,5-dicarboxy-2,5-dihydrofurans: Structure, Mechanism and Influence over Stereochemistry" **Michael A. Shipman**, Stephen Sproules, Claire Wilson and Mark D. Symes, Royal Soc. Open Sci, **2019**, 6, 5, 190336..

X-ray Diffraction and refinement services were performed by C. Wilson (University of Glasgow). DFT calculations were performed by S. Sproules (University of Glasgow). Unless otherwise stated all other experimental work was performed by M. A. Shipman and the paper was co-authored by M. A. Shipman, S. Sproules, and M. D. Symes.

Synopsis

2,5-Dicarboxy-2,5-dihydrofurans are key constituents of a number of natural products and have roles as intermediates in the formation of other such compounds of interest. Typically, these species are synthesised using toxic Pb(IV) salts. Electrochemical syntheses of 2,5-diacetoxy-2,5-dihydrofuran that do not require the use of lead have been reported, but a general lack of experimental detail has prevented these procedures from being more widely adopted. Moreover, no electrochemical study has yet reported the ratio of *cis* and *trans* isomers produced. Herein, we compare the chemical, lead-based route to 2,5-diacetoxy-2,5-dihydrofuran with a fully-described electrosynthesis method. In doing so, we have discovered that the *cis* and *trans* isomers of this compound were previously incorrectly assigned in the literature, an error that we correct by obtaining the crystal structure of *cis*-2,5-diacetoxy-2,5-dihydrofuran. This allows the ratios of the isomers as prepared by the chemical (2:1 *cis*:*trans*) and electrochemical (7:5 *cis*:*trans*) methods to be obtained. Through experimental and computational insights, we propose a mechanism for the electrochemical synthesis of 2,5-dicarboxy-2,5-dihydrofurans and go some way towards validating this mechanism by synthesising 2,5-dibutoxy-2,5-dihydrofuran electrochemically for the first time. We hope that these findings will provide some greater clarity to the literature surrounding the electrosynthesis and potential applications of 2,5-dicarboxy-2,5-dihydrofurans.

4.1 - Introduction

2,5-Dicarboxy-2,5-dihydrofurans can be found in natural products such as aplysulphurin,[1] the thuridillins[2] and the prunolides.[3] They have also been used as building blocks in the preparation of species such as aflatoxin B_1,[4] and related moieties can be found in the dendrillolides[5] and aplyviolene.[6] Moreover, 2,5-diacetoxy-2,5-dihydrofuran has been employed as a precursor to various butenolides,[7] nucleosides,[8] and molecules with potential pharmaceutical[9-11] and technological applications.[12]

In the majority of cases, these 2,5-dicarboxy-2,5-dihydrofurans are prepared by reaction of furan with the appropriate tetracarboxy salt of lead according to the general method of Elming and Clauson-Kaas.[13] An attractive route for obtaining such products without the use of toxic lead salts is the electrochemical oxidation of furan in the presence of acetate to give 2,5-diacetoxy-2,5-dihydrofuran. This approach was first reported by Wilson and Lippincott (1956),[14] and subsequently developed firstly by Baggaley and Brettle (1968),[15] and then Shono and co-workers (1981).[7] However, little attention seems to have been paid to this electrochemical route in recent years, aside from a report by Horii *et al.* describing the electrosynthesis of 2,5-diacetoxy-2,5-dihydrofuran in a thin-layer flow cell.[16] This latter work is also the only report of the electrochemical synthesis of a 2,5-dicarboxy-2,5-dihydrofuran with a comprehensive and detailed experimental procedure. To date, all these electrosynthesis methods have been conducted under constant current conditions.

A complicating factor with both the chemical (Pb-promoted) and electrochemical methods for the preparation of 2,5-dicarboxy-2,5-dihydrofurans is the fact that two isomers of the product are possible, one where the carboxy substituents are *trans* to one another and one where they have a *cis* arrangement (see Figure 4.1). Hitherto, it has not proved possible to control which isomer forms to any significant degree using either the chemical or electrochemical methods. Moreover, even in the case of the simplest of these species, 2,5-diacetoxy-2,5-dihydrofuran, an unambiguous identification of the two isomers remains elusive.

Against this background, the initial aims of the project were to determine the absolute structure of the 2,5-diacetoxy-2,5-dihydrofuran sterioisomers, as definitive assignment of the stereoisomers is essential if 2,5-dicarboxy-2,5-dihydrofurans are to realise their potential as building blocks in organic synthesis. In addition, any insights into affording a greater control over the stereoselectivity of this reaction would also be most useful from a more synthetic and practical approach.

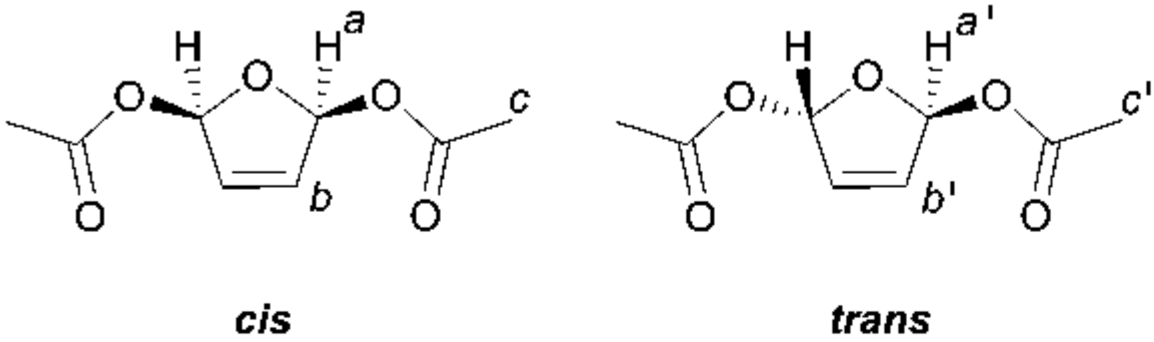

cis

trans

Figure 4.1: The *cis* and *trans* isomers of 2,5-diacetoxy-2,5-dihydrofuran discussed in this chapter. Italic letters on these structures correspond to the ^{1}H NMR signal assignments in the Experimental Section.

Herein, we describe our attempts to determine the stereoselectivity of the electrochemical synthesis of 2,5-diacetoxy-2,5-dihydrofuran under batch conditions and to provide a more detailed methodology for this process than has been reported to date. In the course of this study, we isolated and purified the mixture of 2,5-diacetoxy-2,5-dihydrofuran isomers. This in turn allowed us to assign for the first time and unambiguously the structural identities of each isomer. Contrary to our expectations and the previous literature reports,[4,17-18] we show that the crystalline isomer is in fact the *cis* isomer (and not the *trans* isomer as had been assumed). This fact obviously has a major bearing on trying to gain control over which isomer forms and also has implications for using the products of this reaction in subsequent chemical syntheses. As a direct result of this discovery, we propose a route by which carboxylate groups add to electrochemically-oxidised furans and validate this model by reversing the stereoselectivity for the *cis* isomer generally displayed when using acetate, by using the bulkier substituent butyrate to give predominantly the *trans* product. We hope that these findings will allow deeper insight into the electrosynthesis (and potential applications) of 2,5-dicarboxy-2,5-dihydrofurans.

4.2 - Results and Discussion

4.2.1 - Chemical Synthesis and Characterisation of 2,5-diacetoxy-2,5-dihydrofuran

Before exploring the electrochemical synthesis of 2,5-diacetoxy-2,5-dihydrofuran, we first undertook its chemical synthesis using lead acetate according to the method of Holzapfel and Williams[4] (itself an adaptation of the procedure described by Elming and Clauson-Kaas[13]). This provided us with a benchmark against which to compare the isomeric ratios of our electrochemical experiments, as the relative ratios of the two isomers can be readily discerned by ^{1}H NMR (see below). These experiments also provided sufficient quantities of material to allow the isolation of crystals of suitable quality for single crystal X-ray diffraction (see Experimental Section 4.4.3).

Figure 4.2 (below) shows unambiguously that the crystalline form of 2,5-diacetoxy-2,5-dihydrofuran is the *cis* isomer, in which the two acetate moieties have added to the same face of the furan ring. In the product, the five-membered ring itself remains reasonably unpuckered (O1—C2—C3—C4 = 8.05(18)°, C2—O1—C5—C4 = 13.59(16)°, C2—C3—C4—C5 = 0.26(18)°, C3—C4—C5—O1 = 8.45(17)° and C5—O1—C2—C3 = 13.45(16)°) with a short C3—C4 interaction of 1.312(2) Å consistent with a carbon-carbon double bond. Meanwhile, the bond lengths between C2 and C3, and between C4 and C5 (1.494(2) Å and 1.490(2) Å respectively), are both much closer to those typical of carbon-carbon single bonds. The bond angles between the acetate substituents and the ring (O1—C2—O4 = 109.18(12)° and O4—C2—C3 = 107.46(13)° for one acetate and O1—C5—O2 = 110.14(12)° and O2—C5—C4 = 106.87(13)° for the other) suggest a largely tetrahedral geometry around carbons C2 and C5. All this is consistent with the structure of the *cis* isomer drawn in Figure 4.1, where the furan ring has been oxidised and two acetate units have added to the same side of the ring through carbon-oxygen bonds in the 2- and 5-positions.

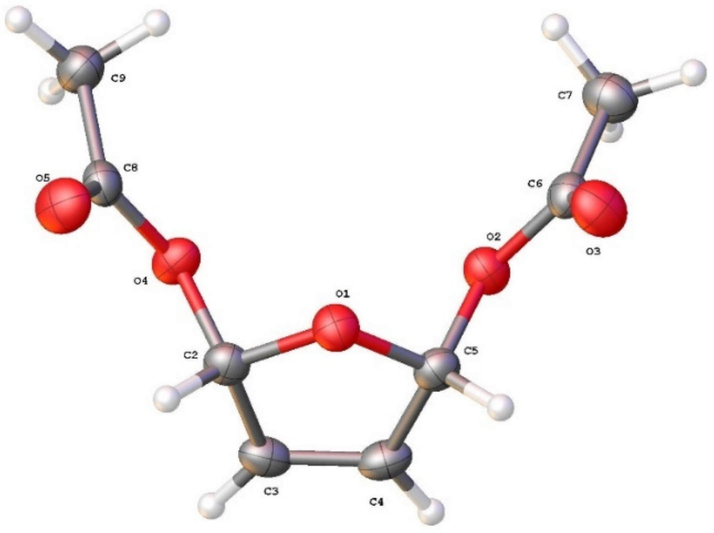

Figure 4.2: The crystal structure of *cis*-2,5-diacetoxy-2,5-dihydrofuran. Crystallographic details can be found appendix A1. Colour scheme: C = grey, O = red, H = white.

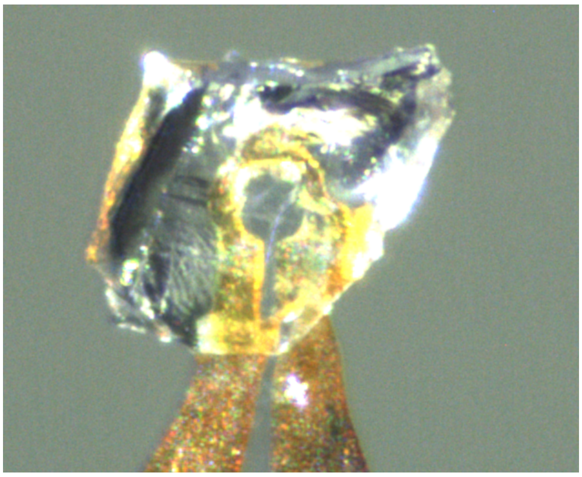

Figure 4.3: A single crystal of *cis*-2,5-diacetoxy-2,5-dihydrofuran, as mounted in the diffractometer.

Armed with this information, we were then able to assign the signals in the ^{1}H NMR spectrum of isomeric 2,5-diacetoxy-2,5-dihydrofuran definitively for the first time. Figure 4.4 shows an ^{1}H NMR plot of the outcome of a typical chemical synthesis of 2,5-diacetoxy-2,5-dihydrofuran after removal of the lead salts by filtration and washing out the excess acetic acid by aqueous extraction (bottom spectrum)

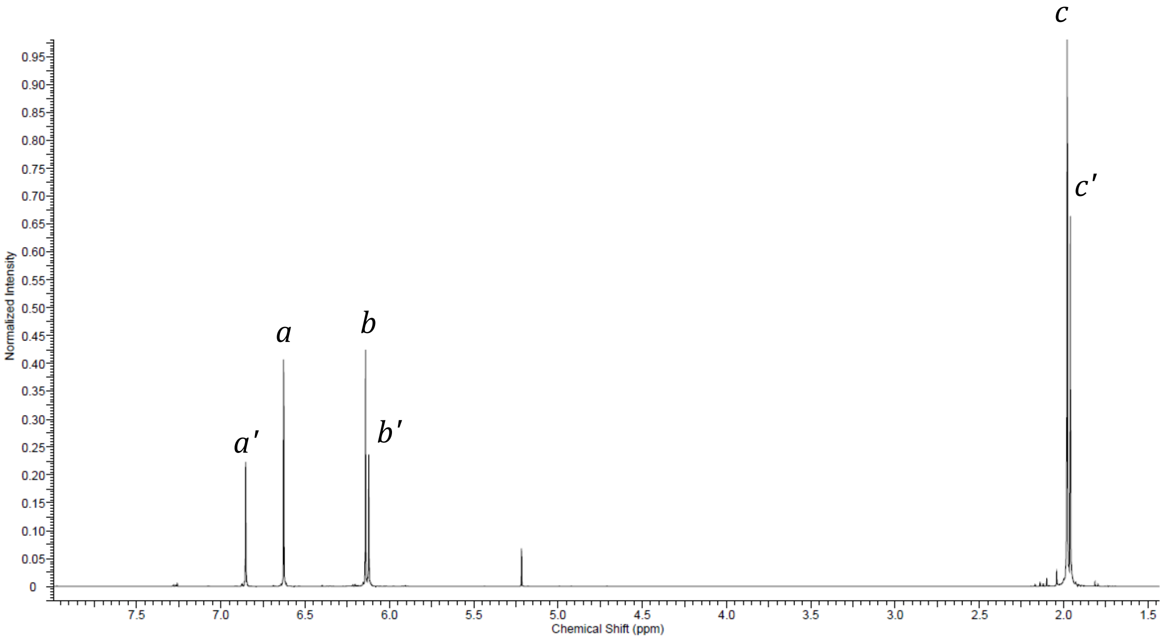

Figure 4.4: ^{1}H NMR spectrum of a mixture of *trans*- and *cis*-2,5-diacetoxy-2,5-dihydrofuran in $CDCl_3$ obtained *via* chemical synthesis

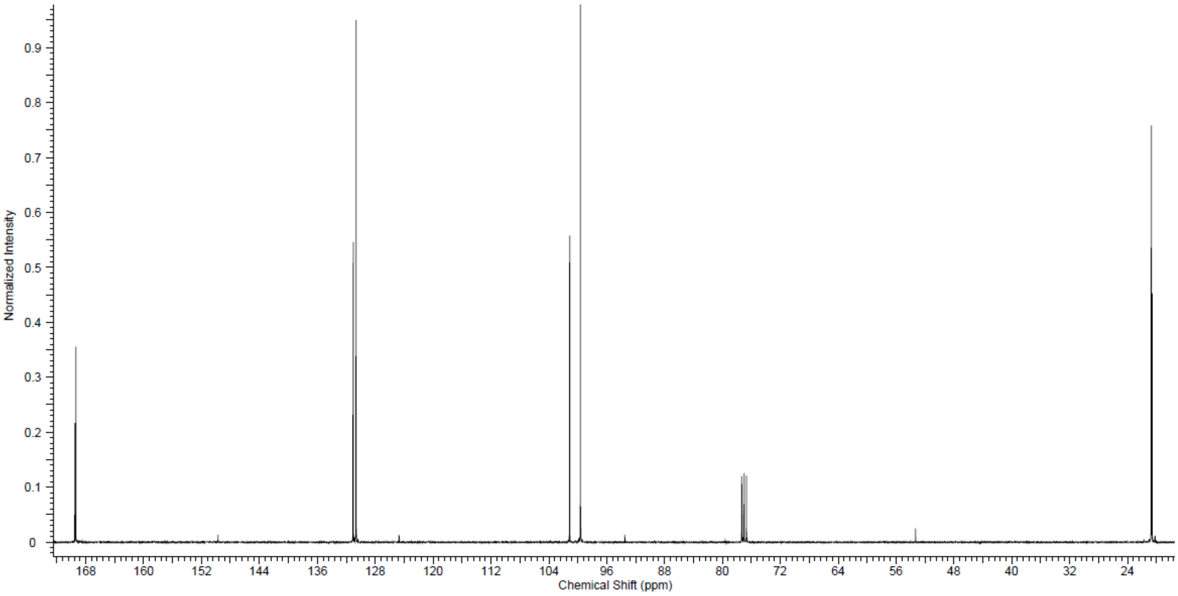

Figure 4.5: ^{13}C NMR spectrum of a mixture of *trans*- and *cis*-2,5-diacetoxy-2,5-dihydrofuran in $CDCl_3$ obtained *via* chemical synthesis.

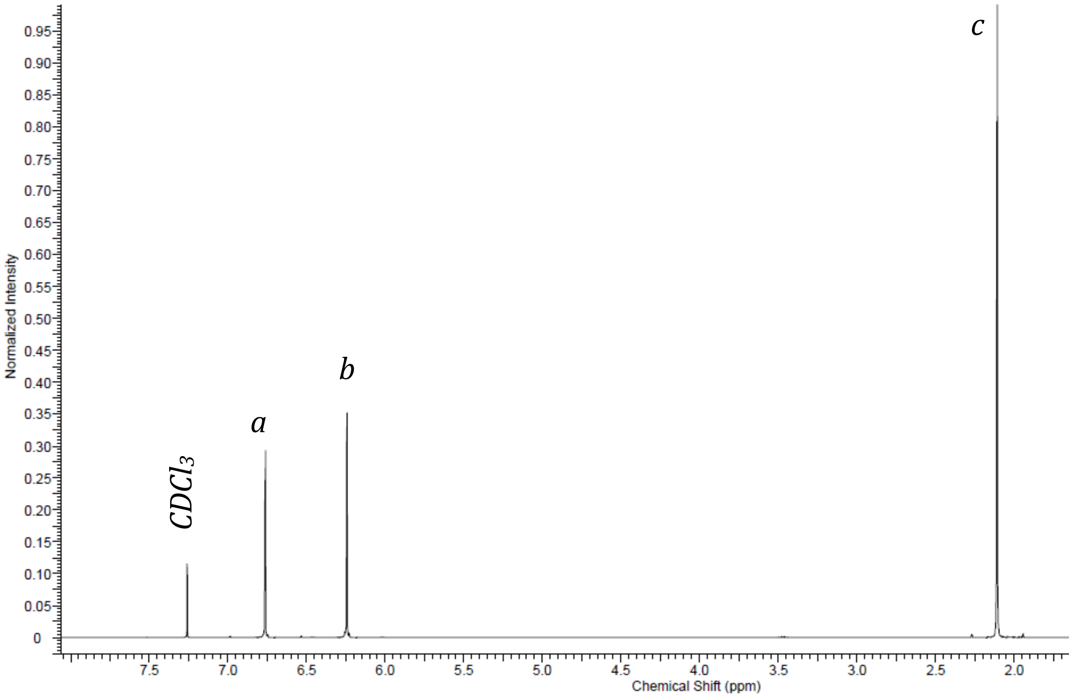

Figure 4.6: ^{1}H NMR spectrum of *cis*-2,5-diacetoxy-2,5-dihydrofuran in $CDCl_3$.

Figure 4.6 shows the ^{1}H NMR spectrum of the crystalline material whose structure is shown in Figure 4.3, and which therefore corresponds to the *cis* isomer. On the basis of the chemical shifts shown by this purified isomer, it seems apparent that the two signals at 6.86 and 6.13 ppm (fig. 4.4) arise from the *trans* isomer and the two signals in between the aforementioned correspond to the *cis* isomer.

This is borne out in figure 4.7, which shows the ^{1}H NMR spectrum of the remaining product material after removal of the crystals; clearly the ratio of the peaks for the *cis* isomer relative to that for the *trans* isomer have decreased in intensity as some of the *cis* isomer has been removed as crystals.

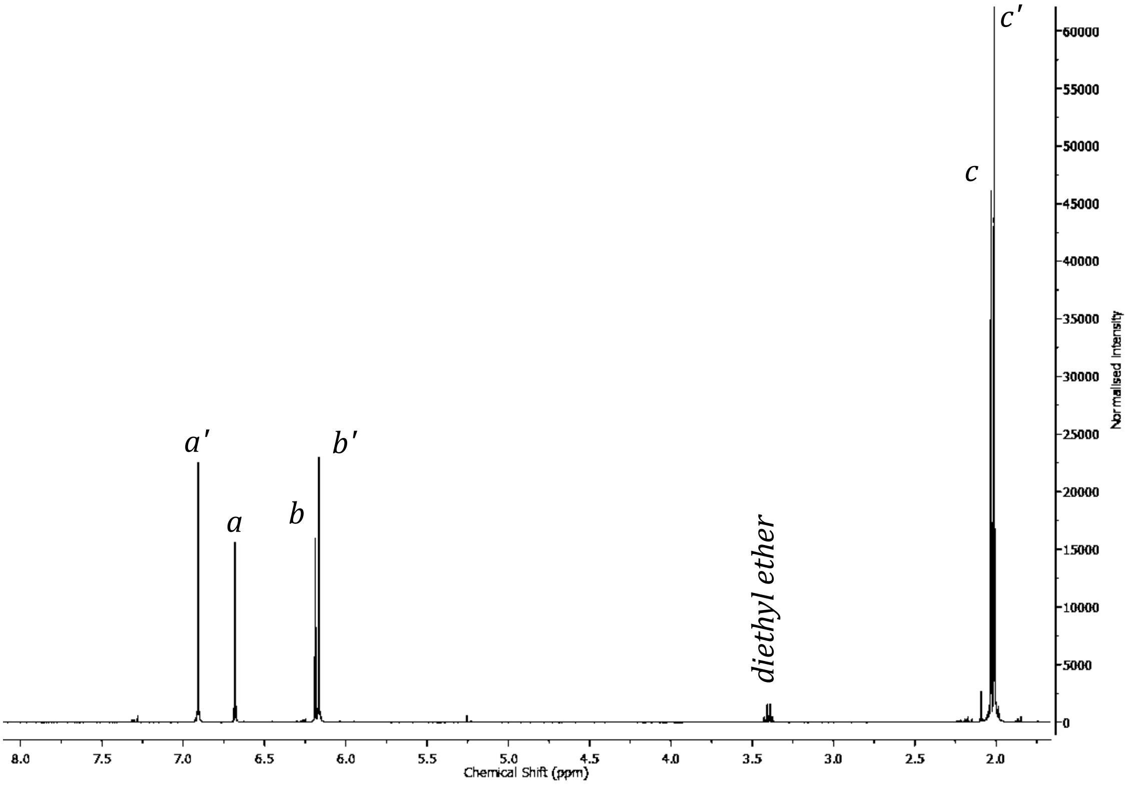

Figure 4.7: ^{1}H NMR spectrum of trans-2,5-diacetoxy-2,5-dihydrofuran in $CDCl_3$

A Heteronuclear Multiple Quantum Coherence (HMQC) analysis then allows the two signals for each isomer to be assigned to the relevant protons on the basis of the cross-peaks seen in the associated ^{1}H and ^{13}C NMR spectra (Figures 4.8 and 4.9).

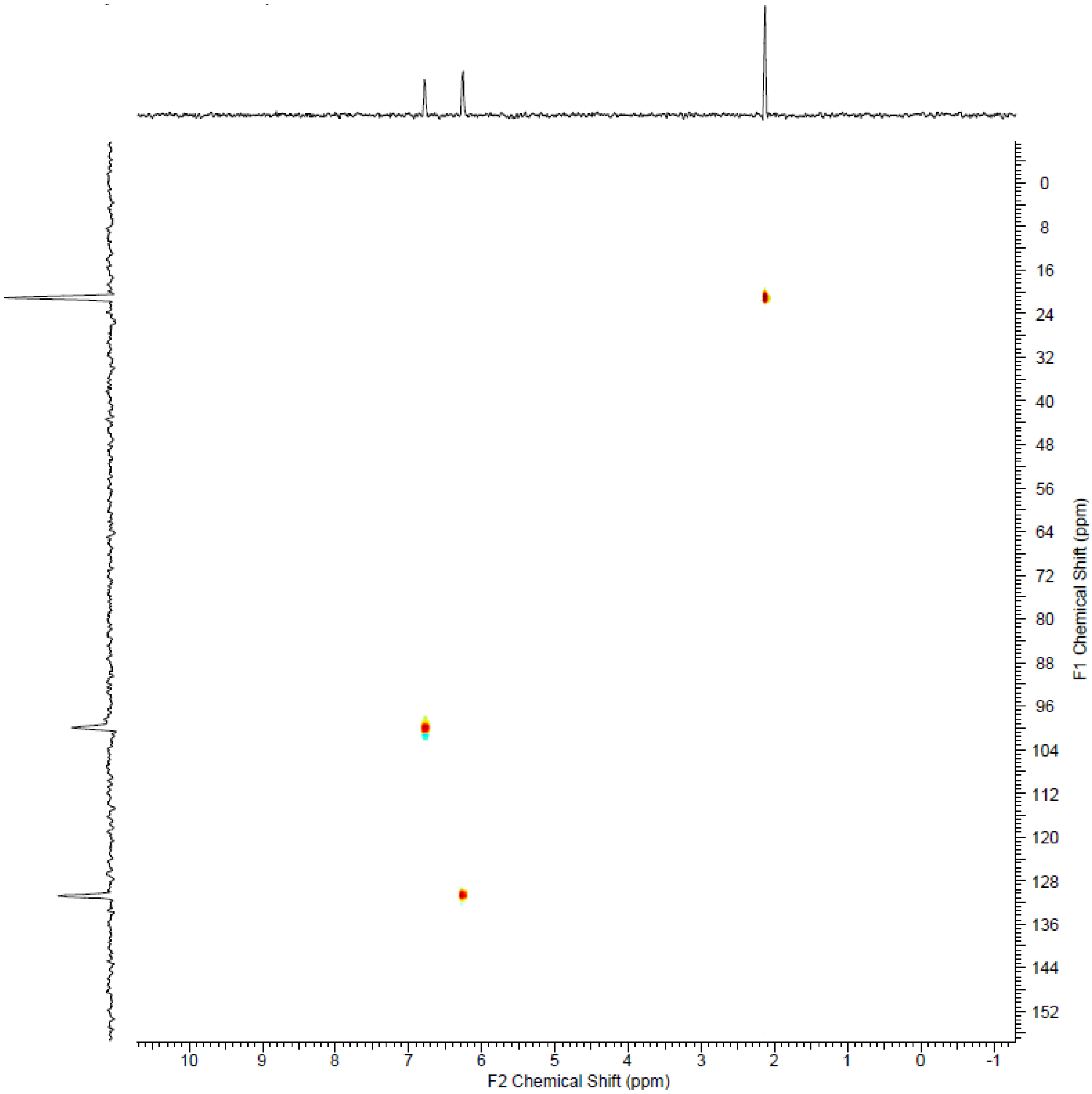

Figure 4.8: HMQC spectrum of *cis*-2,5-diacetoxy-2,5-dihydrofuran in $CDCl_3$.

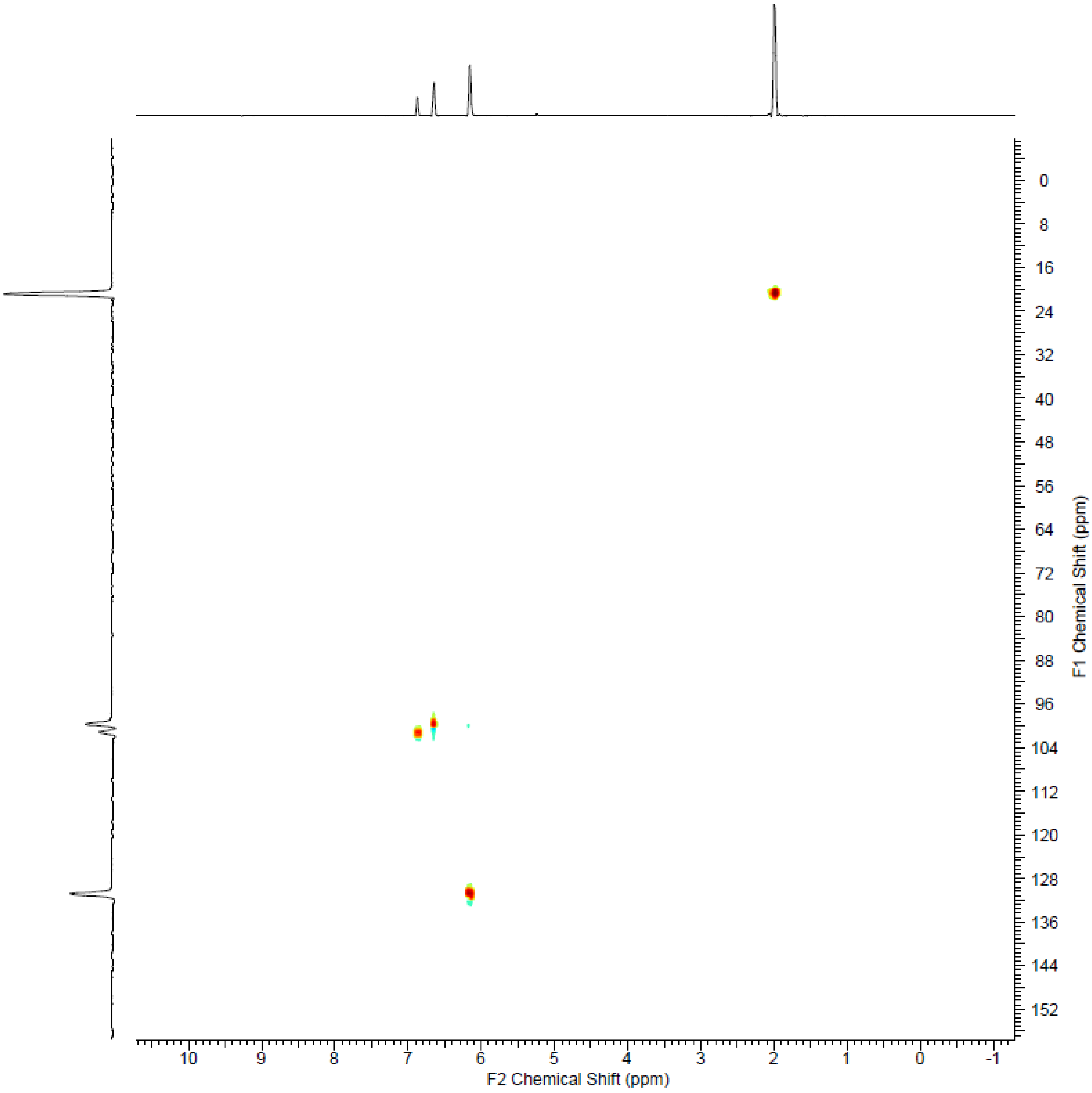

Figure 4.9: HMQC spectrum of a mixture of *trans*- and *cis*-2,5-diacetoxy-2,5-dihydrofuran in $CDCl_3$ obtained *via* chemical synthesis.

Further corroboration is to be gained from a ^1H NMR correlation spectrum (COSY), which shows that the inner peaks couple to each other (but not the outer peaks, Figure 4.10).

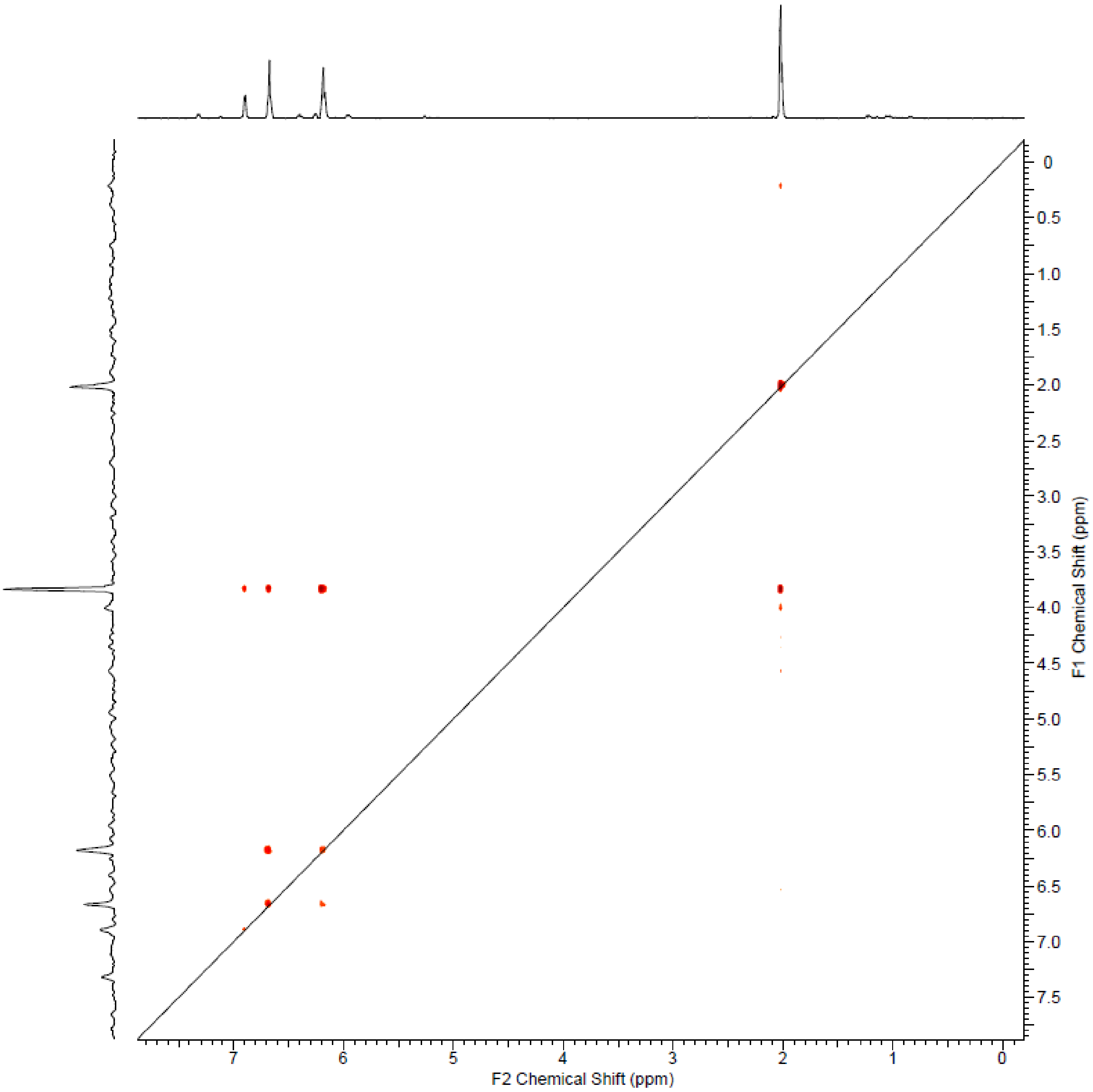

Figure 4.10: COSY spectrum of a mixture of *trans*- and *cis*-2,5-diacetoxy-2,5-dihydrofuran in $CDCl_3$ obtained *via* chemical synthesis.

This then leads to the assignments shown in Figure 4.11. With this information in hand, we performed multiple repeats of this chemical synthesis method and (through analysis of the ^1H NMR spectra after removal of acetic acid and lead salts) we were able to show that the *cis* isomer is the dominant product under these chemical conditions, forming in a ratio of *cis*:*trans* of 1.88(±0.03):1. This ratio is in very good agreement with that reported by Holzapfel and Williams[4] (2:1 major:minor), but we note that these authors (and others[17,18]) previously (incorrectly) assumed the major isomer to be the *trans* isomer on the basis of NMR coupling constants and mechanistic considerations. However, by isolating the *cis* form and solving its crystal structure, we show that in fact the *cis* form is the major isomer.

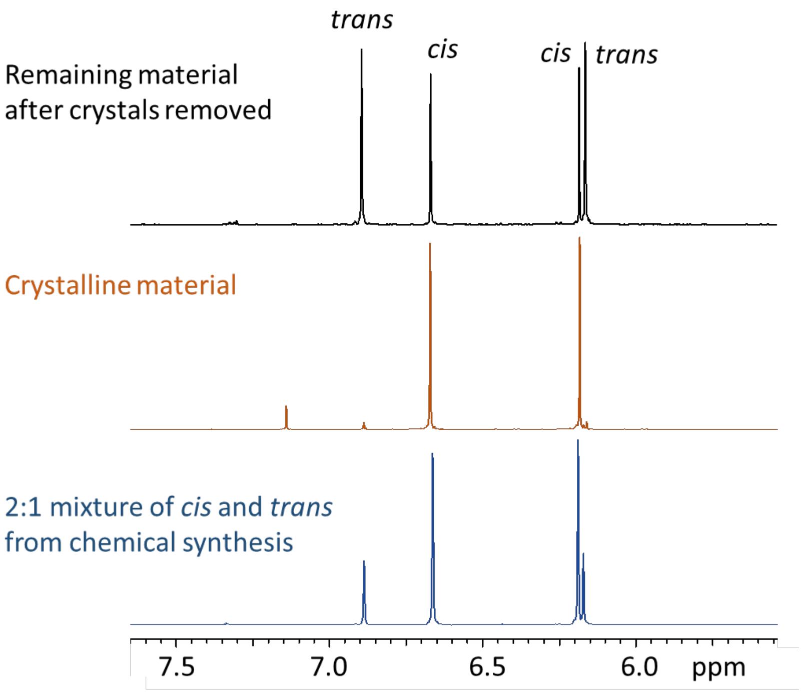

Figure 4.11: Stacked partial ^{1}H NMR spectra (400 MHz, 298 K, $CDCl_3$) of the outcome of a typical chemical synthesis of 2,5-diacetoxy-2,5-dihydrofuran (bottom spectrum), the crystalline material (*cis*-2,5-diacetoxy-2,5-dihydrofuran, middle spectrum) and the remaining product material after removal of the crystals (top spectrum).

4.2.2 - Electrochemical Synthesis of 2,5-diacetoxy-2,5-dihydrofuran

With the ability to now obtain the ratios of the two isomers of 2,5-diacetoxy-2,5-dihydrofuran from integration of the appropriate peaks in the ^{1}H NMR spectrum, we were able to study the *cis-trans* ratio produced by electrochemical oxidation of furan in the presence of acetic acid for the first time. Accordingly, a 0.5 M solution of sodium acetate in 4:1 acetic acid:acetonitrile was cooled to 0 °C in an ice bath and then charged with furan to give a 0.07 M solution of furan in the electrolyte (see Experimental Section). Bulk electrolysis was then conducted on this solution in a single chamber cell using a large surface area reticulated vitreous carbon working electrode, a graphite rod counter electrode and a Pt wire pseudo reference electrode at an applied potential of +3 V (*vs.* Pt). The ice bath was necessary to slow down the rate of furan evaporation (b.p. = 31 °C), so that meaningful Faradaic yields could be estimated. Even so, we found it convenient to limit the total charge passing during these experiments to no more than 30% of that required to produce full conversion of the furan. This not only enabled experiments of short duration to be performed (reducing anomalies due to furan evaporation) but also provided some useful insights into the mechanism of furan oxidation (*vide infra*).

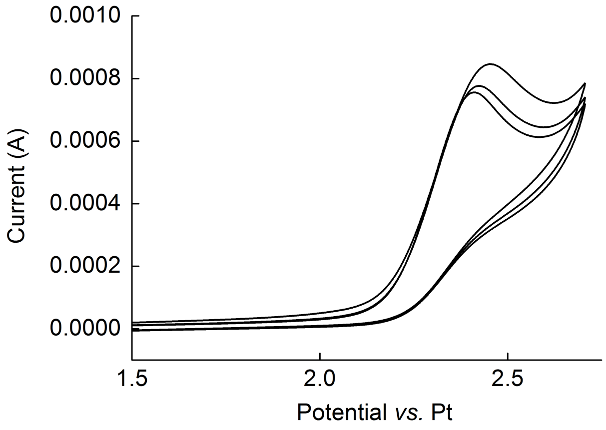

Figure 4.12: Cyclic voltammogram of 0.11 M furan in a single chamber cell in a mixed acetate electrolyte (2 g sodium acetate in 10 mL acetonitrile / 40 mL acetic acid) under an atmosphere of nitrogen. The scan rate was 100 mV/s. A glassy carbon foil (area = 2 cm^2) was used as the working electrode, and the counter and reference electrodes were both Pt wires.

In a typical bulk electrolysis, 0.5 mL (0.468 g, 6.88 mmol) of furan was dissolved in 100 mL of electrolyte and subjected to an anodic potential of +3 V (*vs.* Pt; see Figure 4.12 for a cyclic voltammogram) until 109 C had been passed. This corresponds to about 8% of the total charge required to oxidise this amount of furan by two electrons. Using Faraday's law, this in turn equates to a maximum theoretical yield of 2,5-diacetoxy-2,5-dihydrofuran of 0.56 mmol (assuming a two-electron oxidation process). In the event, the combined yields of the crystals (pure *cis* isomer) and oil (a mixture of *cis* and *trans* isomers) from this experiment was 83 mg (0.45 mmol), corresponding to a Faradaic yield of 80%.

Multiple repeats of the above reaction were performed passing various amounts of charge. In all cases, after bulk electrolysis had been terminated, the reaction mixture was poured into a large volume of water and extracted with dichloromethane. Repeated washing of the dichloromethane phase removed the vast majority of the excess acetate salts. After concentration under reduced pressure, the resulting brown oil was added to an equal volume of diethyl ether, giving a dark brown solid and yellow solution. Concentration of this solution *in vacuo* yielded a yellow oil, whose ^{1}H NMR spectrum showed it to consist almost exclusively of a mixture of the *cis* and *trans* isomers of 2,5-diacetoxy-2,5-dihydrofuran.

The ratio of *trans* and *cis* isomers was then judged on the basis of the integration of these NMR spectra, giving a *cis*:*trans* ratio of 1.38(±0.18):1, or 7:5 *cis*:*trans*. Hence the electrochemical route appears to be a lot less selective towards the *cis* product than the chemical route (the latter gives ~2:1 *cis*:*trans*). Table 1 shows a comparison of our electrochemical conditions and results with those from previous electrosynthesis studies.

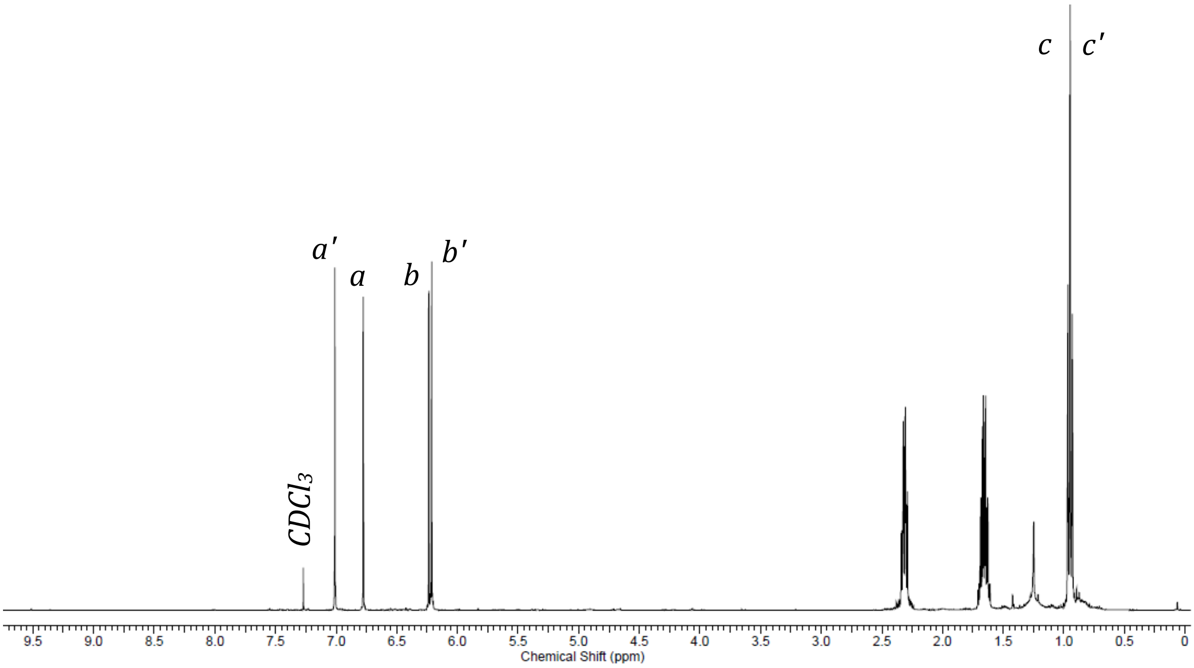

Figure 4.13: ^1H NMR spectrum of a mixture of *trans*- and *cis*-2,5-dibutoxy-2,5-dihydrofuran in $CDCl_3$ obtained *via* electrochemical synthesis.

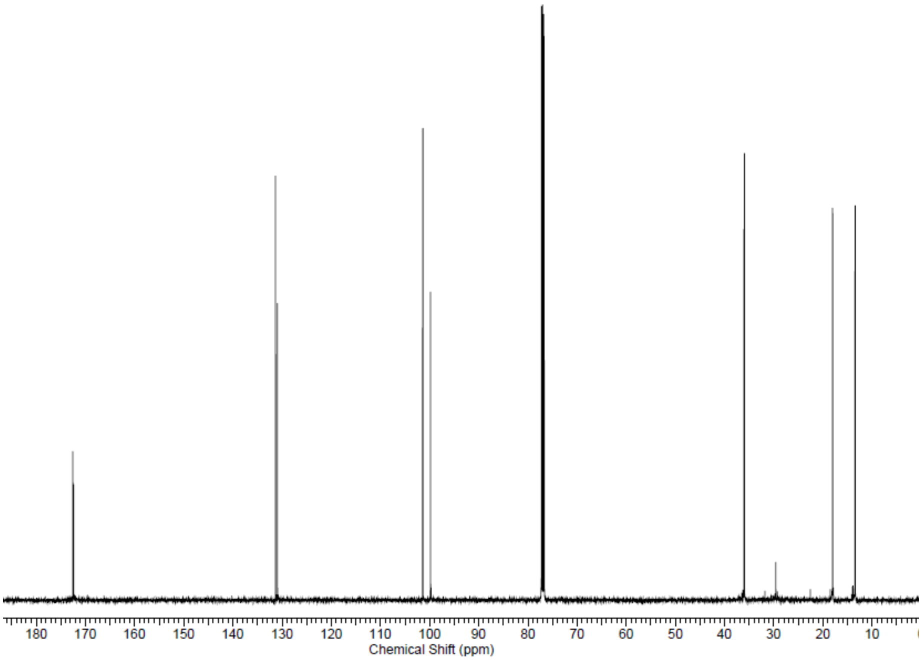

Figure 4.14: ^{13}C NMR spectrum of a mixture of *trans*- and *cis*-2,5-dibutoxy-2,5-dihydrofuran in $CDCl_3$ obtained *via* electrochemical synthesis.

Table 1: A comparison of the previous electrochemical routes for the synthesis of 2,5-diacetoxy-2,5-dihydrofuran and the results from this paper.

#	Anode	Cathode	Cell voltage	Faradaic efficiency	*Cis-trans* ratio	Conditions	Ref
1	Pt	Pt	AC electrolysis	-	-	Batch [a]	14
2	Pt	Hg	100 V DC	-	-	Batch [b]	15
3	Pt	Carbon	-	46%	-	Batch [c]	7
4	Graphite	Pt	-	40% [d]	-	Flowcell [e]	16
5	Reticulated carbon	Graphite	3 V *vs.* Pt	80%	7:5	Batch [c]	This work
6 [f]	Reticulated carbon	Graphite	3 V *vs.* Pt	45%	9:10	Batch	This work

[a] In 1 M potassium acetate in acetic acid. [b] In 0.6 M sodium acetate in acetic acid. [c] In 0.5 M sodium acetate in 4:1 acetic acid:acetonitrile. [d] At a flow-rate of 1 mL/min. [e] In acetic acid without additional electrolyte.

[f] For the electrosynthesis of 2,5-**dibutoxy**-2,5-dihydrofuran from 0.36 M sodium butyrate in a 2:3 (by volume) solution of acetonitrile and butyric acid.

4.2.3 - Insights into the mechanism of 2,5-diacetoxy-2,5-dihydrofuran electrosynthesis

During the course of these studies, an intriguing observation was made; despite the fact that the charges that were passed were typically only sufficient to bring about a partial oxidation of the furan, no evidence for the generation of any mono-substituted furans (such as a putative 2-acetoxy-2,5-dihydrofuran) was ever observed. This was even the case if samples of electrolyte from ongoing bulk electrolyses were extracted and examined by ^{1}H NMR spectroscopy without any workup or concentration under reduced pressure. This in turn suggested that the mechanism of oxidation strongly favoured a second oxidation reaction after the first acetate had added, or indeed that the addition of both acetate groups might be concerted.

In this context, both Yoshida[19] and Atobe[20] and their co-workers have proposed that the somewhat related electrosynthesis of dimethoxylated furans by electro-oxidation of furan occurs by an ECEC (Electrochemical-Chemical-Electrochemical-Chemical) mechanism, as shown in Scheme 1. Hence furan is first oxidised at the electrode to give a radical cation, which then reacts with the first methoxy anion give the mono-substituted radical species. A second electrochemical oxidation of this radical at the anode produces a closed-shell cation which undergoes attack by the second methoxy anion to generate the dimethoxylated product.

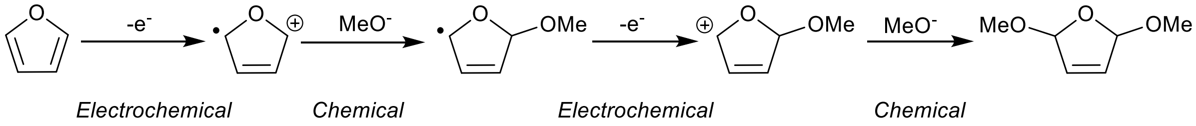

Scheme 1: The ECEC mechanism proposed by Yoshida[41] and Atobe[42] for the electrosynthesis of 2,5-dimethoxy-2,5-dihydrofuran.

To place this proposed mechanism in a more formal context, we performed DFT calculations on the various likely intermediate species that would form in the analogous ECEC pathway for the electro-synthesis of 2,5-diacetoxy-2,5-dihydrofuran, and these results are summarised in Scheme 2. Hence the initial one-electron oxidation of furan is significantly endergonic (by 126.5 kcal mol^{-1}) and produces a radical cation where the radical and cation can be considered to reside predominantly at the 2- and 5-positions, in agreement with the suggested mechanism in Scheme 1. A direct two-electron oxidation of furan can be ruled out on the basis of the very high energy barrier (314.9 kcal mol^{-1}) to the formation of the dication (grey lines in Scheme 2). Hence a stepwise pathway is likely to prevail.

After the formation of the radical cation, acetate then adds to the cation leading to a stabilisation of the system of around 10 kcal mol^{-1}. A second electrochemical oxidation reaction then occurs to generate a cation at the 5-position of the furan ring, where stabilisation by the formation of an oxonium ion is possible. This second oxidation is considerably less endergonic than the first oxidation reaction (by over 34 kcal mol^{-1}), suggesting that this second oxidation reaction should proceed very rapidly after the first acetate has added to the furan, provided that the anodic bias continues to be supplied. This in turn offers an explanation for the absence of any mono-substituted products, as the neutral mono-substituted radical is easier to oxidise than the starting material, and hence rapidly undergoes a second oxidation once formed. This cation then reacts with a second acetate anion to generate the di-substituted products. The energies predicted for the transition states leading to the *cis* and *trans* products (and indeed the energies predicted for the *cis* and *trans* products themselves) are within the 3-5 kcal mol^{-1} error usual for DFT and are therefore not considered to be significantly different from each other in this analysis.

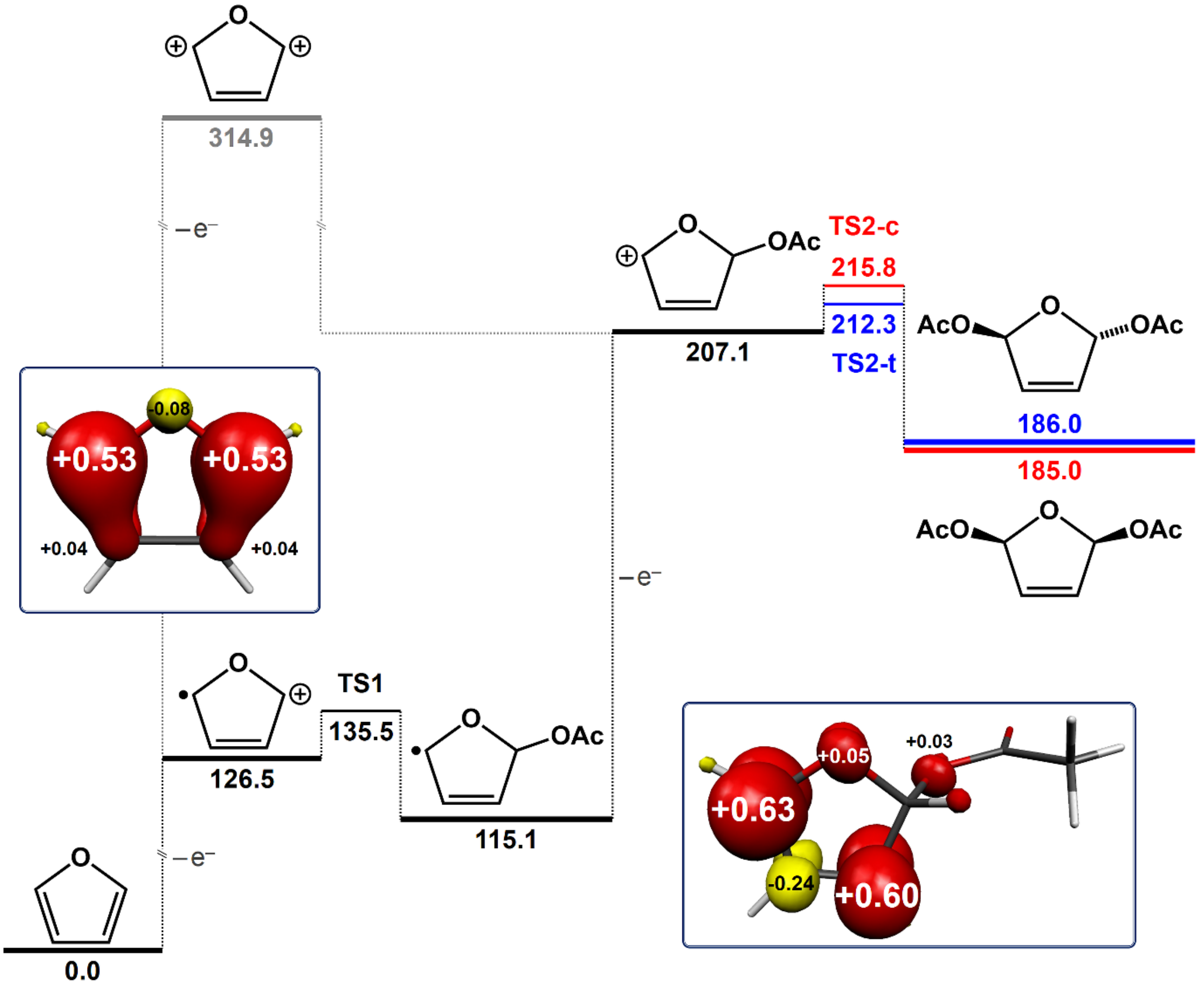

Scheme 2: The proposed reaction pathway for the electrosynthesis of 2,5-diacetoxy-2,5-dihydrofuran computed at the B3LYP level of theory. The red horizontal lines refer to *cis*-2,5-diacetoxy-2,5-dihydrofuran, and the blue horizontal lines to *trans*-2,5-diacetoxy-2,5-dihydrofuran. All values are given in kcal mol^{-1}. Insets show the Mulliken spin population analysis for the radical cation and mono-substituted neutral radical (red: α-spin; yellow: β-spin).

4.2.4 - Electrochemical Synthesis of 2,5-dibutoxy-2,5-dihydrofuran

If correct, then the above mechanism implies that the second transition state (TS2) is critical for determining the stereochemistry of the resulting products. Molecular representations of the closed-shell cationic intermediate immediately preceding this transition state (manipulated and visualised using the program Avogadro,[21,22] see Figure 4.15) suggest that addition of a particularly bulky carboxylate group in the first addition step could have an influence on the *cis*:*trans* ratio of the products by virtue of that bulky group partially blocking the face to which it adds to further nucleophilic attack. The expected result of this would be an increase in the amount of *trans* product produced relative to the *cis*, as nucleophilic addition to the opposite face of the furan ring would be less sterically challenged.

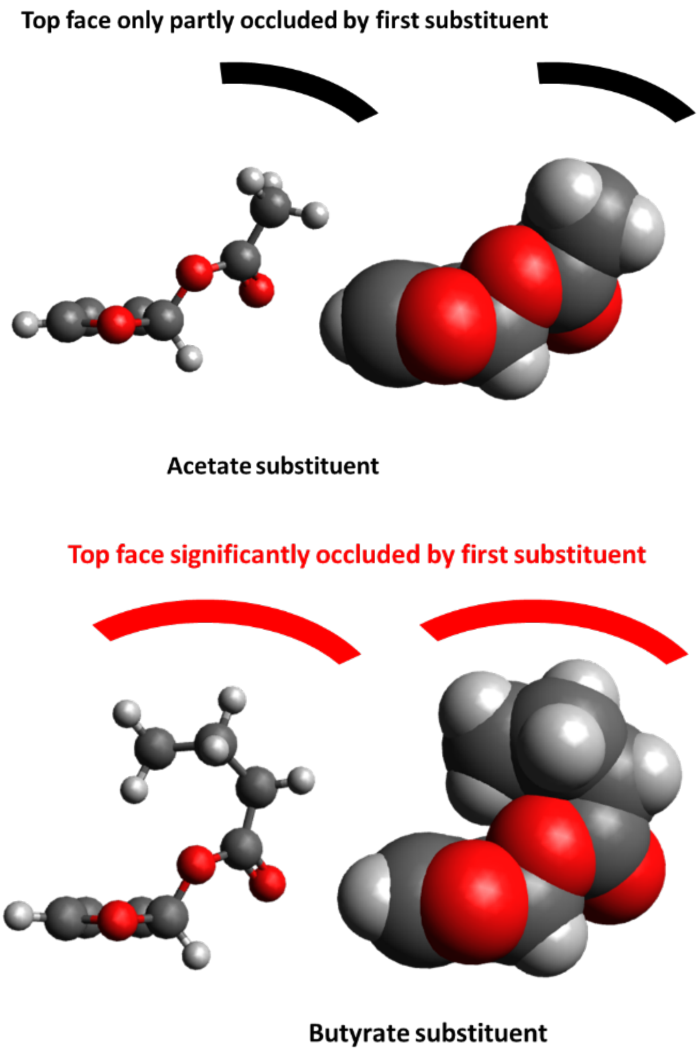

Figure 4.15: Wire and stick and space-filling models showing the effect that a bulky substituent (butyrate, right) has on the shielding of one face of the furan ring to the addition of a second carboxylate moiety, compared to the much smaller acetate substituent (left). The butyrate substituent is shown in a particularly shielding conformation; other

conformations are similar in energy but less shielding. However, it is to be expected that the conformation shown (and other very shielding conformations similar to it) will be adopted in solution for a not insignificant proportion of the time.

To test this hypothesis, we conducted the electrochemical oxidation of furan (0.07 M) in an electrolyte consisting of 0.36 M sodium butyrate in a 2:3 (by volume) solution of acetonitrile and butyric acid. All other parameters were kept as close as possible to those employed using the acetate/acetic acid electrolyte (see Experimental Section). In a typical bulk electrolysis, 0.5 mL (0.468 g, 6.88 mmol) of furan was dissolved in 100 mL of this electrolyte and subjected to an anodic potential of +3 V (*vs.* Pt) until 396 C had been passed. This corresponds to 30% of the total charge required to oxidise this amount of furan by two electrons. Using Faraday's law, this in turn equates to a maximum theoretical yield of 2,5-dibutoxy-2,5-dihydrofuran of 2.05 mmol (assuming a two-electron oxidation process). In the event, the combined yield of *cis* and *trans* isomers from this experiment after workup and purification was 222 mg (0.92 mmol), corresponding to a Faradaic yield of 45%. This lower Faradaic yield for isolated 2,5-dibutoxy-2,5-dihydrofuran relative to 2,5-diacetoxy-2,5-dihydrofuran is likely to be due to greater losses for 2,5-dibutoxy-2,5-dihydrofuran during the work-up and purification steps (for example, the need for column chromatography). The isomers of 2,5-dibutoxy-2,5-dihydrofuran were obtained in a ratio of *cis*:*trans* of 0.88(±0.1):1, indicating a distinct reversal in the stereoselectivity of the electrochemical synthesis from 7:5 in favour of *cis* when using acetate to 10:9 in favour of *trans* when using the bulkier butyrate substituent. This suggests that the stepwise ECEC mechanism proposed for the electrosynthesis of 2,5-diacetoxy-2,5-dihydrofurans in Scheme 2 is indeed operating.

4.3 – Conclusions

In conclusion, we have solved the crystal structure of *cis*-2,5-diacetoxy-2,5-dihydrofuran for the first time, which has allowed us to assign the two isomers of 2,5-diacetoxy-2,5-dihydrofuran to their respective ^{1}H NMR spectra. This has led to the realisation that the previous assignments of the ^{1}H NMR spectra of *cis* and *trans*-2,5-diacetoxy-2,5-dihydrofuran were incorrect. As a result of this discovery, we have been able to give reliable information on the ratio of these isomers that form during the electrochemical oxidation of furan in acetate electrolytes, also for the first time (a ratio of 7:5 *cis*:*trans* under our conditions). A mechanism for this reaction consistent with our experimental observations was proposed and then partially validated by conducting an analogous electrosynthesis of 2,5-dibutoxy-2,5-dihydrofuran using the much bulkier butyrate substituent. As predicted by the postulated mechanism, the greater steric hindrance led to a shift in stereoselectivity in favour of the *trans* isomer, resulting in a *cis*:*trans* ratio of 9:10. The implications of these findings for controlling product distributions in other electrosynthesis reactions on furan substrates are currently under investigation in our laboratories.

4.4 – Experimental methodology and materials

4.4.0 - General Experimental Remarks:

Unless otherwise stated, all syntheses were conducted under nitrogen in air- and moisture-free solvents obtained from a commercial solvent purification system. Water used was of 'ultra-pure' grade (18.2 MΩ resistivity) and dispensed from a SG Ultraclear TWF UV device. Sodium acetate (≥99%), sodium butyrate (98%), butyric acid (≥99%), furan (≥99%), diethyl ether (≥99.8%), and lead(IV) acetate (96% + 5-10% glacial acetic acid) were supplied by Sigma Aldrich. Acetonitrile (≥99%), sodium carbonate (≥99.9%) and nitric acid (70%) were supplied by Fisher Scientific. Acetic acid (99.9%) was purchased from VWR. Liquid nitrogen was supplied by BOC. HCl was obtained from Honeywell Fluka.

All ^1H and ^{13}C NMR spectra were recorded on a Bruker AV 400 instrument (unless otherwise stated), at a constant temperature of 300 K. Chemical shifts are reported in parts per million from low to high field. Standard abbreviations indicating multiplicity were used as follows: m = multiplet, s = singlet. Melting points were gauged using a Stuart Scientific SMP10 melting point apparatus. Experiments performed at "room temperature" were carried out at 20 °C. Electrochemical experiments were performed as below. Chemical synthesis of 2,5-diacetoxy-2,5-dihydrofuran was carried out by adapting the method of Holzapfel and Williams[4] (in particular the workup step), which allowed crystals of suitable quality for single crystal X-ray diffraction to be obtained (see below). The data which underpin this work are available *via Enlighten*, the University of Glasgow's open access online data repository.[23]

4.4.1 - Electrochemical Methods:

Electrochemical studies were performed in a single chamber cell in a three-electrode configuration using a CH Instruments CHI600 series potentiostat. Bulk electrolyses were performed using a large surface area reticulated vitreous carbon electrode (Alvatek Ltd., UK) as the working electrode, a Pt wire pseudo reference electrode, and a graphite rod (99.9995%, Alfa Aesar) as the counter electrode. Working electrodes were washed with water, followed by aqua regia (3:1 mixture of conc. HCl : HNO_3), then rinsed with water and acetone prior to use. Counter electrodes were sanded using 800 grit sandpaper to remove surface contamination. They were then sonicated for 1 minute in water to remove any fine graphite particles, followed by a rinsing with water, then acetone. The electrochemical cells were rinsed with aqua regia, water, and acetone prior to use. Electrodes and glassware were dried under a stream of N_2 to facilitate removal of any remaining acetone.

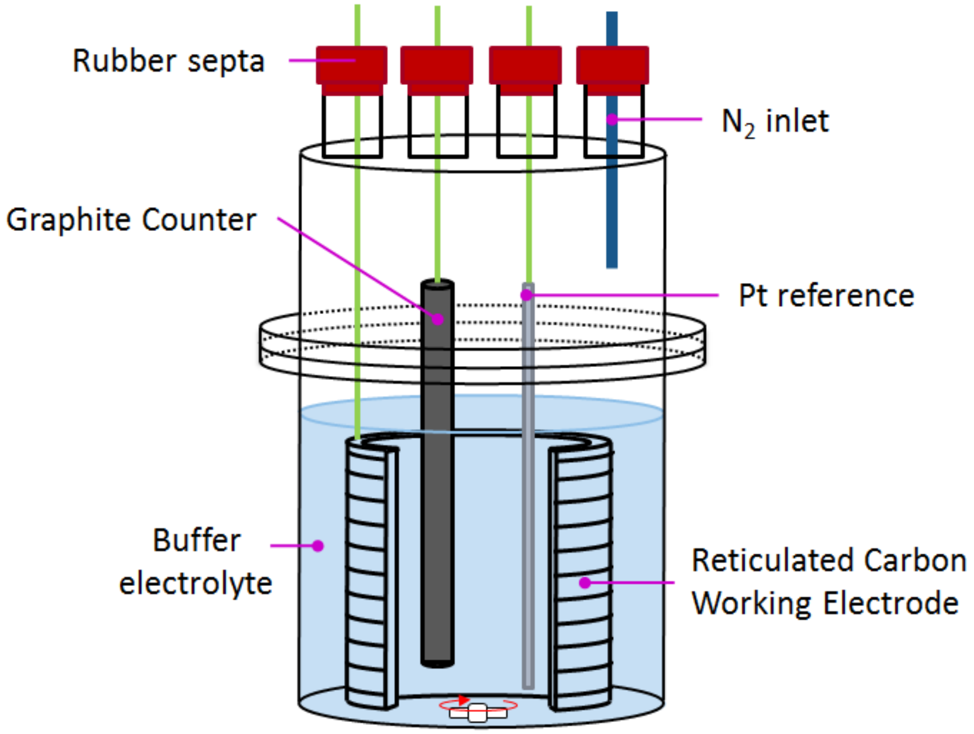

Figure 4.16: A typical set-up used for the bulk electrolysis experiments reported in this paper.

A typical cell set-up is shown in Figure 4.16 (below). The use of a sealable cell allowed the entire experiment to be conducted under an inert atmosphere of nitrogen. The electrolyte was first transferred to the cell under a constant stream of N_2, and the cell was then lowered into an ice bath and the temperature allowed to equilibrate before furan was injected through a septum into the electrolyte. Bulk electrolyses were performed under potentiostatic control with stirring at a potential of 3 V *vs*. Pt (~2 V *vs*. SHE, gauged by obtaining the position of the standard couple potassium ferricyanide[24] in the electrolyte).

4.4.2 - Electrosynthesis and purification of 2,5-diacetoxy-2,5-dihydrofuran:

To a suspension of sodium acetate (4.00 g, 48.8 mmol) in acetonitrile (20 mL) was added 80 mL acetic acid. The mixture was stirred until all the solids were dissolved, then transferred to the electrochemical cell described in Figure 4.16, cooled to 0 °C in an ice bath and the solution degassed for 1 h using a constant stream of nitrogen. After this time, furan (0.50 mL, 0.468 g, 6.88 mmol) was injected into the electrolyte under nitrogen. The constant flow of nitrogen was then immediately switched to a static atmosphere to limit furan evaporation. Bulk electrolysis was then initiated at a potential of 3 V (*vs*. Pt), and the charge passed was monitored. After bulk electrolysis, the reaction mixture was added to a water (~300 mL) and extracted from aqueous solution with an equal volume of dichloromethane. The organic phase was then washed with water to remove any residual acetic acid. Concentration of the organic phase *in vacuo,* resulted in a viscous brown oil. This oil was added to an equal volume of diethyl ether, precipitating a dark brown solid (which was filtered off and discarded) and a yellowish solution. Concentration of this solution *in vacuo* yielded a yellow oil, whose ^{1}H NMR spectrum showed it to consist almost exclusively of a mixture of the *cis* and *trans* isomers of 2,5-diacetoxy-2,5-dihydrofuran, and whose analytical data were in agreement with those reported previously (save for the assignment of the *cis* and *trans* isomers, see below).[4] We therefore give the assigned ^{1}H NMR data as follows: *cis*-2,5-diacetoxy-2,5-dihydrofuran ($CDCl_3$, 400 MHz), δ = 6.64 (s, 2H, *cis*-H_a), 6.15 (s, 2H, *cis*-H_b), 1.99 (s, 6H, *cis*-H_c); *trans*-2,5-diacetoxy-2,5-dihydrofuran ($CDCl_3$, 400 MHz), δ = 6.86 (s, 2H, *trans*-H_a), 6.13 (s, 2H, *trans*-H_b), 1.97 (s, 6H, *trans*-H_c). Assignments of signals to groups of protons are based on 2D (COSY and HMQC) spectra and letter codes correspond to those shown in Figure 4.1. Integrations are only to be compared with other signals in the same isomer (*vide infra* for a discussion of the relative amounts of *cis*- and *trans*-2,5-diacetoxy-2,5-dihydrofuran formed under various conditions). ^{13}C NMR for *cis*-2,5-diacetoxy-2,5-dihydrofuran ($CDCl_3$, 100 MHz), δ = 169.6 (**C**=O), 130.8 (**C**=C in furan ring), 99.8 (sp^3 **C** in furan ring), 20.9 (-**C**H$_3$). ^{13}C NMR for *trans*-2,5-diacetoxy-2,5-dihydrofuran ($CDCl_3$, 100 MHz), δ = 169.7 (**C**=O), 131.1 (**C**=C in furan ring), 101.1 (sp^3 **C** in furan ring), 20.8 (-**C**H$_3$). Sample 1D NMR spectra are shown in section 4.2.2, along with COSY and HMBC spectra (Figures 4.7-4.10).

4.4.3 - Separation of isomers of 2,5-diacetoxy-2,5-dihydrofuran

To separate the isomers of 2,5-diacetoxy-2,5-dihydrofuran, the yellow oil of the mixture of isomers was dissolved in an equal volume of diethyl ether. The resulting solution was then cooled by immersion in a bath of liquid nitrogen, causing pale yellow crystals to form. At this point, the supernatant solution was decanted and replaced with fresh (room temperature) diethyl ether, which had the effect of re-dissolving the crystals. This solution was then again cooled by immersion in liquid nitrogen, causing crystallisation. The supernatant was again removed. By repeated cool-crystallise-decant cycles, all the colour could be removed from the crystals. The products of this process were thus a yellow solution of the combined decants and colourless crystals. The yellow solution was then concentrated *in vacuo* to give a yellow oil, and the colourless crystals and yellow oil were then analysed separately (see Results and Discussion). The crystals were found to have a melting point of 51-53 °C, in excellent agreement with that reported by Elming and Clauson-Kaas after recrystallisation from methanol (51-52 °C).[13]

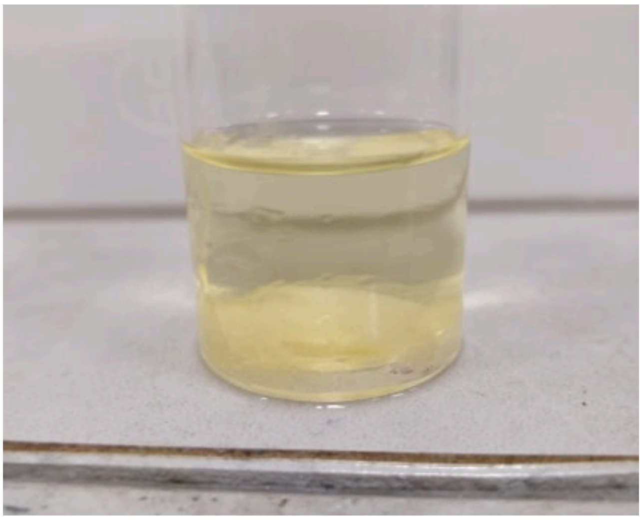

Figure 4.17: Recrystallization from a partially frozen mixture of *cis/trans*-2,5-diacetoxy-2,5-dihydrofuran in diethyl ether, showing crystals of *cis*-2,5-diacetoxy-2,5-dihydrofuran.

4.4.4 - Electrosynthesis of 2,5-dibutoxy-2,5-dihydrofuran

Sodium butyrate (4.00 g, 36.3 mmol) was suspended in acetonitrile (40 mL), and 60 mL butyric acid was added. The mixture was stirred until all the solids were dissolved, then transferred to the electrochemical cell described in Figure 4.16, cooled to 0 °C in an ice bath and the solution degassed for 1 h using a constant stream of nitrogen. After this time, furan (0.50 mL, 0.468 g, 6.88 mmol) was injected into the electrolyte under nitrogen. The constant flow of nitrogen was then immediately switched to a static atmosphere to limit furan evaporation. Bulk electrolysis was then initiated at a potential of 3 V (*vs.* Pt), and the charge passed was monitored. After bulk electrolysis, the pH of the reaction mixture was adjusted to pH 8 with a 1 M solution of sodium carbonate and extracted from aqueous solution with an equal volume of dichloromethane. The organic phase was then washed with water to remove any residual butyrate salts. Concentration of the organic phase *in vacuo,* resulted in a viscous brown oil. This oil was added to an equal volume of diethyl ether, precipitating a dark brown solid (which was filtered off and discarded) and a yellowish solution. Concentration of this solution *in vacuo* yielded a yellow oil. This was passed through a silica plug (eluting in dichloromethane) and the solvent removed *in vacuo* to give a pale yellow oil whose ^{1}H NMR spectrum showed it to consist of a mixture of the *cis* and *trans* isomers of 2,5-dibutoxy-2,5-dihydrofuran. This compound has been reported and characterised before,[13] but no NMR data were reported. Hence we can now report this data as follows: ^{1}H NMR ($CDCl_3$, 400 MHz), δ = 7.01 (s, 2H, *trans*-H_a), 6.78 (s, 1.8H, *cis*-H_a), 6.24 (s, 1.8H, *cis*-H_b), 6.21 (s, 2H, *trans*-H_b), 2.34-2.29 (m, 8H, ROOC-C$\mathbf{H_2}$-CH_2-CH_3 (*cis* and *trans* signals overlap)), 1.71-1.61 (m, 8H, ROOC-CH_2-C$\mathbf{H_2}$-CH_3 (*cis* and *trans* signals overlap)), 0.97-0.93 (m, 12H, ROOC-CH_2-CH_2-C$\mathbf{H_3}$ (*cis* and *trans* signals overlap)). Letter codes for the protons on the furan ring correspond to those shown in Figure 4.1. ^{13}C NMR ($CDCl_3$, 125 MHz), δ = 172.5 and 172.4 (*cis* and *trans* **C**=O), 131.3 and 131.0 (*cis* and *trans* **C**=C in furan ring), 101.4 and 99.8 (*cis* and *trans* sp^3 **C** in furan ring), 36.1 and 36.0 (*cis* and *trans* ROOC-**C**H_2-CH_2-CH_3), 18.1 and 18.0 (*cis* and *trans* ROOC-CH_2-**C**H_2-CH_3), 13.5 (×2) (*cis* and *trans* -**C**H_3). These NMR spectra are shown in Figures 4.6 and 4.7.

4.4.5 - Calculations

The program package ORCA was used for all calculations.[25] The input geometry for all molecules were generated using ArgusLab.[26] The geometries of all molecules were fully optimized by a spin-unrestricted DFT method employing the BP86 functional with acetonitrile as solvent.[27,28] Triple-ζ-quality basis sets with one set of polarization functions (def2-TZVP) were used for all atoms.[29,30] The RIJCOSX approximation combined with the appropriate auxiliary basis set was used to speed up the calculations.[31-33] The conductor like screening model (COSMO) was used for all calculations.[34-36] The self-consistent field calculations were tightly converged (1×10^{-8} E_h in energy, 1×10^{-7} E_h in the charge density, and 1×10^{-7} in the maximum element of the DIIS[37,38] error vector). The geometry was converged with the following convergence criteria: change in energy $<10^{-5}$ E_h, average force $<5 \times 10^{-4}$ E_h Bohr^{-1}, and the maximum force 10^{-4} E_h Bohr^{-1}. The geometry search for all complexes was carried out in redundant internal coordinates without imposing geometry constraints. Single point calculations were performed on optimized coordinates using the B3LYP functional using the same regime of basis sets and solvent.[39, 40] The stability of all solutions was checked by performing frequency calculations: no negative frequencies were observed. Spin density plots were obtained using Molekel.[41]

4.4.6 - Crystallography

Crystallographic data were collected at the University of Glasgow on a Bruker D8 VENTURE diffractometer equipped with a Photon II CMOS detector, with an Oxford Cryosystems N-Helix device mounted on an IμS 3.0 (dual Cu and Mo) microfocus sealed tube generator. A colourless, block-shaped crystal of dimensions 0.32 × 0.20 × 0.11 mm was used for single crystal X-ray diffraction data collection. $C_8H_{10}O_5$ crystallised in the monoclinic space group $P2_1/c$, with unit cell dimensions a = 11.7447 (17), b = 9.7503 (12), c = 7.8734 (10), β = 96.676 (5)° and V = 895.5 (2) Å^3, T = 150 K. 6125 reflections were measured by ω scans, 1631 independent reflections with R_{int} = 0.025, $\theta_{\max}$ = 25.3°, $\theta_{\min}$ = 2.7° using Mo $K\alpha$ radiation, λ = 0.71073 Å. The structure was solved using SHELXT[42] and refined using SHELXL[43] (both within OLEX2[44]). OLEX2 was also used for molecular graphics and to prepare material for publication. CCDC 1895453 contains the supplementary crystallographic data for this paper. More details on the crystallographic data and its collection can be found in appendix A1.

4.5 - References

1. Karuso P, Skelton BW, Taylor WC, White AH. 1984 The constituents of marine sponges. I. The isolation from Aplysilla sulphurea (Dendroceratida) of (1R*, 1'S*, 1'R*,3R*)-1-Acetoxy-4-ethyl-5-(1,3,3-trimethylcyclohexyl)-1,3-dihydroisobenzofuran-1'(4),3-carbolactone and the determination of its crystal structure. *Aust. J. Chem.* **37**, 1081-1093. (https://doi.org/10.1071/CH9841081)
2. Somerville MJ, Katavic PL, Lambert LK, Pierens GK, Blanchfield JT, Cimino G, Mollo E, Gavagnin M, Banwell MG, Garson MJ. 2012 Isolation of Thuridillins D–F, Diterpene Metabolites from the Australian Sacoglossan Mollusk Thuridilla splendens; Relative Configuration of the Epoxylactone Ring. *J. Nat. Prod.* **75**, 1618–1624. (http://doi.org/10.1021/np300442s)
3. Carroll AR, Healy PC, Quinn RJ, Tranter CJ. 1999. Prunolides A, B, and C: Novel Tetraphenolic Bis-Spiroketals from the Australian Ascidian *Synoicum prunum*. *J. Org. Chem.* **64**, 2680–2682. (http://doi.org/10.1021/jo981881j)
4. Holzapfel CW, Williams DBG. 1995 A Facile Route to 3a,8a-Dihydrofuro[2,3-*b*]benzofurans. *Tetrahedron*, **51**, 8555-8564. (https://doi.org/10.1016/0040-4020(95)00456-I)
5. Molinski TF, Faulkner DJ, He CH, Van Duyne GD, Clardy J. 1986 Three new rearranged spongian diterpenes from chromodoris macfarland: reappraisal of the structures of dendrillolides A and B. *J. Org. Chem.* **51**, 4564–4567. (https://doi.org/10.1021/jo00374a014)
6. Hambley TW, Poiner A, Taylor WC. 1986 Diterpene metabolites of the marine sponge chelonaplysilla violacea: Aplyviolene and aplyviolacene. *Tetrahedron Lett.* **27**, 3281-3282. (https://doi.org/10.1016/S0040-4039(00)84775-9)
7. Shono T, Matsumura Y, Yamane Si. 1981 Facile Synthesis of 4-Substituted Butenolides from Furan. *Tetrahedron Lett.* **22**, 3269-3272. (https://doi.org/10.1016/S0040-4039(01)81881-5)
8. Trost BM, Shi Z. From Furan to Nucleosides. 1996 *J. Am. Chem. Soc.* **118**, 3037–3038. (https://doi.org/10.1021/ja9537336)
9. Williams DBG, Evans SJ. 2004 Use of palladium-mediated allylic substitution reactions in the synthesis of 2,5-disubstituted-2,5-dihydrofurans. *Tetrahedron Lett.* **45**, 7189-7192. (https://doi.org/10.1016/j.tetlet.2004.08.046)
10. Rao DS, Reddy TR, Babachary K, Kashyap S. 2016 Regioselective vicinal functionalization of unactivated alkenes with sulfonium iodate(I) reagents under

metal-free conditions. *Org. Biomol. Chem.* **14**, 7529-7543. (https://doi.org/10.1039/C6OB01179A)

11. Tanimori S, Kato Y, Kirihata M. 2006 Simple Preparation of New Functionalized Furan Derivatives via Sequential C–C and C–O Bond Formation Mediated by Palladium-Phosphine Catalyst. *Synthesis*, 865-869. (https://doi.org/10.1055/s-2006-926321)
12. Smet M, Corens D, Dehaen W. 2003 Synthesis of novel dendritic molecules based on pyrroloanthracene units. *ARKIVOC*, 51-67. (http://dx.doi.org/10.3998/ark.5550190.0004.405)
13. Elming N, Clauson-Kaas N. 1952 The Acyloxylation of Furan with Lead Tetraacyloxylates; *Cis-Trans* Isomerism of 2,5-Diacyloxy-2,5-dihydrofurans and 2,5-Diacyloxytetrahydrofurans. *Acta Chem. Scand.* **6**, 535-544. (http://doi.org/10.3891/acta.chem.scand.06-0535)
14. Wilson CL, Lippincott WT. 1956 Anodic Reactions 1. Kolbe Electrosynthesis of Ethane Using Alternating Current. *J. Electrochem. Soc.* **103**, 672-675. (http://doi.org/10.1149/1.2430189)
15. Baggaley AJ, Brettle R. 1968 Anodic Oxidation. Part 1V. Some Reactions with Furans. *J. Chem. Soc. C*, 969-974. (http://doi.org/10.1039/J39680000969)
16. Horii D, Atobe M, Fuchigami T, Marken F. 2006 Self-Supported Methoxylation and Acetoxylation Electrosynthesis Using a Simple Thin-Layer Flow Cell. *J. Electrochem. Soc.* **153**, D143-D147. (http://doi.org/10.1149/1.2209565)
17. Jacobsen JP, Nielsen JT, Schaumburg K. 1971 1H NMR Spectra of cis- and trans-2,5-Diacetoxy-2,5-dihydrofuran. *Acta Chem. Scand.* **25**, 2785-2786. (http://doi.org/10.3891/acta.chem.scand.25-2785)
18. Barfield M, Spear RJ, Sternhell S. 1975 Interproton spin-spin coupling across a dual path in 2,5-dihydrofurans and phthalans. *J. Am. Chem. Soc.* **97**, 5160–5167. (http://doi.org/10.1021/ja00851a023)
19. Yoshida K, Fueno T. 1987 Concurrent Anodic Cyanation and Methoxylation of Methylated Furans. Oxidation Potential and Reactivity, and Stereochemical Control of Addition. *Bull. Chem. Soc. Jpn.* **60**, 229-240. (https://doi.org/10.1246/bcsj.60.229)
20. Horii D, Atobe M, Fuchigami T, Marken F. 2005 Self-supported paired electrosynthesis of 2,5-dimethoxy-2,5-dihydrofuran using a thin layer flow cell without intentionally added supporting electrolyte. *Electrochem. Commun.* **7**, 35–39. (https://doi.org/10.1016/j.elecom.2004.10.012)

21. 2016 *Avogadro*, an open–source molecular builder and visualization tool. v. 1.2.0. https://avogadro.en.softonic.com/

22. Hanwell MD, Curtis DE, Lonie DC, Vandermeersch T, Zurek E, Hutchison GR. 2012 Avogadro: an advanced semantic chemical editor, visualization, and analysis platform. *J. Cheminf.* **4**, 17. (http://doi.org/10.1186/1758-2946-4-17)

23. Shipman MA, Sproules S, Wilson C, Symes MD. 2019 Data from: Towards a Better Understanding of the Electrochemical Synthesis of 2,5-dicarboxy-2,5-dihydrofurans: Structure, Mechanism and Influence over Stereochemistry. Enlighten: Research Data repository for the University of Glasgow. (http://dx.doi.org/10.5525/gla.researchdata.745)

24. Vanýsek P. 2014 Electrochemical Series. In *CRC Handbook of Chemistry and Physics*, 95th ed.; Taylor and Francis: Vol. 5, pp 80-89.

25. Neese F. 2012 The ORCA program system. *WIREs Comput. Molec. Sci.* **2**, 73-78. (http://doi.org/10.1002/wcms.81)

26. Thompson M. 2005 ArgusLab 4.01, Planaria Software LLC, Seattle. http://www.ArgusLab.com

27. Becke AD. 1988 Density-functional exchange-energy approximation with correct asymptotic behavior. *Phys. Rev. A*, **38**, 3098-3100. (https://doi.org/10.1103/PhysRevA.38.3098)

28. Perdew JP. 1986 Density-Functional Approximation for the Correlation Energy of the Inhomogeneous Electron Gas. *Phys. Rev. B*, **33**, 8822-8824. (https://doi.org/10.1103/PhysRevB.33.8822)

29. Ahlrichs R, May K. 2000 Contracted All-Electron Gaussian Basis Sets for Atoms Rb to Xe. *Phys. Chem. Chem. Phys.* **2**, 943-945. (https://doi.org/10.1039/A908859H)

30. Weigend F, Ahlrichs R. 2005 Balanced basis sets of split valence, triple zeta valence and quadruple zeta valence quality for H to Rn: Design and assessment of accuracy. *Phys. Chem. Chem. Phys.* **7**, 3297–3305. (http://doi.org/10.1039/B508541A)

31. Eichkorn K, Treutler O, Öhm H, Häser M, Ahlrichs R. 1995 Auxiliary basis sets to approximate Coulomb potentials. *Chem. Phys. Lett.* **240**, 283-290. (https://doi.org/10.1016/0009-2614(95)00621-A)

32. Eichkorn K, Weigend F, Treutler O, Ahlrichs R. 1997 Auxiliary Basis Sets for Main Row Atoms and Transition Metals and their Use to Approximate Coulomb

Potentials. *Theor. Chem. Acc.* **97**, 119-124. (https://doi.org/10.1007/s002140050244)

33. Neese F, Wennmohs F, Hansen A, Becker U. 2009 Efficient, Approximate and Parallel Hartree-Fock and Hybrid DFT Calculations. A 'Chain-Of-Spheres' Algorithm for the Hartree-Fock Exchange. *Chem. Phys.* **356**, 98-109. (https://doi.org/10.1016/j.chemphys.2008.10.036)
34. Klamt A, Schüürmann G. 1993 COSMO: A New Approach to Dielectric Screening in Solvents with Explicit Expressions for the Screening Energy and its Gradient. *J. Chem. Soc., Perkin Trans. 2*, 799-805. (https://doi.org/10.1039/P29930000799)
35. Klamt A. 1995 Conductor-like Screening Model for Real Solvents: A New Approach to the Quantitative Calculation of Solvation Phenomena. *J. Phys. Chem.* **99**, 2224-2235. (https://doi.org/10.1021/j100007a062)
36. Klamt A, Jonas V. 1996 Treatment of the outlying charge in continuum solvation models. *J. Chem. Phys.* **105**, 9972-9981. (https://doi.org/10.1063/1.472829).
37. Pulay P. 1980 Convergence Acceleration of Iterative Sequences. The Case of scf Iteration. *Chem. Phys. Lett.* **73**, 393-398. (https://doi.org/10.1016/0009-2614(80)80396-4)
38. Pulay P. 1982 Improved SCF Convergence Acceleration. *J. Comput. Chem.* **3**, 556-560. (https://doi.org/10.1002/jcc.540030413)
39. Becke AD. 1993 Density-functional thermochemistry. III. The role of exact exchange. *J. Chem. Phys.* **98**, 5648-5652. (https://doi.org/10.1063/1.464913)
40. Lee C, Yang W, Parr RG. 1988 Development of the Colle-Salvetti correlation-energy formula into a functional of the electron density. *Phys. Rev. B*, **37**, 785-789. (https://doi.org/10.1103/PhysRevB.37.785)
41. Varetto U. 2010 Molekel 5.4, Advanced Interactive 3D-Graphics for Molecular Sciences, Swiss National Supercomputing Center. https://ugovaretto.github.io/molekel/
42. Sheldrick GM. 2015 *SHELXT* - Integrated space-group and crystal-structure determination. *Acta Cryst.* A**71**, 3-8. (https://doi.org/10.1107/S2053273314026370)
43. Sheldrick GM. 2015 Crystal structure refinement with *SHELXL*. *Acta Cryst.* C**71**, 3-8. (https://doi.org/10.1107/S2053229614024218)
44. Dolomanov OV, Bourhis LJ, Gildea RJ, Howard JAK, Puschmann H. 2009 OLEX2: a complete structure solution, refinement and analysis program. *J. Appl. Cryst.* **42**, 339-341. (http://dx.doi.org/10.1107/S0021889808042726)

Chapter 5

Investigations into Aldehyde Activation by Cage-Based Acid Catalysis

5.1 – Introduction

Organometallic supramolecular structures are well known within the scientific community. Since Alfred Werner received the Nobel Prize for his seminal work on octahedral transition metals, supramolecular chemistry has grown into a thriving field. The simplicity of the combination of metal nodes and coordinating organic ligands has catapulted this field into the forefront of research, especially in recent decades. This has culminated with the discovery of the supramolecular coordination complex (SCC) and by extension the metal-organic framework (MOF).

SCCs have been shown to be a very interesting category of molecules as well as having a simple and efficient synthesis. Essentially, organic ligands with multiple coordination sites of specific angular arrangements are chosen to form the building blocks of the molecule. In the presence of deliberately chosen metal centres to coordinate to, they self-assemble into discrete supramolecular geometries[1] By simply changing the coordination angles and shape of the bridging ligand, a specific conformational arrangement may be chosen. These differ from MOFs, in that instead of being comprised of a possibly infinite network of unit cells, an SCC conforms to specific self-contained structure geometries and sizes. Such structures can take the shape of various polyhedra, a few of which are shown in figures 5.1A-C (below).

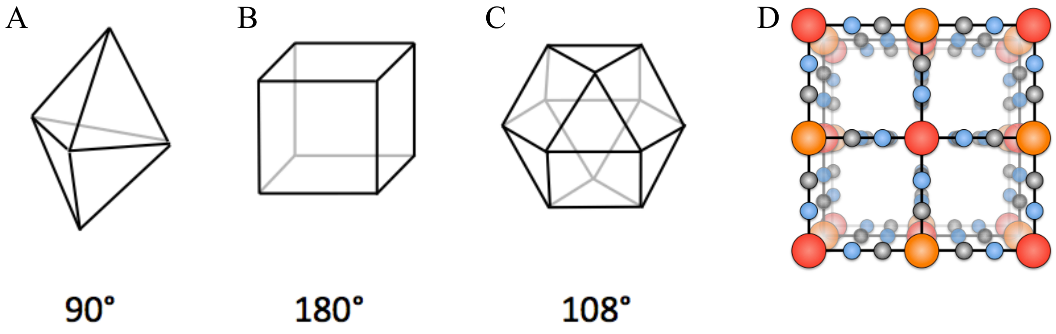

Figure 5.1A: A trigonal bipyramidal SCC arising from a ligand angle of 90°. B: A cubic SCC arising from a ligand angle of 180°. C: Cuboctahedral SCC arising from a ligand angle of 108°. D: Structural form of Prussian blue ($Fe^{III}_4[Fe^{II}(CN)_6]_3$,[1] where red = Fe^{III}, orange = Fe^{II}, Blue = N, black = C), an example of a MOF with potential for infinite extrapolation in all planes.

Self-assembling supramolecular coordination complexes fascinate chemists on account of the cavity within their structure. The properties of these cavities can be markedly different to the bulk solution, as well as being large enough to sequester small molecules. In this way, SCC's may be thought of as molecular cages.

It is this ability to enforce well-defined microenvironments on species hosted in their cavities [2-17] that has led to applications in areas such as molecular recognition,[18-22] catalysis, [23-30] resolutions and separations, [31-35] and stabilization of otherwise reactive species [36-43] to name but a few. However, perhaps the most promising area of application of such cages is their potential to accelerate organic transformations.[44-69]

The potential for enhanced or altered reactivity inside cages is very well exemplified by the work of Raymond, Bergmann and co-workers using assemblies of the type M_4L_6 (M = Ga^{III}, Al^{III}, In^{III}, Fe^{III}, TiI^{V}, or Ge^{IV}, and L = N,N'-bis(2,3-dihydroxybenzoyl)-1,5-diaminonaphthalene).[70, 71] These cages have been shown to facilitate the formation of (and stabilize) hydrolysis-prone species such as iminium and phosphonium cations in water, [72-74] and also to give rise to dramatically increased pKa values for protonated amines bound within their cavities.[75] Moreover, these cages have been used to promote a number of traditionally acid-catalyzed reactions, such as the hydrolysis of orthoformates (figure 5.2, overleaf), [76, 77] terpene cyclizations (figure 5.3, overleaf), [78] acetal hydrolysis, [79, 80] (figure 5.4, page 107) Nazarov cyclizations (figure 5.5, page 108), [81-83] and Prins reactions (figure 5.6, page 109).[84]

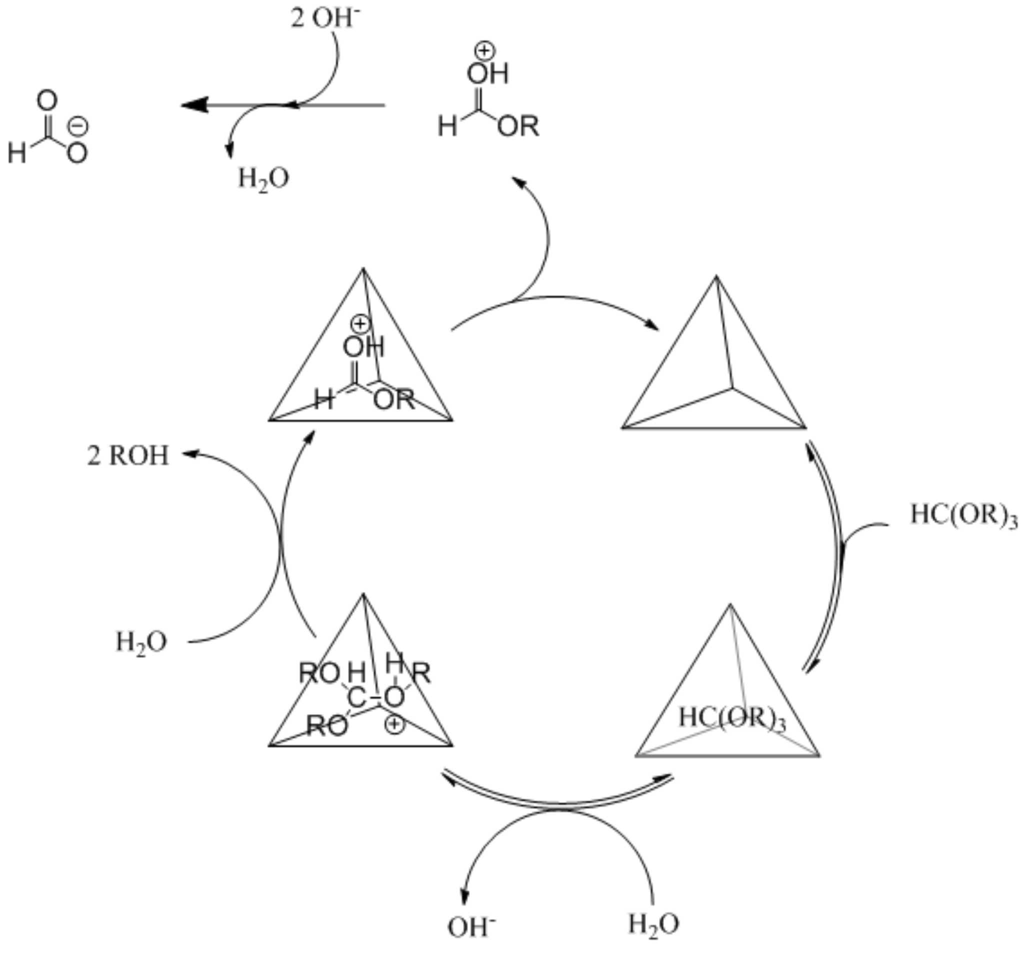

Figure 5.2: The mechanism for cage-based catalytic orthoformate hydrolysis as proposed by Raymond and coworkers [75,76]

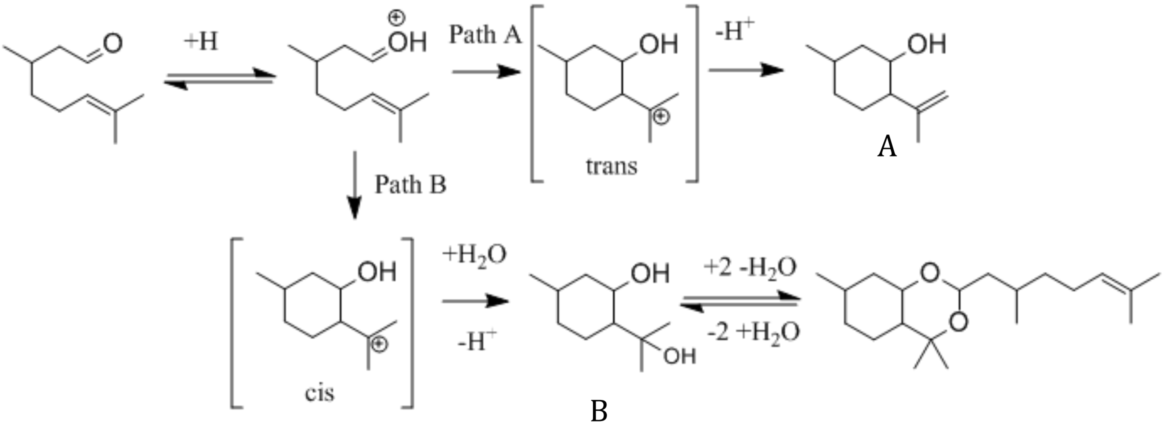

Figure 5.3: mechanism for the proton-mediated cyclisation of terpenes proposed by Raymond. Path A results in a mixture of isomers of product A when catalysed by a cage molecule, and path B shows the acid-catalysed reaction, with a strong preference for product B

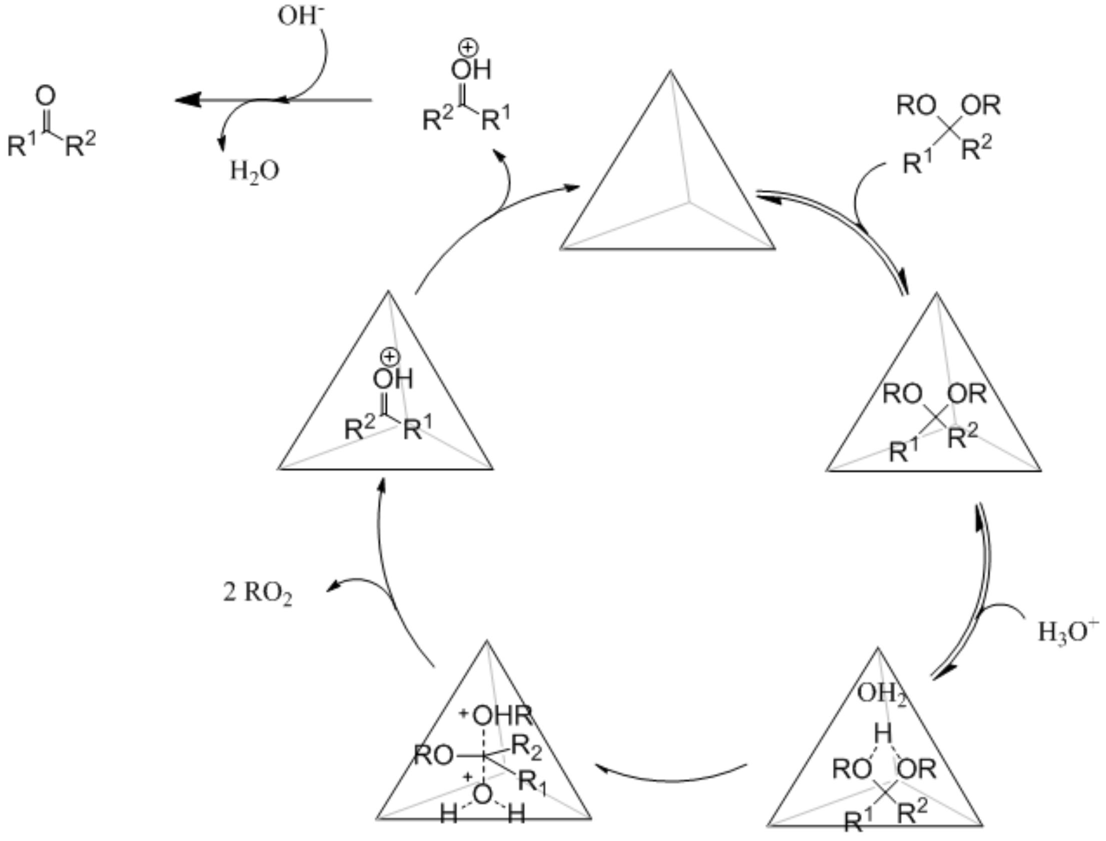

Figure 5.4: Mechanism proposed by Raymond *et. al* for cage-based acetal hydrolysis

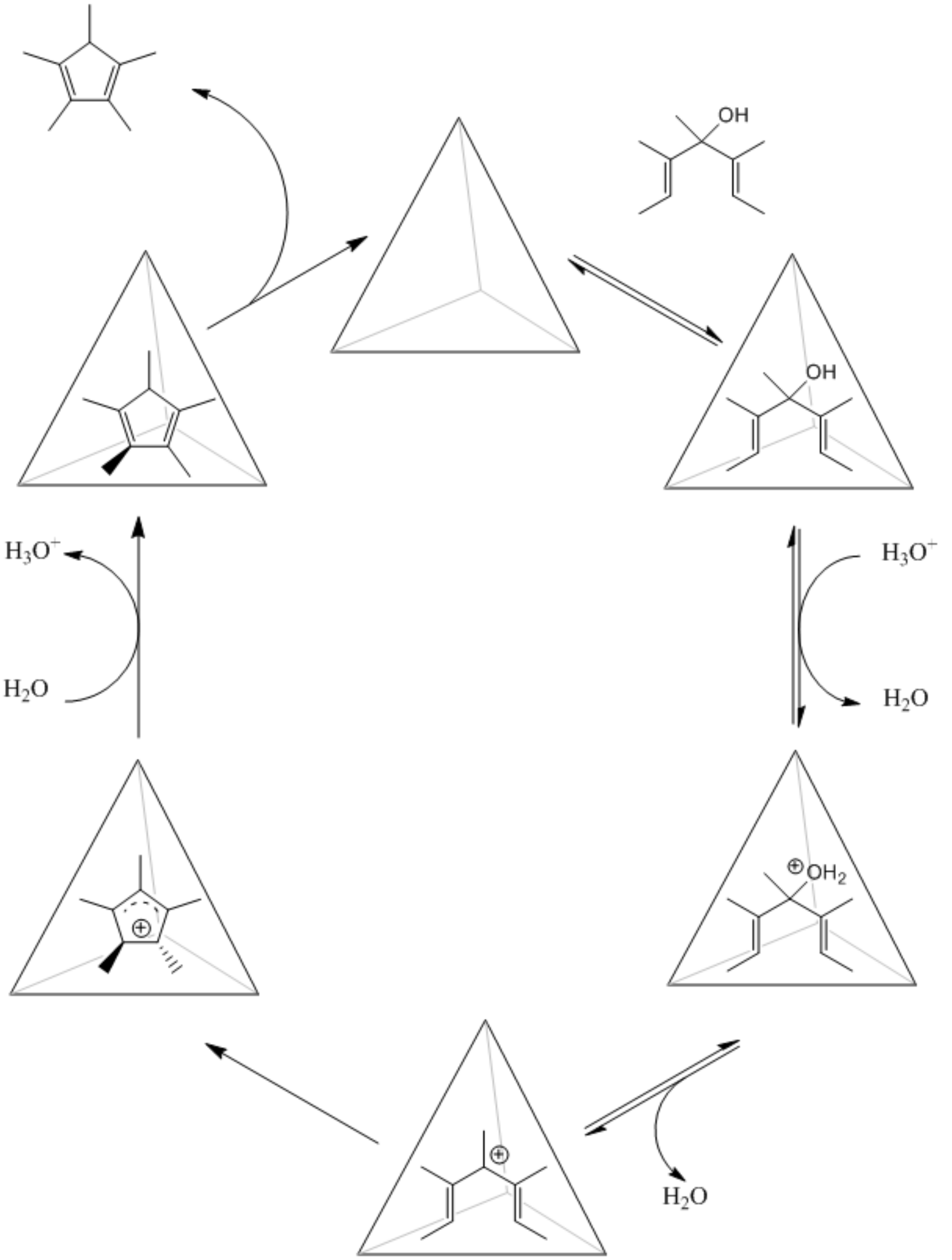

Figure 5.5: The proposed mechanism for the cage-catalysed Nazarov cyclisation of 1,4-pentadien-3-ols

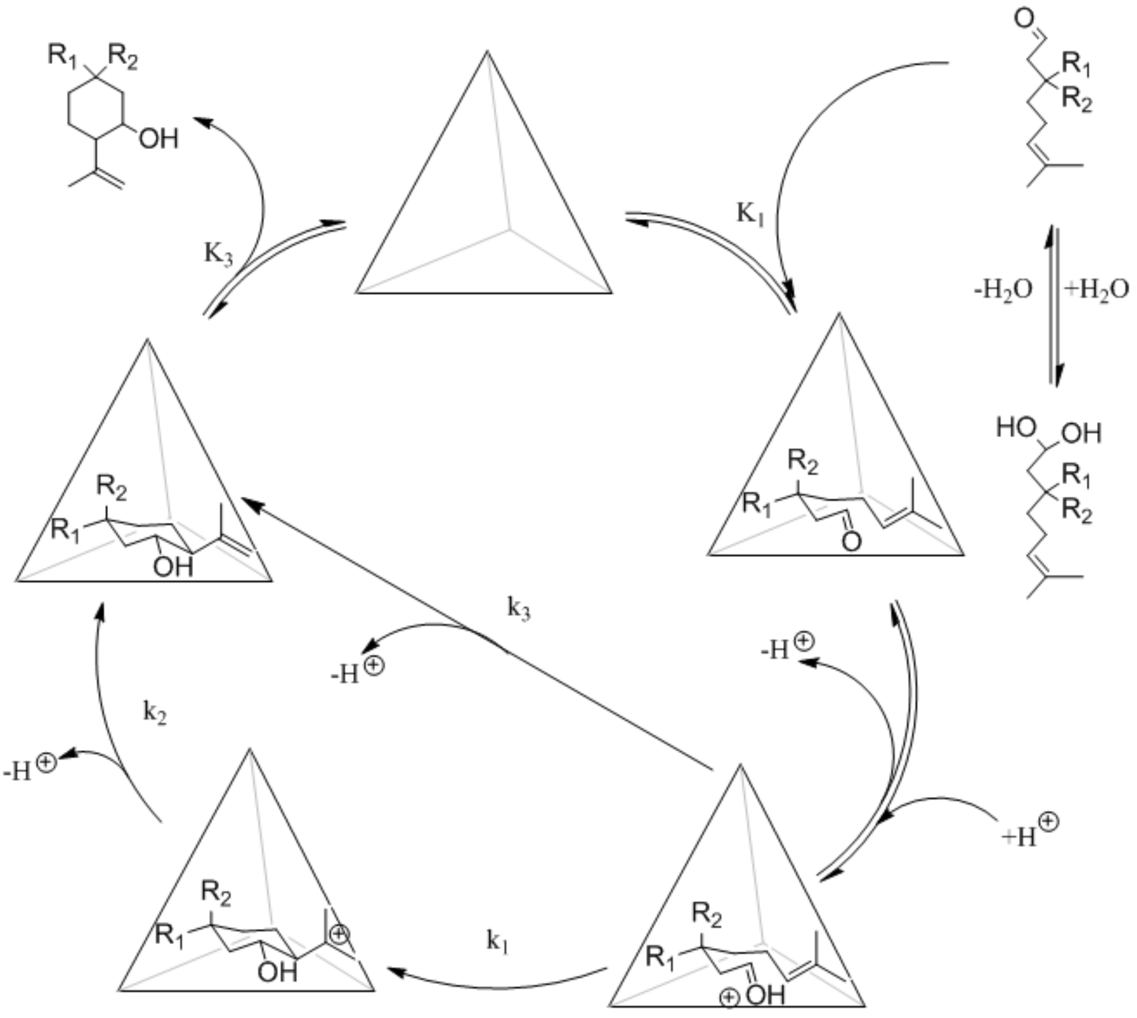

Figure 5.6: Mechanistic scheme for host-catalysed Prins reaction, showing both stepwise (k_1,k_2) and concerted (k_3) reactions.

Such observations have led Raymond and his colleagues to propose that the underlying cause of this enhanced reactivity is related to the ability of the cage to stabilize positively-charged transition states and radicals, possibly through interaction of the aromatic units (in the ligands forming the edges of the cage) with the carbocations that develop in the substrates during these reactions.[56, 84, 85] In this way, one can view these cages as stabilizing species that are normally only stable in acid solution, even though the medium outside the cage may be neutral or even basic.

Amongst the numerous diverse cage architectures that have been reported to date, the tetrahedral Fe_4L_6 iminopyridine complex (figure 5.7, below) reported by Nitschke and co-workers in 2008 stands out on account of its ease of synthesis (self-assembling in aqueous solution from commercial reagents, a scheme of which is shown in section 5.4.2). [86] It is also both water-soluble and amenable to interrogation by solution-phase NMR spectroscopy. These cages have been the subject of fairly intense study over the past 10 years or so,[87] but the potential for catalytic activity with these cages remains underexplored, with only a few reported examples to date.[52, 88, 89]

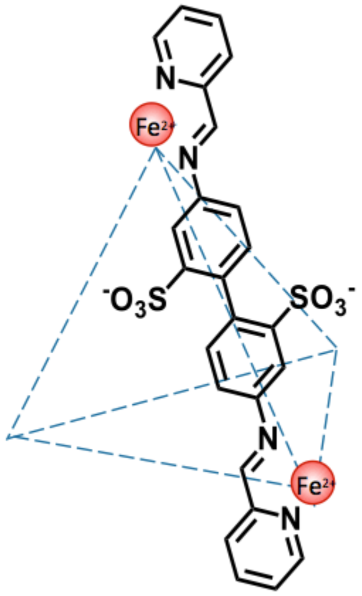

Figure 5.7: The tetrahedral Fe_4L_6 cage designed by Nitschke (the structure of only one edge is shown, and the counterion has been omitted for clarity)

This begs the question as to whether the acid catalysis demonstrated by the tetrahedral Raymond cages is a general phenomenon that could also manifest in these Fe_4L_6 iminopyridine cages. Therefore, our initial aim was to determine whether the cavity of these Fe_4L_6 cages might also mimic a bulk acidic environment, and therefore lead to reaction outcomes that were difficult, or otherwise impossible to achieve under neutral or basic conditions.

To this end, we aimed to study the reduction of carbonyls to the corresponding alcohols in the presence and absence of the tetrahedral Fe_4L_6 Nitschke cage complex at neutral pH using the mild reducing agent sodium cyanoborohydride ($NaCNBH_3$). Cyanoborohydride reductions of aldehydes and ketones to the corresponding alcohols should be an excellent test-reaction for these purposes, as these reactions normally only work well in acid solutions, whilst cyanoborohydride is widely held to be incapable of reducing more recalcitrant carbonyls such as esters at all. [90-94]

Given this, we hypothesized that if these cages were indeed competent for accelerating acid-catalyzed reactions, then any small carbonyl compounds that could be induced to bind within these cages would show enhanced rates of reduction using $NaCNBH_3$ relative to the analogous reaction conditions in the absence of cage. To the best of our knowledge, carbonyl hydrogenations have yet to be demonstrated using any type of supramolecular coordination cage.

Herein, we report the enhanced conversion of aldehydes to their corresponding alcohols using the weak hydride donor sodium cyanoborohydride in aqueous solution containing catalytic amounts of the Nitschke Fe_4L_6 cage. We show that the cage architecture is essential for this enhanced conversion and show that the cage is a general catalyst for the reduction of these carbonyls to their corresponding alcohols under our very mild conditions.

Our investigations began by treating solutions of the Nitschke Fe_4L_6 cage in water with varying amounts of the small aromatic aldehyde furfural (the structure of which is shown in figure 5.12, pg. 118), and monitoring the changes in the ^1H NMR spectra of these mixtures over time. It became apparent that there was indeed a shift in the peak positions of the furfural suggesting both incorporation inside the cage molecule itself, and more interestingly a potential change in pKa of the aldehyde group. By introducing a hydride source, we determined that there was indeed an activation occurring promoted by host-guest interactions. After briefly investigating reaction kinetics and the most efficient ratio of cage to furfural, we decided to expand the scope of substrates used to investigate steric and electronic effects of the guest molecule on total conversion.

5.2 - Results and discussion

5.2.1 – Furfural Encapsulation

A 1: 1 mixture of the Nitschke Fe_4L_6 cage (see section 5.3.1, *vide infra*) and furfural was stirred in aqueous solution at 50°C to determine if furfural host-guest activity were possible.

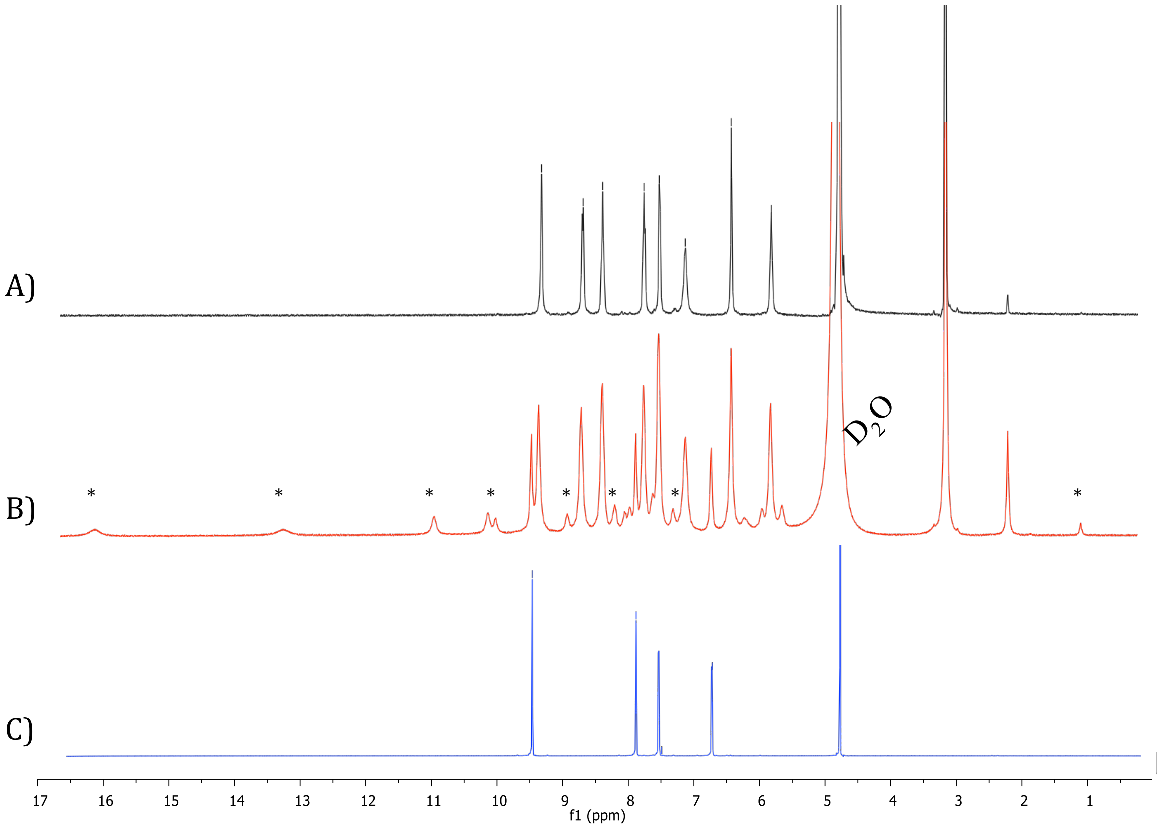

Figure 5.8: ^{1}H NMR spectra of A) Nitschke cage in D_2O, B) an aqueous mixture of the Nitschke cage and furfural in D_2O after 6 hours stirred at 50 °C under nitrogen atmosphere, C) furfural stirred for 20 minutes in D_2O at 50 °C

As shown in figure 5.8, it is possible to see the characteristic peak patterns of both furfural [^{1}H NMR (400 MHz, D2O) δ **9.46** (s, 1H), **7.89** (s, 1H), **7.50** (s, 1H), **6.73** (s, 1H).] and the Nitschke cage [1H NMR (400 MHz, D2O) δ **9.33** (s, 12H), **8.69** (s, 12H), **8.40** (s, 12H), **7.76** (s, 12H), **7.53** (s, 12H), **7.14** (s, 12H), **6.44** (s, 12H), **5.82** (s, 12H), **3.17** (s, NMe_4).] Post stirring, new peaks appear at δ **16.11**, **13.22**, **10.92**, **10.08**, **9.98**, **8.88**, **8.16**, **7.07**, and **2.17**. Several of these peaks result from reactions on the cage itself with oxygen (especially within the region of 9 – 5 ppm). As such, it is difficult to gauge any meaningful shift in the majority of the aldehyde peaks. The far-shifted peaks at 16.11 and 13.22 ppm however are of particular interest; there is a fair assumption that this dramatic downfield shift is indicative of a change in chemical environment. This would have the effect of making the carbonyl carbon more electrophilic, consistent with the work undertaken by

Raymond and coworkers. [76] With this in mind, we decided to assess whether it were possible to use a weak hydride source to convert furfural to furfuryl alcohol.

5.2.2 – Furfural controls

The first control was to see if this activation did take place. To achieve this, a tenfold excess of aldehyde was allowed to mix with a small amount of the cage. The cage-incorporated aldehyde mixture was then mixed with one molar equivalent (relative to the furfural) of a hydride source. Initially $NaBH_4$ was used, however we discovered that the conditions were too harsh, and the cage had a tendency to decompose. As shown in figure 5.9A (below), the reaction between cage-bound furfural and the milder $NaBH_3CN$ results in a mixture of furfural and furfuryl alcohol (as denoted by peaks marked with *), with some minor side products. In contrast, the reaction of furfural and $NaBH_3CN$ without cage (figure 5.9B, below) while still occurring to some extent, has a much higher proportion of unreacted substrate.

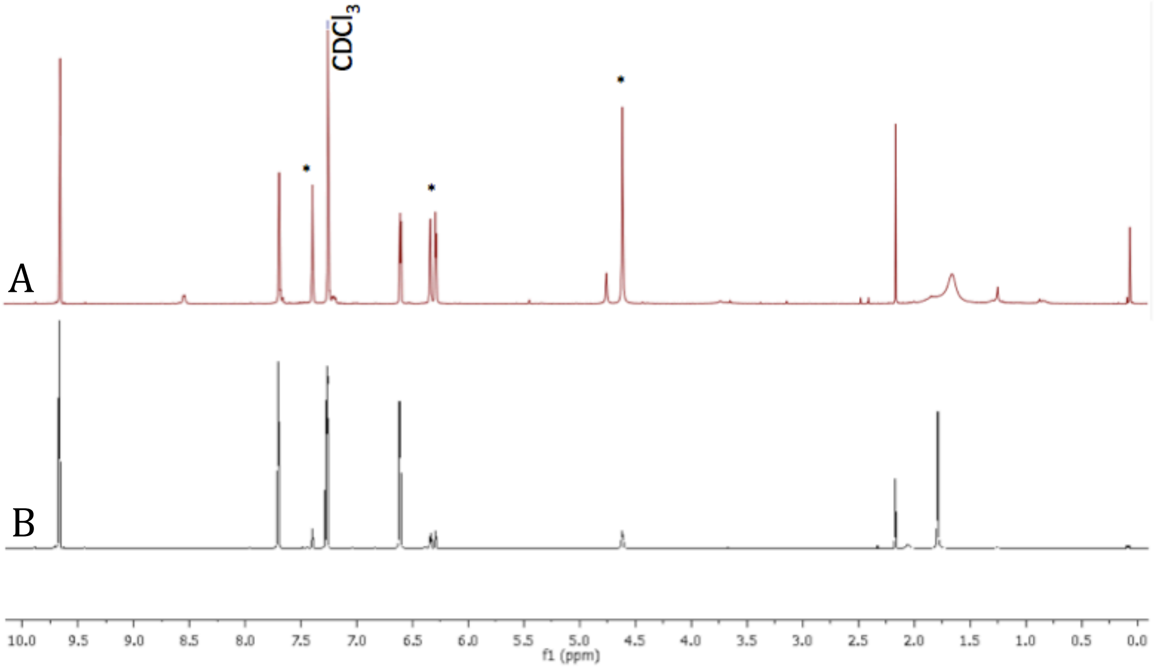

Figure 5.9: ^{1}H NMR spectra of: A) crude product mixture from the reaction of $NaBH_3CN$ with cage-bound furfural. B) crude product mixture from the reaction of $NaBH_3CN$ with furfural in solution. Peaks marked with * are furfuryl alcohol.

The next information of interest was to determine the minimum concentration of cage that would have the most tangible benefits for catalysis. Given the immense molecular size difference between the furfural and the Nitschke cage, we found it most beneficial to frame this in the context of the substrate to molar equivalents of cage. The varying amounts of cage and furfural were given a reaction time of 48 hours at 50 °C under a nitrogen atmosphere, and the resulting yields are tabulated below.

Table 5.1: Averaged yields from reactions with different molar equivalents present (yields based on product / substrate ratios)

Cage loading	Aldehyde Conversion (%)
0 eq	16%
0.085 eq	25%
0.021 eq	24%
0.043 eq	29%
0.85 eq	88%

As one can see in table 5.1, while there might be an increase in conversion dependent on the concentration of cage present, there is already reactivity between the furfural in solution and the cyanoborohydride. It was also found that using recycled cage in subsequent reactions yielded conversions of 24%, almost quartering the caged-based activity. Evidently, there is a marked difference between when cage is present and when not. Also, while there is a loss in activity in recycled cage one could effectively recrystallize and re-use it (albeit with a loss of activity resulting in ~20% less conversion).

When varying the temperature for these controls, it was discovered that at room temperature, the reaction seemed progress to the same extent regardless of the amount of cage that was present. Increasing the temperature up to 70 °C had the effect of increasing reaction yield, however this was a universal increase; even when there was no cage present, the conversion increased to a surprising extent. Based on this, it was decided that 50 °C would be the most appropriate reaction temperature, as it would afford the greatest comparative difference in yield between cage being present, and not being present. It was also determined that due to the small volumes of substrate needed, errors were being introduced when volumetrically measuring out. As such, volumetric measuring was abandoned in favor of a mass measurement.

5.2.3 – Reaction kinetics

Reaction kinetics were investigated by setting up concurrent samples and removing each one as the time point dictated. The yield was determined in this case by using the substrate/product ratios from NMR spectroscopy. Plotting them verses time affords a view of the progress of reaction. As it can be seen in figure 5.10 (below), the reaction without cage present comparatively proceeds extremely sluggishly; even after 6 hours reaction time the yield doesn't reach 10%. Over the course of 20 hours, the conversion approaches 20% at a near constant rate. In stark contrast however, introduction of the hydride to the mixture of furfural with 0.1 eq cage present immediately results in a 5% yield, reacting steadily over the course of 4 hours before starting to slow down. At around the 6 hour mark (equivalent to ~85%) the majority of the activity appears to halt, and the reaction proceeds more sluggishly until the end of the experiment.

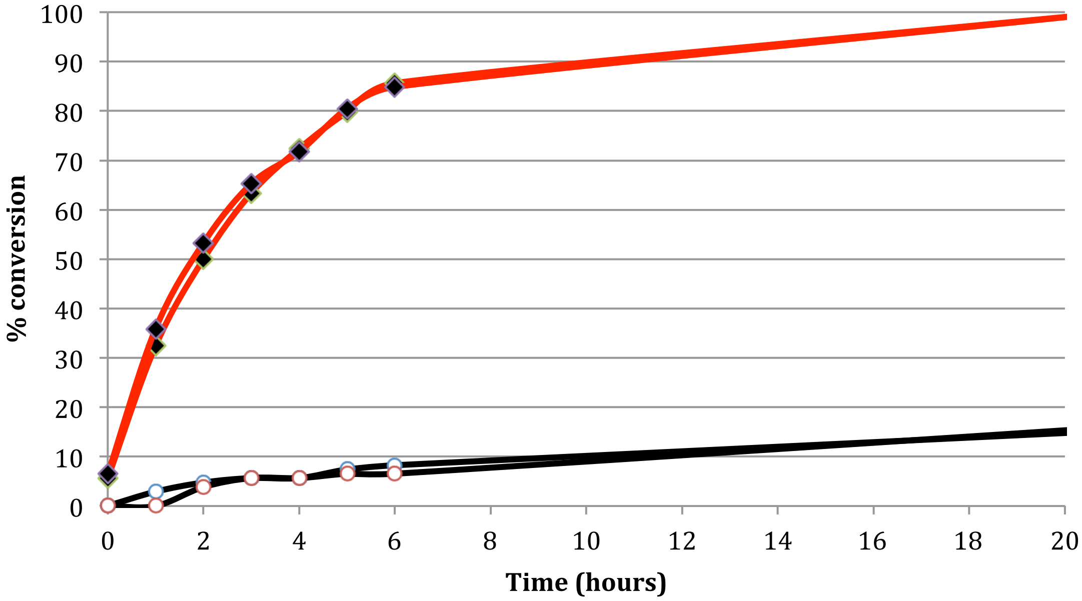

Figure 5.10: Kinetics trace of time vs. percent conversion of furfural to furfuryl alcohol. Red traces indicate the presence of cage molecule, black traces indicate a lack of cage. Yields were calculated using the ratio method

5.2.4 – Isolated yields vs. ratio

To verify the results of the control reactions, reactions were undertaken to determine the isolated yield for furfuryl alcohol. When crude product mixtures were refined *via* column chromatography, we found a surprising difference in yield between reactions where the yields were calculated via the ratio method. With an equivalent reaction time of 6 hours at

50 °C under a nitrogen atmosphere, the ratio method can work out at 14% higher than the isolated yield (based on an 87% and 75% yield respectively)

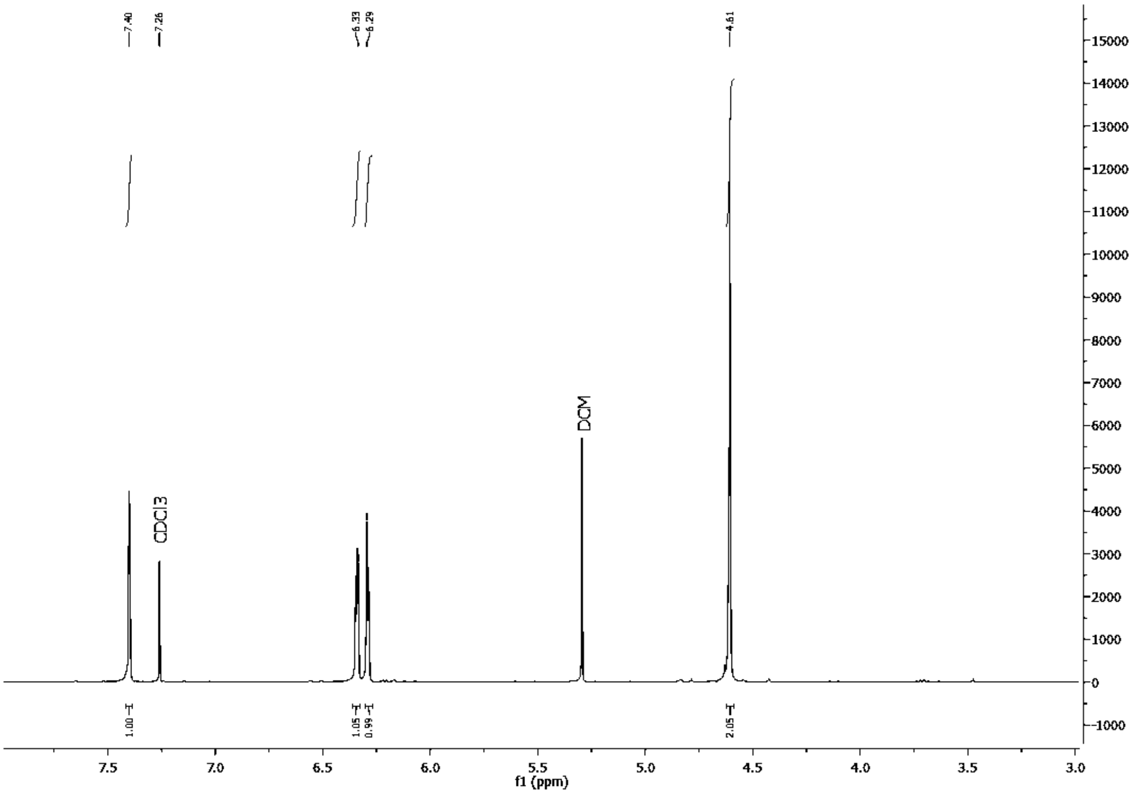

Figure 5.11: ^{1}H NMR spectrum of isolated furfuryl alcohol from crude product mixture. The mixture contained DCM, which was subtracted from overall mass during yield calculation. (1H NMR (400 MHz, CDCl3) δ 7.40 (s, 1H), 6.33 (m, 1H), 6.29 (s, 1H), 4.61 (s, 2H).)

Due to these findings, it became apparent that the yields varied quite drastically when comparing an isolated yield to one determined by substrate / product ratios. It is known that cyanoborohydride can disrupt the imine bond. This would have the effect of a small proportion of the substrate ligand swapping with the pyridine of the cage molecule. If any amount of ligand swapping were occurring between the cage and the substrate, then it would logically follow that substrate used in this process would not be accounted for when using the ratio method. Similarly, using the NMR ratios in an extracted product mixture does not account for any material that is not in solution and therefore visible by NMR. On the other hand, it could also be that some material is “lost” on the column and cannot be recovered. In this context isolated yields were from this point taken in preference, and verified where possible with a DMSO internal standard (see section 5.4.8).

5.2.5 – Increasing the scope of substrates examined

Given the prospect of the reaction occurring somewhat as expected, we thought it safe to start to investigate molecular features and their propensity to change the reactivity of the guest molecule. The aim was to investigate the steric and electronic effects arising from different functional groups, while still generally maintaining the overall aromatic structure. Each aldehyde used (for structures, see figure 5.12 below) is discussed in depth throughout this section, followed by a summarized table of conversions (*vide infra*). NMR spectra and peak data may be found in section 5.5.7 (page 127).

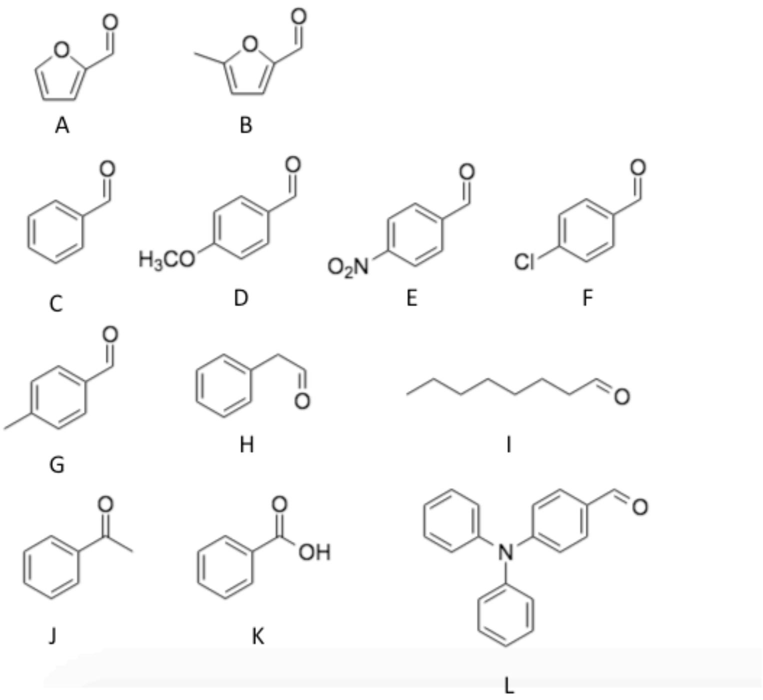

Figure 5.12 : The various substrates used to investigate the steric and electronic properties of guest molecules on reactivity. A) furfural, B) 5-methylfurfural, C) benzaldehyde, D) anisaldehyde, E) nitrobenzaldehyde, F) chlorobenzaldehyde, G) tolualdehyde, H) phenyl acetaldehyde, I) octanal, J) acetophenone, K) benzoic acid, L) 4-(diphenylamino) benzaldehyde

Benzaldehyde was the choice for initially expanding the scope of aldehydes examined. It is of similar size and hydrophobicity, as well as containing a relatively easy to access aldehyde group. The similarities between the substrates were reflected in the conversion yield of benzyl alcohol, with similarly high yields between 63-89 %. This is not unexpected, as it is a simple ring structure with no functional groups in it to exert many changes to the electronic nature of the molecule. 5-Methylfurfural was chosen as the next substrate of interest. With a simple methyl group, it provided a relatively small increase in the steric properties of the substrate. Thus, it provided a smooth transition from simple ring structures to molecules with more functional groups that have an effect on the charge distribution of the molecule. The reactions had a similar success to the previous two, with yields as high as 85% observed. Similar in choice to methylfurfural, p-tolualdehyde afforded another slight increase to the overall size of the substrate molecule without introducing electronic effects. Reactions with this substrate yielded conversions generally between 20-30 % with cage present, and 3% when not. This suggests that due to the substrates being larger, it is harder for them to fit inside the cage, and thus be converted.

Post investigation into steric effects, we began to investigate electronic effects introduced to the guest molecule, firstly in the use of methoxybenzaldehyde as a substrate. The reaction yields were fairly consistently in the 37-41% range, with a single potential outlier. The same reaction without cage present had a similarly predictable conversion rate to previous substrates, not even reaching 5%.

Phenyl acetaldehyde was another guest molecule investigated for its steric properties. The yields were fairly consistent around 30-33%, with no conversion found in the reaction without cage. In a similar vein, investigation into the effect of chain-based steric effects was accomplished *via* the use of 1-ocatanal Although the yield for this substrate is extremely low (0-3% conversion), as one can see from the HNMR spectrum of 1-octanol below there is still a slight conversion of aldehyde taking place.

The low yield is not unexpected, as despite its hydrophobicity such a large chain molecule would be an unsuitable guest for the Fe_4L_6 cage. The need to restrict the degrees of freedom of the alkyl chain in order to fit the molecule into the cage itself would be extremely enthalpically unfavourable. This size constraint on the guest molecule is further exemplified when using an extremely bulky substrate such as 4-(N,N'-Diphenylamino)benzaldehyde (4-DAP), which displays no quantifiable yield for the corresponding alcohol. Undoubtedly, the sheer size of the substrate molecule makes it unable to fit inside the cage, providing quite compelling evidence that the catalysis occurs inside the cage itself. Without encapsulation into the cage and subsequent activation of the aldehyde group, it is unlikely to convert to any meaningful extent.

Spurred on by these results we chose chlorobenzaldehyde and nitrobenzaldehyde as the ideal candidates to test the effects of an increase the electron withdrawal effect of the functional groups, and determine how this affects the conversion yields. Experimentally, 4-chlorobenzaldehyde was the most variable in terms of yields, with conversions with a wide range of 28-76% observed. Contrasting with this was a low yield of just 3% when there

was no cage present in the reaction. Interestingly, 4-chlorobenzaldehyde had by far the highest number of side-products produced, including three potential alcohol molecules (as determined by TLC and a vanillin dip-test). Unfortunately only one of these alcohol products could be successfully recovered via the column (see table 3 in section 5.3.5). This indicates that the products were in such low quantity given the scale of the reaction that they were lost in the column. The results for nitrobenzaldehyde are similarly wide-spread. As table 5.2 shows, the yield is consistently either 39% or 57%. While the true reaction yield is probably in between either of these numbers, this shows that the nitro-substituted benzaldehyde is consistently easier to convert than its chloro-substituted counterpart.
The most surprising thing with this substrate is the control reaction conversion at a suspiciously high 23%. While this could easily be an indicator of something going awry during experimentation, it could be an indicator that heavily electron-withdrawing substituents such as a nitro group may have an extensive effect on the ability of the guest aldehyde to convert. If they withdraw electron density from the carbonyl carbon, one would expect the substrate to be more reactive.

Instead of just limiting the substrates to aldehydes, we sought to elucidate the limits of this reaction to more difficult to reduce molecules. To this end, we chose to use the equivalent simple aromatic ketone and carboxylic acid. Somewhat unexpectedly, the reaction with acetophenone as a substrate did proceed; albeit in a similarly erratic fashion to previous substrates. A highly variable yield of 0-44% was found, with no quantifiable product when no cage molecule was used. When benzoic acid was used as a substrate, here was no identifiable conversion. The electron density and delocalized charge of a carboxylic acid group provide a particularly difficult barrier for a prospective hydride, and with a pKa of 4.20, it is to be expected that the reaction would not occur.

As one would expect given the variety of different substrates used, the conversions vary quite drastically (as shown in figure 5.21, and table 5.2, below). In general, it appears that the stoichiometrically smaller aldehydes have a higher conversion rate to those with more bulky substituents. Somewhat alarmingly however, the yield variations for some of the alcohol products suggest all is not as it should be. Even when removing potential outliers and averaging the data left, there is a significant deviation between each reaction with the same guest molecule.

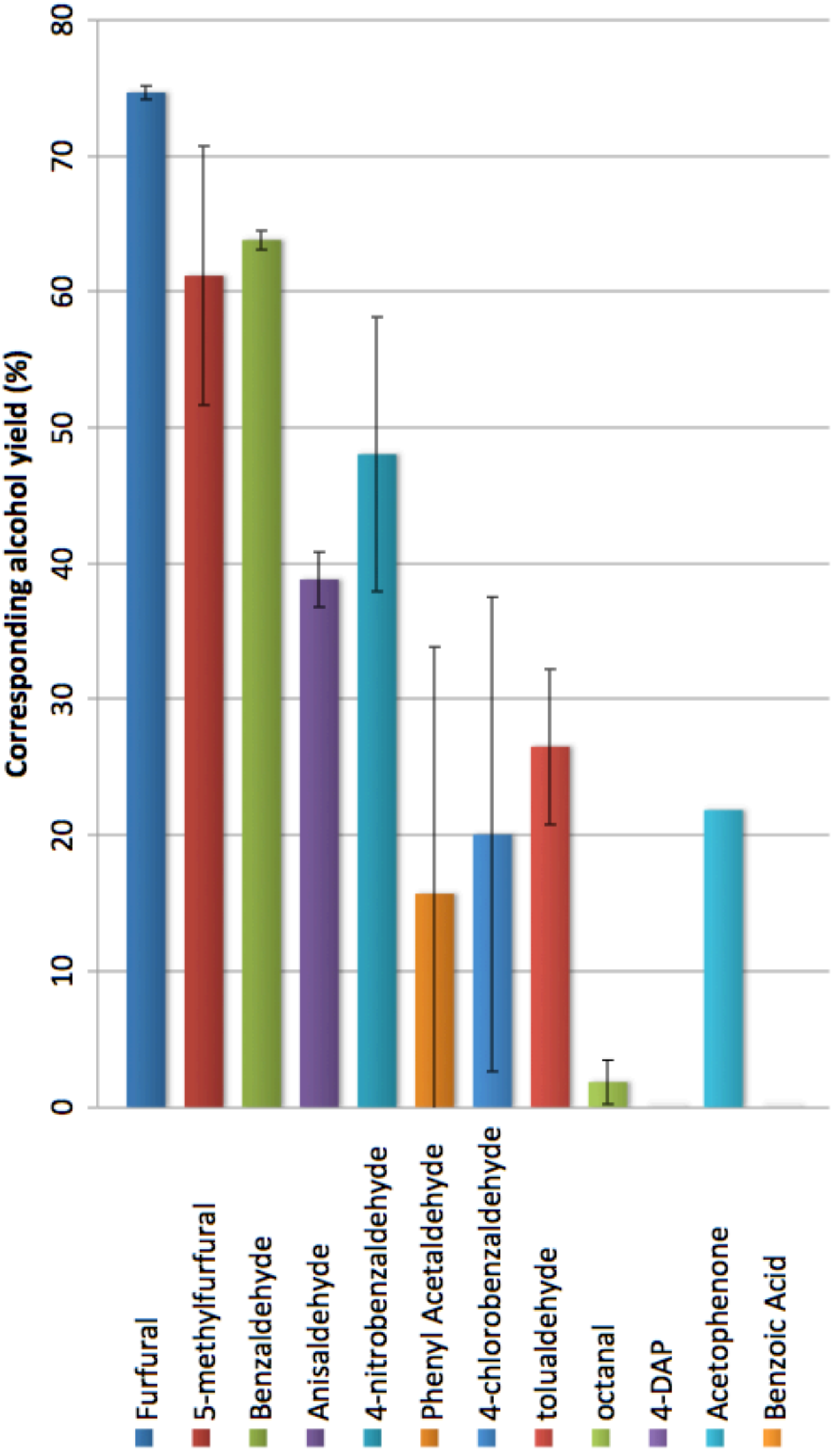

Figure 5.13: average reaction yields for substrates (errors based on standard deviation)

Table 5.2: Conversion yields for different substrates reacted with $NaBH_3CN$ in the presence of the Nitschke cage. Control reactions were performed at the same conditions, with no cage present

	Corresponding Alcohol Yield (%)				
substrate	1	2	3	4	Control
furfural	74	75	14	33	4
5-methylfurfural	63	87	51	70	3
benzaldehyde	64	89	64	63	9
4-methylbenzaldehyde	25	79	22	33	2
4-methoxybenzaldehyde	38	54	41	37	4
4-chlorobenzaldehyde	28	0	32	76	2
4-nitrobenzaldehyde	39	57	39	57	23
phenyl acetaldehyde	33	0	0	30	0
1-octanal	3	0*	3	-	0
4-(Diphenylamino)benzaldehyde	0	-	-	-	0
acetophenone	44	-	0*	-	0
benzoic Acid	0	-	-	-	-

* indicates trace of product in post-column NMR. Values highlighted in red denote potential outliers.

In terms of introduced errors that could account for this deviation, phantom catalysis [95] can be ruled out, as the magnetic stirrers used were new where possible (or once used and acid washed where not possible). The cage used was created in large quantity for use in multiple data sets, inspected periodically for purity, and was kept in a dry environment while not in use. It was however observed that oxygen being present in the reaction atmosphere had the effect of partially oxidizing the cage in solution. While every effort was made to limit this from affecting the reaction (see experimental section 5.3), the aldehyde substrates themselves were not degassed under vacuum or via freeze/pump/thaw methods. As such, they could have introduced a small amount of dissolved oxygen.

Interestingly, the majority of the yield data that appears to be outliers are from the same batch of reactions. This data set was the last run to use a particular batch of $NaBH_3CN$, prior to a new sample being opened. In addition to this, it is well known that some of the aldehydes used polymerize readily if not kept under specific conditions (phenyl acetaldehyde and furfural were found to be particularly susceptible to this issue). Given these caveats, it is not unreasonable to attribute some of the yield variation, however small, to chemical spoilage

One of the main curiosities throughout the experimental work was an occasional shift to a deep blue colour, seemingly at random and not dependant on the guest molecule being analysed at the time. This is undoubtedly the note of a change in some way to the cage molecule itself that is not attributable to simple oxidation (which results in a brown solution/suspension and similar yields to the control experiment), however we were not able to investigate the effects of reaction conditions on the cage itself.

5.4 – Conclusions and future work

In conclusion, we have shown that the Nitschke cage not only sequesters small aromatic aldehydes, but also places them in an environment that activates the aldehyde proton for conversion to the corresponding alcohol. While the results may vary by quite a drastic amount, it can be seen that conversion most definitely occurs. Unfortunately due to time constraints it was evidently not possible to narrow the deviation within the yield data, with some results varying by unacceptable amounts. With some slight adjustments to experimental protocol however (such as thoroughly degassing the substrates themselves), it should be possible to decrease these errors. To this end, a more thorough kinetics experiment based on isolated yields would undoubtedly assist in this endeavor.

Within the same school of thought, the difference between isolated yields and the ratio method of yield varied at some times by as much as 50%. Given that the ratio method is used quite often in this field of research, it would be prudent to determine why this is the case. Given this context, it would be useful to conduct more experiments on the properties of the cage throughout the experiment. In example: the extent that the hydride source affects the cage molecule was quite surprising, and it begs the question as to whether there is a reduction agent that would be able to react with the substrate and leave the cage itself intact.

A natural extension to this work would be to establish the full extent of functional groups that can be activated by the Nitschke cage and reacted. If aldehydes (and to a certain extent ketones) can be converted in traditionally unfavorable conditions, what else can be? In addition; while the conversion of aldehydes has been observed, it would be interesting to see if it is possible to reverse the process.

5.5 - Experimental methods and materials

5.5.1 – General experimental remarks

Unless otherwise stated, water used in this experiment was of ultra-pure grade (at least 18.4 MΩ cm^{-1} resistance) and degassed with N_2. Reusable glassware and stirrer bars were cleaned with concentrated aqua regia (3:1 mixture of conc. hydrochloric acid : nitric acid), prior to being quenched. They were then rinsed successively with H_2O and acetone, and dried under a nitrogen stream. All ^1H spectra were recorded on a Bruker AV 400 instrument (unless otherwise stated), at a constant temperature of 300 K. Chemical shifts are reported in parts per million from low to high field. Standard abbreviations indicating multiplicity were used as follows: m = multiplet, s = singlet.

Iron (II) sulfate heptahydrate (≥99%), Vanillin (99%), Furfural (99%), Benzaldehyde (≥99%), and 5-methylfurfural (99%) were purchased from Sigma-Aldridge. 4,4'-Diaminobiphenyl-2,2'-disulfonic acid (≥70%), tetramethylammonium hydroxide (98%), sodium cyanoborohydride (95%), dimethyl sulfoxide (99.8%), nitrobenzaldehyde (99%), anisaldehyde (99%), phenyl acetaldehyde (95%), Octanal (99%) Acetophenone (99%), Chlorobenzaldehyde (99%) were purchased from Alfa Aesar. Nitric Acid (70%), Sulfuric acid (≥95%), hexane (≥95%), acid-washed sand, Sodium bicarbonate (≥99.7%) were purchased from Fischer Scientific. Ethanol (100%), dichloromethane (100%), magnesium sulfate, and Acetone (≥95%) were purchased from VWR. Hydrochloric acid was purchased from Honeywell. Silica 60 (0.04-0.063mm) was purchased from Merck. 4-(N,N`-Diphenylamino)benzaldehyde was purchased from TCI. D2O (99.9%) and $CDCl_3$ (99.8%) were purchased from Cambridge Isotope Laboratories. Pyridine-2-carboxaldehyde (99%) was purchased from Acros Organics

5.5.2 – Cage synthesis

Fe_4L_6 cage was synthesised *via* as outlined by Nitschke [86] but scaled up by a factor of four. 4 g ($1.16x10^{-2}$ moles, 6 eq) 4,4'-Diaminobiphenyl-2,2'-disulfonic acid, 1.5 g ($5.3x10^{-3}$ moles, 4 eq) Iron (II) sulfate heptahydrate and 2.95 g ($1.6x10^{-2}$ moles, 4 eq) tetramethylammonium hydroxide pentahydrate were weighed into a clean 250ml round-bottomed flask. A clean stirrer bar was inserted and the flask sealed with a clean septa. The air inside was immediately purged with three successive vacuum / N_2 purge cycles to render the atmosphere inside inert, and 100 ml H_2O was added. The mixture was stirred at 50°C until all solids had dissolved, resulting in a clear orange solution. 1.95 ml ($2.0x10^{-2}$ moles, 12 eq) pyridine-2-carboxaldehyde was then added to this solution, which immediately turned a dark and intense purple colour. This was left to stir for 18 hours at 50°C.

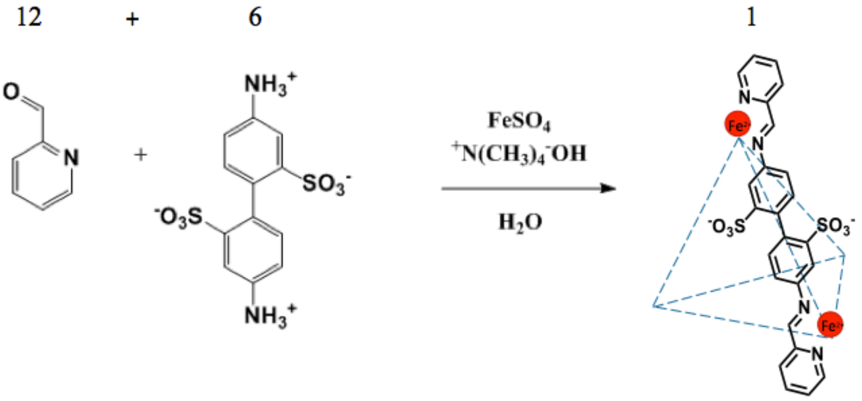

Figure 5.14: Synthesis scheme of the Nitschke Fe_4L_6 cage

To purify the cage molecule, while the solution was still at reaction temperature it was transferred to a crystallization dish and sealed in a vapor-diffusion chamber (filled with N_2-degassed acetone as the antisolvent, see figure 5.23). To facilitate minimal oxidation of cage, the atmosphere inside the chamber was purged with a stream of N_2 prior to sealing.

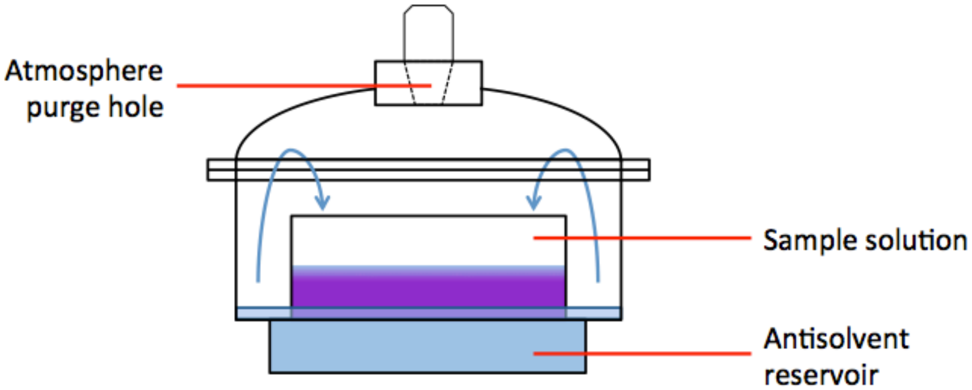

Figure 5.15: vapour-diffusion crystallization setup

The crude mixture was left to crystallise until the solution changed to a clear brown colour and crystals were observed in the dish. At this point the supernatant was discarded and the cage product immediately and thoroughly rinsed with more acetone, prior to being dried overnight on a hi-vacuum line. The reaction yielded large needle-shaped lustrous dark purple crystals [^{1}H NMR (400 MHz, D2O) δ **9.33** (s, 12H), **8.69** (s, 12H), **8.40** (s, 12H), **7.76** (s, 12H), **7.53** (s, 12H), **7.14** (s, 12H), **6.44** (s, 12H), **5.82** (s, 12H), **3.17** (s, NMe_4)].

5.5.3 – Furfural incorporation

100 mg (2.55×10^{-5} moles, 0.85 eq.) cage molecule was weighed out into a clean 14 ml sample vial, and dissolved in x ml D2O. 4 µl furfural (3×10^{-4} moles, 1 eq.) was added to this solution under a nitrogen stream, and the vial sealed with a clean septum. The atmosphere inside the vial was further purged for 1 minute with a nitrogen line to ensure a strict inert atmosphere, a nitrogen balloon was added and the sample was stirred for 6 hours at 50°C. The mixture was allowed to cool to room temperature and an aliquot was taken for NMR analysis.

5.5.4 - Aldehyde Reactions and controls

100 mg cage (2.55×10^{-5} moles, 0.85 eq) of cage and 3×10^{-4} moles of the corresponding aldehyde were weighed into a new 14 ml sample vial. A clean magnetic stirrer was inserted, and the vial was sealed with a clean septum. The air inside the vial was purged with a stream of nitrogen, prior to a nitrogen balloon being affixed (both to regulate pressure and keep an inert atmosphere). The mixture was allowed to stir for an hour at 50 °C to mix fully and sequester before a solution of 19 mg $NaBH_3CN$ (3×10^{-4} moles, 1 eq) in 1 ml H_2O was added. This was stirred for 6 hours at 50°C, before being allowed to cool to room temperature and then extracted and purified. Kinetics reactions were above, albeit only stirred for the duration required. Control reactions were as above, but with the associated control in place.

5.5.5 – Product purification

The crude product mixture was added to a clean 100ml separating funnel, with the sample vial being rinsed with 5ml H_2O. 15 ml saturated Na_2CO_3 solution was added to neutralize the sulfonic acid groups (reducing suspension build-up) and the resulting mixture was extracted with 5 x 20ml DCM. The aqueous phase was reserved, and the organic phase was dried over MgSO4, gravity filtered, reduced *in vacuo,* and analysed by ^{1}H NMR.

A chromatography column (internal diameter : 1 cm) was set up using 20 ml silica and a 1: 5 mixture of DCM : n-hexane. The crude product mixture was dissolved in the minimal amount of the same solvent mixture, and wet-loaded on to the top. Aliquots were removed from each of the 5 ml fractions, subjected to TLC (thin-layer chromatography) and developed first under UV light, and then via vanillin dip (7.5 g vanillin dissolved in 125 ml ethanol with 1.25 ml concentrated H_2SO_4). Co-spots of the corresponding alcohol product were used wherever possible. Positive testing fractions (as indicated by vivid blue or pink spots) were collated and reduced *in vacuo*, prior to being analysed *via* NMR.

Table 5.3 : Crude / refined product column information

		Appearance	
Substrate	Rf value	Pre column	Post column
Furfural	0.22	Brown oil	Colourless oil
5-methylfurfural	0.13	Brown oil	Pale yellow oil
Benzaldehyde	0.22	Colourless oil	Colourless oil
Anisaldehyde	0.13	Colourless oil	Colourless oil
4-nitrobenzaldehyde	0.23	Yellow crystals	White crystals
Phenyl Acetaldehyde	0.20	Clear oil	Pink oil
4-chlorobenzaldehyde	0.20	Colourless solid	Clear oil
tolualdehyde	0.20	Brown oil	Brown oil
1-octanal	0.22	Colourless oil	Colourless oil
4-(Diphenylamino)benzaldehyde	-	-	-
Acetophenone	0.11	Colourless oil	Colourless oil
Benzoic Acid	-	-	-

5.5.6 – Yield calculations

There were three methods of yield calculations used in this chapter: checking the ratio of product to starting material via HNMR spectroscopy, using DMSO as an internal standard (at 1 eq of the starting material), and obtaining isolated compound yields. Unless otherwise stated, reaction yields are based on isolated yields.

5.5.7 - NMR Data

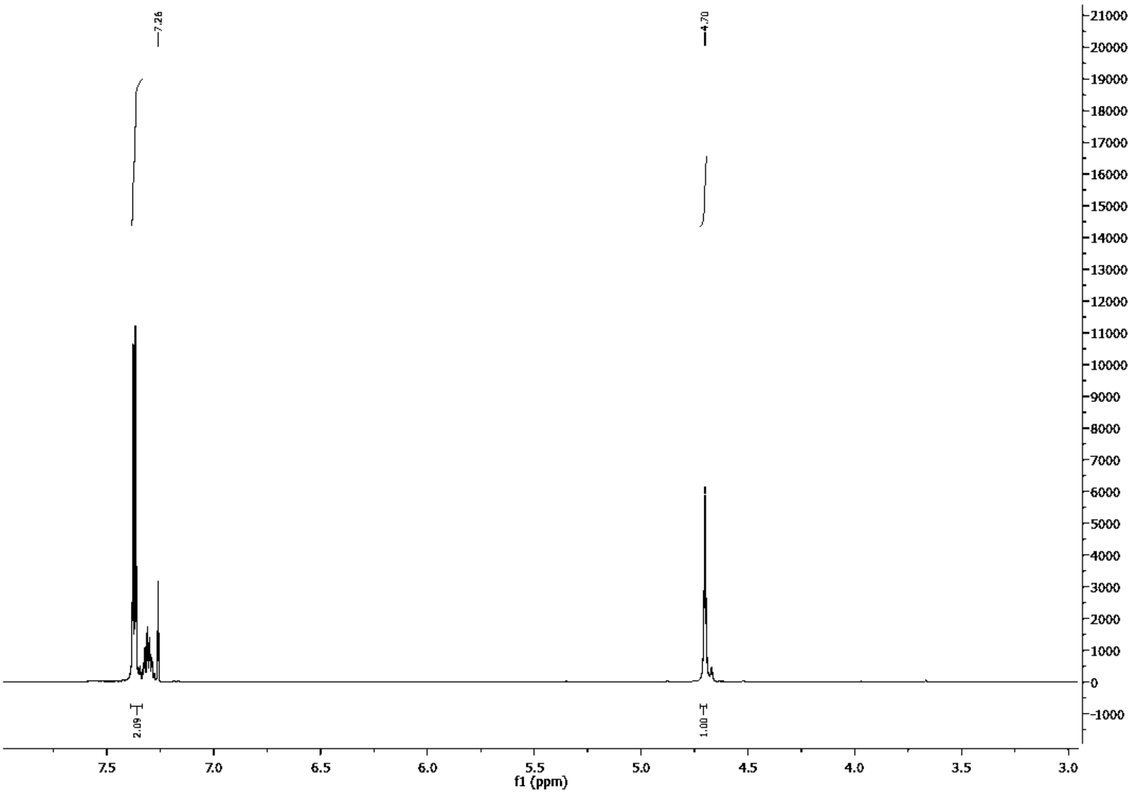

Figure 5.16: ^{1}H NMR spectrum of isolated Benzyl alcohol from reaction of benzaldehyde and $NaCNBH_3$ in the presence of cage. Mixture contained DCM, which was subtracted from overall yield during calculation. (1H NMR (400 MHz, CDCl3) δ 7.37 (d, J = 4.4 Hz, 1H), 7.33 – 7.27 (m, 1H), 4.70 (s, 1H).)

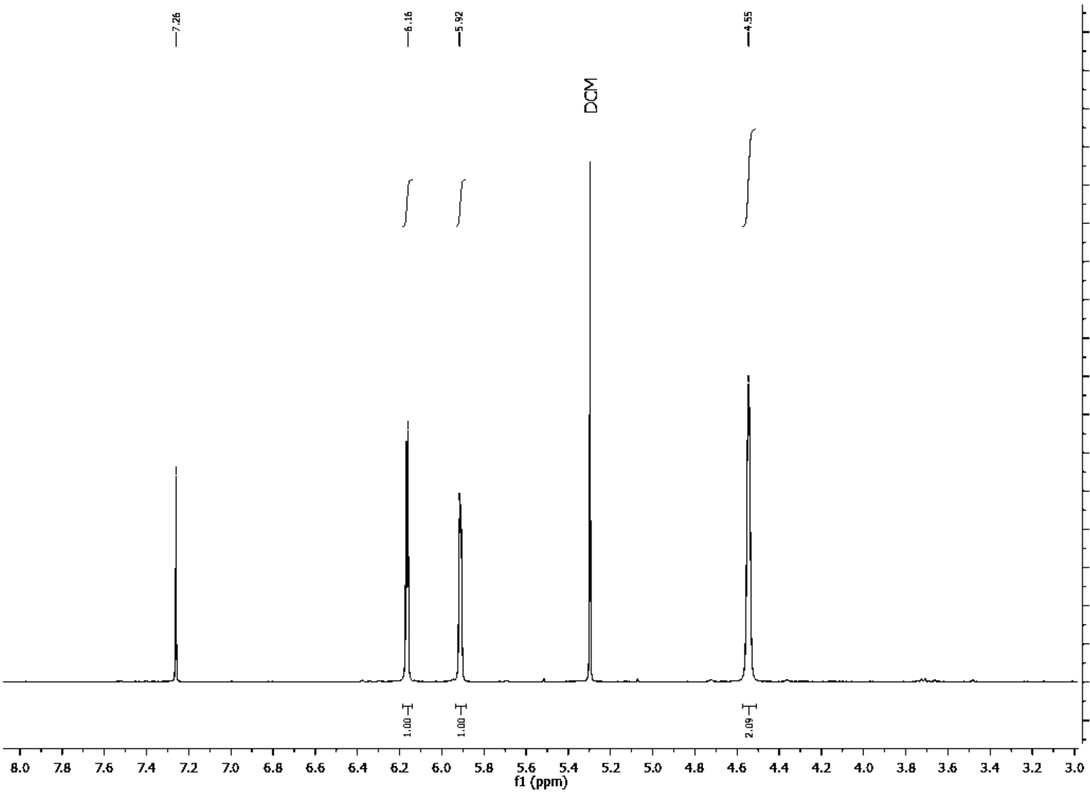

Figure 5.17: ^{1}H NMR spectrum of isolated 5-methylfurfural alcohol from reaction of 5-methylfurfural and $NaCNBH_3$ in the presence of cage. Mixture contained DCM, which was subtracted from overall yield during calculation. (1H NMR (400 MHz, CDCl3) δ 6.16 (d, 1H), 5.92 (d, 2H), 4.55 (s, 3H).)

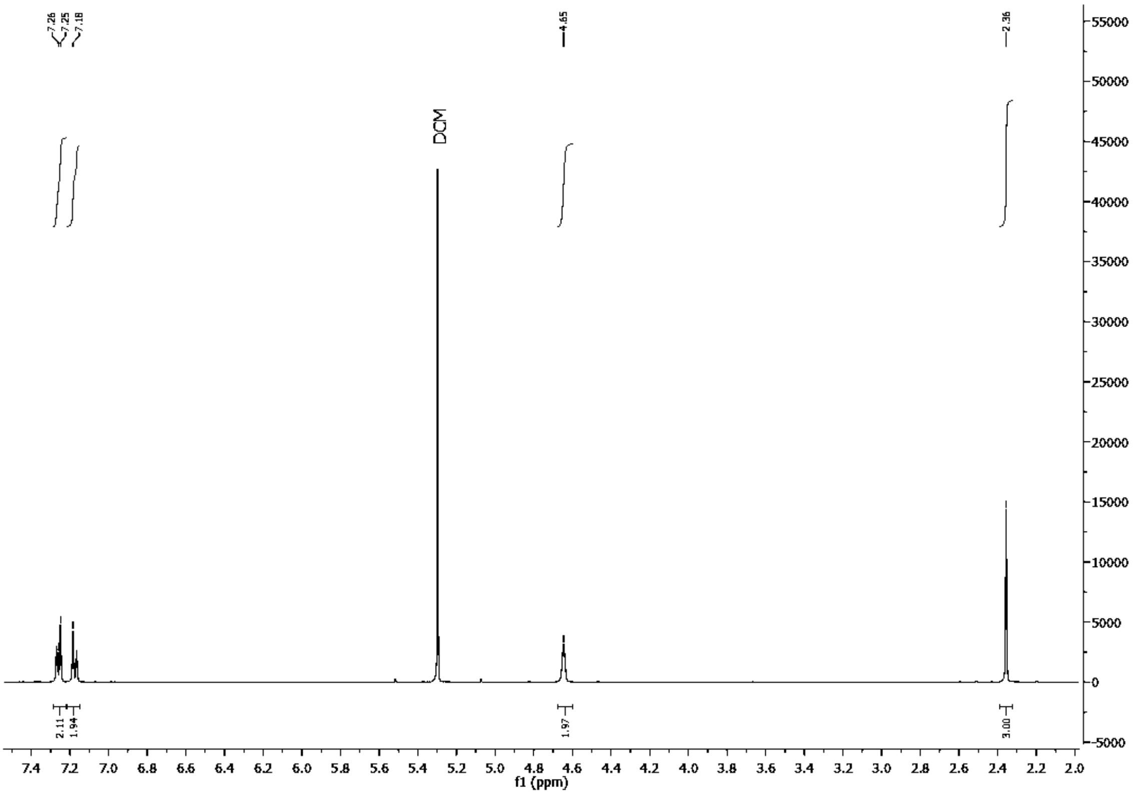

Figure 5.18: ^{1}H NMR spectrum of isolated 4-methylbenzyl alcohol from reaction of 4-methylbenzaldehyde (p-tolualdehyde) and $NaCNBH_3$ in the presence of cage. Mixture contained DCM, which was subtracted from overall yield during calculation. (1H NMR (400 MHz, CDCl3) δ 6.16 (d, 1H), 5.92 (d, 1H), 4.55 (s, 2H).)

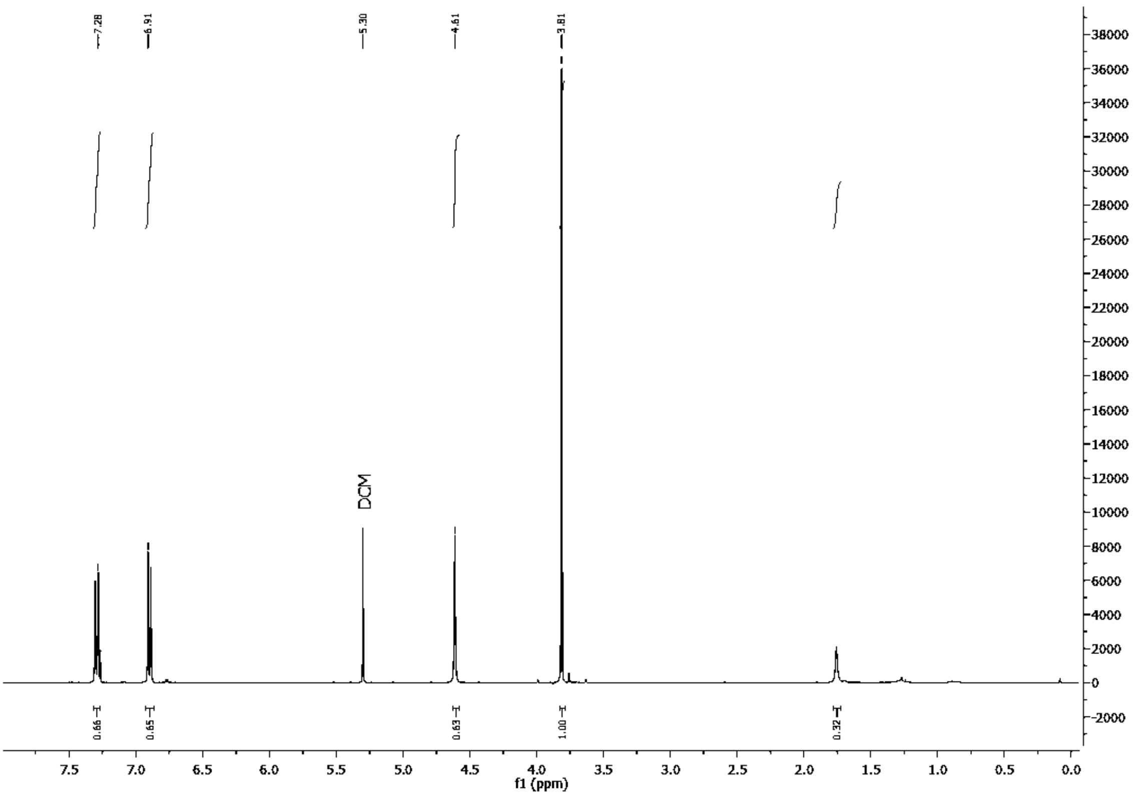

Figure 5.19: ^{1}H NMR spectrum of isolated 4-methoxybenzyl alcohol from reaction of 4-methoxybenzaldehyde (p-anisaldehyde) and $NaCNBH_3$ in the presence of cage. Mixture contained DCM, which was subtracted from overall yield during calculation. (1H NMR (400 MHz, CDCl3) δ 7.31 – 7.27 (m, 2H), 6.92 – 6.87 (m, 1H), 4.61 (s, 1H), 3.81 (s, 2H).)

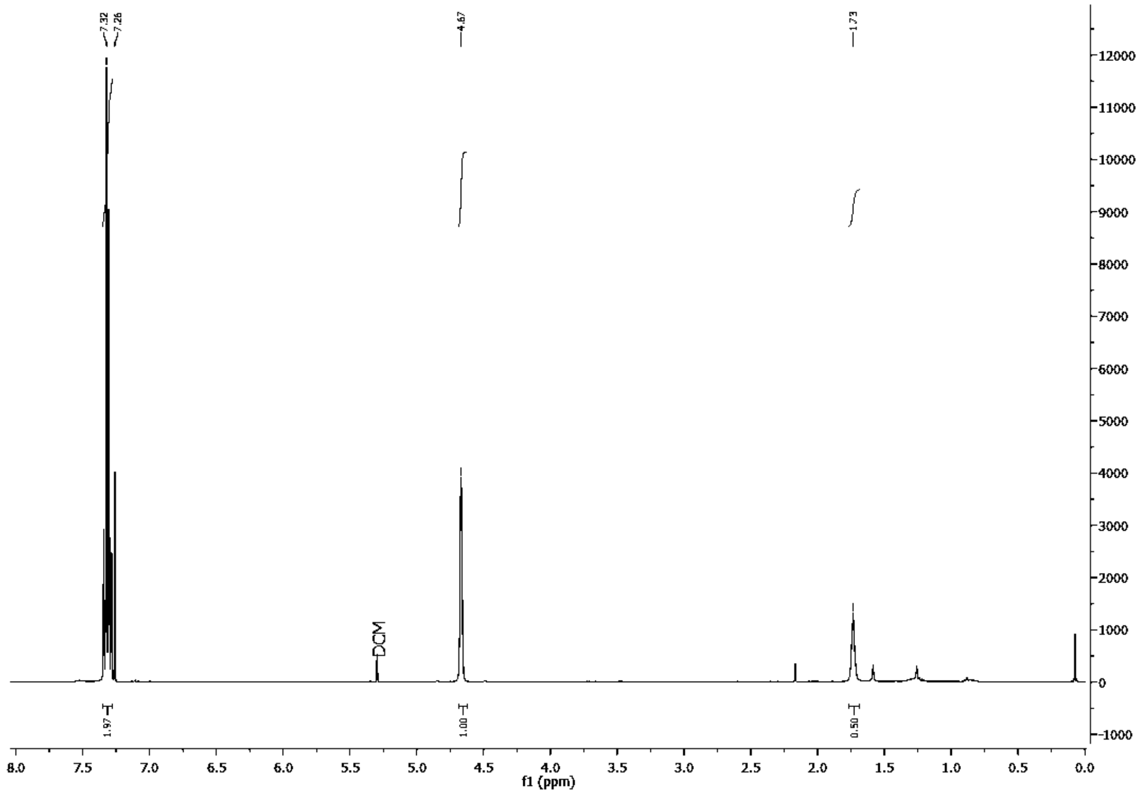

Figure 5.20: ^{1}H NMR spectrum of isolated 4-chlorobenzyl alcohol from reaction of 4-chlorobenzaldehyde and $NaCNBH_3$ in the presence of cage. Mixture contained DCM, which was subtracted from overall yield during calculation. (^{1}H NMR (400 MHz, CDCl3) δ 7.35-7.28 (m, 4H), 4.67 (s, 1H), 1.73 (s, 1H).)

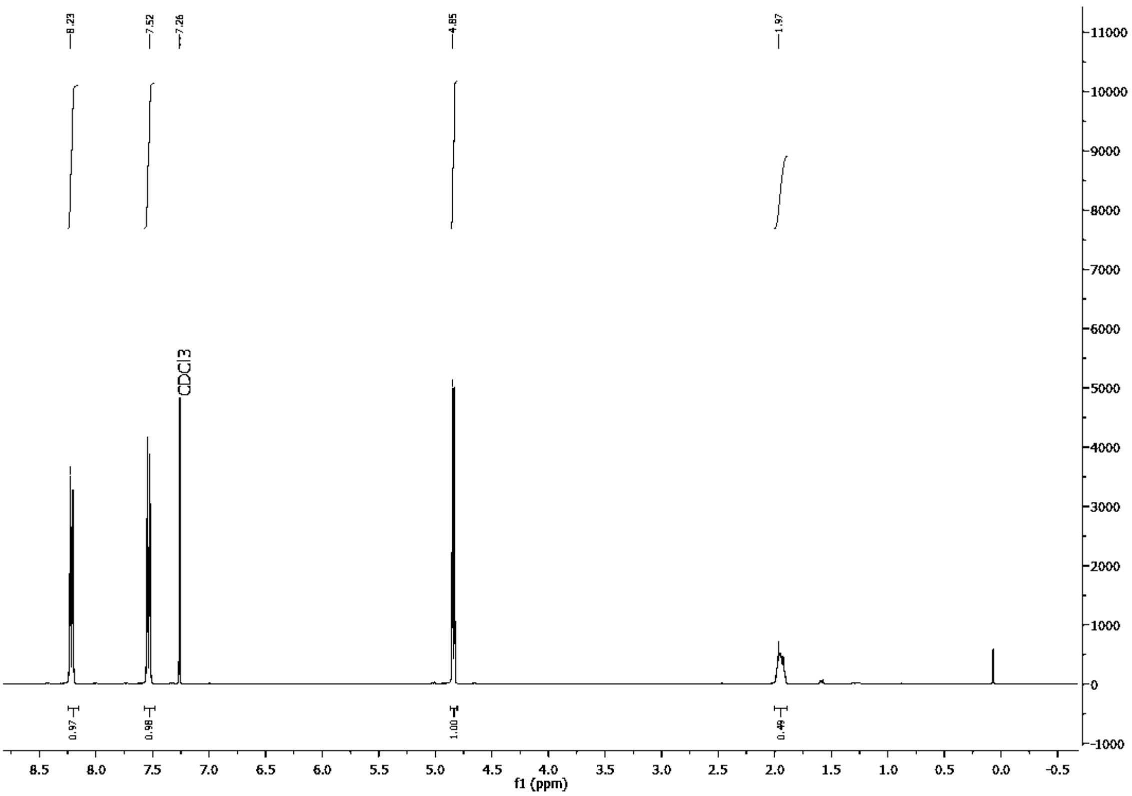

Figure 5.21: ^{1}H NMR spectrum of isolated 4-nitrobenzyl alcohol from reaction of 4-nitrobenzaldehyde and $NaCNBH_3$ in the presence of cage. Mixture contained DCM, which was subtracted from overall yield during calculation. (1H NMR (400 MHz, CDCl3) δ 8.23 (d, 1H), 7.52 (d, 1H), 4.85 (s, 1H), 1.97 (s, 1H).)

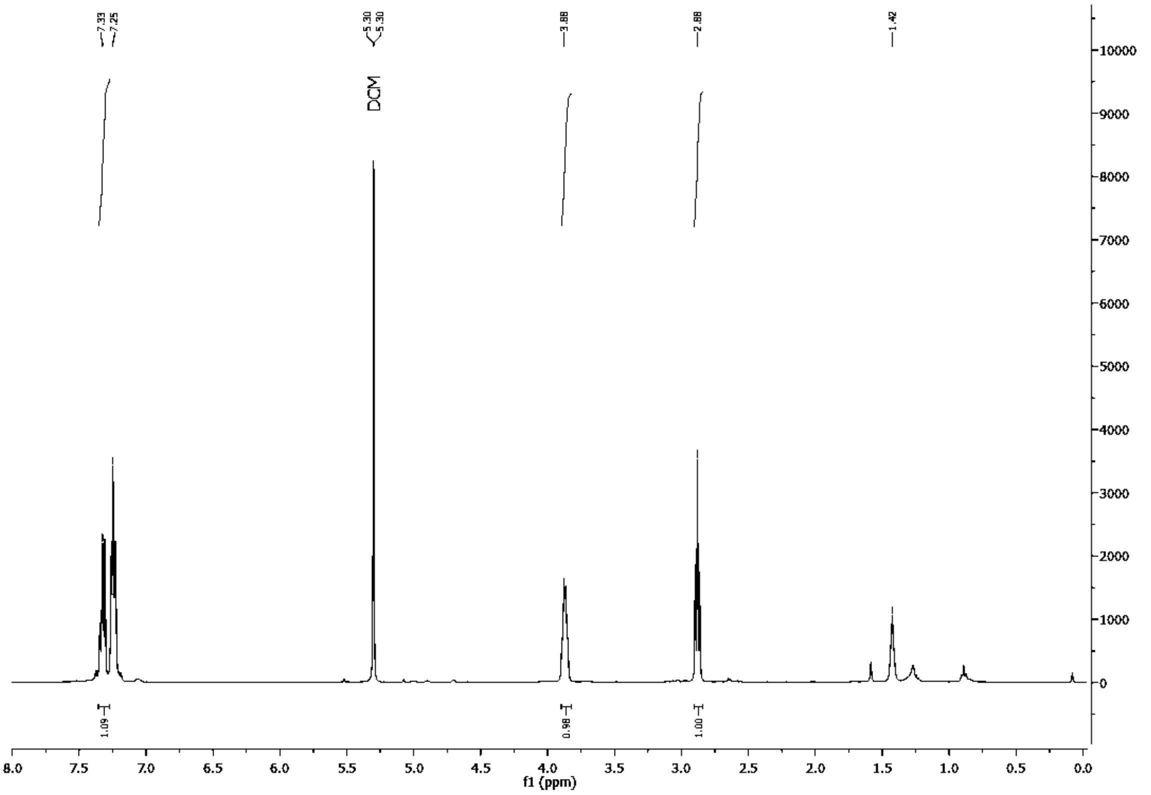

Figure 5.22: ^{1}H NMR spectrum of 2-phenylethyl alcohol from a reaction of phenyl acetaldehyde and $NaCNBH_3$ in the presence of cage. Mixture contained DCM, which was subtracted from overall yield during calculation. (1H NMR (400 MHz, CDCl3) δ 7.33 (s, 1H), 7.25 (s, 2H), 2.88 (s, 1H).)

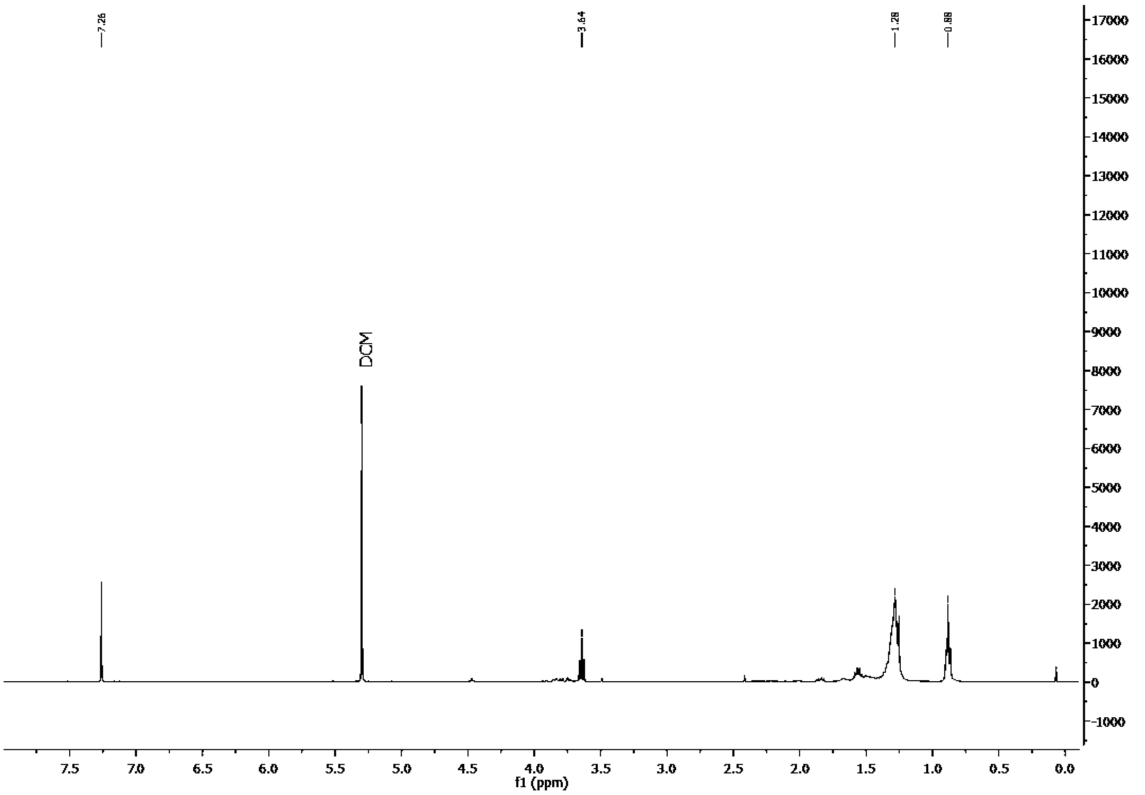

Figure 5.23: ^{1}H NMR spectrum of isolated 1-octanol from reaction of 1-octanal and $NaCNBH_3$ in the presence of cage. Mixture contained DCM, which was subtracted from overall yield during calculation. (1H NMR (400 MHz, CDCl3) δ 3.64 (s, 1H), 1.60 – 1.55 (m, 1H), 1.28 (s, 13H), 0.88 (s, 4H).)

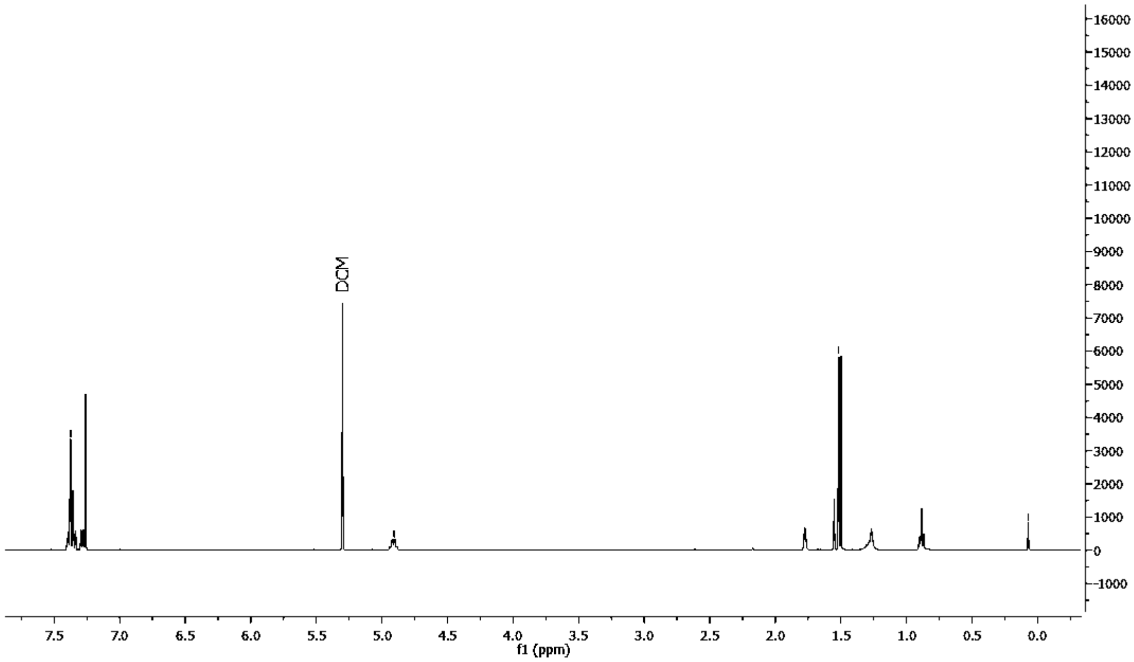

Figure 5.24: ^{1}H NMR spectrum of isolated 1-phenylethyl alcohol from reaction of acetophenone and $NaCNBH_3$ in the presence of cage. Mixture contained DCM, which was subtracted from overall yield during calculation. (^{1}H NMR (400 MHz, CDCl3) δ 7.37 (s, 1H), 4.91 (s, 1H), 1.77 (d, 1H), 1.52 (s, 1H).)

5.7 - References

1. Muñoz, M.J.P. and E.C. Martínez, *Prussian Blue and Its Analogues. Structure, Characterization and Applications*, in *Prussian Blue Based Batteries*. 2018, Springer. p. 9-22.
2. Tan, C., et al., *Supramolecular Coordination Cages for Asymmetric Catalysis.* Chemistry–A European Journal, 2019. **25**(3): p. 662-672.
3. Mastalerz, M., *Shape‐persistent organic cage compounds by dynamic covalent bond formation.* Angewandte Chemie International Edition, 2010. **49**(30): p. 5042-5053.
4. Bloch, W.M. and G.H. Clever, *Integrative self-sorting of coordination cages based on 'naked'metal ions.* Chemical Communications, 2017. **53**(61): p. 8506-8516.
5. Breiner, B., J.K. Clegg, and J.R. Nitschke, *Reactivity modulation in container molecules.* Chemical Science, 2011. **2**(1): p. 51-56.
6. Castilla, A.M., W.J. Ramsay, and J.R. Nitschke, *Stereochemistry in subcomponent self-assembly.* Accounts of chemical research, 2014. **47**(7): p. 2063-2073.
7. Chakrabarty, R., P.S. Mukherjee, and P.J. Stang, *Supramolecular coordination: self-assembly of finite two-and three-dimensional ensembles.* Chemical reviews, 2011. **111**(11): p. 6810-6918.
8. Chen, L., et al., *Controllable coordination-driven self-assembly: from discrete metallocages to infinite cage-based frameworks.* Accounts of chemical research, 2014. **48**(2): p. 201-210.
9. Cook, T.R. and P.J. Stang, *Recent developments in the preparation and chemistry of metallacycles and metallacages via coordination.* Chemical reviews, 2015. **115**(15): p. 7001-7045.
10. Han, Y.-F., et al., *Stepwise formation of organometallic macrocycles, prisms and boxes from Ir, Rh and Ru-based half-sandwich units.* Chemical Society Reviews, 2009. **38**(12): p. 3419-3434.
11. Lusby, P.J., *Supramolecular coordination chemistry.* Annual Reports Section" A"(Inorganic Chemistry), 2012. **108**: p. 292-314.
12. Roberts, D.A., B.S. Pilgrim, and J.R. Nitschke, *Covalent post-assembly modification in metallosupramolecular chemistry.* Chemical Society Reviews, 2018. **47**(2): p. 626-644.
13. Schulze, A.C., K. Focker, and I.M. Oppel, *Koordinationschemie-Koordinationskafige als Nanolabore-Reaktionsgefasse fur ungewohnliche Reaktionen.* Nachrichten aus der Chemie, 2009. **57**(5): p. 507.
14. Severin, K., *Supramolecular chemistry with organometallic half-sandwich complexes.* Chemical Communications, 2006(37): p. 3859-3867.
15. Tranchemontagne, D.J., et al., *Reticular chemistry of metal–organic polyhedra.* Angewandte Chemie International Edition, 2008. **47**(28): p. 5136-5147.
16. Wang, W., Y.-X. Wang, and H.-B. Yang, *Supramolecular transformations within discrete coordination-driven supramolecular architectures.* Chemical Society Reviews, 2016. **45**(9): p. 2656-2693.
17. Zarra, S., et al., *Molecular containers in complex chemical systems.* Chemical Society Reviews, 2015. **44**(2): p. 419-432.
18. Bloch, W.M., et al., *Geometric Complementarity in Assembly and Guest Recognition of a Bent Heteroleptic cis-[Pd2 LA 2 LB 2] Coordination Cage.* Journal of the American Chemical Society, 2016. **138**(41): p. 13750-13755.
19. Borsley, S., et al., *Nanopore detection of single‐molecule binding within a metallosupramolecular cage.* Chemistry–A European Journal, 2018. **24**(18): p. 4542-4546.

20. Borsley, S., et al., *Electrostatic forces in field-perturbed equilibria: nanopore analysis of cage complexes.* Chem, 2019. **5**(5): p. 1275-1292.
21. Gidron, O., et al., *Chiroptical Detection of Nonchromophoric, Achiral Guests by Enantiopure Alleno‐Acetylenic Helicages.* Angewandte Chemie International Edition, 2014. **53**(49): p. 13614-13618.
22. Ward, M.D. and P.R. Raithby, *Functional behaviour from controlled self-assembly: challenges and prospects.* Chemical Society Reviews, 2013. **42**(4): p. 1619-1636.
23. Brown, C.J., et al., *Supramolecular catalysis in metal–ligand cluster hosts.* Chemical reviews, 2015. **115**(9): p. 3012-3035.
24. Catti, L., Q. Zhang, and K. Tiefenbacher, *Advantages of Catalysis in Self‐Assembled Molecular Capsules.* Chemistry‐A European Journal, 2016. **22**(27): p. 9060-9066.
25. Durot, S., J. Taesch, and V. Heitz, *Multiporphyrinic cages: architectures and functions.* Chemical reviews, 2014. **114**(17): p. 8542-8578.
26. Leenders, S.H., et al., *Transition metal catalysis in confined spaces.* Chemical Society Reviews, 2015. **44**(2): p. 433-448.
27. Otte, M., *Size-selective molecular flasks.* ACS Catalysis, 2016. **6**(10): p. 6491-6510.
28. Wiester, M.J., P.A. Ulmann, and C.A. Mirkin, *Enzyme mimics based upon supramolecular coordination chemistry.* Angewandte Chemie International Edition, 2011. **50**(1): p. 114-137.
29. Yoshizawa, M., J.K. Klosterman, and M. Fujita, *Functional molecular flasks: new properties and reactions within discrete, self‐assembled hosts.* Angewandte Chemie International Edition, 2009. **48**(19): p. 3418-3438.
30. Zhang, D., A. Martinez, and J.-P. Dutasta, *Emergence of hemicryptophanes: from synthesis to applications for recognition, molecular machines, and supramolecular catalysis.* Chemical reviews, 2017. **117**(6): p. 4900-4942.
31. Grommet, A.B., et al., *Anion Exchange Drives Reversible Phase Transfer of Coordination Cages and Their Cargoes.* Journal of the American Chemical Society, 2018. **140**(44): p. 14770-14776.
32. Hou, Y.-J., et al., *Design and Enantioresolution of Homochiral Fe (II)–Pd (II) Coordination Cages from Stereolabile Metalloligands: Stereochemical Stability and Enantioselective Separation.* Journal of the American Chemical Society, 2018. **140**(51): p. 18183-18191.
33. Kieffer, M., et al., *Embedding and Positioning of Two FeII4L4 Cages in Supramolecular Tripeptide Gels for Selective Chemical Segregation.* Angewandte Chemie, 2019.
34. Luo, D., X.P. Zhou, and D. Li, *Beyond Molecules: Mesoporous Supramolecular Frameworks Self‐Assembled from Coordination Cages and Inorganic Anions.* Angewandte Chemie International Edition, 2015. **54**(21): p. 6190-6195.
35. Preston, D., J.E. Lewis, and J.D. Crowley, *Multicavity [Pd n L4] 2 n+ Cages with Controlled Segregated Binding of Different Guests.* Journal of the American Chemical Society, 2017. **139**(6): p. 2379-2386.
36. Galan, A. and P. Ballester, *Stabilization of reactive species by supramolecular encapsulation.* Chemical Society Reviews, 2016. **45**(6): p. 1720-1737.
37. Hooley, R.J., et al., *Cavitands with introverted functionality stabilize tetrahedral intermediates.* Journal of the American Chemical Society, 2007. **129**(50): p. 15639-15643.
38. Horiuchi, S., T. Murase, and M. Fujita, *Noncovalent trapping and stabilization of dinuclear ruthenium complexes within a coordination cage.* Journal of the American Chemical Society, 2011. **133**(32): p. 12445-12447.

39. Iwasawa, T., R.J. Hooley, and J. Rebek, *Stabilization of labile carbonyl addition intermediates by a synthetic receptor.* Science, 2007. **317**(5837): p. 493-496.
40. Mal, P., et al., *White phosphorus is air-stable within a self-assembled tetrahedral capsule.* Science, 2009. **324**(5935): p. 1697-1699.
41. Riddell, I.A., T.K. Ronson, and J.R. Nitschke, *Mutual stabilisation between M II 4 L 6 tetrahedra and M II X 4 2− metallate guests.* Chemical science, 2015. **6**(6): p. 3533-3537.
42. Rizzuto, F.J., W.J. Ramsay, and J.R. Nitschke, *Otherwise unstable structures self-assemble in the cavities of cuboctahedral coordination cages.* Journal of the American Chemical Society, 2018. **140**(36): p. 11502-11509.
43. Xi, S.F., et al., *Enhanced Stabilization of G‐Quadruplex DNA by [Ni4L6] 8+ Cages with Large Rigid Aromatic Ligands.* European Journal of Inorganic Chemistry, 2017. **2017**(29): p. 3533-3541.
44. Bianchini, G., et al., *Efficient isonitrile hydration through encapsulation within a hexameric self-assembled capsule and selective inhibition by a photo-controllable competitive guest.* Chemical Communications, 2013. **49**(46): p. 5322-5324.
45. Bräuer, T.M., Q. Zhang, and K. Tiefenbacher, *Iminium Catalysis inside a Self‐Assembled Supramolecular Capsule: Modulation of Enantiomeric Excess.* Angewandte Chemie International Edition, 2016. **55**(27): p. 7698-7701.
46. Bräuer, T.M., Q. Zhang, and K. Tiefenbacher, *Iminium catalysis inside a self-assembled supramolecular capsule: scope and mechanistic studies.* Journal of the American Chemical Society, 2017. **139**(48): p. 17500-17507.
47. Cai, L.-X., et al., *Water-soluble redox-active cage hosting polyoxometalates for selective desulfurization catalysis.* Journal of the American Chemical Society, 2018. **140**(14): p. 4869-4876.
48. Cullen, W., et al., *Catalysis in a cationic coordination cage using a cavity-bound guest and surface-bound anions: inhibition, activation, and autocatalysis.* Journal of the American Chemical Society, 2018. **140**(8): p. 2821-2828.
49. Cullen, W., et al., *Highly efficient catalysis of the Kemp elimination in the cavity of a cubic coordination cage.* Nature chemistry, 2016. **8**(3): p. 231.
50. Gonell, S., et al., *Self-assembled M 12 L 24 nanospheres as a reaction vessel to facilitate a dinuclear Cu (i) catalyzed cyclization reaction.* Chemical science, 2019. **10**(5): p. 1316-1321.
51. Guo, J., et al., *Regio‐and Enantioselective Photodimerization within the Confined Space of a Homochiral Ruthenium/Palladium Heterometallic Coordination Cage.* Angewandte Chemie International Edition, 2017. **56**(14): p. 3852-3856.
52. Holloway, L.R., et al., *Tandem reactivity of a self-assembled cage catalyst with endohedral acid groups.* Journal of the American Chemical Society, 2018. **140**(26): p. 8078-8081.
53. Howlader, P., et al., *Urea-functionalized self-assembled molecular prism for heterogeneous catalysis in water.* Journal of the American Chemical Society, 2016. **138**(5): p. 1668-1676.
54. Jans, A.C., et al., *A Switchable Gold Catalyst by Encapsulation in a Self‐Assembled Cage.* Chemistry‐A European Journal, 2016. **22**(42): p. 14836-14839.
55. Jiao, J., et al., *Design and assembly of chiral coordination cages for asymmetric sequential reactions.* Journal of the American Chemical Society, 2018. **140**(6): p. 2251-2259.
56. Kaphan, D.M., et al., *A supramolecular microenvironment strategy for transition metal catalysis.* Science, 2015. **350**(6265): p. 1235-1238.

57. Kuijpers, P.F., et al., *A self-assembled molecular cage for substrate-selective epoxidation reactions in aqueous media.* ACS Catalysis, 2016. **6**(5): p. 3106-3112.
58. Lee, S.J., et al., *Cavity-tailored, self-sorting supramolecular catalytic boxes for selective oxidation.* Journal of the American Chemical Society, 2008. **130**(50): p. 16828-16829.
59. Levin, M.D., et al., *Scope and mechanism of cooperativity at the intersection of organometallic and supramolecular catalysis.* Journal of the American Chemical Society, 2016. **138**(30): p. 9682-9693.
60. Li, H., et al., *Stepwise construction of discrete heterometallic coordination cages based on self-sorting strategy.* Journal of the American Chemical Society, 2014. **136**(8): p. 2982-2985.
61. Martí-Centelles, V., A.L. Lawrence, and P.J. Lusby, *High activity and efficient turnover by a simple, self-assembled "artificial Diels–Alderase".* Journal of the American Chemical Society, 2018. **140**(8): p. 2862-2868.
62. Murase, T., Y. Nishijima, and M. Fujita, *Cage-catalyzed Knoevenagel condensation under neutral conditions in water.* Journal of the American Chemical Society, 2011. **134**(1): p. 162-164.
63. Noh, T.H., et al., *Motion of an isolated water molecule within a flexible coordination cage: Structural properties and catalytic effects of ionic palladium (II) complexes.* Journal of the American Chemical Society, 2011. **133**(5): p. 1236-1239.
64. Preston, D., et al., *A Nona‐nuclear Heterometallic Pd3Pt6 "Donut"‐Shaped Cage: Molecular Recognition and Photocatalysis.* Angewandte Chemie International Edition, 2018. **57**(28): p. 8659-8663.
65. Ueda, Y., et al., *Permeable self-assembled molecular containers for catalyst isolation enabling two-step cascade reactions.* Journal of the American Chemical Society, 2017. **139**(17): p. 6090-6093.
66. Wang, X., et al., *Tuning the Porphyrin Building Block in Self‐Assembled Cages for Branched‐Selective Hydroformylation of Propene.* Chemistry‐A European Journal, 2017. **23**(59): p. 14769-14777.
67. Yoshizawa, M., et al., *Cavity‐directed, highly stereoselective [2+ 2] photodimerization of olefins within self‐assembled coordination cages.* Angewandte Chemie International Edition, 2002. **41**(8): p. 1347-1349.
68. Yoshizawa, M., M. Tamura, and M. Fujita, *Diels-Alder in aqueous molecular hosts: unusual regioselectivity and efficient catalysis.* Science, 2006. **312**(5771): p. 251-254.
69. Zhang, Q. and K. Tiefenbacher, *Terpene cyclization catalysed inside a self-assembled cavity.* Nature chemistry, 2015. **7**(3): p. 197.
70. Caulder, D.L., et al., *Design, formation and properties of tetrahedral M4L4 and M4L6 supramolecular clusters1.* Journal of the American Chemical Society, 2001. **123**(37): p. 8923-8938.
71. Caulder, D.L., et al., *The self‐assembly of a predesigned tetrahedral M4L6 supramolecular cluster.* Angewandte Chemie International Edition, 1998. **37**(13‐14): p. 1840-1843.
72. Brumaghim, J.L., M. Michels, and K.N. Raymond, *Hydrophobic chemistry in aqueous solution: stabilization and stereoselective encapsulation of phosphonium guests in a supramolecular host.* European Journal of Organic Chemistry, 2004. **2004**(22): p. 4552-4559.

73. Dong, V.M., et al., *Molecular recognition and stabilization of iminium ions in water.* Journal of the American Chemical Society, 2006. **128**(45): p. 14464-14465.
74. Ziegler, M., J.L. Brumaghim, and K.N. Raymond, *Stabilization of a reactive cationic species by supramolecular encapsulation.* Angewandte Chemie International Edition, 2000. **39**(22): p. 4119-4121.
75. Hong, C.M., et al., *Self-assembled tetrahedral hosts as supramolecular catalysts.* Accounts of chemical research, 2018. **51**(10): p. 2447-2455.
76. Pluth, M.D., R.G. Bergman, and K.N. Raymond, *Acid catalysis in basic solution: a supramolecular host promotes orthoformate hydrolysis.* Science, 2007. **316**(5821): p. 85-88.
77. Pluth, M.D., R.G. Bergman, and K.N. Raymond, *Supramolecular catalysis of orthoformate hydrolysis in basic solution: An enzyme-like mechanism.* Journal of the American Chemical Society, 2008. **130**(34): p. 11423-11429.
78. Hart-Cooper, W.M., et al., *Selective monoterpene-like cyclization reactions achieved by water exclusion from reactive intermediates in a supramolecular catalyst.* Journal of the American Chemical Society, 2012. **134**(43): p. 17873-17876.
79. Pluth, M.D., R.G. Bergman, and K.N. Raymond, *Catalytic deprotection of acetals in basic solution with a self‐assembled supramolecular "nanozyme".* Angewandte Chemie International Edition, 2007. **46**(45): p. 8587-8589.
80. Pluth, M.D., R.G. Bergman, and K.N. Raymond, *The acid hydrolysis mechanism of acetals catalyzed by a supramolecular assembly in basic solution.* The Journal of organic chemistry, 2008. **74**(1): p. 58-63.
81. Hastings, C.J., R.G. Bergman, and K.N. Raymond, *Origins of large rate enhancements in the nazarov cyclization catalyzed by supramolecular encapsulation.* Chemistry–A European Journal, 2014. **20**(14): p. 3966-3973.
82. Hastings, C.J., et al., *Enzymelike catalysis of the Nazarov cyclization by supramolecular encapsulation.* Journal of the American Chemical Society, 2010. **132**(20): p. 6938-6940.
83. Hong, C.M., et al., *Deconvoluting the role of charge in a supramolecular catalyst.* Journal of the American Chemical Society, 2018. **140**(21): p. 6591-6595.
84. Hart-Cooper, W.M., et al., *The effect of host structure on the selectivity and mechanism of supramolecular catalysis of Prins cyclizations.* Chemical science, 2015. **6**(2): p. 1383-1393.
85. Pluth, M.D., R.G. Bergman, and K.N. Raymond, *Proton-mediated chemistry and catalysis in a self-assembled supramolecular host.* Accounts of chemical research, 2009. **42**(10): p. 1650-1659.
86. Mal, P., et al., *An unlockable‐relockable iron cage by subcomponent self‐assembly.* Angewandte Chemie International Edition, 2008. **47**(43): p. 8297-8301.
87. Zhang, D., T.K. Ronson, and J.R. Nitschke, *Functional capsules via subcomponent self-assembly.* Accounts of chemical research, 2018. **51**(10): p. 2423-2436.
88. Bolliger, J.L., A.M. Belenguer, and J.R. Nitschke, *Enantiopure water‐soluble [Fe4L6] cages: host‐guest chemistry and catalytic activity.* Angewandte Chemie International Edition, 2013. **52**(31): p. 7958-7962.
89. Salles Jr, A.G., et al., *A self-organizing chemical assembly line.* Journal of the American Chemical Society, 2013. **135**(51): p. 19143-19146.
90. Borch, R.F., M.D. Bernstein, and H.D. Durst, *Cyanohydridoborate anion as a selective reducing agent.* Journal of the American Chemical Society, 1971. **93**(12): p. 2897-2904.

91. Box, V.G. and P.C. Meleties, *Reductive, selective deoxygenation of acylbenzo [b] furans, aromatic aldehydes and ketones with NaBH3CN-TMSCl.* Tetrahedron letters, 1998. **39**(39): p. 7059-7062.
92. Hutchins, R.O. and D. Kandasamy, *Reductions of conjugated carbonyl compounds with cyanoborohydride in acidic media.* The Journal of Organic Chemistry, 1975. **40**(17): p. 2530-2533.
93. Kim, S., et al., *Zinc-modified cyanoborohydride as a selective reducing agent.* The Journal Of Organic Chemistry, 1985. **50**(11): p. 1927-1932.
94. Kouhkan, M. and B. Zeynizadeh, *Wet SiO 2 as a suitable media for fast and efficient reduction of carbonyl compounds with NaBH 3 CN under solvent-free and acid-free conditions.* Bulletin of the Korean Chemical Society, 2010. **31**(10): p. 2961-2966.
95. Pentsak, E.O., et al., *Phantom Reactivity in Organic and Catalytic Reactions as a Consequence of Microscale Destruction and Contamination-Trapping Effects of Magnetic Stir Bars.* ACS Catalysis, 2019. **9**(4): p. 3070-3081.

Chapter 6

Conclusions

There are numerous challenges facing a chemist if they want to use small common molecules as building blocks for more complex chemistry. These difficulties can be as simple as having large bond energies to break; yet they can prove to be significant obstacles. In spite of this, the potential benefits (availability of resources, greener and more sustainable chemistry, and higher reaction efficiency to name a few) continue to encourage interest in various scientific disciplines. We have chosen to investigate three main topics within the confines of small molecule activation: electrocatalysis, electrosynthesis, and supramolecular coordination complex catalysis.

Electrochemical methods of synthesis and catalysis are quite attractive, as they offer a reaction route that relies on an externally applied potential to overcome energy barriers in lieu of traditional chemical methods. As such, electrochemical methods can lessen the need for potentially toxic and/or environmentally hazardous chemicals, or remove the need for them all together. In addition, the control over the applied potential means that reactions can be tuned to specific redox active species, reducing or eliminating unwanted side reactions. As an example of this, we investigated the previously reported ability of Sn(II) phthalocyanines to reduce nitrogen to ammonia. We have shown that they are not electrocatalysts for the reduction of nitrogen to ammonia.[1] There is no evidence for electrocatalysis by cyclic voltammetry, and a similar ammonia yield from electrolysis is obtained under both nitrogen and argon. Ammonia (or species producing ammonia) are present in as-supplied Sn(II) phthalocyanine, and this complex also seems to decompose under cathodic bias. On the basis of these results, we suggest that any apparent ammonia formation is due to the decomposition of (or possible impurities in) the Sn(II) phthalocyanine, and not electro-reduction of N_2 as previously claimed. Evidently the energy barriers associated with the current reaction mechanism are too high to overcome if one wants to keep supposed catalyst molecules from breaking apart under applied potentials

We have also solved the crystal structure of *cis*-2,5-diacetoxy-2,5-dihydrofuran for the first time.[2] During assignment the two isomers of 2,5-diacetoxy-2,5-dihydrofuran to their respective ^{1}H NMR spectra, we determined that previous assignments of the ^{1}H NMR spectra of *cis* and *trans*-2,5-diacetoxy-2,5-dihydrofuran were incorrect. In addition, we have been able to give reliable information on the ratio of these isomers that form during the electrochemical oxidation of furan in acetate electrolytes (a ratio of 7:5 *cis*:*trans* under our conditions). As predicted by a postulated mechanism, the greater steric hindrance led to a shift in stereoselectivity in favour of the *trans* isomer, resulting in a *cis*:*trans* ratio of 9:10. While both chemical and electrochemical produce this mixture of isomers, it goes to show that electrosynthetic procedures can be an invaluable tool in driving reactions to produce specified isomers.

An important factor in using small-molecules for synthesis is the need to control the environment around the molecule itself to facilitate overcoming the at times intimidating energy barriers. The 'gold-star standard' for this mode of action undoubtedly goes to enzymes such as the earlier discussed nitrogenase, which overcomes the impressive N≡N bond energy of 945 kJ mol^{-1}. The method enzymes use to achieve this is to encapsulate their substrates and place them in the right environment to overcome the energy barriers involved in their subsequent reactions. Supramolecular coordination complexes (also known as cages) have been shown to have a similar action, displaying the ability to activate guest molecules within their cavities (the environment of which can differ quite drastically to the bulk solution), and promote acid-catalysed reactions. To this end, we have determined that the Nitschke Fe_4L_6 cage not only sequesters small aromatic aldehydes, but also places them in a conformation that activates the carbonyl for reduction to the corresponding alcohol. Our findings indicate that only a small amount (one 10th molar equivalents) can have conversion yields of up to 75%, comparing with 5% when no cage was present. While the yield varies (by at times an alarming amount), the general trend is that guest molecules with smaller size or electron-withdrawing functional groups convert more readily than those with no electronic effects or larger size.

In summary, we have shown that controlling the environment around a molecule, and providing precise control over redox behavior are useful tools in the investigations of small-molecule activation. While they are important by themselves, it would be interesting to explore the combination of the two; encapsulating a guest to provide a more reactive substrate, followed by the application of the redox potential required for the reaction. In this context, a decorated or functionalized electrode would be very effective, as the very nature of a substrate's encapsulation would put it in contact with the applied potential.

Given more time, it would be ideal to investigate these topics further. Given the importance of ammonia synthesis on the global scale, any yield increase would be extremely beneficial. While it appears that ammonia synthesis does not work via the phthalocyanine route, it would also be interesting to look at whether it is possible to increase the stability of large structures such as phthalocyanine for other transformations, either by directly decorating an electrode, or by creating a more soluble phthalocyanine base. Given the success of cage-based catalysis it would be interesting to ascertain if it were possible to create more of a host-guest system using phthalocyanine (possibly with the use of pendant groups above the metal centre to coordinate associated molecules with) to drive electrosynthesis forward.

While we have shown that stereoselectivity is not only possible *via* electrosynthetic methods, but also quite an effective way of selecting a major isomer. It does beg the question of whether the introduction of a host-guest molecule would be able to further enforce this selectivity or even change the isomer preference. In addition, it raises questions as to what other synthetically important base molecules could be produced electrochemically. Within the same school of thought, it would be prudent to investigate if it were possible to increase the isomer ratio change associated the transformation. Undoubtedly this would require something within the system to try and enforce a stricter geometry for the starting molecule to enforce strict selectivity as a whole.

Finally, an interesting avenue of research to be to determine what environments cage molecules can mimic. While we have proved the ability of them to provide a bulk-acid microenvironment for molecule transformations, it would be intriguing to ascertain the true limits of what cage molecules can achieve. Furthermore, given that the cage-based transformations have so far required the use of a hydride source, it would be an idea to see if electrochemical methods could be used to generate these species in-situ. Lastly, it would be prudent to see if a catalyst embedded within a cage itself would increase the yield of these reactions.

Bibliography

1) **M. A. Shipman** and M. D. Symes, *A re-evaluation of Sn(II) phthalocyanine as a catalyst for the electrosynthesis of ammonia.* Electrochimica Acta, **2017**. 258: p. 618-622.

2) **M. A. Shipman** and M. D. Symes, *Recent progress towards the electrosynthesis of ammonia from sustainable resources.* Catalysis Today, **2017**. 286: p. 57-68

3) **M. A. Shipman**, S. Sproules, C. Wilson and M. D. Symes, *Towards a Better Understanding of the Electrosynthesis of 2,5-dicarboxy-2,5-dihydrofurans: Structure, Mechanism and Influence over Stereochemistry*, Royal Soc. Open Sci, **2019**, 6, 5, 190336.

Chapter 7

Appendices

A5.1 - Supplementary Computational Data

Geometry Optimized Coordinates for Furan

C	-1.80824864713518	1.18328544324190	0.00011953239508
C	-0.37469075882240	1.07750643071161	-0.00010138117473
C	-0.08714155159193	-0.25699783013190	0.00004363692989
O	-1.24815447430304	-0.99513387907364	-0.00001745284793
C	-2.28849117222436	-0.09480797473561	-0.00002977173500
H	-2.40054186472663	2.09347377423108	0.00019764194279
H	0.34447802827272	1.89125230034324	-0.00021466082149
H	0.83460133246966	-0.82864952790133	0.00015737735687
H	-3.28399648193884	-0.52511507568535	-0.00015492204549

Total energy = -229.98146206 E_h

Geometry Optimized Coordinates for Furanium Radical

C	-1.37546756220224	1.86058597676796	0.13889118583408
C	-0.03714131176468	1.54050828105590	0.28585559904490
C	0.06096371172575	0.14666608950156	0.06889551754110
O	-1.16012327287906	-0.38725705425565	-0.20176323860802
C	-2.03947702317764	0.64832551949901	-0.16175055487928
H	-1.85472164882365	2.83044065241948	0.22911335114645
H	0.79540753431498	2.19692740123955	0.51943193739830
H	0.89930225904897	-0.54552750576724	0.07886844115849
H	-3.08116149724242	0.40723972953944	-0.35864919163603

Total energy = – 229.75460866 E_h

Geometry Optimized Coordinates for Furanium Dication

C	-1.33914566742290	1.88614291247649	0.14826737183340
C	-0.01885027288570	1.56192073901730	0.29192474887618
C	0.07493437616790	0.18102023188911	0.07625234416883
O	-1.22207737505797	-0.40048416111189	-0.21513544209537
C	-2.04793883885400	0.57680695469328	-0.17517019715449
H	-1.85107280907828	2.84510155900215	0.23137912572293
H	0.82601967567981	2.20742060682124	0.52673357764649
H	0.89668595221618	-0.54211329405187	0.07994508893994
H	-3.11097385176502	0.38209354126420	-0.36530357093793

Total energy = – 229.38755187 E_h

Cartesian Coordinates for **TS1**

C	-1.375467562	1.860585977	0.138891186
C	-0.037141312	1.540508281	0.285855599
C	0.060963712	0.146666090	0.068895518
O	-1.160123273	-0.387257054	-0.201763239
C	-2.039477023	0.648325520	-0.161750555
H	-1.854721649	2.830440653	0.229113351
H	0.795407534	2.196927402	0.519431937
H	0.899302259	-0.545527506	0.078868441
H	-3.081161498	0.407239730	-0.358649192
O	-0.282547581	0.180596687	4.489137538
C	0.412287991	0.034603866	3.436342144
O	0.050838055	0.351148158	2.259348593
C	1.818831422	-0.578341728	3.582481956
H	2.052505676	-0.826611423	4.625858846
H	2.574039494	0.126186924	3.202235282
H	1.894589779	-1.489659884	2.969402387

Total energy = -458.36740651 E_h

Geometry Optimized Coordinates for 2-Acetylfuranyl Radical

C	-1.48638333037037	1.58841764178893	-0.12077957774466
C	-0.12853358175708	1.42749359117565	0.12182256629350
C	0.10342767444013	-0.00405345718842	0.45770867953988
O	-1.18073897538139	-0.64378169402084	0.28685427106476
C	-2.09306630405854	0.34303081938490	-0.01200107808121
O	0.44950475087082	-0.16979540934410	1.88277530934526
C	1.61817801213295	-0.75230583571833	2.29314411663903
O	1.78689299955278	-0.84711000791430	3.49850958295502
C	2.61626295304655	-1.23080598736280	1.27149664914237
H	-2.00538789870576	2.51311535810562	-0.35890346927573
H	0.65445659515682	2.17987695440035	0.11365381044604
H	0.83607191507893	-0.54741585616931	-0.15011106820177
H	-3.12060059000076	0.01584836218334	-0.13452228712748
H	2.20229688112145	-2.06299324584646	0.68311677461839
H	3.50675944514269	-1.58133599664703	1.80204804552251
H	2.89897389273078	-0.43114814782721	0.57365513786410

Total energy = – 458.40312718 E_h

Geometry Optimized Coordinates for 2-Acetylfuranium

C	-1.59864633197084	1.43612351333527	-0.16920240533906
C	-0.33590203832187	1.67805117649723	0.26236759013765
C	0.32936426408478	0.39202706687443	0.61446330063384
O	-0.79009702368525	-0.62442315024354	0.40815947019756
C	-1.79898037050747	0.02719911964158	-0.06374233694946
O	0.78248072616115	0.33411739055909	1.91375882469501
C	1.80313039457685	-0.58832547073091	2.29290243403328
O	2.11063885911612	-0.54125003856071	3.45463431840178
C	2.36932855818910	-1.48689871232631	1.24108874552746
H	-2.33975287217210	2.14261303474712	-0.52999145281193
H	0.18211070729256	2.63284376706853	0.32981456327194
H	1.06642437029187	0.09799638280963	-0.15102317838163
H	-2.67971251283210	-0.55797289049481	-0.33700105845649
H	1.58433050230597	-2.09457154224282	0.76984962559406
H	3.10133512919021	-2.14597890086042	1.71713570166993
H	2.87206207728101	-0.90451365707337	0.45525332077605

Total energy = -458.23565691 E_h

Cartesian Coordinates for **TS2-t**

C	-1.592972418	1.435963281	-0.185853997
C	-0.330228111	1.677890943	0.245716036
C	0.335038203	0.391866833	0.597811766
O	-0.784423090	-0.624583384	0.391507902
C	-1.793306452	0.027038887	-0.080393935
O	0.788154704	0.333957156	1.897107304
C	1.808804384	-0.588485706	2.276250943
O	2.116312883	-0.541410273	3.437982837
C	2.375002517	-1.487058948	1.224437271
H	-2.334078970	2.142452803	-0.546643066
H	0.187784635	2.632683533	0.313163025
H	1.072098286	0.097836147	-0.167674691
H	-2.674038602	-0.558133123	-0.353652683
H	1.590004448	-2.094731778	0.753198127
H	3.107009103	-2.146139137	1.700484249
H	2.877736013	-0.904673894	0.438601861
O	-1.068454912	-0.421987390	-2.108438770
C	-1.235884475	-0.735793852	-3.327445498
O	-0.310424258	-0.975885944	-4.165323953
C	-2.681709351	-0.838698502	-3.851293864
H	-3.418921816	-0.613720773	-3.069769500
H	-2.866484096	-1.851789192	-4.239607878
H	-2.824486382	-0.143028087	-4.692578657

Total energy = -686.85446843 E_h

Cartesian Coordinates for **TS2-c**

C	-1.592972418	1.435963281	-0.185853997
C	-0.330228111	1.677890943	0.245716036
C	0.335038203	0.391866833	0.597811766
O	-0.784423090	-0.624583384	0.391507902
C	-1.793306452	0.027038887	-0.080393935
O	0.788154704	0.333957156	1.897107304
C	1.808804384	-0.588485706	2.276250943
O	2.116312883	-0.541410273	3.437982837
C	2.375002517	-1.487058948	1.224437271
H	-2.334078970	2.142452803	-0.546643066
H	0.187784635	2.632683533	0.313163025
H	1.072098286	0.097836147	-0.167674691
H	-2.674038602	-0.558133123	-0.353652683
H	1.590004448	-2.094731778	0.753198127
H	3.107009103	-2.146139137	1.700484249
H	2.877736013	-0.904673894	0.438601861
O	-2.502856248	0.047076030	2.001945553
C	-3.371225715	0.136519633	2.924129082
O	-3.125134195	0.273808893	4.163786430
C	-4.857430412	0.075122171	2.520588834
H	-4.984332836	-0.047676226	1.437217704
H	-5.369219289	0.995278427	2.841011168
H	-5.350742721	-0.761841022	3.038506451

Total energy = -686.84963368 E_h

Geometry Optimized Coordinates for *trans*-2,5-diacetoxy-2,5-dihydrofuran

C	-1.16188681483011	2.65806055702918	0.19892864367968
C	0.05182559377903	2.31088361174873	0.62487245204403
C	0.22004810117031	0.82573265673963	0.50748459281452
O	-1.00190255822555	0.34751159159462	-0.05584491881233
C	-1.89235195709133	1.44053536908628	-0.28377561942716
O	-2.12153097839456	1.59173821661760	-1.71125148254906
H	-1.59963616924252	3.65332550017193	0.16526031364183
H	0.83230191709904	2.95769394115257	1.01952259951963
H	1.06879945816188	0.50646525977400	-0.11267122488642
H	-2.85273483840374	1.25132453923867	0.21428057646828
O	0.38359459222412	0.28351624602545	1.84576538321577
C	0.85098649986012	-0.99764467629276	2.02830794761875
O	0.94032612998005	-1.38642332075066	3.17950314068857
C	1.21637357941986	-1.82057183906698	0.82353567545207
C	-3.01955522145056	0.77933085279274	-2.36435273258420
C	-3.79146634082239	-0.24081512336656	-1.57279276957992
O	-3.13513636484826	0.94850493928437	-3.56528771377764
H	0.37430841387465	-1.89115687226279	0.12143763837446
H	1.50164729279713	-2.82128458417193	1.16020325857485
H	2.06313323881584	-1.36685907085769	0.28750801847888
H	-4.47235688952017	0.25678174074110	-0.86613273369490
H	-3.12138790205308	-0.88753223223116	-0.99095506833081
H	-4.38041440429974	-0.84595413899631	-2.26859095692887

Total energy = -686.90202676 E_h

Geometry Optimized Coordinates for *cis*-2,5-diacetoxy-2,5-dihydrofuran

C	-1.29787539536271	2.16900305239171	-0.58160221923907
C	-0.02424253862330	1.96484979642927	-0.24575811227983
C	0.15351279872392	0.54558664654466	0.20407072056486
O	-1.10869404050805	-0.08466387900383	-0.02223678851610
C	-2.07578631396932	0.90205925658421	-0.38448640558030
O	-3.02802894834537	1.12475419869815	0.69163180327801
H	-1.75940549603715	3.09050698697197	-0.92897371462735
H	0.79369627511426	2.68216374184082	-0.25419667597166
H	0.92148248901055	-0.01755309955241	-0.34068226920453
H	-2.61241662467693	0.54720830107437	-1.27331818807751
O	0.48977762539329	0.56548462911073	1.61857463924666
C	0.99919429639763	-0.55480127401026	2.23338159085233
O	1.24051441507686	-0.46257567706722	3.42398784908668
C	1.22322585504136	-1.79808324677748	1.41680715631590
C	-4.08802466723540	0.26868299722569	0.87837965056345
O	-4.82214685439851	0.50643476235507	1.82138196737499
C	-4.27902829280533	-0.87863426066729	-0.07562988799449
H	0.30609247228562	-2.10134160072251	0.89446238211558
H	1.54881495911764	-2.59869153340447	2.08759936719740
H	2.00183711525004	-1.62778862439241	0.65833825697609
H	-5.11087294302964	-1.49251544287013	0.28328701602399
H	-3.37150731428548	-1.49234843182660	-0.15387382097079
H	-4.52034773713398	-0.50582323493207	-1.08191811213430

Total energy = -686.90273226 E_h

A5.2 - Additional single crystal crystallographic data for *cis*-2,5-diacetoxy-2,5-dihydrofuran

Refinement

Crystal data, data collection and structure refinement details are summarized in Table 1.

Computing details

Data collection: *APEX3* Ver. 2016.9-0 (Bruker-AXS, 2016); cell refinement: *SAINT* V8.37A (Bruker-AXS, 2016); data reduction: *APEX3* Ver. 2016.9-0 (Bruker-AXS, 2016); program(s) used to solve structure: XT (Sheldrick, 2015); program(s) used to refine structure: XL (Sheldrick, 2008); molecular graphics: Olex2 (Dolomanov *et al.*, 2009); software used to prepare material for publication: Olex2 (Dolomanov *et al.*, 2009).

(2018gu0020_150k_r1)

Crystal data

$C_8H_{10}O_5$	$F(000) = 392$
$M_r = 186.16$	$D_x = 1.381$ Mg m^{-3}
Monoclinic, $P2_1/c$	Mo $K\alpha$ radiation, $\lambda = 0.71073$ Å
$a = 11.7447$ (17) Å	Cell parameters from 5942 reflections
$b = 9.7503$ (12) Å	$\theta = 2.7$–$25.3°$
$c = 7.8734$ (10) Å	$\mu = 0.12$ mm^{-1}
$\beta = 96.676$ (5)°	$T = 150$ K
$V = 895.5$ (2) Å^3	Block, colourless
$Z = 4$	0.32 × 0.2 × 0.11 mm

Data collection

Bruker D8 VENTURE diffractometer	1631 independent reflections
Radiation source: microfocus sealed tube, INCOATEC Iμs 3.0	1517 reflections with $I > 2\sigma(I)$
Multilayer mirror optics monochromator	$R_{\text{int}} = 0.025$
Detector resolution: 7.4074 pixels mm^{-1}	$\theta_{\max} = 25.3°$, $\theta_{\min} = 2.7°$
ϕ and ω scans	$h = -12 \rightarrow 14$
Absorption correction: multi-scan *SADABS2016*/2 (Bruker,2016/2) was used for absorption correction. wR2(int) was 0.1582 before and 0.0643 after correction. The Ratio of minimum to maximum transmission is 0.8875. The λ/2 correction factor is Not present.	$k = -11 \rightarrow 11$
$T_{\min} = 0.661$, $T_{\max} = 0.745$	$l = -9 \rightarrow 9$
6125 measured reflections	

Refinement

Refinement on F^2	Primary atom site location: dual
Least-squares matrix: full	Hydrogen site location: inferred from neighbouring sites
$R[F^2 > 2\sigma(F^2)] = 0.040$	H-atom parameters constrained
$wR(F^2) = 0.107$	$w = 1/[\sigma^2(F_o^2) + (0.0445P)^2 + 0.554P]$ where $P = (F_o^2 + 2F_c^2)/3$
$S = 1.10$	$(\Delta/\sigma)_{max} = 0.001$
1631 reflections	$\Delta\rangle_{max} = 0.36$ e Å^{-3}
120 parameters	$\Delta\rangle_{min} = -0.25$ e Å^{-3}
0 restraints	

Fractional atomic coordinates and isotropic or equivalent isotropic displacement parameters (Å^2)

	x	y	z	U_{iso}*/U_{eq}
O1	0.27502 (10)	0.45847 (11)	0.20054 (14)	0.0260 (3)
O2	0.39227 (9)	0.65113 (11)	0.25709 (14)	0.0268 (3)
O3	0.54271 (11)	0.51178 (13)	0.23740 (17)	0.0367 (3)
O4	0.14957 (10)	0.52238 (11)	0.39486 (14)	0.0270 (3)
O5	0.11600 (11)	0.30235 (12)	0.45999 (17)	0.0364 (3)
C2	0.15928 (14)	0.48707 (17)	0.2187 (2)	0.0249 (4)
H2	0.108113	0.408574	0.179267	0.030*
C3	0.13112 (14)	0.61265 (17)	0.1134 (2)	0.0278 (4)
H3	0.056790	0.651233	0.088365	0.033*
C4	0.22511 (15)	0.66125 (17)	0.0609 (2)	0.0282 (4)
H4	0.229359	0.740379	-0.008498	0.034*
C5	0.32422 (14)	0.57320 (17)	0.1268 (2)	0.0255 (4)
H5	0.370093	0.545145	0.033274	0.031*
C6	0.50173 (14)	0.60878 (17)	0.3021 (2)	0.0256 (4)
C7	0.56068 (16)	0.69836 (19)	0.4384 (2)	0.0352 (4)
H7A	0.529621	0.791561	0.425588	0.053*
H7B	0.643053	0.700262	0.428329	0.053*
H7C	0.548128	0.662185	0.550831	0.053*
C8	0.13694 (13)	0.41800 (17)	0.5055 (2)	0.0252 (4)
C9	0.15346 (15)	0.46831 (19)	0.6857 (2)	0.0317 (4)
H9A	0.233709	0.494960	0.715955	0.048*
H9B	0.133661	0.395190	0.762455	0.048*
H9C	0.103850	0.547820	0.696982	0.048*

Atomic displacement parameters (Å^2)

	U^{11}	U^{22}	U^{33}	U^{12}	U^{13}	U^{23}
O1	0.0276 (6)	0.0195 (6)	0.0308 (6)	0.0027 (4)	0.0032 (5)	0.0007 (5)
O2	0.0262 (6)	0.0251 (6)	0.0292 (6)	0.0009 (5)	0.0033 (5)	-0.0041 (5)
O3	0.0332 (7)	0.0334 (7)	0.0433 (7)	0.0074 (5)	0.0034 (6)	-0.0061 (6)
O4	0.0352 (7)	0.0214 (6)	0.0247 (6)	-0.0035 (5)	0.0048 (5)	-0.0029 (5)
O5	0.0470 (8)	0.0230 (6)	0.0390 (7)	-0.0075 (5)	0.0043 (6)	-0.0005 (5)
C2	0.0268 (8)	0.0240 (8)	0.0235 (8)	-0.0005 (6)	0.0011 (6)	-0.0037 (6)
C3	0.0286 (9)	0.0293 (9)	0.0244 (8)	0.0058 (7)	-0.0025 (6)	-0.0033 (7)
C4	0.0385 (10)	0.0247 (8)	0.0210 (8)	0.0045 (7)	0.0013 (7)	0.0022 (7)
C5	0.0301 (9)	0.0242 (8)	0.0225 (8)	0.0001 (7)	0.0044 (6)	-0.0013 (6)
C6	0.0258 (8)	0.0245 (8)	0.0273 (8)	-0.0004 (7)	0.0068 (7)	0.0044 (7)
C7	0.0363 (10)	0.0316 (9)	0.0363 (10)	-0.0021 (8)	-0.0019 (7)	-0.0005 (8)
C8	0.0194 (8)	0.0264 (9)	0.0299 (8)	-0.0008 (6)	0.0033 (6)	0.0014 (7)
C9	0.0330 (9)	0.0347 (10)	0.0277 (9)	-0.0037 (7)	0.0050 (7)	0.0008 (7)

Geometric parameters (Å, º) for (2018gu0020_150k_r1)

O1—C2	1.4110 (19)	C4—H4	0.9500
O1—C5	1.414 (2)	C4—C5	1.490 (2)
O2—C5	1.4413 (19)	C5—H5	1.0000
O2—C6	1.358 (2)	C6—C7	1.490 (2)
O3—C6	1.201 (2)	C7—H7A	0.9800
O4—C2	1.4463 (19)	C7—H7B	0.9800
O4—C8	1.359 (2)	C7—H7C	0.9800
O5—C8	1.200 (2)	C8—C9	1.493 (2)
C2—H2	1.0000	C9—H9A	0.9800
C2—C3	1.494 (2)	C9—H9B	0.9800
C3—H3	0.9500	C9—H9C	0.9800
C3—C4	1.312 (2)		
C2—O1—C5	109.25 (12)	C4—C5—H5	111.5
C6—O2—C5	117.09 (12)	O2—C6—C7	110.87 (14)
C8—O4—C2	117.57 (12)	O3—C6—O2	122.87 (15)
O1—C2—O4	109.18 (12)	O3—C6—C7	126.26 (16)
O1—C2—H2	111.6	C6—C7—H7A	109.5
O1—C2—C3	105.03 (13)	C6—C7—H7B	109.5
O4—C2—H2	111.6	C6—C7—H7C	109.5
O4—C2—C3	107.46 (13)	H7A—C7—H7B	109.5
C3—C2—H2	111.6	H7A—C7—H7C	109.5
C2—C3—H3	125.3	H7B—C7—H7C	109.5

C4—C3—C2	109.32 (15)	O4—C8—C9	110.57 (14)
C4—C3—H3	125.3	O5—C8—O4	123.13 (15)
C3—C4—H4	125.2	O5—C8—C9	126.30 (16)
C3—C4—C5	109.51 (15)	C8—C9—H9A	109.5
C5—C4—H4	125.2	C8—C9—H9B	109.5
O1—C5—O2	110.14 (12)	C8—C9—H9C	109.5
O1—C5—C4	105.00 (13)	H9A—C9—H9B	109.5
O1—C5—H5	111.5	H9A—C9—H9C	109.5
O2—C5—C4	106.87 (13)	H9B—C9—H9C	109.5
O2—C5—H5	111.5		
O1—C2—C3—C4	-8.05 (18)	C5—O1—C2—O4	-101.54 (14)
O4—C2—C3—C4	108.12 (15)	C5—O1—C2—C3	13.45 (16)
C2—O1—C5—O2	101.13 (14)	C5—O2—C6—O3	0.7 (2)
C2—O1—C5—C4	-13.59 (16)	C5—O2—C6—C7	-179.57 (13)
C2—O4—C8—O5	-11.8 (2)	C6—O2—C5—O1	84.18 (16)
C2—O4—C8—C9	167.82 (13)	C6—O2—C5—C4	-162.30 (13)
C2—C3—C4—C5	-0.26 (18)	C8—O4—C2—O1	-86.10 (16)
C3—C4—C5—O1	8.45 (17)	C8—O4—C2—C3	160.49 (13)
C3—C4—C5—O2	-108.53 (15)		

Document origin: *publCIF*.[S]

Special details

Geometry. All esds (except the esd in the dihedral angle between two l.s. planes) are estimated using the full covariance matrix. The cell esds are taken into account individually in the estimation of esds in distances, angles and torsion angles; correlations between esds in cell parameters are only used when they are defined by crystal symmetry. An approximate (isotropic) treatment of cell esds is used for estimating esds involving l.s. planes.

References

- Dolomanov, O. V., Bourhis, L. J., Gildea, R. J., Howard, J. A. K. & Puschmann, H. (2009). *J. Appl. Cryst.* **42**, 339–341.
- Sheldrick, G. M. (2008). *Acta Cryst.* A**64**, 112–122.
- Sheldrick, G. M. (2015). *Acta Cryst.* A**71**, 3–8.